Structures Research
Report 2012 / 72909-
74040

University of Florida
Civil and Coastal Engineering

UF

GATOR Engineering
University of Florida
Civil and Coastal Engineering

Final Report December 2012

Experimental Validation Of Bracing Recommendations For Long-Span Concrete Girders

Principal investigators:
Gary R. Consolazio, Ph.D.
H. R. (Trey) Hamilton, III, Ph.D., P.E.

Graduate research assistant:
Megan Salvetti Beery

Department of Civil and Coastal Engineering
University of Florida
P.O. Box 116580
Gainesville, Florida 32611

Sponsor:
Florida Department of Transportation (FDOT)

Contract:
UF Project Nos. 00072909 and 00074040
FDOT Contract No. BDK75 977-03

DISCLAIMER

SI (MODERN METRIC) CONVERSION FACTORS

*APPROXIMATE CONVERSIONS **TO** SI UNITS*

SYMBOL	WHEN YOU KNOW	MULTIPLY BY	TO FIND	SYMBOL
LENGTH				
in	inches	25.4	millimeters	mm
ft	feet	0.305	meters	m
yd	yards	0.914	meters	m
mi	miles	1.61	kilometers	km
AREA				
in^2	square inches	645.2	square millimeters	mm^2
ft^2	square feet	0.093	square meters	m^2
yd^2	square yard	0.836	square meters	m^2
ac	acres	0.405	hectares	ha
mi^2	square miles	2.59	square kilometers	km^2
VOLUME				
fl oz	fluid ounces	29.57	milliliters	mL
gal	gallons	3.785	liters	L
ft^3	cubic feet	0.028	cubic meters	m^3
yd^3	cubic yards	0.765	cubic meters	m^3
NOTE: volumes greater than 1000 L shall be shown in m^3				
MASS				
oz	ounces	28.35	grams	g
lb	pounds	0.454	kilograms	kg
T	short tons (2000 lb)	0.907	Megagrams	Mg (or "t")
TEMPERATURE (exact degrees)				
^oF	Fahrenheit	5(F-32)/9 or (F-32)/1.8	Celsius	^oC
ILLUMINATION				
fc	foot-candles	10.76	lux	lx
fl	foot-Lamberts	3.426	candela/m^2	cd/m^2
FORCE and PRESSURE or STRESS				
kip	1000 pound force	4.45	Kilonewtons	kN
lbf	pound force	4.45	newtons	N
lbf/in^2	pound force per square inch	6.89	kilopascals	kPa

Technical Report Documentation Page

1. Report No.	2. Government Accession No.	3. Recipient's Catalog No.
4. Title and Subtitle Experimental Validation Of Bracing Recommendations For Long-Span Concrete Girders		5. Report Date December 2012 6. Performing Organization Code 8. Performing Organization Report No.
7. Author(s) Gary R. Consolazio, H.R. (Trey) Hamilton, Megan Salvetti Beery		2012/72909-74040
9. Performing Organization Name and Address University of Florida Department of Civil and Coastal Engineering 365 Weil Hall, P.O. Box 116580 Gainesville, FL 32611-6580		10. Work Unit No. (TRAIS) 11. Contract or Grant No. BDK75 977-03
12. Sponsoring Agency Name and Address Florida Department of Transportation Research Management Center 605 Suwannee Street, MS 30 Tallahassee, FL 32399-0450		13. Type of Report and Period Covered Final Report April 2008 – November 2012 14. Sponsoring Agency Code
15. Supplementary Notes		

16. Abstract

During bridge construction, flexible support conditions provided by steel-reinforced neoprene bearing pads supporting precast, prestressed concrete girders may allow the girders to become unstable, rolling about an axis parallel to the span of the girders. Additionally, skew and/or slope angles significantly reduce bearing pads roll stiffness, which reduces girder buckling capacity under gravity and wind loading conditions.

In this project, roll stiffnesses for bearing pads under skewed and sloped conditions were determined from experimental data gathered using a test device designed to measure such values. The test device reproduced the forces and deformations that act on a bearing pad in the field while simultaneously permitting axial load, skew angle, and slope angle to be controlled independently, so that the effect of each on bearing pad roll stiffness could be quantified. In total, 108 bearing pad tests were performed on three different standard types of bearing pad, with varying severities of imposed skew and slope angle.

Full-scale girder buckling tests, designed and conducted to experimentally quantify the influence of bearing pad roll stiffness on girder buckling capacity, were also included in this project. The pads used to support each end of the test girder during the buckling tests were the same pads previously tested to determine roll stiffness. In total, nine girder buckling tests were conducted, with various skew and slope conditions imposed on the bearing pads.

Following completion of the experimental tests, analytical (finite element) models of the experimental test conditions were developed and validated by comparing buckling capacities quantified from analytical simulations to experimental test results. Analytical buckling capacities were found to differ from experimental test results by no more than 15% over a range of ideal, skewed, and sloped bearing pad support conditions. Based on this favorable level of agreement, the analytical modeling and analysis techniques employed in this study were deemed suitable for use in developing bracing recommendations for long-span concrete girders supported on reinforced elastomeric bearing pads.

17. Key Words Bridge construction, bearing pad, skew, slope, roll stiffness, girder stability, buckling capacity, experimental testing, finite element analysis	18. Distribution Statement No restrictions.

19. Security Classif. (of this report)	20. Security Classif. (of this page)	21. No. of Pages	22. Price
Unclassified	Unclassified	200	

Form DOT F 1700.7 (8-72). Reproduction of completed page authorized

ACKNOWLEDGEMENTS

The authors thank the Florida Department of Transportation (FDOT) for providing the funding that made this research possible. Additionally, the authors acknowledge the significant contributions made by FDOT Structures Research Center personnel. The following individuals contributed greatly to the success of this project by providing technical insights and suggestions; fabricating and constructing testing-systems and test-articles; providing data acquisition; and conducting tests: the late Marcus Ansley, Sam Fallaha, David Wagner, William Potter, Stephen Eudy, Chris Weigly, Paul Tighe, Tony Hobbs, David Allen, Frank Cobb, and several others.

EXECUTIVE SUMMARY

During bridge construction, flexible support conditions provided by steel-reinforced neoprene bearing pads supporting precast, prestressed concrete girders may allow the girders to become unstable, rolling about an axis parallel to the span of the girders. Additionally, skew and/or slope angles significantly reduce bearing pads roll stiffness, which reduces girder buckling capacity under gravity and wind loading conditions.

In this project, roll stiffnesses for bearing pads under skewed and sloped conditions were determined from experimental data gathered using a test device designed to measure such values. The test device reproduced the forces and deformations that act on a bearing pad in the field while simultaneously permitting axial load, skew angle, and slope angle to be controlled independently, so that the effect of each on bearing pad roll stiffness could be quantified. In total, 108 bearing pad tests were performed on three different standard types of bearing pad, with varying severities of imposed skew and slope angle.

Full-scale girder buckling tests, designed and conducted to experimentally quantify the influence of bearing pad roll stiffness on girder buckling capacity, were also included in this project. The pads used to support each end of the test girder during the buckling tests were the same pads previously tested to determine roll stiffness. In total, nine girder buckling tests were conducted, with various skew and slope conditions imposed on the bearing pads.

Following completion of the experimental tests, analytical (finite element) models of the experimental test conditions were developed and validated by comparing buckling capacities quantified from analytical simulations to experimental test results. Analytical buckling capacities were found to differ from experimental test results by no more than 15% over a range of ideal, skewed, and sloped bearing pad support conditions. Based on this favorable level of agreement, the analytical modeling and analysis techniques employed in this study were deemed suitable for use in developing bracing recommendations for long-span concrete girders supported on reinforced elastomeric bearing pads.

TABLE OF CONTENTS

LIST OF FIGURES

LIST OF TABLES

CHAPTER 1
INTRODUCTION

1.1 Introduction

Precast, pretensioned concrete bridge girders in simple span construction are typically supported on reinforced neoprene bearing pads (Figure 1.1a). Neoprene bearing pads transfer vertical load from the girder to the support and allow lateral movement of the girder, which can be caused by thermal expansion and contraction. The self-weight of the girder is gradually applied to the bearing pad during girder placement. Before diaphragm or deck installation, the girder may become unstable and rotate about an axis parallel to the span of the girder (Figure 1.1b). Bearing pad roll stiffness, combined with the effects of bracing stiffness and torsional buckling, dictates the point of girder instability under girder self-weight (gravity) loading. In the case of girders supported by reinforced neoprene bearing pads, the roll stiffness of the end restraints can be severely reduced by skew angle (Figure 1.2) and slope angle (Figure 1.3). According to the Precast Concrete Institute (PCI) Bridge Design Manual (2003), skew angle is defined as the angle between the centerline of a support and a line normal to the roadway centerline (Figure 1.2). Slope angle is defined as the vertical angle between the bottom surface of the girder and the top surface of the bearing pad (Figure 1.3), and may be produced by camber (induced by eccentric prestressing of the girder), construction tolerances, bridge grade, or a combination of all three. Previous analytical research (Consolazio et al. 2007) was conducted to analytically quantify the roll stiffness of bearing pads under various angles of skew and slope. In that study, it was found that the roll stiffness of bearing pads—and therefore the buckling capacity of bridge girders—is significantly reduced by the imposition of skew and slope angles.

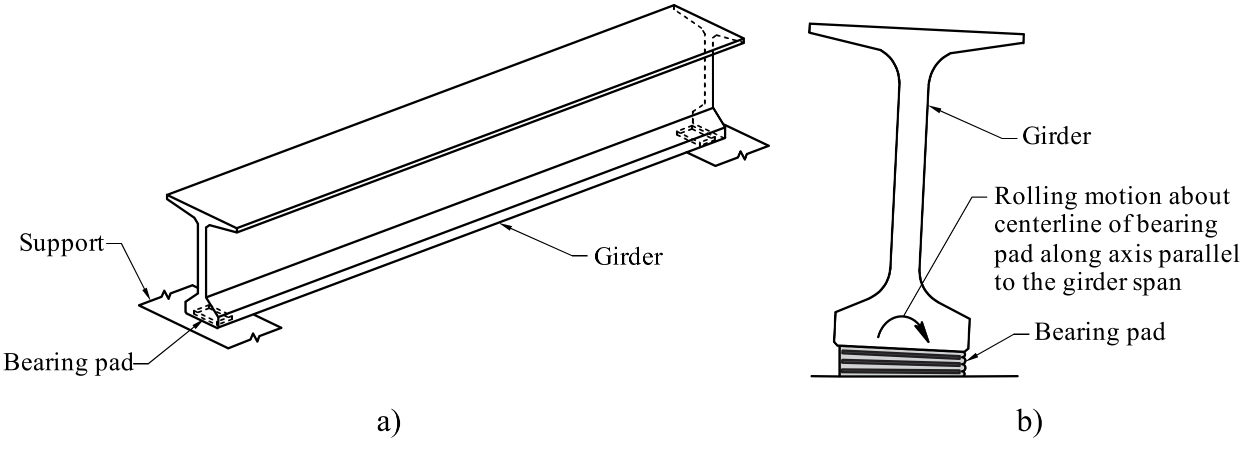

a) b)

Figure 1.1. Description of physical system: a) Girder supported on bearing pads during bridge construction; b) Rolling motion of girder that occurs during instability (buckling)

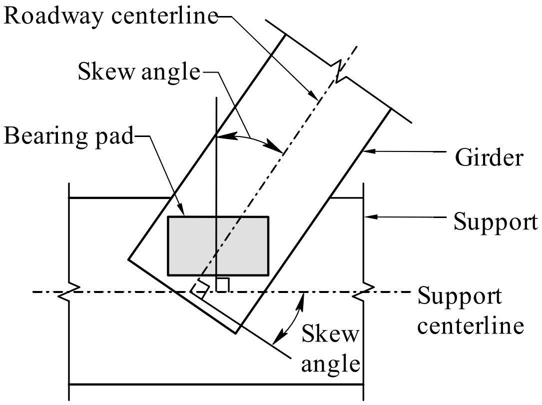

Figure 1.2. Plan view of girder, pad, and support with skew angle defined

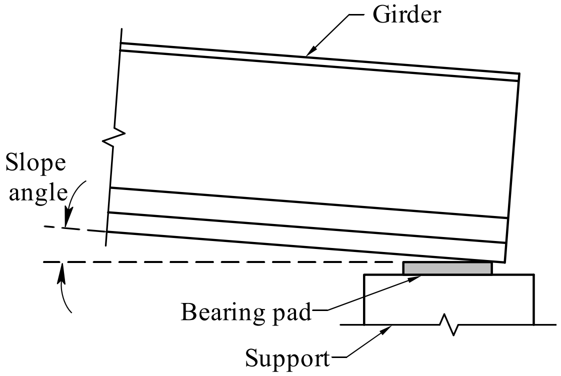

Figure 1.3. Elevation view of girder, pad, and support with slope angle defined

1.2 Objective

The research presented in this report was conducted to experimentally expand upon the previous analytical research (Consolazio et al. 2007) conducted to determine the effect of imposed skew and slope angles on the roll stiffness of bearing pads and the buckling capacity of girders supported on bearing pads. There were two distinct phases of the work presented in this report: isolated roll stiffness tests, and girder buckling tests. In the isolated roll stiffness tests, roll stiffnesses for bearing pads under skew and slope conditions were determined from experimental data gathered using a test device designed to measure such values. In the second phase, a full-scale girder buckling test program was designed and conducted to experimentally quantify the influence of bearing pad roll stiffness on girder buckling capacity. The pads used to support each end of the test girder were the same pads previously tested—to determine roll stiffness—in the first (roll stiffness) phase of this study.

1.3 Scope

In the first phase of this study, an experimental test device was developed to enable determination of bearing pad roll stiffness under the types of loading conditions that arise during bridge construction. The bearing pad test device reproduced the forces acting on a bearing pad in the field while simultaneously permitting axial load, skew angle, and slope angle to be controlled independently, so that the effect of each on bearing pad roll stiffness could be quantified. A total of 108 tests were performed on three different standard types of bearing pad, with varying severity of imposed skew and slope angle.

The second phase of this study, included the design and construction of: a full-scale test girder; a vertical loading system; and end supports that enabled various combinations of slope and skew to be imposed on the supporting bearing pads. In total, nine (9) buckling tests were conducted, with various skew and slope conditions imposed on the supporting bearing pads.

All experimental tests, including both the first phase isolated bearing pad tests and second phase full-scale girder buckling tests, were performed at the Florida Department of Transportation (FDOT) Marcus H. Ansley Structures Research Center in Tallahassee, Florida.

Analytical (finite element) models of the experimental test conditions were developed and used to simulate the experimental buckling tests. Validation of the models was then carried out by comparing buckling capacities quantified from analytical simulations to experimental test results.

CHAPTER 2
BACKGROUND

2.1 Literature review

Although the roll stiffness of a bearing pad is important in regard to girder instability during the construction process, most research to date has focused on bearing pad stiffnesses that relate to the final constructed configuration of the bridge. The influence of roll stiffness of bearing pads on girder instability during the construction stage has not been adequately explored. Similarly, several research programs have conducted experimental tests to investigate girder instability, but focused primarily on lateral torsional buckling. The effect of reduced bearing pad roll stiffness—due to skew and slope angles—on girder buckling capacity has not yet been quantified in the literature.

2.2 Bearing pad properties

Isolated experimental bearing pad tests have been conducted to quantify bearing pad stiffness parameters, such as the effect of shear strain rate on the shear modulus of bearing pads (Allen et al., 2010), stress capacities and stress-strain limits of cotton duck bridge bearing pads in shear, compression, and rotation (Lehman et al., 2005), and long term load effects on bearing performance (Doody and Noonan, 1999). Muscarella and Yura (1995) also experimentally analyzed isolated bearing pads to determine the shear, compressive, and rotational stiffnesses, with emphasis on the difference in behavior of flat and tapered bearings. However, the rotational stiffness they calculated was about an axis perpendicular to the span of the girder, or a rotation induced by service loads, as opposed to girder instability during construction. Similarly, Vidot-Vega et al. (2009) experimentally determined the rotational stiffness of multiple bearing pads resisting moment in series due to rotation about an axis perpendicular to the span of the girder, using a test device comprised of a continuous span over the support, pertaining to the final constructed configuration of the bridge.

Using analytical modeling, Yazdani et al. (2000) computed bearing pad shear, axial, and roll stiffnesses to determine the effect of neoprene bearing pads on the performance of fully constructed precast prestressed concrete bridges. Green et al. (2001) focused on the effect of skew angle on the performance of the final constructed bridge, examining the deflection and tensile stresses in girders with varying severity of skew, also through the use of analytical models. The current study, therefore, is unique in that it focused on experimentally evaluating the influence of imposed skew and slope angles on the roll stiffness—about an axis parallel to the girder span—of bearing pads as related to girder instability during the construction process.

2.3 Girder buckling

As previously stated, several experimental tests have been conducted to investigate girder instability, including lateral torsional buckling testing of steel I-shapes (Yura and Phillips, 1992), lateral-torsional buckling behavior of fiber reinforced polymer I-shaped cross-sections (Stoddard, 1997), and lateral stability of slender rectangular reinforced concrete beams (Kalkan, 2009). Deaver (2003) investigated torsional bracing by simulating buckling of a two-beam system with midspan bracing. Mast examined the lateral bending stability of prestressed concrete beams when they are suspended from lifting loops (Mast 1989) and supported below by elastomeric bearing pads and on trucks and tractors (Mast 1993). Lateral-torsional buckling and rollover instability of prestressed concrete girders supported on bearing pads was investigated by Hurff (2010). However, Hurff focused on the instability due to girder self-weight eccentricity caused by fabrication imperfections (prestress eccentricity, cracking, solar radiation) and support conditions (unlevel bearing surface).

The current study, therefore, is unique in that experimental tests were performed to quantify the influence of bearing pad roll stiffness on the buckling capacity of a test girder, which was supported on bearing pads with known roll stiffnesses under skewed and sloped conditions.

CHAPTER 3
BEARING PAD ROLL STIFFNESS DETERMINATION

3.1 Experimental test setup

In this study, an experimental test device (Figure 3.1) was developed to enable determination of bearing pad roll stiffness under the types of loading conditions that arise during bridge construction. A key aspect in the design of the test device was the need to maintain a constant axial load on the bearing pad (to simulate constant gravity-induced girder reactions) as roll rotation of the pad occurred. Equally important, the test device was designed to be capable of simulating girder support conditions in which skew, slope, or combined skew and slope were present.

A structural tube within the device represented the bridge girder axis and was used to impose, and hold constant, the slope angle and the axial load on the pad. Two 5 in. thick steel bearing plates at the center of the test device, which were effectively rigid in comparison to the stiffness of the bearing pad, represented the bottom surface of the girder and the top surface of the bridge abutment, respectively. Simulating a skewed alignment between girder and bearing pad was achieved by positioning the pad at the desired skew angle (relative to the axis of the tube) between the steel bearing plates. To simulate girder roll-off, load was applied to the outriggers of the test frame, which rotated the device about the centerline of the bearing pad, parallel to the axis of the tube. Hinges located below the ends of the tube allowed the testing frame to rotate freely. As constructed, the test device was capable of imposing desired combinations of axial load, skew angle, and slope angle on the bearing pad for the purpose of evaluating pad roll stiffness. Detailed fabrication plans for the bearing pad test device are provided in Appendix A.

Each bearing pad test conducted in this study consisted of three stages: positioning, clamping, and rolling. In the positioning stage, the bearing pad and test device were configured to impose the desired skew and slope angles on the pad. Subsequently, axial load was gradually applied to the bearing pad—by applying clamp loads to the top surfaces of both ends of the tube—until a target axial load on the pad was achieved (Figure 3.2a). Holding the axial load constant, a moment was then applied to the test device—through application of vertical roll loads acting at the ends of the outriggers (Figure 3.2b)—to produce a roll rotation on the pad, thereby simulating the unrestrained rolling motion of a girder during instability (buckling) in the field. For each test thus performed, bearing pad roll stiffness was quantified by determining the slope of the linear relationship between moment imposed on the pad, and the resulting measured roll angle.

Rotations and loads imposed on the pad during each of these stages were identified using coordinate axes defined in Figure 3.1. Examining the global x-y-z coordinate system, both the x- and y-axes were level (horizontal), had their origins at the top surface of the undeformed bearing pad, and were aligned with the centerlines of the outriggers and tube, respectively. The global z-axis was aligned vertically; positive upward.

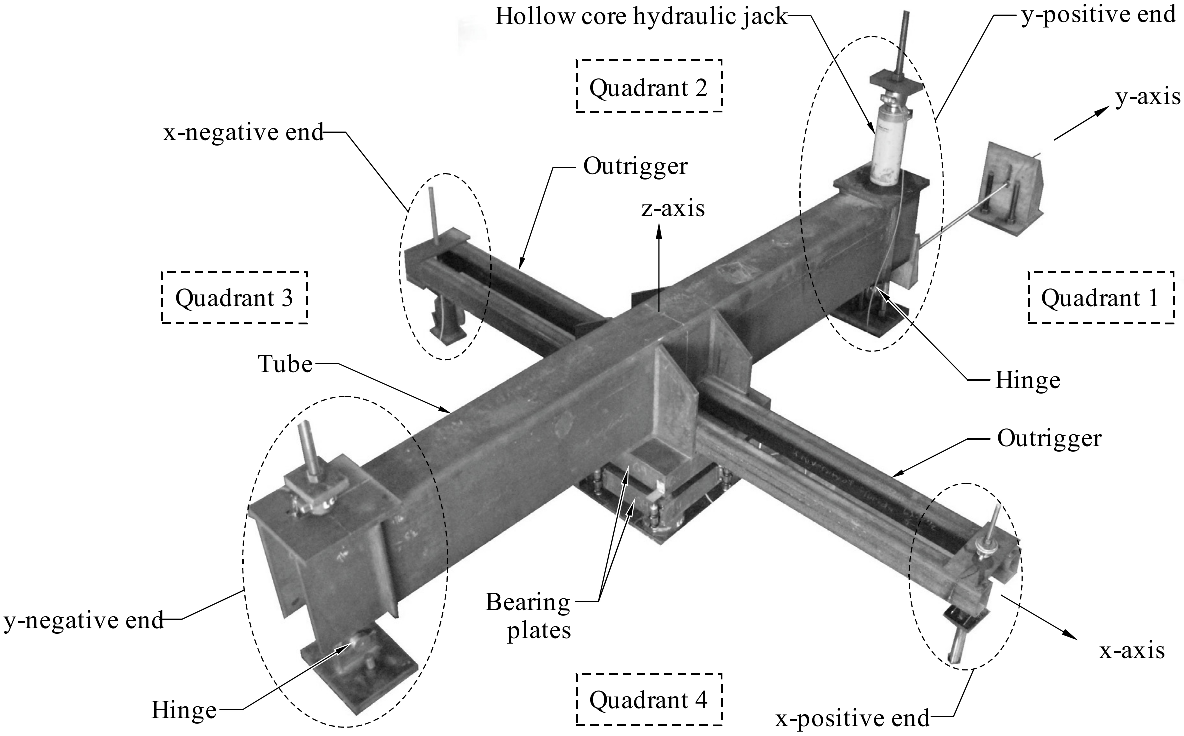

Figure 3.1. Bearing pad test device

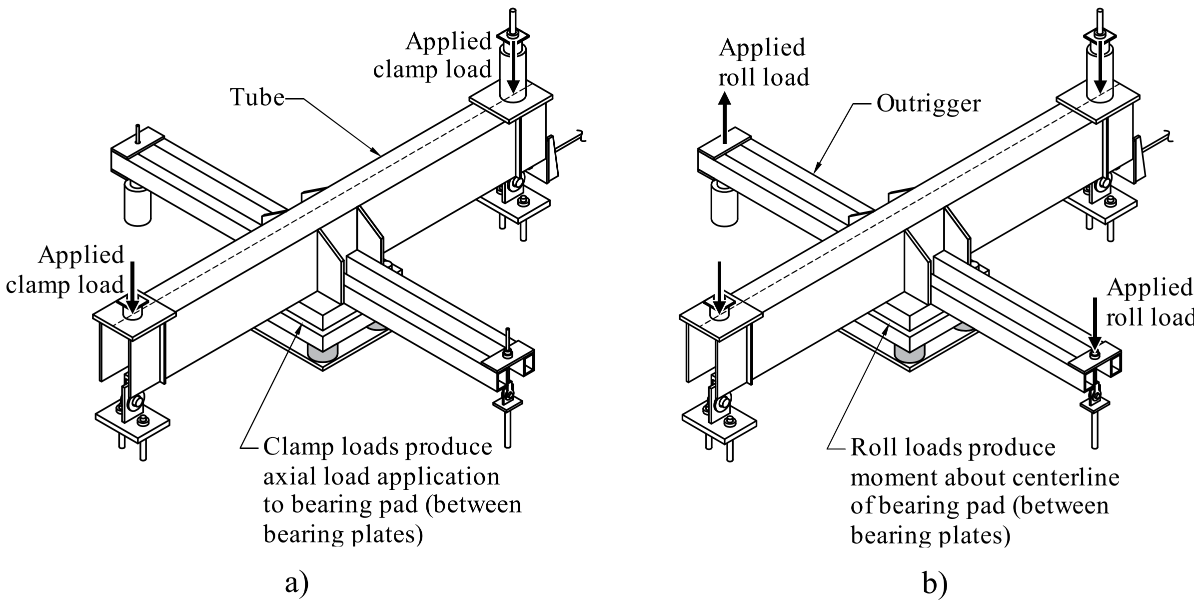

Figure 3.2. Load application to bearing pad test device:
a) Clamp loads during clamping stage; b) Roll loads during roll stage

3.2 Instrumentation

Multiple instrumentation devices were used during the roll stiffness tests to measure applied load (load cells), roll and slope angles (inclinometer) and displacement (displacement sensors). In many tests, redundant instrumentation was used to verify primary measurements and provide a additional readings in the event of sensor failure. A naming convention for the instrumentation was developed to reflect the instrument type and its specific location on the bearing pad test device. Each instrument name was of the form of T-Loc, where “T” indicated the type of instrument, and “Loc” indicated the location of the instrument. The previously described global coordinate system (Figure 3.1) and its associated quadrants were used as a basis for naming each location. An overview of the instrumentation plan is shown in Figure 3.3.

3.2.1 Load cells

As summarized in Figure 3.4, each load cell name began with the letter “L” to indicate that load was being measured, and ended with the position of the load cell within the bearing pad test device. Position of axial load cells was indicated by quadrant (e.g., L1 was located in quadrant 1, L23 was located between quadrants 2 and 3) while position of clamp and roll load cells was indicated by axis (e.g., Lypos was located at the positive y-axis of the test device).

Axial load cells (Interface, model 1232, 100 kip capacity), which were used to measure total axial load applied to the bearing pad, were located below the steel bearing plates and were arranged in a statically determinate “tripod” configuration (labeled L1, L23, and L4; Figure 3.5) to ensure that contact between load cells and bearing plates was maintained at all times. Using a tripod configuration also enabled the location of the bearing pad pressure resultant to be determined, relative to the center of the bearing pad, at any point during a roll stiffness test. Clamp load cells (Geokon, model 3000, 200 kip capacity), located at the ends of the tube along the y-axis (labeled Lypos and Lyneg; Figure 3.3) provided a redundant measure of axial load applied to the bearing pad. Washer load cells (Interface, model LW25100, 30 kip capacity) were used to measure vertical roll loads applied to the ends of the outriggers and to compute roll moments imposed on the bearing pad (labeled Lxpos and Lxneg; Figure 3.3). A washer load cell (Interface, model LW25100, 30 kip capacity) was also used to measure any shear force inadvertently imposed on the bearing pad in the sloped testing configuration. Note that no shear force was detected during any experiments conducted.

3.2.2 Inclinometer

A dual axis inclinometer (FRABA Posital CanOPEN, +/-0.087 rad. range, 17 μrad. resolution) was used to measure both the slope and roll angles imposed on the bearing pad, about the x-axis and y-axis, respectively. As the roll loads (and corresponding moments) were applied, the inclinometer measured the roll angle imposed on the bearing pad (about the y-axis). To ensure accurate readings, the inclinometer was mounted to the top bearing plate, which was effectively rigid and would not deform under applied loads.

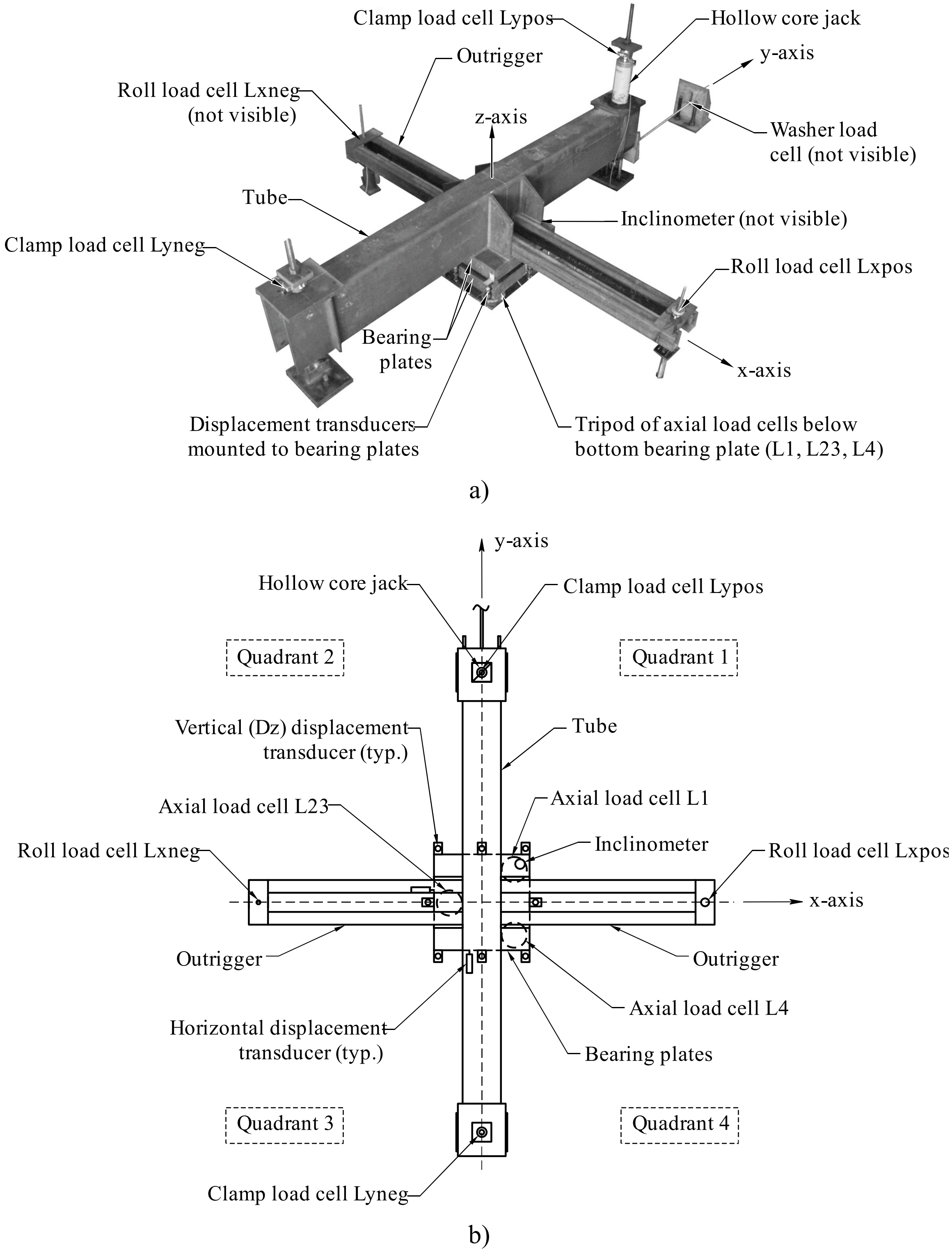

Figure 3.3. Instrumentation plan for roll stiffness tests:
a) Isometric view; b) Plan view

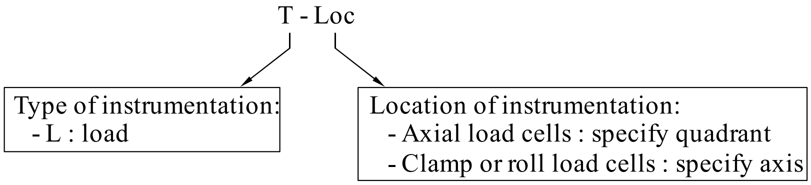

Figure 3.4. Naming convention for load cells used in roll stiffness tests

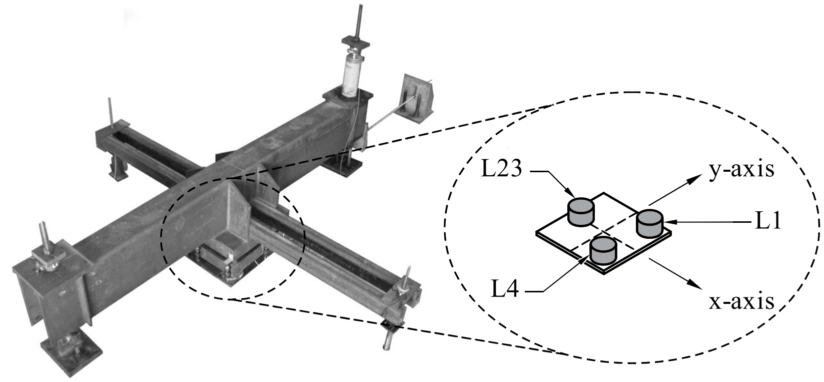

Figure 3.5. Tripod of axial load cells

3.2.3 Displacement transducers

Displacement transducers [TML models CDP-50 and CDP-100, which have 50 mm and 100 mm (2 in. and 4 in.) strokes respectively] were used to measure both relative and absolute displacements of the two bearing plates along each axis of the test device (Figure 3.6). Horizontal transducers—along the x-axis and y-axis—were mounted to stands and measured absolute displacement. Vertical transducers—along the z-axis—measured relative displacement between the two plates. As summarized in Figure 3.7, each displacement transducer name began with “Dx, Dy, or Dz” to indicate the axis along which the displacement was being measured, followed by the position of the transducer within the bearing pad test device. The position of horizontal transducers is indicated by plate. For example, sensor Dx1 measured horizontal displacement of the top plate along the x-axis and Dx2 measured the x-axis displacement of the bottom plate. The position of vertical transducers was indicated by quadrant, not plate (e.g., Dz1 was used to measure relative displacement between the top and bottom plates along the z-axis, located in quadrant 1).

Redundancy in roll angle measurement was achieved by using vertical (Dz) displacement transducers to measure relative vertical displacements between the steel bearing plates. Knowing the horizontal distance between the displacement transducers, the roll angle imposed on the bearing pad was calculated from the relative displacement measurements and used to confirm the inclinometer reading. Horizontal displacement transducers (Dx and Dy) were also used to monitor horizontal movements of the bearing plates to confirm that shear deformations generated in the bearing pad remained negligibly small during testing.

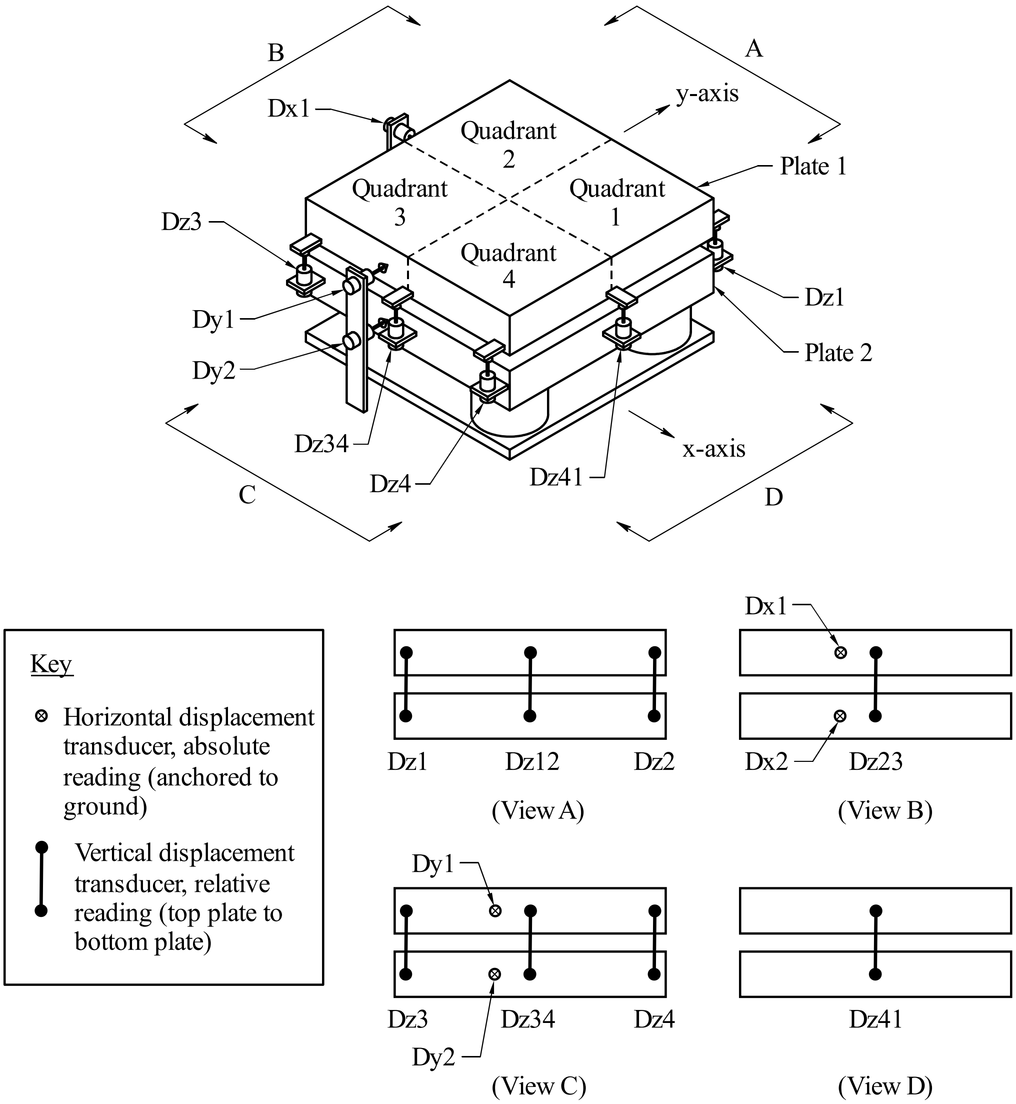

Figure 3.6. Displacement transducers

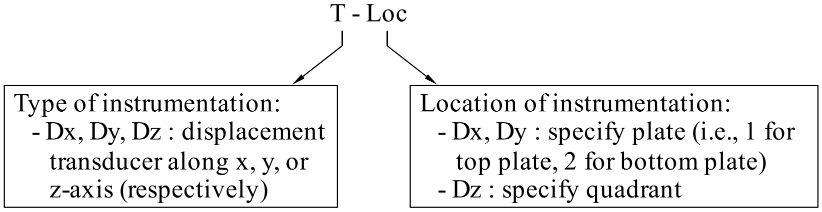

Figure 3.7. Naming convention for displacement transducers used in roll stiffness tests

CHAPTER 4
BEARING PAD TEST PROCEDURE

4.1 Introduction

As noted earlier, each bearing pad roll stiffness test conducted in this study involved three distinct stages: positioning, clamping, and rolling. In this chapter, the procedure for performing each stage is described.

4.2 Positioning stage

Each test began by positioning the test device on the bearing pad so as to produce the desired slope and skew angles. Slope angle was defined as the vertical angle (Figure 4.1) between the ŷ-axis (aligned with the sloped tube) and the y-axis (defined previously). Slope was imposed on the bearing pad by rotating the upper portion test device (the portion above the bearing pad) about the global x-axis of the system. In non-sloped tests, the tube was positioned level (horizontal) and the y- and ŷ-axes were identical.

Once the desired slope angle was imposed, the elevation of the y-negative end of the tube (Figure 4.1) was "locked-off" at the correct height, such that it remained constant throughout the test. A threaded rod connected the tube to the clevis and plate system acting as a hinge, which was anchored to the floor. To lock off the height of the tube, a nut was threaded down snugly against the top of the y-negative end of the tube (Figure 4.2). Note that the line passing through the y-positive and y-negative hinges was also sloped, and aligned with the ŷ-axis, ensuring that the top portion of the test device rolled about the ŷ-axis, thereby mimicking girder motion during a buckling/overturning event (Figure 4.1). A rotating head laser level, located in quadrant 1, was used to position the hinges at the correct heights (Figure 4.3). The laser is initially leveled at the height of the undeformed bearing pad, and subsequently rotated to indicate a horizontal axis. For non-sloped tests, the hinges were positioned at the same height as the top of the pad (along the y-axis). For sloped tests, the hinges were offset to achieve the desired slope (aligned with the ŷ-axis).

Skew angle was imposed, during insertion of the bearing pad between the bearing plates, by rotating the bearing pad about the z-axis (Figure 4.4). Skew angle was defined as the angle between the long axis of the bearing pad and the x-axis of the test device. When positioning the bearing pad at the desired skew angle, the bearing pad was also centered at the z-axis as illustrated in Figure 4.4.

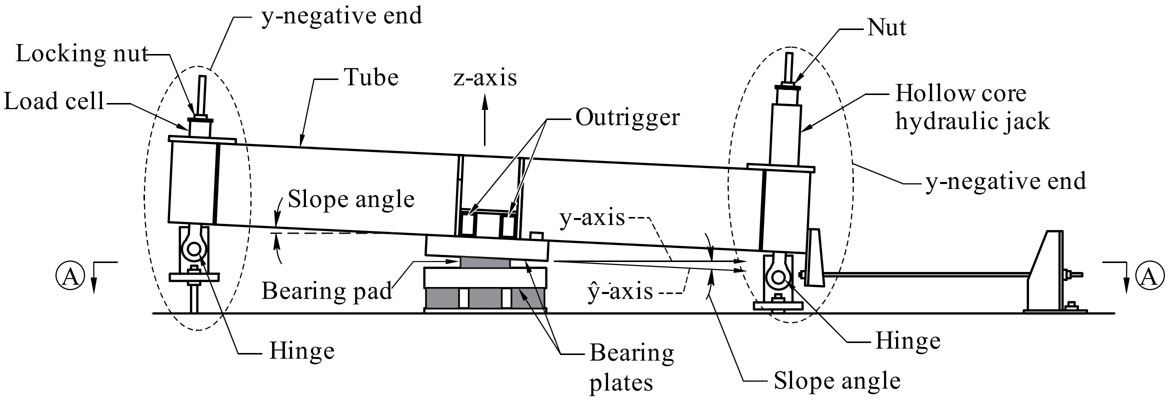

Figure 4.1. Elevation view of test device: imposing slope (positioning stage)

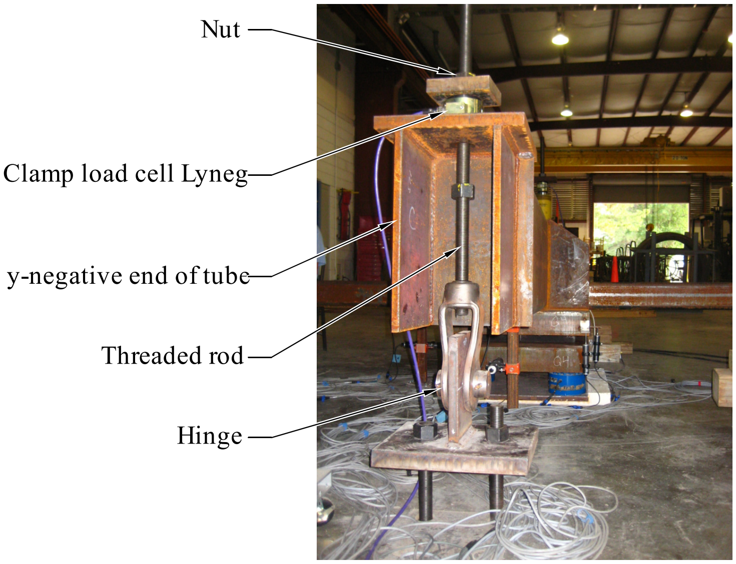

Figure 4.2. Photograph of y-negative end of bearing pad test device

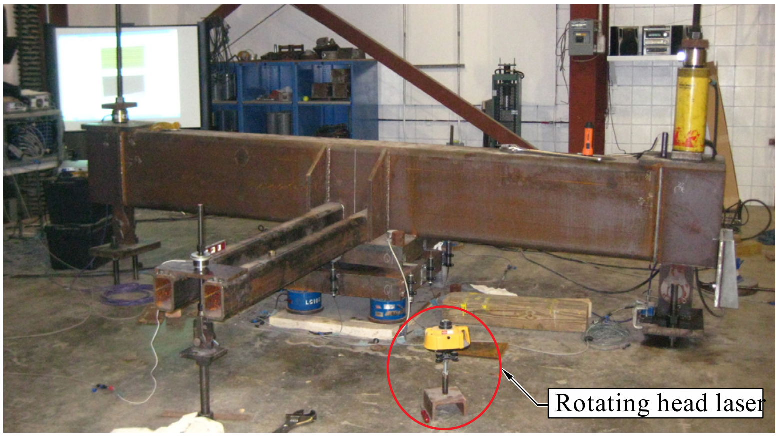

Figure 4.3. Rotating head laser, used to set height of hinges during positioning stage

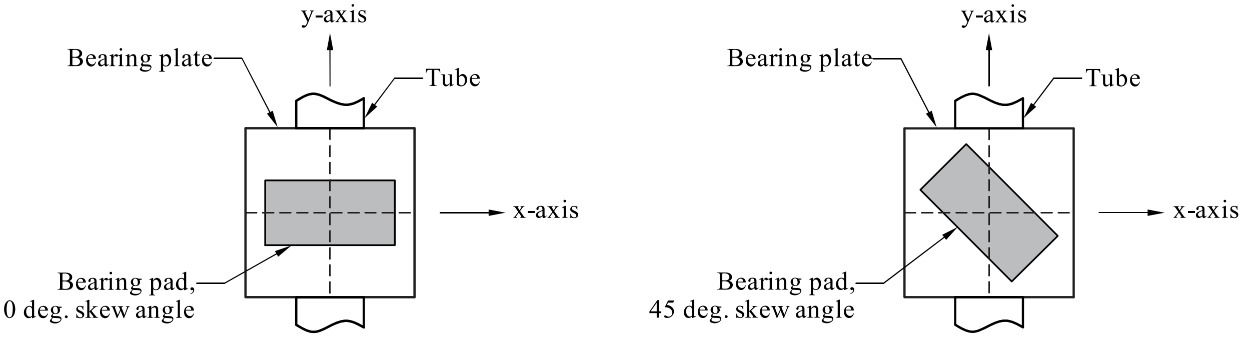

Figure 4.4. Imposing skew during the positioning stage; 0 deg. and 45 deg. skew shown (see Section A-A, Figure 4.1)

4.3 Clamping stage

During the clamping stage, axial load was gradually applied to the bearing pad by applying clamp loads to the top surfaces of both ends of the tube (Figure 4.5). At the beginning of the clamping stage, the piston of the hollow core hydraulic jack on the y-positive end was fully retracted, and the y-negative end of the tube was "locked-off". A threaded rod and nut connected the tube to the hinge, which was anchored to the floor (Figure 4.6). As the piston was subsequently extended, the y-positive end of the tube moved in the negative z-direction (downward), while the movement of the y-negative end of the tube remained restrained. This caused the load produced by the hydraulic jack on the y-positive end of the tube to be mirrored at the y-negative end. While applying the clamp loads using restrained movement, a slight increase of the slope on the pad occurred but was accounted for in advance (during the positioning stage) such that the tube was at the correct slope at the end of the clamping stage. Full application of the target axial load—read by the triad of load cells L1, L23, and L4—signified the end of the clamping stage, after which the load was held constant for the remainder of the test (to within an acceptable deviation from the target axial load of +/-5% of the target axial load).

Since the clamp loads were applied perpendicular to the top surface of the tube (Figure 4.5), the potential existed for inducing a shear load on the bearing pad (in the y-direction) when the test device was configured with a non-zero slope angle. Therefore, to properly simulate field conditions (where no shear load would be induced), a shear restraint rod (Figure 4.7) was used to prevent the top frame from moving in the y-direction relative to the bottom bearing plate. A washer load cell, located in-line with the shear restraint device, was used to monitor the amount of shear being diverted from the bearing pad. Measured load cell data showed that an insignificant amount of shear was being rerouted to the restraint device. Further, the horizontal displacement transducers along the y-axis (Dy1 and Dy2) on the bearing plates showed that there was no significant relative movement between the two plates, indicating that there was no shear in the bearing pad. The combination of no relative movement between the plates and no shear load detected in the restraint device indicated that no significant shear load was induced in the pads during testing.

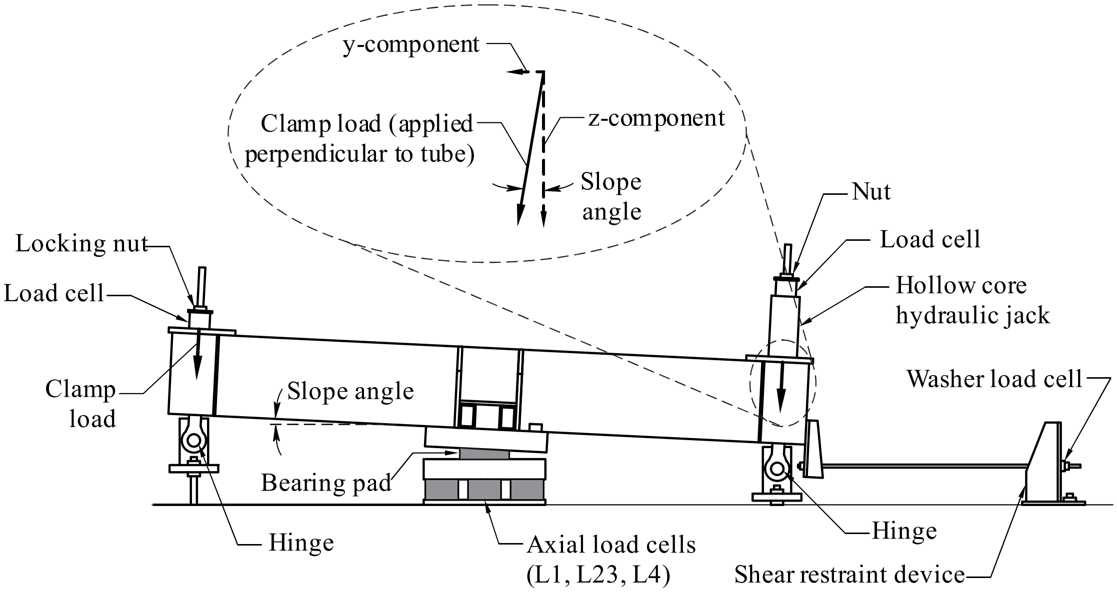

Figure 4.5. Elevation view of test device: applying axial load (clamping stage)

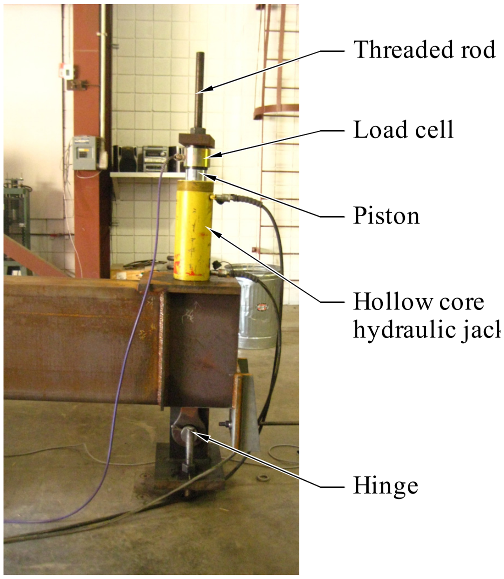

Figure 4.6. Photograph of y-positive end of bearing pad test device

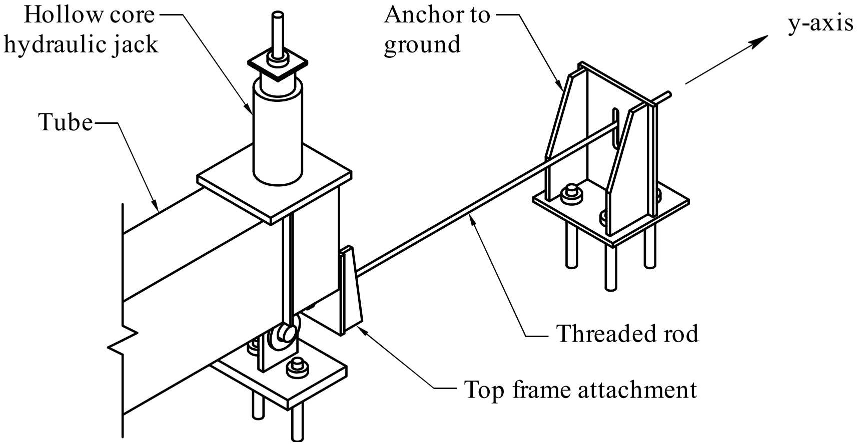

Figure 4.7. Shear restraint anchor

4.4 Rolling stage

Girder roll (rotation) in the field, as would occur during buckling, was simulated in the laboratory by rolling the test device about an axis parallel to the longitudinal axis of the bottom of the tube, aligned with the center of the bearing pad, referred to as the ŷ-axis (Figure 4.1). Equal and opposite vertical roll loads were applied to the ends of the outriggers to impose moment about the centerline of the bearing pad (Figure 4.8). At the beginning of the rolling stage, no roll loads were applied to the ends of the outriggers. As the rolling stage progressed, moment and corresponding roll rotation were increased in a stepwise manner, allowing the change of roll rotation to be measured at each load increment.

Individual roll loads were applied iteratively to induce moment on the bearing pad, first gradually increasing the upward load to the x-negative outrigger until a specific target was reached, and then by increasing the downward load to the x-positive outrigger until the loads being read by both roll load cells (Lxpos and Lxneg) were equal. A representative load time history measured by the roll load cells (Lxpos and Lxneg) during a roll stiffness test is shown in Figure 4.10. Throughout the roll stage of each test, the method of roll load application was load-controlled. A hydraulic jack provided the upward load to the x-negative outrigger (Figure 4.9a), which was increased gradually until a specific load difference was read between the two roll load cells. With the hydraulic jack locked off, the displacement of the x-negative end of the outrigger was maintained while load was applied to the x-positive end of the outrigger. A nut was threaded downward to bear against the end of the x-positive outrigger (Figure 4.9b); the downward displacement produced was dependent upon the number of turns of the nut. As the nut was turned, load increased in load cell Lxpos and load decreased in load cell Lxneg (Figure 4.10). By turning the nut until both roll load cells read equal loads (to within an acceptably small tolerance), a pure moment was induced on the bearing pad about its centerline. When the loads in both roll load cells were equal, a data point was recorded to indicate pure moment application to the bearing pad (Figure 4.10). Multiple sets of moment and roll angle were imposed using this iterative process, allowing moment to be measured as a function of roll rotation, to ultimately determine the roll stiffness of a bearing pad.

During the rolling stage, an increase in axial load occurred as the tube "lifted off" of the bearing pad. To maintain constant axial load during the clamp stage (to within the acceptable tolerance of +/-5% of the target axial load), the piston of the hollow core jack was manually adjusted (extended or retracted).

A representative load-time history graph of axial load during a roll stiffness test (measured by the tripod of load cells L1, L23 and L4) for a non-sloped case is shown in Figure 4.11. Data points are shown, which indicate a pure moment applied to the bearing pad. The first data point on the graph marks the end of the clamping stage, before the rolling stage (axial load fully applied, zero moment applied). As shown, at the first data point, approximately 50% of the axial load was distributed to load cell L23 and 25% of the load was distributed to each of the load cells L1 and L4. This distribution indicated that the resultant position of the axial load was centered within the bearing pad. As the roll stage progressed, load decreased in load cell L23 and increased in both L1 and L4. This action indicated that, as the roll loads were increased, the resultant of the axial load became increasingly eccentric towards the x-positive edge of the bearing pad. The tests ended when the bearing pad moment-roll graph significantly softened or the load measured by load cell L23 dropped below 15% of the total axial load applied.

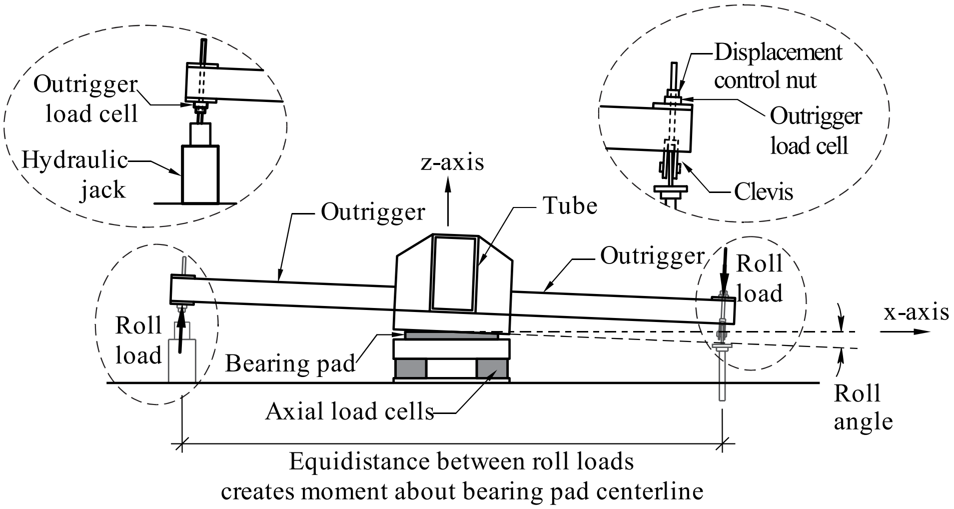

Figure 4.8. Applying loads to outriggers during rolling stage

a)

b)

Figure 4.9. Photographs of ends of outriggers during rolling stage:
a) Hydraulic jack, x-negative end; b) Displacement system, x-positive end

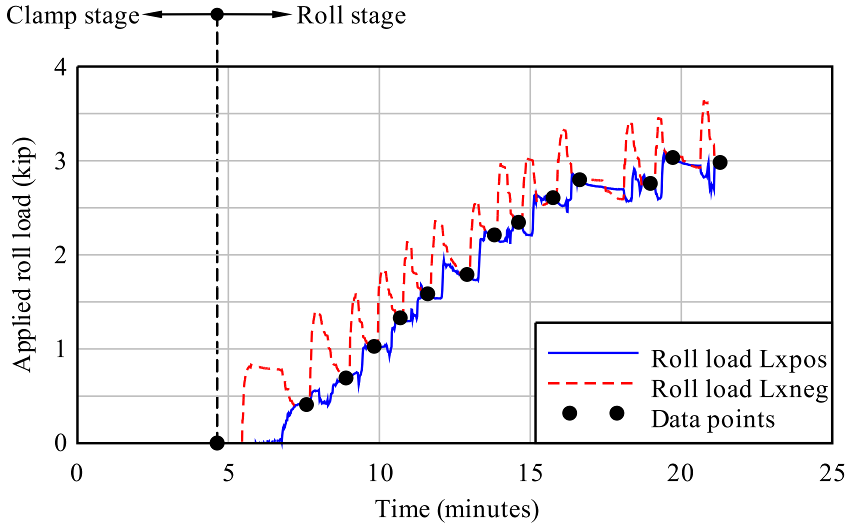

Figure 4.10. Representative roll load time history (test A1-0-0 shown)

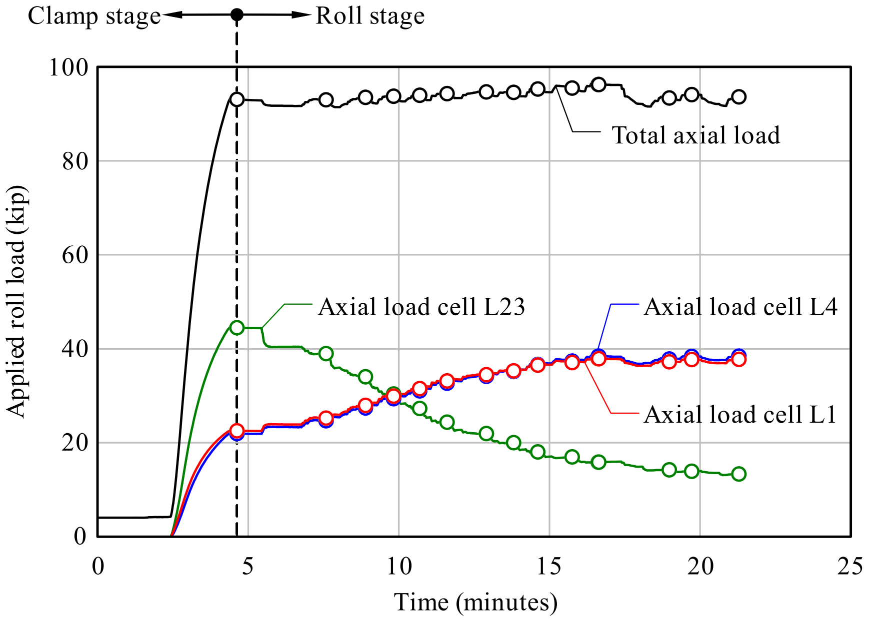

Figure 4.11. Representative axial load time history, data points shown for each individual data trace (test A1-0-0 shown)

CHAPTER 5
BEARING PAD TEST SPECIMENS AND DETAILS

5.1 Bearing pads tested

Composite bearing pad details for prestressed concrete girder cross-sections are specified in the Florida Department of Transportation (FDOT) *Design Standards, Index No. 20500* (FDOT 2010a). The three different pad sizes (denoted A, B, and C; Figure 5.1, Table 5.1) tested for roll stiffnesses in this study were those typically used in conjunction with the American Association of State Highway and Transportation Officials (AASHTO) Type V and VI sections as well as the Florida Bulb-Tee sections (FDOT 2010a). Basing the standard bearing pad sizes on girder cross-section, the AASHTO Type V and VI and Florida Bulb-Tee sections are often used in long-span configurations, making them more prone to girder instability than the smaller sections. Two specimens of each pad type were tested, for a total of six specimens (denoted A1, A2, B1, B2, C1, and C2), so that the repeatability of the test results could be evaluated.

Although the FDOT *Design Standards* (FDOT 2010a) specify required shear moduli for the standard bearing pads, the AASHTO *LRFD Bridge Design Specifications Table 14.7.5.2-1* (AASHTO 2004) provides a relationship between shear modulus and durometer hardness. To determine whether the bearing pads acquired for this study were manufactured in accordance with the FDOT requirements, the durometer hardness of each specimen was measured. The measured values were then compared to the equivalent durometer hardnesses that were determined to match the shear moduli specified by FDOT. It was found that each specimen had a measured durometer hardness equal to or exceeding the FDOT requirements (Table 5.1), except specimen C2. In addition to confirming durometer hardness, prior to the end of the test program, external elastomer cover material around the edges of bearing pads C1 and C2 was trimmed off to visually confirm the thicknesses of the internal elastomer layers (Figure 5.2). Both of the bearing pads modified through this trimming process—referred to as pads C1mod and C2mod to distinguish from the original, unchanged pads C1 and C2—had internal elastomer layers of uniform thickness that were within +/-0.12 in. of the tolerance suggested by the National Cooperative Highway Research Program (NCHRP) *Report 449* (Yura et al. 2001) and AASHTO *M251* (1997).

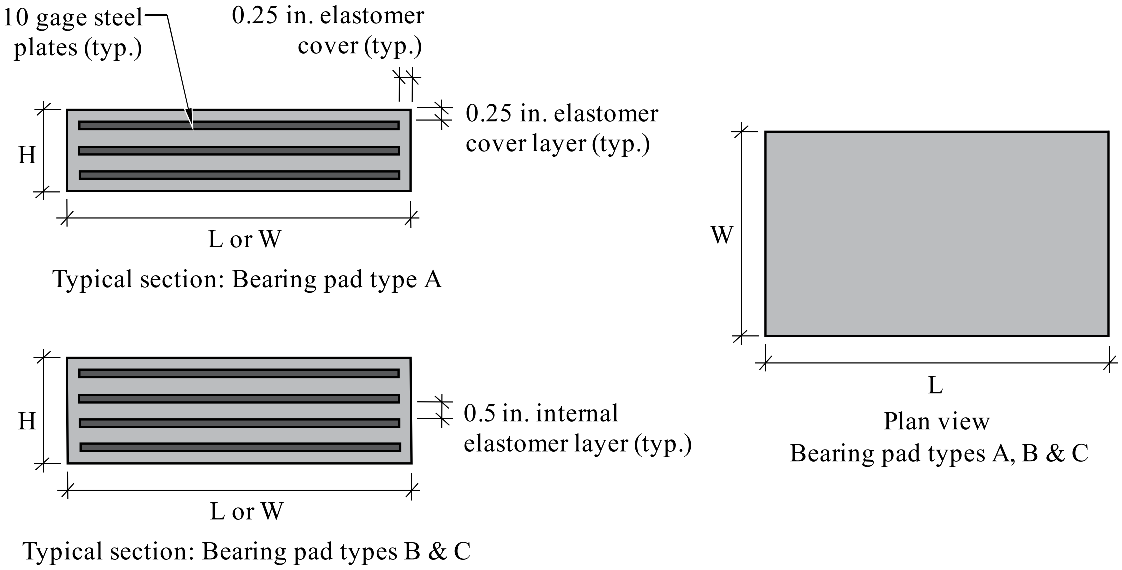

Figure 5.1. Identification of bearing pad dimensions (see Table 5.1 for actual dimensional values)

Table 5.1. Bearing pad dimensions, shear modulus, and durometer hardness for each specimen

	Bearing pad type					
	A		B		C	
Bearing pad length, L (in.)	11		14		12	
Bearing pad width, W (in.)	24		24		23	
Bearing pad height, H (in.)	1-29/32		2-9/16		2-9/16	
Number of internal plates	3		4		4	
Shear modulus (psi)	110		110		150	
Equivalent durometer hardness (Grade)	50		50		60	
Bearing pad specimen	A1	A2	B1	B2	C1	C2
Measured durometer hardness (Grade)	53	50	53	52	61	53

Figure 5.2. Modified type C bearing pad, Perimeter elastomer cut away to enable visual confirmation of steel shim thicknesses and locations

5.2 Test matrix

Each bearing pad specimen was first tested under non-skewed, non-sloped conditions and then tested under different combinations of skew and slope to determine the effect of each on bearing pad roll stiffness. Girder camber construction tolerances are capable of producing an end slope of approximately 0.02 rad, but bridge grade can potentially increase this value if not properly offset by sloping the beam seat. The maximum skew angle that is recommended by the FDOT before a circular bearing pad should be considered is 45 deg. Therefore, maximum slope angle tested was conservatively taken as 0.04 rad. (based on camber, construction tolerance, and bridge grade) and the maximum skew angle tested was 45 deg. At the extreme, a combination of both 0.04 rad. of slope and 45 deg. of skew was tested. Intermediate slope angles of 0.02 rad. and 0.03 rad. were also included in the study to quantify roll stiffness reduction as a function of slope severity.

The naming system used to identify each *configuration* tested was T-x-y, where x=skew angle (deg.), and y=slope angle (rad.). For example, test configuration T-45-04 refers to a test performed at a 45 deg. skew angle and a 0.04 rad. slope angle. Bearing pad specimen identifiers (A1, A2, B1, B2, C1, C2) were also combined with configuration indicators to identify specific tests. For example, A1-45-04 refers to a test performed on bearing pad specimen A1 at a 45 deg. skew angle and a 0.04 rad. slope angle. When discussing an averaged value—such as roll stiffness—between two specimens, A-45-04 refers to the average value of all tests performed on A1-45-04 and A2-45-04.

Using this naming convention, the skewed and sloped test conditions that were conducted on each bearing pad are presented in Table 5.2, in which an “X” indicates that tests were performed in that given configuration. Multiple (2-5) test repetitions were performed in each configuration and on each specimen to ensure repeatability of the test device and results. A total of 108 isolated bearing pad roll stiffness tests were performed. Individually determined axial load levels were assigned to each bearing pad type (A, B, C) to ensure similar bearing pad axial pressures, regardless of bearing pad size. Also, while all pad configurations were tested under high axial load (pressure), for cases B1-0-0, B2-0-0, and C1-0-0, additional low load (pressure) tests were also performed.

Table 5.2. Configurations tested for each specimen

	Bearing pad specimen					
	A1	A2	B1	B2	C1	C2
Low axial load level (kip)	-	-	67	67	69	-
High axial load level (kip)	92	92	101	101	97	97
Test Configuration T-0-0	X		X		X, X*	
Test Configuration T-0-02	X		X		X*	
Test Configuration T-0-03			X		X*	
Test Configuration T-0-04	X					
Test Configuration T-45-0	X		X		X	
Test Configuration T-45-02	X		X		X	
Test Configuration T-45-04	X		X		X	

* test configuration performed on modified bearing pad

5.3 Repeated axial compression

Prior to conducting this study, it was not known whether repeated loading, which is known to cause softening of neoprene when loaded in shear (Gent 2001), would affect the roll stiffness results obtained. Cyclic softening of neoprene under shear loading is called the Mullins effect and is recognized by the American Society for Testing and Materials (ASTM) as a phenomenon that must be accounted for when experimentally determining the shear modulus of a bearing pad (ASTM 2003). Although there is no ASTM requirement for testing a bearing pad cyclically in compression, it was deemed necessary to do so in this study to determine if a similar effect occurred when testing for roll stiffness. Multiple tests were performed on each bearing pad specimen, and in each configuration, however significant softening of the bearing pad was never observed. Therefore, it was concluded that no axial softening phenomenon, similar to the Mullins effect for shear, was present at the axial load levels used in this test program.

5.4 Variation of axial compression load

As noted previously, selected roll stiffness tests were performed at both low and high axial loads to determine whether variations in axial load would affect bearing pad roll stiffness. The low and high loads assigned to each bearing pad type were chosen to approximate the self-weight end reactions of the Florida Bulb-Tee 72 and 78 sections, at the longest length reasonable for current design practice (Consolazio et al. 2007). At the maximum practical span length of 140 ft, the end reaction of the Florida Bulb-Tee 72 was used as the low axial load, whereas the end reaction of a Florida Bulb-Tee 78 with a span of 160-180 ft was used as the high axial load. Roll stiffness test results indicated that, over an axial load range that is typical of field conditions, bearing pad roll stiffness varied only moderately as a function of axial load level (average roll stiffness at low load was approximately 22% smaller than roll stiffness at high load). Ultimately, the high axial load level was chosen for the remainder of the test program, to represent the self-weight of a long-span Florida Bulb-Tee 78.

CHAPTER 6
BEARING PAD TEST RESULTS

6.1 Results

For a given girder cross-section, span length, and bearing pad type, girder stability is greatest when bearing pad roll stiffness is maximized. Ideal conditions for maximizing bearing pad roll stiffness correspond to the T-0-0 (non-skewed, non-sloped) configuration included in the test program. Confirming the ideal nature of the non-skewed, non-sloped configuration, the T-0-0 test results for each pad always had a higher initial roll stiffness than pads tested in the most severe non-ideal configuration, T-45-04 (45 deg. skew, 0.04 rad. slope). In Figure 6.1, a representative set of moment-rotation results, obtained from testing of pad B2 in the T-0-0 and T-45-04 configurations, illustrates the extent to which roll stiffness may be reduced by the introduction of non-ideal conditions. Performed on the same bearing pad specimen and at the same axial load level, the tests that generated the results shown in Figure 6.1 differed only in skew and slope. As will be demonstrated later, intermediate configurations (e.g. T-45-0, skewed but not sloped) had, on average, roll stiffnesses that fell between the two extreme cases (ideal: T-0-0 and severe: T-45-04).

Moment-rotation curves obtained for all roll stiffness test performed in this study, grouped by bearing pad specimen, are presented in Figure 6.2. Generally, the moment-rotation curves for the intermediate cases fell between the two extreme cases (T-0-0 and T-45-04), with good repeatability of the data within each specimen and configuration. Whereas tests with zero slope generally exhibited both linear and nonlinear portions of the moment-rotation curve, most of the tests with non-zero slope exhibited moment-rotation curves that remained essentially linear throughout the entire test.

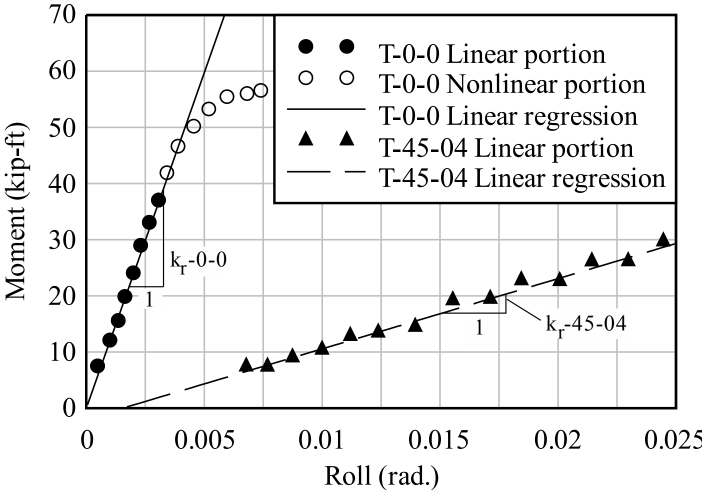

Figure 6.1. Representative moment-rotation curves, configurations T-0-0 and T-45-04 (obtained from testing bearing pad B2)

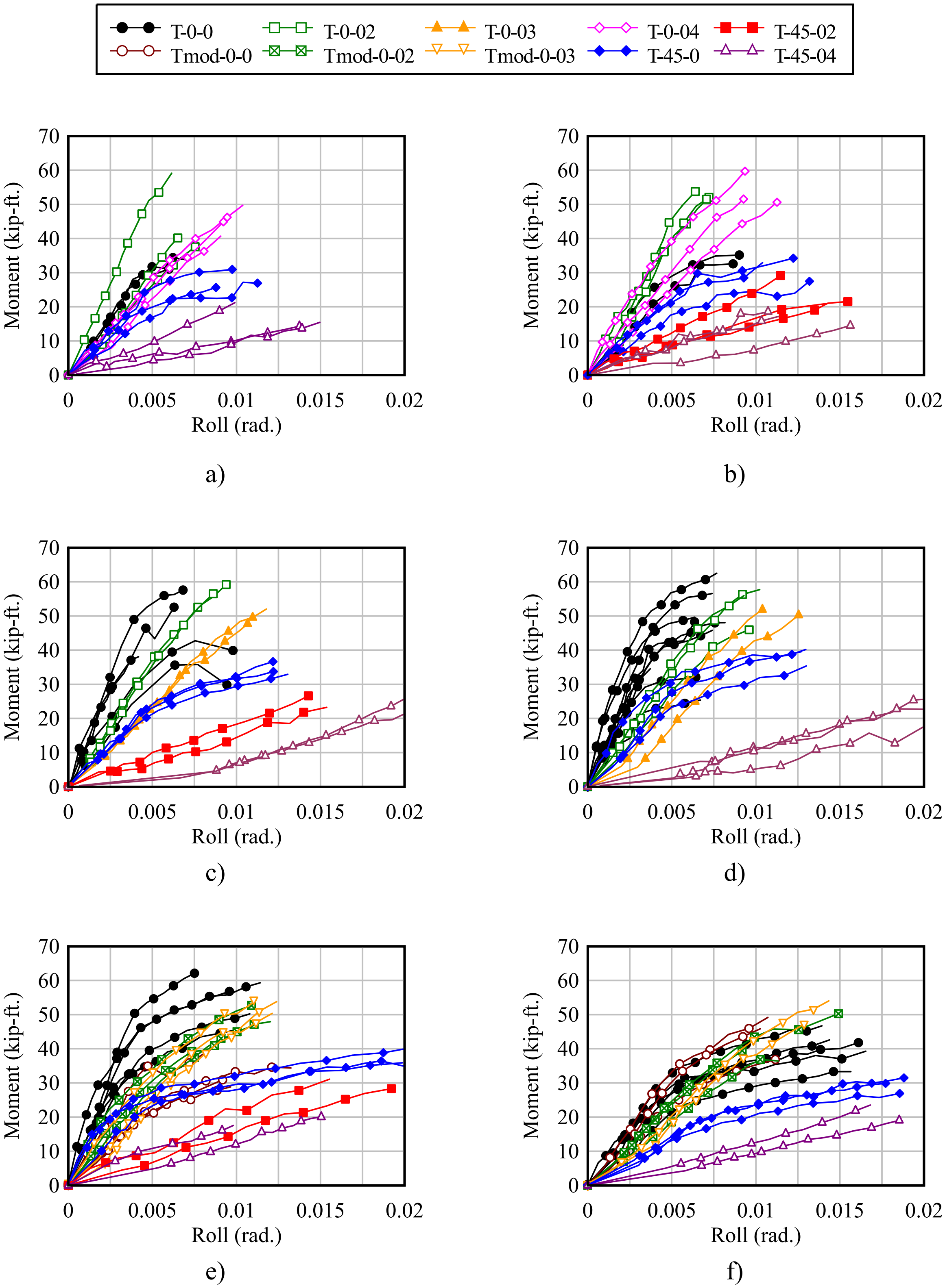

Figure 6.2. Moment-rotation curves for all tests, grouped by pad specimen:
a) pad A1; b) pad A2; c) pad B1; d) pad B2; e) pad C1; f) pad C2

6.2 Data curve fitting

As shown in Figure 6.1, data from the ideal case exhibit an initial, linear roll stiffness that is followed by an apparent softening (reduction in stiffness) at larger roll angles. This stiffness reduction corresponds to the upper bearing plate of the test device gradually losing contact with the pad and eventually “rolling off” the pad. With regard to the calculation of girder buckling capacity, it is the initial, linear roll stiffness of the bearing pad—and therefore the slope of the initial, linear portion of the moment-rotation (roll) curve—that is of primary importance. Hence, an algorithm was established to consistently determine the number of points contained within the initial, linear portion of each moment-rotation data set obtained.

For a single data set, Gaussian kernel smoothing was used to trend the data, removing the oscillations between data points (Figure 6.3). Subsequently, tangent lines were generated (using finite difference expressions for derivatives) for the smoothed curve at the x-values corresponding to the data points of the original data set. Separately, a linear regression line was generated using a truncated data set that included only the points that fell below 50% of the maximum moment recorded for that data set, excluding the first point (points 2-7 for the example data set, as shown in Figure 6.3a). The first data point was excluded in the linear regression line generation because of potential ‘take-up’ in the bearing pad test device that could affect the correct fitting of the regression line (particularly in the combined skewed, sloped cases). Then, the slope of the linear regression line was compared to the slope of the tangent line at the last point considered in the truncated data set. For example, for the data set presented in Figure 6.3a, the slope of the linear regression line fit through points 2-7 was compared to the slope of the tangent line at point 7. If the two slopes differed by less than 15%, an additional point was added to the truncated data set, and the regression was recomputed. For example, if points 2-7 were used to generate the first regression line (Figure 6.3a), points 2-8 were used to generate the next regression line (Figure 6.3b). This procedure of generating regression lines, and using an additional data point for each iteration, was repeated until the slopes of the two lines differed by greater than 15%. The points used to generate the last regression line with slope within 15% of the tangent slope were then considered to represent the linear portion of the curve. Figure 6.3c illustrates the difference in slopes once the moment-rotation curve begins to soften as the test device rolls off the pad. The roll stiffness (k_r) of each bearing pad was defined as the slope of the linear regression line through the initial, linear portion of the moment-rotation curve (Figure 6.1).

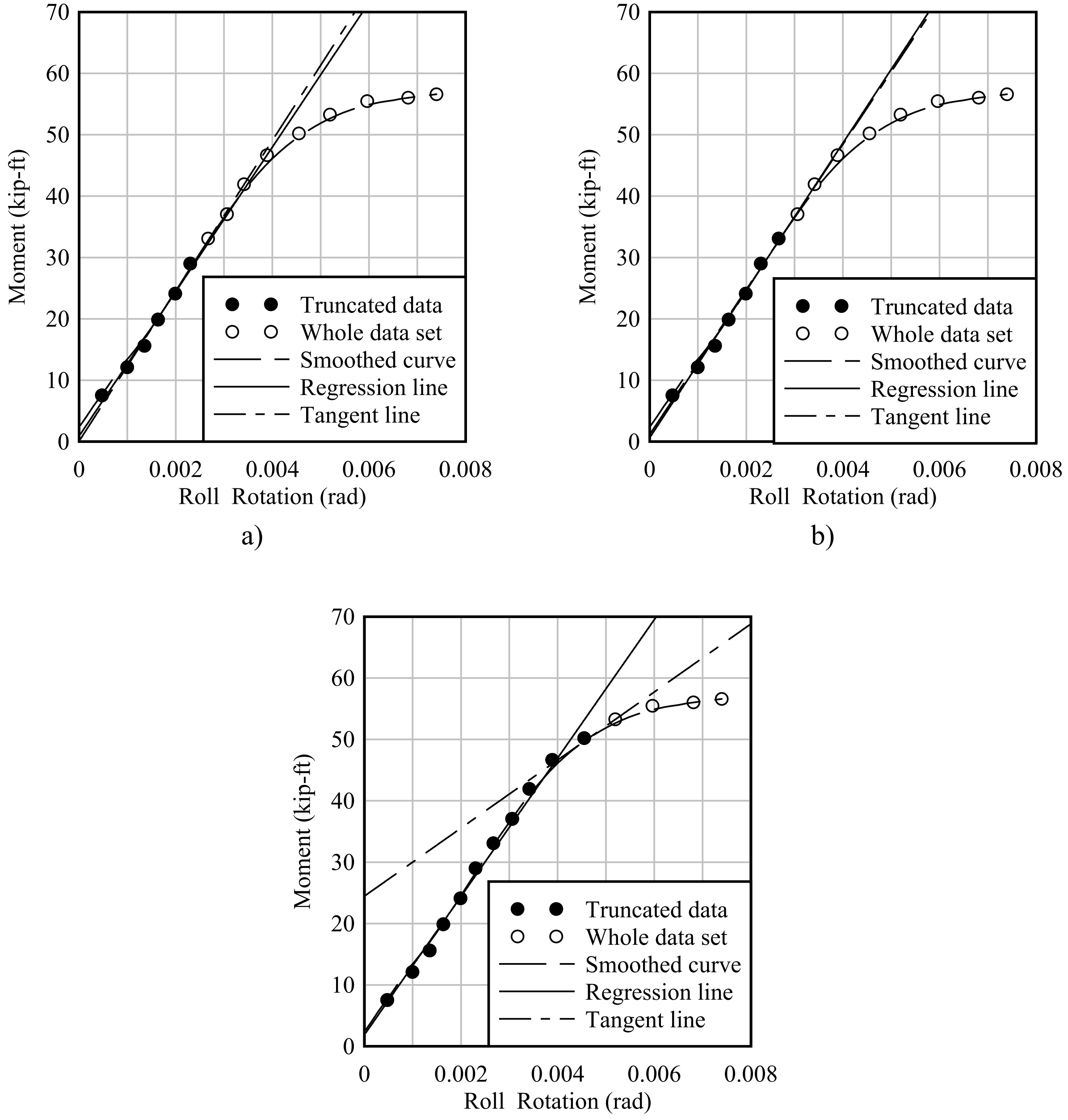

a)

b)

c)

Figure 6.3. Data curve fitting procedure (test B2-0-0 shown):
a) Truncated data includes points 2-7; b) Truncated data includes points 2-8;
c) Truncated data includes points 2-12

6.3 Location of pressure resultants on bearing pads

Initial roll stiffness, as well as whether a bearing pad exhibited linear or nonlinear behavior, depended upon the location of pressure resultants on the bearing pad. Under conditions of combined skew and slope, significant reductions in roll stiffness were clearly evident from the test data. Such reduction of stiffness occurred due to the eccentricity of the pressure resultant of the axial load on the bearing pad. As the bearing pad test device rolled on a bearing pad, the pressure distribution on the pad became more concentrated on the side of the pad that corresponds to the direction of roll. This caused the location of the pressure resultant to move as well, becoming increasingly eccentric from the centerline of the test device (representing a girder) with increasing roll angle.

Figure 6.4 presents pressure distributions and pressure resultant locations at various stages of roll angle leading ultimately to girder instability. In the non-skewed configurations (Figure 6.4a and Figure 6.4b) a large eccentricity between the girder centerline and the pressure resultant is available to resist overturning moment applied during girder roll. In contrast, although the skewed, non-sloped case (Figure 6.4c) begins with a concentric loading similar to the non-skewed, non-sloped case (Figure 6.4a), a smaller eccentricity develops during girder roll, thereby decreasing the roll stiffness. The smallest available eccentricity occurred under the skewed, sloped configuration (Figure 6.4d), which also produced the least roll stiffness. For configurations in which the moment-rotation curves were nonlinear, the eccentricity was most important at intermediate roll angles where the response transitioned from linear to nonlinear. At the point of girder instability, the instantaneous eccentricity was an indicator of the secant stiffness at the corresponding roll angle, which was why the non-skewed cases (with larger eccentricities) exhibited larger overall stiffnesses than did the skewed cases (recall Figure 6.2). The presence of an eccentric pressure distribution at the end of the rolling stage of tests conducted in the non-skewed, non-sloped configuration (Figure 6.4a) is evidenced by bulging at the edge of the pad, as shown in Figure 6.5.

Linearity of the moment-rotation curve from each test was controlled by the portion of the bearing pad that remained in contact with the girder as it became unstable. In sloped configurations, a larger portion of the bearing pad—opposite the direction of girder roll—remained in contact with the girder than in the non-sloped configurations. Losing contact with the girder on the side of the pad opposite the direction of girder roll caused nonlinearity in the moment-rotation curve.

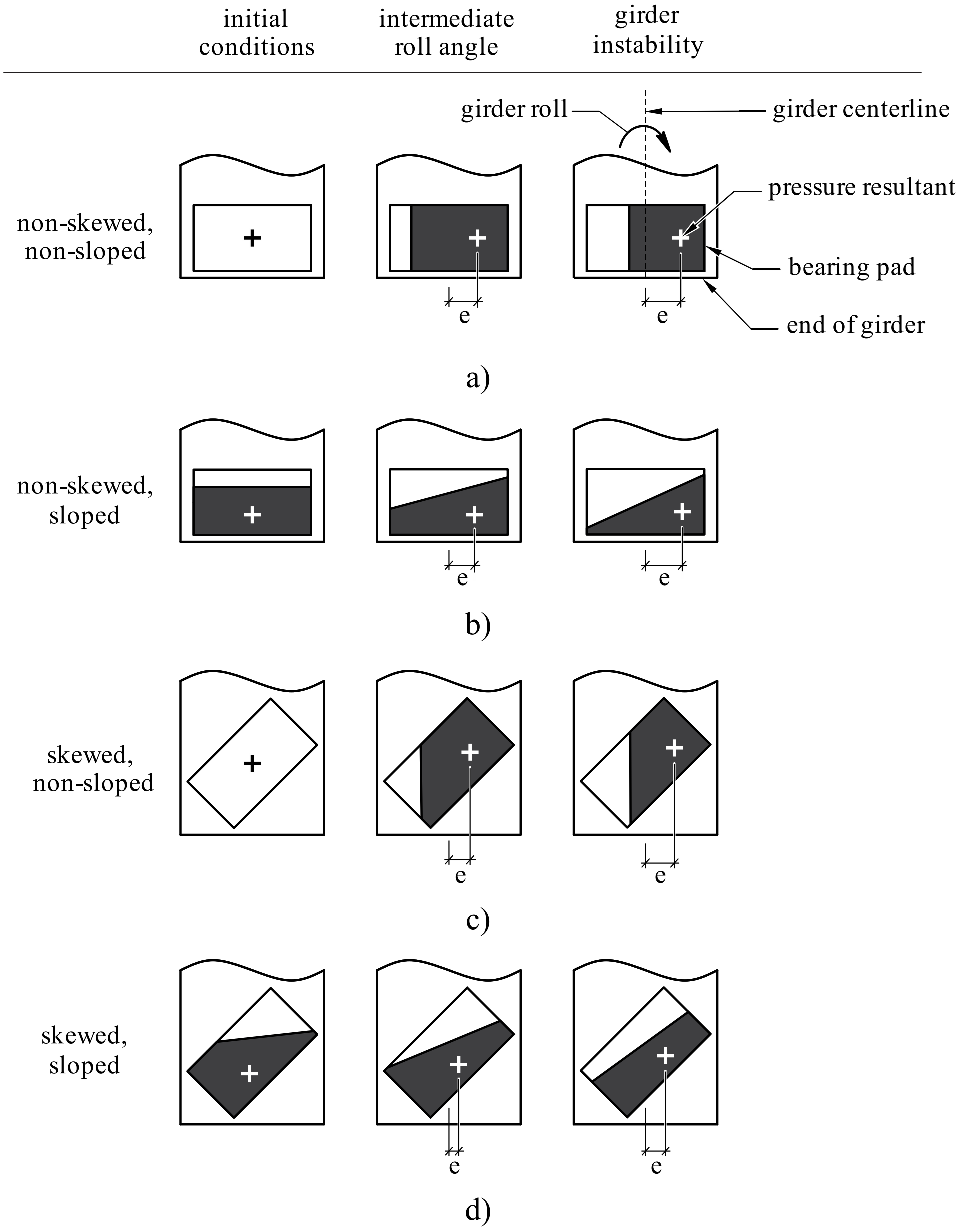

Figure 6.4. Pressure distributions and axial load resultant positions on bearing pad: beginning, intermediate, and end of rolling stage. Configurations: a) Non-skewed, non-sloped; b) Non-skewed, sloped; d) Skewed, non-sloped; d) Skewed, sloped

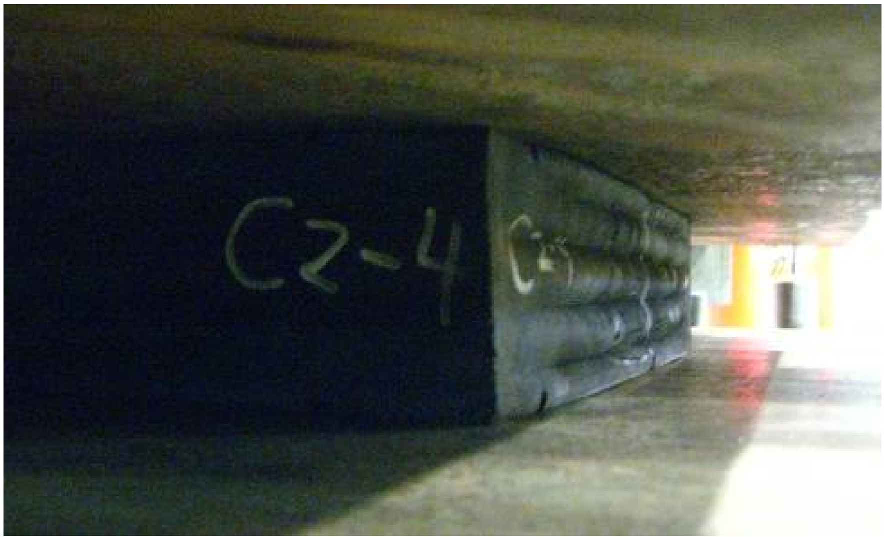

Figure 6.5. Bulging of the internal elastomer layers during roll stiffness test

6.4 Data trends

Individual roll stiffnesses, determined from each test conducted in this study, are shown in Figure 6.6, together with mean values computed for each combination of bearing pad type, skew, and slope. For convenience, the mean roll stiffness for each combination of pad type, skew, and slope are also reproduced in Figure 6.7. Table 6.1 presents corresponding roll stiffness reductions due to combinations of skew and slope as compared to the ideal T-0-0 configuration. Excluding the A-0-02 mean results, within each bearing pad type, the ideal case (T-0-0) had the largest roll stiffness, and the extreme skew and slope case (T-45-04) had the smallest roll stiffness, with intermediate configurations producing roll stiffnesses falling between the two. Examining Figure 6.7, the roll stiffness of the type C bearing pads was generally decreased after the modification of the bearing pads (C-0-0 to Cmod-0-0), which can be attributed to the trimming of the outer layer of rubber.

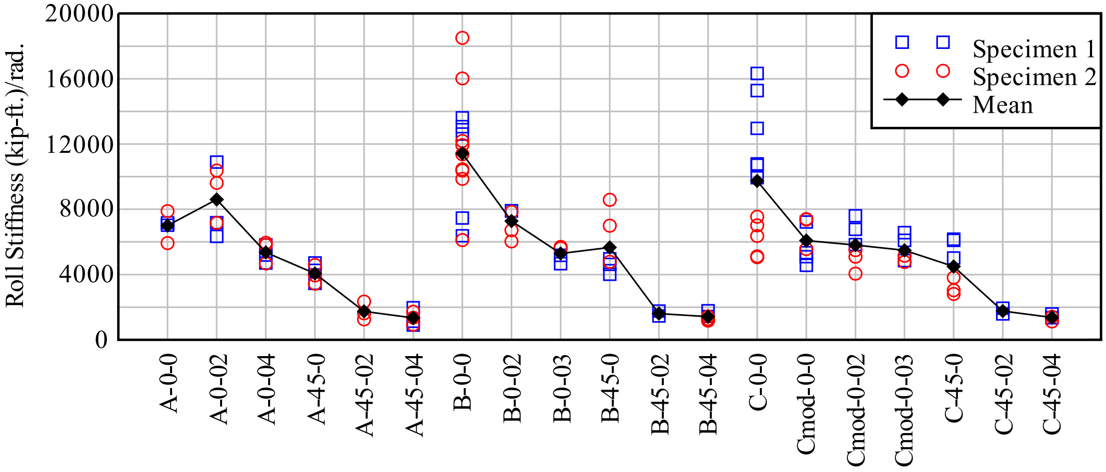

Figure 6.6. Bearing pad roll stiffnesses for all configurations tested

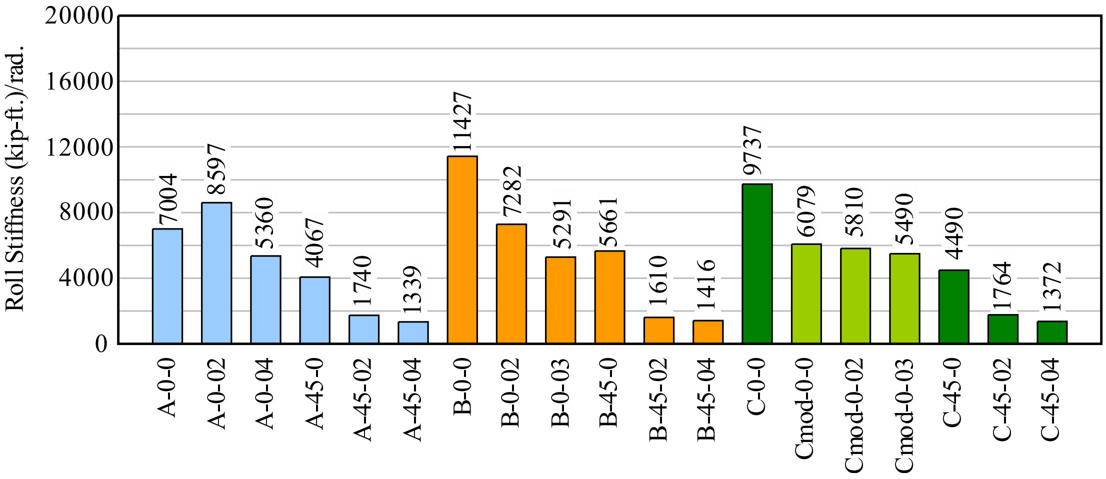

Figure 6.7. Mean bearing pad roll stiffnesses for all configurations tested

Table 6.1. Mean roll stiffness and reduction in roll stiffness due to non-ideal (skewed, sloped) conditions

	Roll stiffness, kip-ft./rad. [Roll stiffness reduction]			
Configuration	Pad A	Pad B	Pad C	Pad Cmod
T-0-0	7004 [0%]	11427 [0%]	9737 [0%]	6079 [38%]*
T-0-02	8597 [-23%]	7282 [36%]	-	5810 [4%]
T-0-03	-	5291 [54%]	-	5490 [10%]
T-0-04	5360 [23%]	-	-	-
T-45-0	4067 [42%]	5661 [50%]	4490 [54%]	-
T-45-02	1740 [75%]	1610 [86%]	1764 [82%]	-
T-45-04	1339 [81%]	1416 [88%]	1372 [86%]	-

*indicates roll reduction due to modification of pad, ideal configuration

6.4.1 Effect of skew and slope combined

The combination of skew and slope produced the most severe reduction of roll stiffness. When slope was combined with skew, the average reductions of roll stiffness—relative to the ideal T-0-0 case—for configurations T-45-02 and T-45-04 were 81% and 85%, respectively. This indicates that reducing the slope angle from 0.04 rad. to 0.02 rad. had little benefit if skew was also present. Furthermore, comparisons of results from test configurations T-45-02 and T-45-04 for each pad type (i.e., A-45-02 vs. A-45-04, B-45-02 vs. B-45-04, C-45-02 vs. C-45-04) reveal that the roll stiffnesses decreased only slightly when moving from the T-45-02 to the T-45-04 condition.

6.4.2 Effect of skew

Comparing test results for configurations T-0-0 to T-45-0 in Figure 6.7, it is evident that significant reductions in bearing pad roll stiffness resulted from the presence of skew only, regardless of specific bearing pad type (A, B, C). Average roll stiffness reduction due to skew alone for all of the bearing pad types was 49%, with little variation in percent reduction when comparing different pad types.

6.4.3 Effect of slope

There was an inconclusive trend in the roll stiffness reduction due to imposed slope angle alone. A reduction in roll stiffness due to increasing slope was observed in the type B bearing pads (i.e. the roll stiffness decreased from B-0-0 to B-0-02, and from B-0-02 to B-0-03). However, for the modified type C bearing pads, when comparing the ideal (Cmod-0-0) configuration to sloped configurations (Cmod-0-02 and Cmod-0-03), insignificant reductions of stiffness resulted from imposed slope angle. [Note that roll stiffness reductions due to slope alone, as produced by configurations Cmod-0-02 and Cmod-0-03, were calculated in comparison to Cmod-0-0 (as opposed to C-0-0)]. Roll stiffness reduction due to slope was also inconclusive due to results obtained from the type A bearing pads, where the roll stiffness increased from A-0-0 to A-0-02, but decreased from A-0-0 to A-0-04. However, this apparent anomaly may be related to the fact that the range of scatter in the data obtained for configuration A-0-02 was greater than that of any other configuration tested on the type A bearing pads (Figure 6.6).

CHAPTER 7
INTRODUCTION TO GIRDER BUCKLING TESTS

7.1 Introduction

The point at which a girder may reach instability in the field, during construction of a bridge, is dictated by several factors, including cross-sectional properties of the girder, span length, geometric imperfections such as sweep, and bearing pad roll stiffness. As discussed previously in Chapter 6, bearing pad roll stiffness is significantly reduced when skew, slope, or a combination of the two is imposed on a pad. In a previous analytical study (Consolazio et al. 2007), it was shown that imposition of skew and/or slope—resulting in reduced bearing pad roll stiffness—leads to decreased girder buckling capacity. In the phase of the present study that is described in this and following chapters, a full-scale girder buckling test program was designed and conducted to experimentally quantify the influence of bearing pad roll stiffness on girder buckling capacity.

7.2 Scope of test program

The scope of the experimental girder buckling test program included the design and construction of: a full-scale test girder; a vertical loading system (consisting of gravity load simulators); and end supports that enabled various combinations of slope and skew to be imposed on the supporting bearing pads (Figure 7.1). The pads used to support each end of the test girder were the same pads previously tested—to determine roll stiffness—in the first phase of this study (described in previous chapters). Rigid end supports elevated the test girder approximately 8 ft. above the lab floor to provide vertical clearance for gravity load simulators that were positioned beneath the beam (Figure 7.1). Each gravity load simulator (described in detail later) applied vertical load to the test girder in a manner that did not introduce any lateral stiffness (restraint). In total, nine (9) buckling tests were conducted, with various skew and slope conditions imposed on the supporting bearing pads. Analytical models corresponding to the test setup were developed and used to simulate the experimental buckling tests. Validation of the models was then carried out by comparing buckling capacities quantified from analytical simulations to experimental test results.

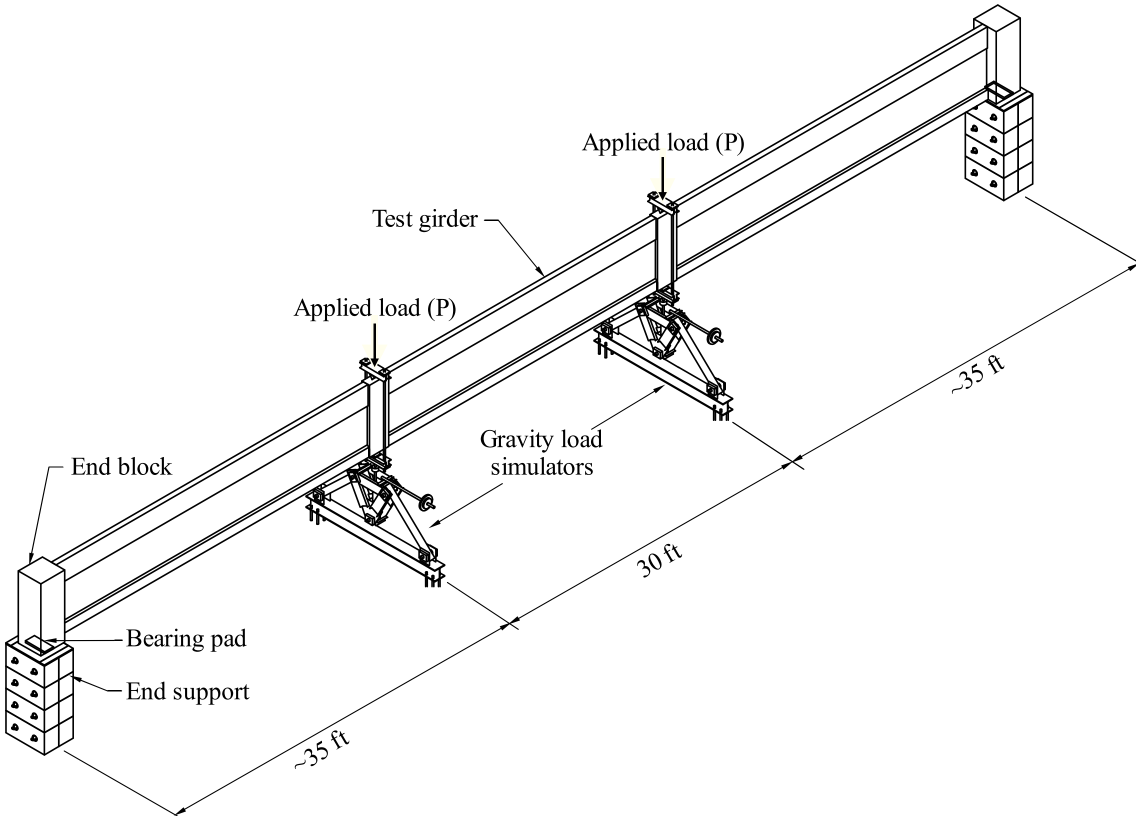

Figure 7.1. Overview of test setup

7.3 Experimental constraints

7.3.1 Length of test girder

Buckling tests were performed inside the FDOT M. H. Ansley Structures Research Center laboratory where the available length the strong floor permitted a maximum physical test girder length of 102 ft. With the overall (end to end) girder length limited to 102 ft., the effective girder span length—as measured from center of bearing pad to center of bearing pad—had to be a few feet shorter to accommodate pad skew at each end of the girder (Figure 7.2). For each pad skew angle tested, both bearing pads had to be completely contained within the footprint of the girder end blocks (i.e., no part of the pad was permitted to protrude beyond the end of the physical length of girder). For reasons that will be discussed in detail later, the type A bearing pads (described previously in Chapter 5) were used to support the ends of the girder during the buckling tests. Rotating the type A bearing pad to the maximum skew angle of 45 deg. and allowing 5/8 in. clearance between the corner of the pad and edge of the girder end block (Figure 7.2), required that the center of the bearing pad be located 13 in. from the edge of the test girder, making the span length 99 ft.-10 in., or approximately 100 ft.

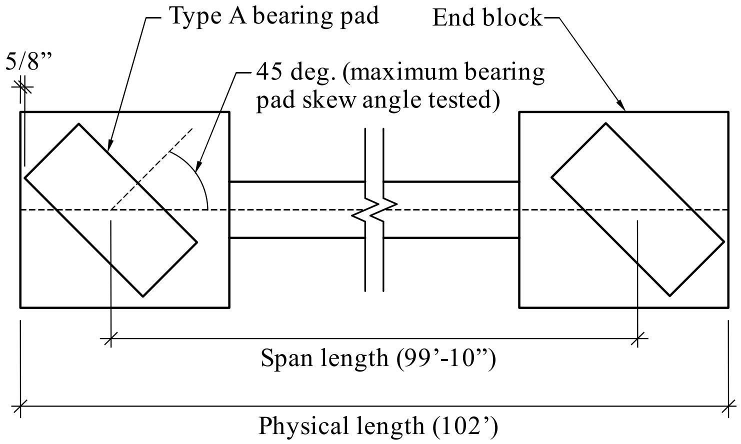

Figure 7.2. Physical length and span length defined

7.3.2 Loading conditions

Under field loading conditions, girder buckling is induced by the self-weight of the girder, which consists of a uniformly distributed vertical load acting through the center of gravity of the girder cross-section. To emulate such field loading conditions in the laboratory, ideally a uniform load would be applied, with no lateral restraint, through the center of gravity of the girder. In this study, devices called 'gravity load simulators' (described in detail later) were designed, fabricated, and used to apply vertical loads—without lateral restraint—to the test girder. Since such devices apply point loads rather than uniformly distributed loads, the uniform field loading condition was approximated in the laboratory using two point loads located approximately at the third points of the girder span (Figure 7.1).

Originally, two possible loading conditions were investigated to determine the level of error that would be introduced by replacing the ideal uniform loading condition with point loads: a single concentrated load applied at midspan, and two equal concentrated loads applied at the third points. For each of the three loading conditions of interest (uniform load, midspan point load, and third point loads), moment diagrams for a simply supported beam, each with the same maximum moment, are presented in Figure 7.3. As shown, the shape of the uniformly loaded moment diagram is most closely matched by the pair of concentrated loads as opposed to the single concentrated load. In fact, the areas under the moment diagrams produced by uniform load and third point loads are exactly equal. Therefore, two point loads were applied to the test girder using gravity load simulators located approximately at the third points of the girder (applying loads at the precise third points was not practical due to laboratory strong floor anchor point locations).

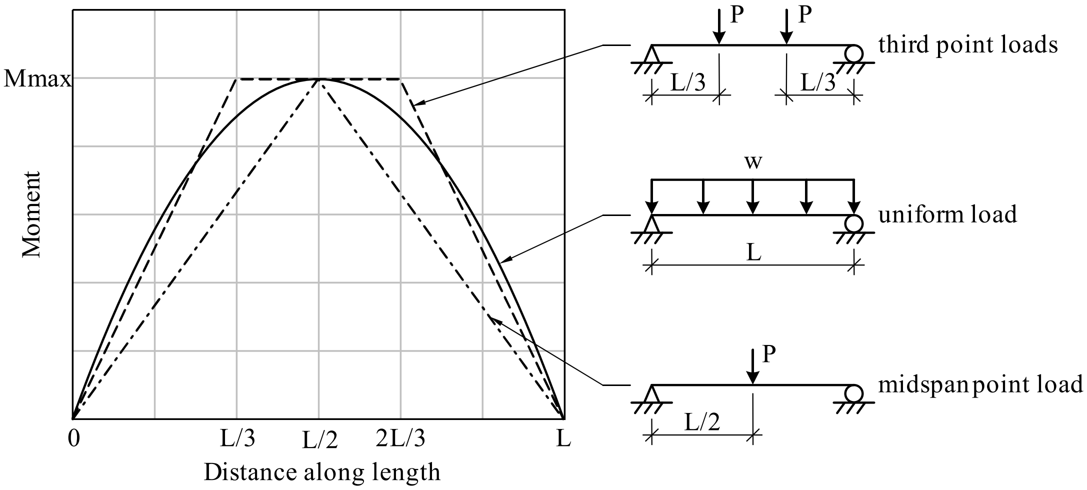

Figure 7.3. Moment diagrams for simply supported beam with various loading conditions

Gravity induced self-weight loads on the girder act, by definition, through the center of gravity of the cross-section. Applying laboratory loads through the center of gravity, however, would have required the introduction of holes through the web of the test girder, creating issues such as the potential for localized crushing of the concrete in the web, or cracking. To avoid these concerns, the point loads were instead applied at the centerline of the top surface of the test girder (Figure 7.1). Finite element analyses of both the center of gravity loading scenario and the top surface loading scenario were conducted to determine if the buckling loads corresponding to each loading scenario were sufficiently in agreement. Analysis results indicated minimal difference in buckling loads, therefore it was deemed acceptable to load the test girder at the top surface of the top flange.

7.3.3 Elastic buckling

The buckling tests conducted in this study were performed for the purposes of experimentally demonstrating sensitivity of buckling capacity to changes in bearing pad roll stiffness, and to collect data for validation of numerical models. Furthermore, to establish confidence in the experimental data, it was desirable to demonstrate repeatability of the test results. Given these objectives, cracking of the concrete girder (particularly partial section cracking) was undesirable as it might have obscured the influence of the pad roll stiffness and would have been very challenging to reproduce analytically. Additionally, section cracking could have lead to differences in beam response from one test repetition to the next (for a fixed bearing pad configuration). American Concrete Institute (ACI) 318-11 Table R18.3.3 states that if a girder enters the transition zone (i.e., the zone between the uncracked and fully cracked conditions), then cracked section properties must be used to determine girder deflection. Since deflection was a key parameter measured during each laboratory buckling tests, it was desirable to design the test girder to buckle elastically so that partially cracked section properties would not need to be used in interpreting the test results. Elastic behavior also ensured repeatability of the tests (which will be clearly demonstrated later in this report) and ensured that the only factor influencing buckling capacity was bearing pad roll stiffness.

CHAPTER 8
GIRDER BUCKLING ANALYSIS

8.1 Introduction

To facilitate the design of a test girder cross-section that would buckle elastically at a span length of approximately 100 ft., finite element models of the girder and support system were developed using the finite element code ADINA (ADINA 2011). Girder models employing a variety of different trial cross-sectional shapes were analyzed under the planned experimental test loading conditions to arrive at a cross-sectional shape that was expected to buckle elastically at a span length of 100 ft. This chapter describes the finite element models and the analysis procedures that were used to quantify girder buckling load and arrive at a suitable girder cross-sectional shape.

8.2 Finite element model of experimental test setup

As noted previously, buckling tests were performed on a full-scale test girder using a vertical loading system consisting of gravity load simulators and load frames. For reasons that will be discussed later in this report, it was necessary to construct the test girder in a segmental manner. Consequently, three component types, each with a distinct cross-sectional shape, were used to form the overall girder: precast segments, closure strips, and end blocks (Figure 8.1). Gravity load simulators were used to apply vertical load to the top of the test girder at the closure strip locations.

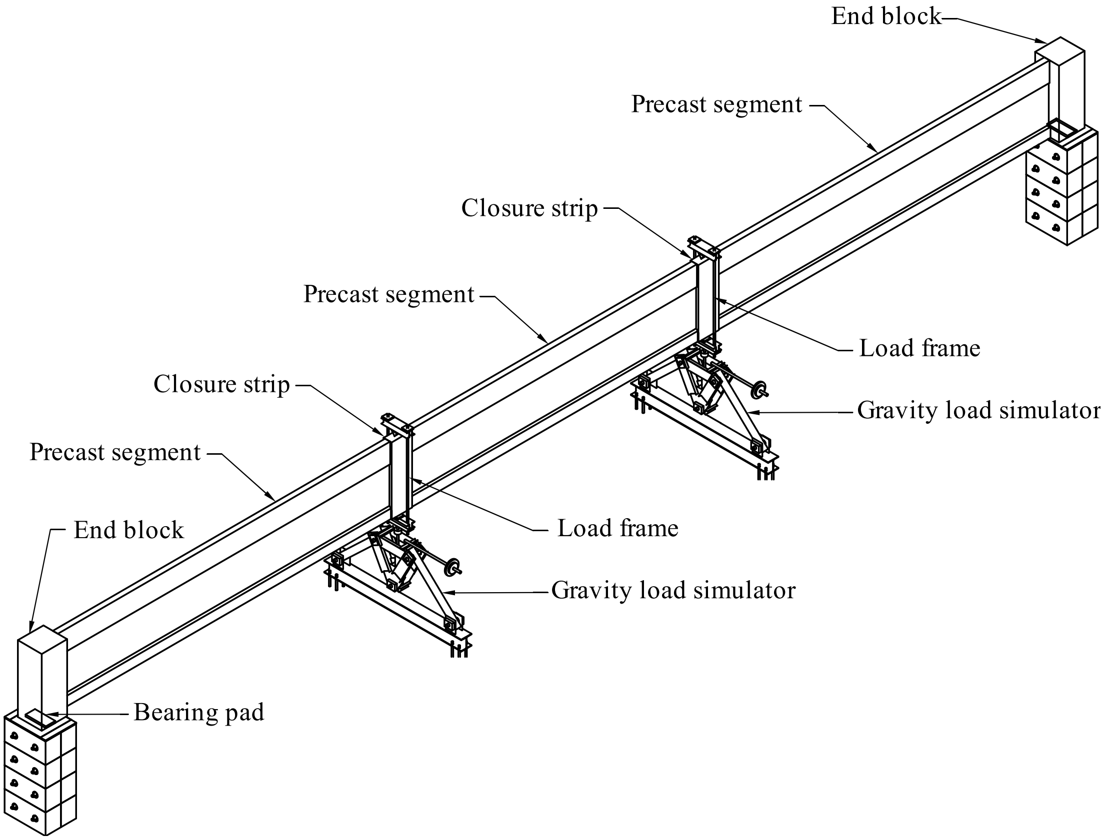

Figure 8.1. Test setup overview

To determine a girder cross-sectional shape that would buckle elastically at a 100 ft span, buckling capacity analyses were carried out by conducting large displacement analyses on system-level models (Figure 8.2) that combined beam elements (representing the test girder) and spring elements (representing the bearing pad). In this approach, loads were incrementally applied to the structure, and at each level of loading, static equilibrium of the structure (stability) was solved for in the deformed configuration of the structure (i.e., taking into account the changes of geometry that occurred as a result of the loads). In order to use such an approach to solve buckling problems, member imperfections (e.g., sweep) must be introduced into the initial configuration of the structure. Sweep imperfection of the girder was introduced by superimposing a second order lateral parabolic shape on the girder with maximum sweep occurring at midspan. Inclusion of sweep in the girder model accounted for construction imperfections and also aided in initiating girder instability under the applied loads.

Concrete components of the test girder were modeled using a linear elastic material model. During the test girder cross-sectional shape development stage of this project, a representative elastic modulus of 4,770 ksi was used for the concrete. This modulus was later updated to reflect results of modulus tests on concrete cylinders from the test girder.

To achieve both computational efficiency and accuracy, a combination of standard Hermitian beam elements and warping beam elements was used to model the girder. Warping effects (resulting from torsion) were accounted for by means of an additional warping degree of freedom in the warping beam elements. In contrast, plane sections remained planar in the Hermitian beam elements. The slender precast segments and closure strips were modeled with warping beam elements to capture warping effects (in case such effects were important). The relatively rigid end blocks were modeled using Hermitian elements. Regardless of type of element (Hermitian or warping), resultant cross-sectional properties were varied along the length of the test girder, depending on the section (precast segment, closure strip, or end block) present at each location (Figure 8.2). The girder elements were geometrically located at the center of gravity (C.G.) of the test cross-section. The eccentricity between the bearing pad (described below) and the C.G. of the section was represented in the model using rigid links (Figure 8.3). Similarly, rigid elements extended upward to loading points at the top surface of the physical beam. Vertical point loads were applied to these locations to simulate vertical loads applied by each gravity load simulator.

Each bearing pad in the system model was represented using a set of six (6) spring elements consisting of three translational springs and three rotational springs (Figure 8.2). Translational springs—representing the shear stiffness of the bearing pad (along the x-axis or y-axis) and axial stiffness (along the z-axis)—were linear and based on stiffness results from previous research (Consolazio et al. 2007). Similarly, rotational springs representing pad torsional stiffness (about the z-axis) and roll about an axis perpendicular to the span of the beam (about the x-axis) were modeled as linear springs, with stiffnesses determined from results of previous research (Consolazio et al. 2007). In contrast, rotational springs about the y-axis (i.e., the roll axis) were *nonlinear*, derived from roll stiffness results (moment-roll curves) quantified in Chapter 6, from the isolated bearing pad experiments.

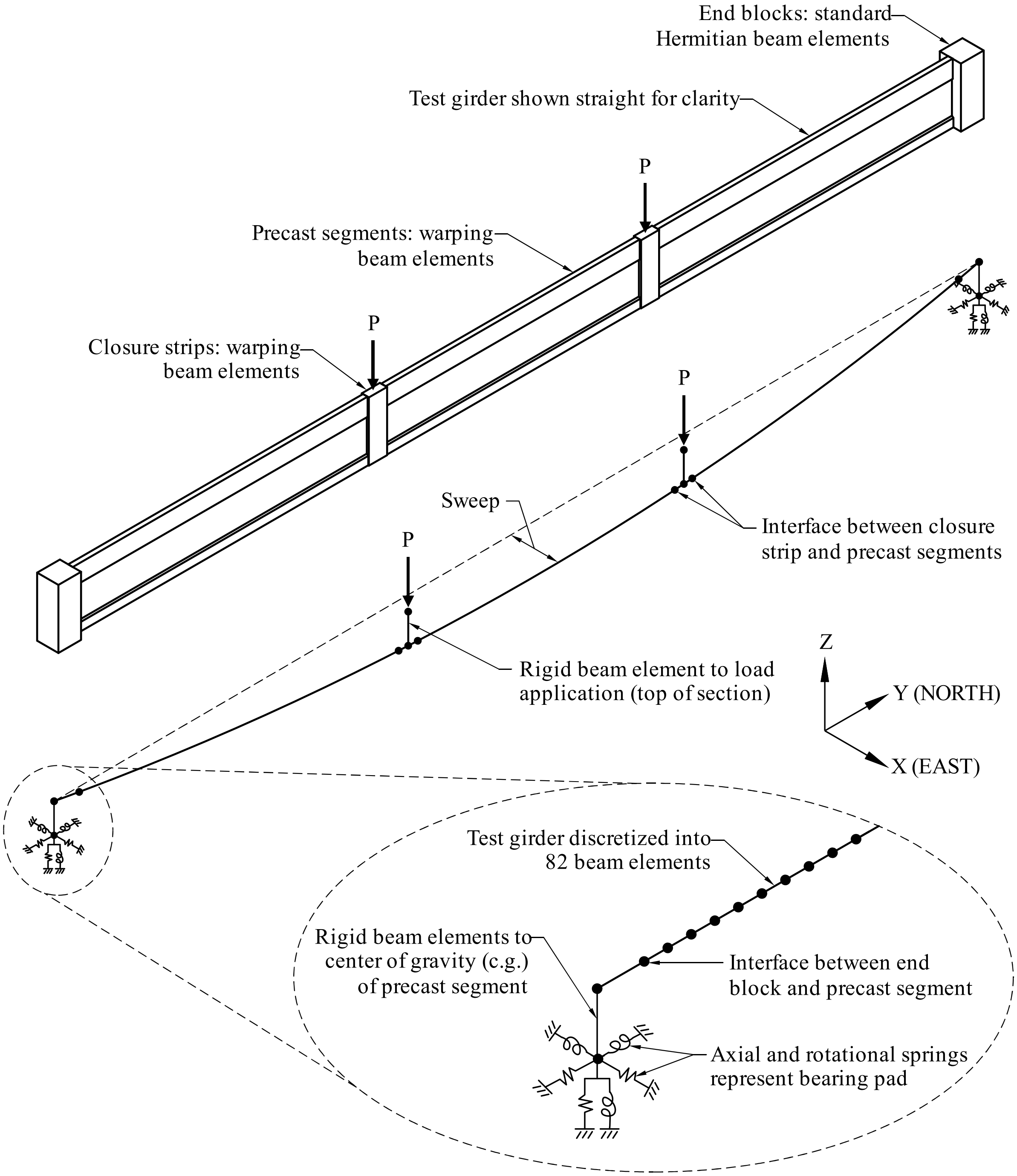

Figure 8.2. Test girder buckling system model

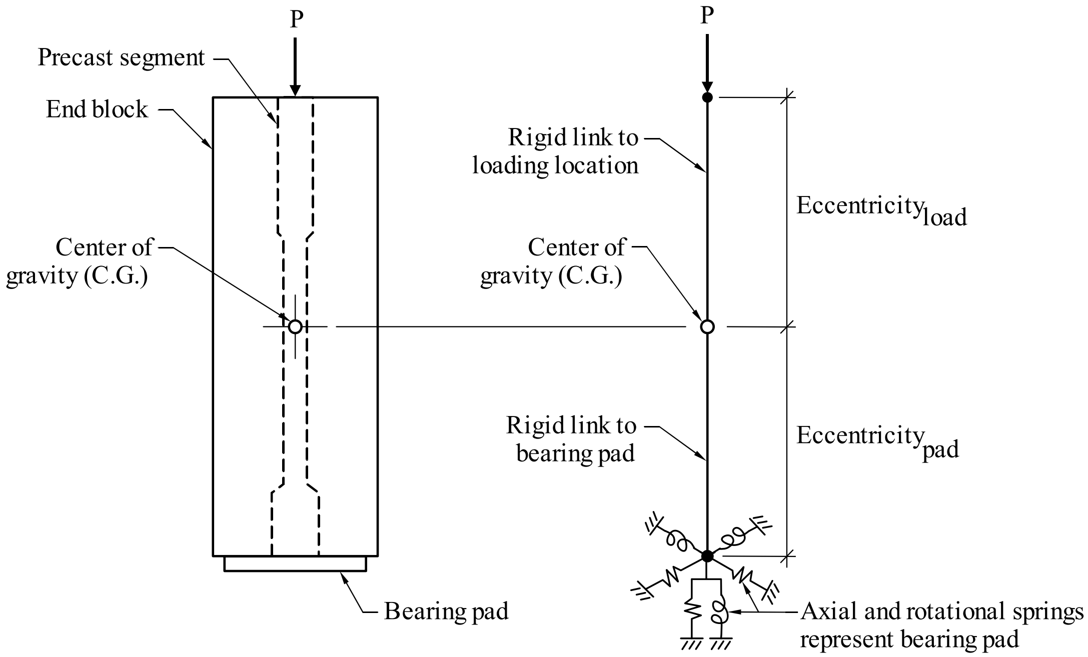

Figure 8.3. Eccentricities of load application point and bearing pad relative to center of gravity of test cross-section

Loads acting on the girder model included uniform self-weight (gravityw loading), which acted through the center of gravity of the section (Figure 8.4a), and concentrated vertical loads applied to the top of the section at the two closure strip locations (Figure 8.4b). To analyze the girder for the purpose of quantifying buckling capacity, loads were applied to the model in two stages (Figure 8.5). The uniform loading was increased in small steps (increments) from zero to the full self-weight of the girder, then held constant while the magnitude of the applied point loads was incrementally increased. At each incremental load step, girder displacements were computed by numerically satisfying static equilibrium of the girder in the deformed geometric configuration. Each buckling simulation was complete once equilibrium could no longer be established, indicating that structural instability (buckling) had occurred.

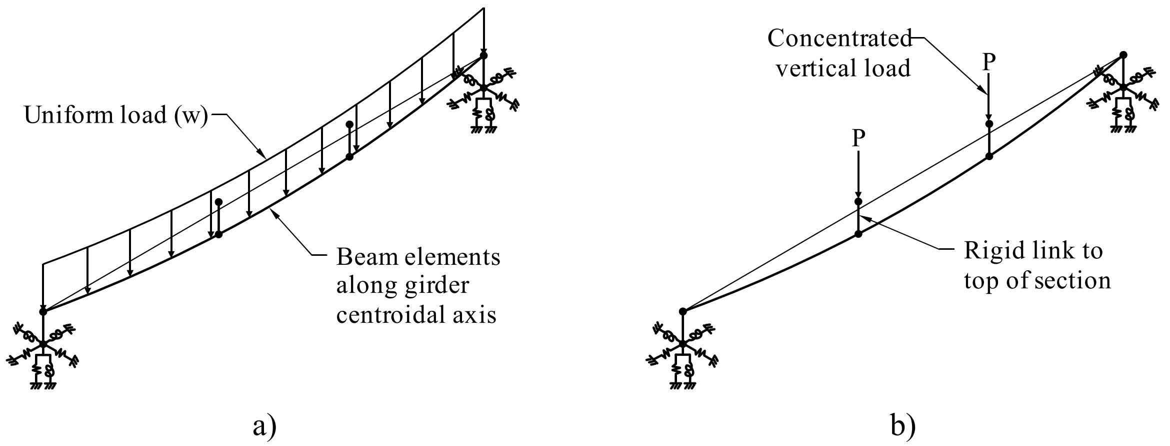

a)

b)

Figure 8.4. Load application on test girder buckling analysis:
a) Uniform load; b) Concentrated vertical loads

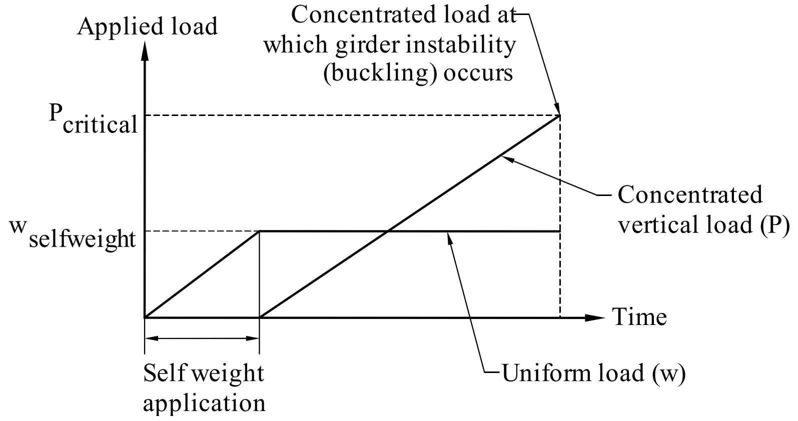

Figure 8.5. Load procedure for buckling analysis

CHAPTER 9
TEST-GIRDER CROSS-SECTION DEVELOPMENT

9.1 Introduction

Under ideal circumstances, buckling tests would be performed on a typical section used in long-span girder construction. During the course of this project, the standard section for long-span construction was updated from the Florida Bulb-Tee (FBT) to the current Florida I-beam (FIB). Using the same pad types tested in the roll stiffness experiments, finite element buckling analyses were performed with the cross-sectional properties of several of the FBT and FIB sections. In the case of the non-skewed, non-sloped bearing pad orientations, the load required to buckle either type of section at the available test span length of 100 ft would cause significant cracking in the girder. To avoid violating one of the initial test setup constraints (the girder must remain in the uncracked zone), alternative cross-sections were explored that would buckle elastically in the laboratory at a 100 ft. span length. Preliminary analysis indicated that the resulting test cross-section would need to be significantly more slender than a typical FBT or FIB section. To limit stresses induced during transportation, the test girder was composed of three individual prestressed precast segments, that were transported on a flatbed truck.

Using segmental construction, post-tensioning was used to form a continuous test girder of the prestressed precast segments, closure strips, and end blocks (Figure 9.1). At the junction between each precast segment was a closure strip, which served as a means of connecting the precast segments together and also served as the location at which concentrated point loads would be applied. End blocks were used to provide sufficient bearing surface areas for the bearing pads located at the ends of the test girder, and to provide anchorage points for the post-tensioning. The remainder of this chapter details each component of the segmental test girder and summarizes the basis for design of each component. Complete construction drawings for the test girder can be found in Appendix B.

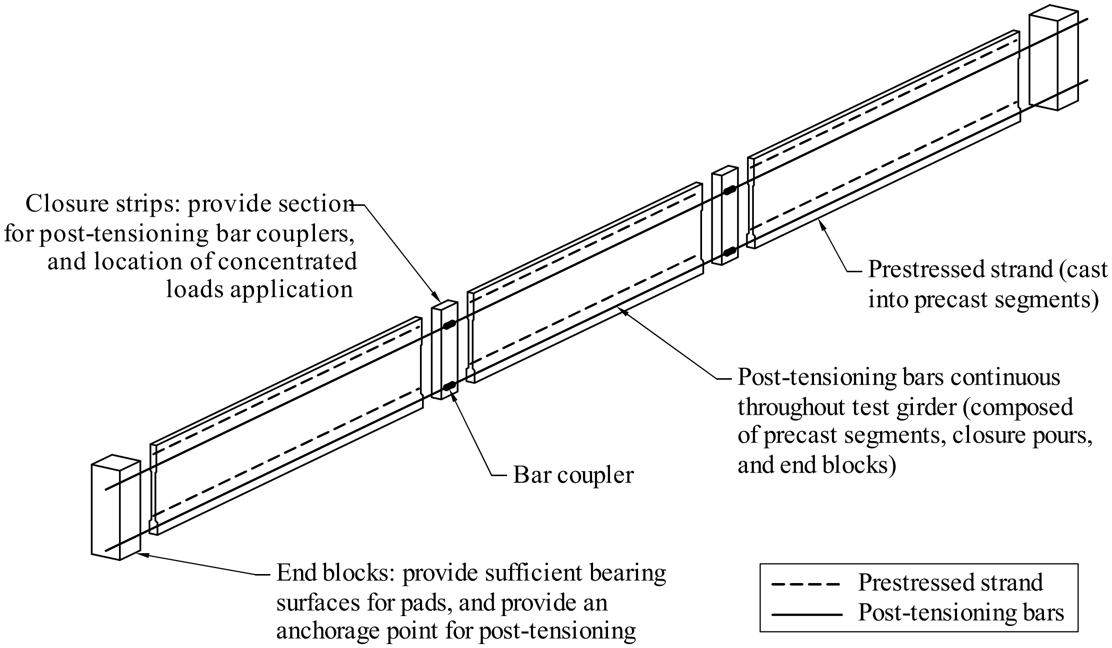

Figure 9.1. Exploded view of test girder with prestressing shown

9.2 Precast segment cross-section design

9.2.1 Design of girder cross-section

Several analytical tools were used in the test girder design process to determine cross-sectional properties of trial cross-sections (Mathcad), predict buckling loads (the finite element analysis software package ADINA), and calculate stresses throughout the test girder using the predicted buckling loads (Mathcad). The procedure for designing the test girder cross-section is summarized in Figure 9.2. Beginning with the standard Florida Bulb-Tee cross-section, a buckling analysis was performed. The strong and weak axis internal moments obtained from the buckling analysis (due to the loads required to cause buckling) were used to calculate concrete stresses along the length of the test girder, which also accounted for stresses due to prestressing. These stress calculations were performed at various stages in the life of the test girder: during prestressing, during transport, and during testing. The calculated stresses at each stage were compared to the transition zone tensile and compressive stress limits required by the FDOT Structures Design Guideline (FDOT, 2012) §4.3.1.C.3 and ACI318-11 §18.3.3, §18.4.1, and §18.4.2. If the calculated stress at any point exceeded these stress limits, then the trial cross-section design was rejected and a new cross-section was developed. A separate cross-sectional analysis program was used to determine cross-section properties (e.g., moments of inertia, torsional constant, warping constant) of trial sections by specifying the cross-section geometry. The cross-sectional properties of the new trial section were subsequently incorporated into the buckling model, and the process of determining the internal moments and checking stresses was repeated.

Following this iterative process, several different test cross-sections were designed and evaluated to check for exceedance of permissible stress limits. For each iteration, the cross-section was altered to decrease the buckling capacity of the test girder, thereby decreasing the stresses in the test girder. In general, for long-span slender flexural elements, buckling capacity is highly sensitive to the weak axis moment of inertia (I_z) and torsional constant (J), in that decreasing either property decreases the buckling load. Hence, maintaining a large strong axis moment of inertia (I_x)—and therefore maintaining a large strong-axis moment capacity of the test girder—was necessary to avoid cracking under the applied buckling load.

The process of increasing slenderness and reducing buckling capacity was initiated with the standard FBT78 cross-section, where portions of the protruding top and bottom flanges were removed (Figure 9.3). An iterative trimming process was carried out in which each subsequent section was designed to be less wide than the previous iteration, while the height remained unchanged, effectively reducing the buckling load while maintaining strong axis moment capacity. Once the flanges were completely removed and the cross-section was still predicted to crack under the applied buckling load, the web thickness was trimmed as well.

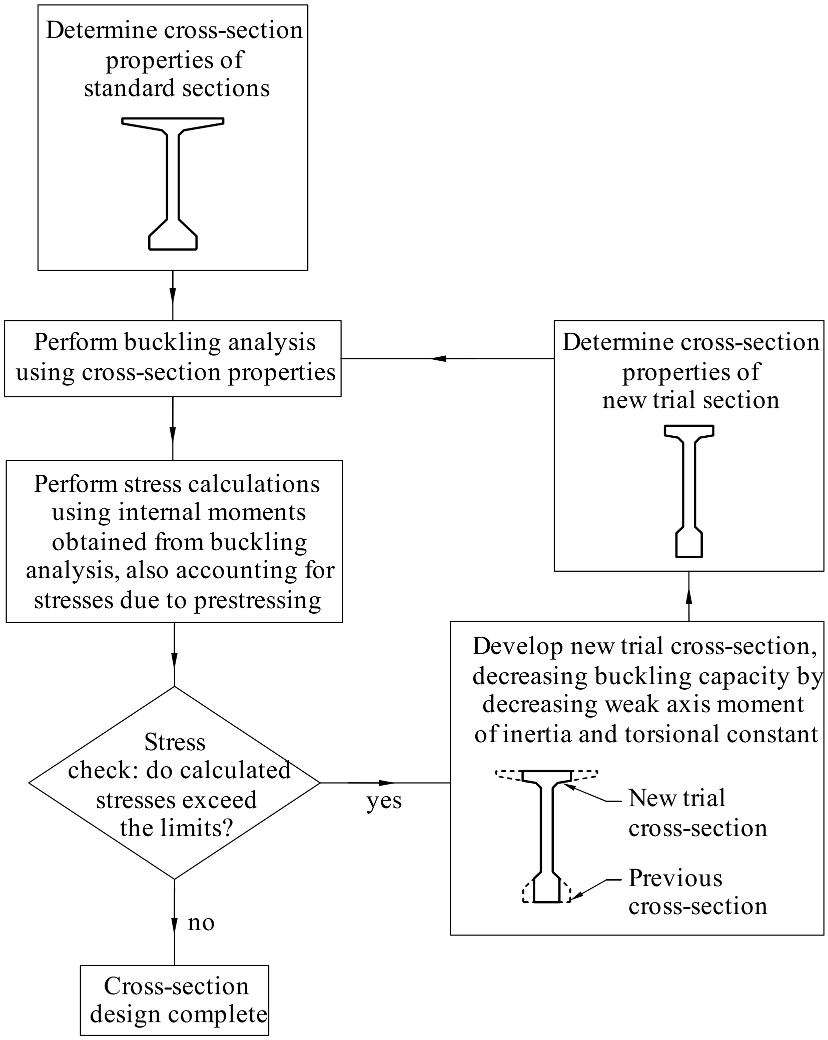

Figure 9.2. Test cross-section design flowchart

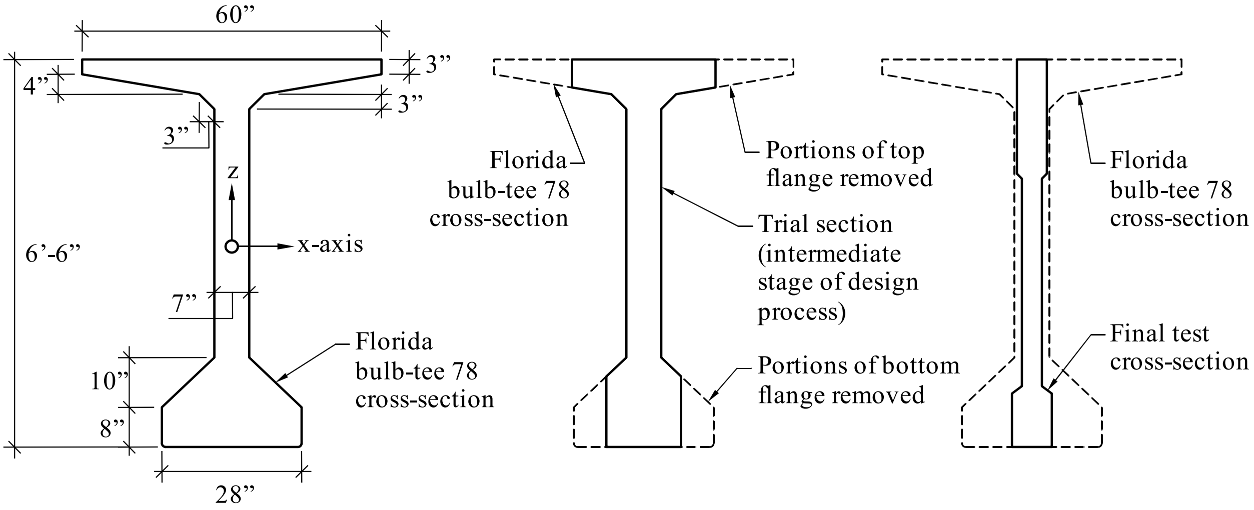

Figure 9.3. Iterative process of precast segment cross-section design

After several iterations, the slenderness of the cross-section became an issue in regard to limiting stresses during transport. Typically, if a girder is 100 ft long, it is transported by spanning between a truck and a trailer thus acting as a simply supported beam (Figure 9.4). Braces are provided at the ends to tie the girder to the truck or trailer and to brace it against overturning. In this manner, long-span prestressed girders can be brought to a job site as a single piece. However, the test girder cross-section in this project was designed to be very slender (relative to a typical bridge girder), and would have been damaged in transport if the test girder were cast and transported as a single 100 ft unit. Consequently, the girder was designed to consist of three segments of approximately equal length to facilitate transport without damage.

Figure 9.4. Transport of bridge girders (photo courtesy of Dr. Robert I. Carr)

To further optimize the section, the trimming approach was continued until only minimum concrete cover (as per ACI 318-11 §7.7.3) was provided to the post-tensioning in the bottom flange. The final precast segment test cross-section (Figure 9.5) was thin (compared to a typical bridge girder) but as tall as a FBT78, with a small weak axis moment of inertia and torsional constant, coupled with a large strong axis moment of inertia to prevent cracking during buckling. Section properties for the final girder cross-section are summarized in Table 9.1. DYWIDAG galvanized steel duct (2.05 in. outer diameter) cast in each girder segment formed a conduit to accommodate DYWIDAG post-tensioned bar (1 in. diameter), extending through the full length of the test girder (Figure 9.1). Pretensioned strands (0.6 in. diameter) were cast in each precast segment, which provided additional compression at the bottom of the segments to prevent cracking during transport and testing. The pretensioned strand at the top of the section was lightly stressed, and served primarily to hang shear reinforcement hooks prior to casting the concrete segments. Mild reinforcement running along the length of each segment was placed throughout the depth of the section.

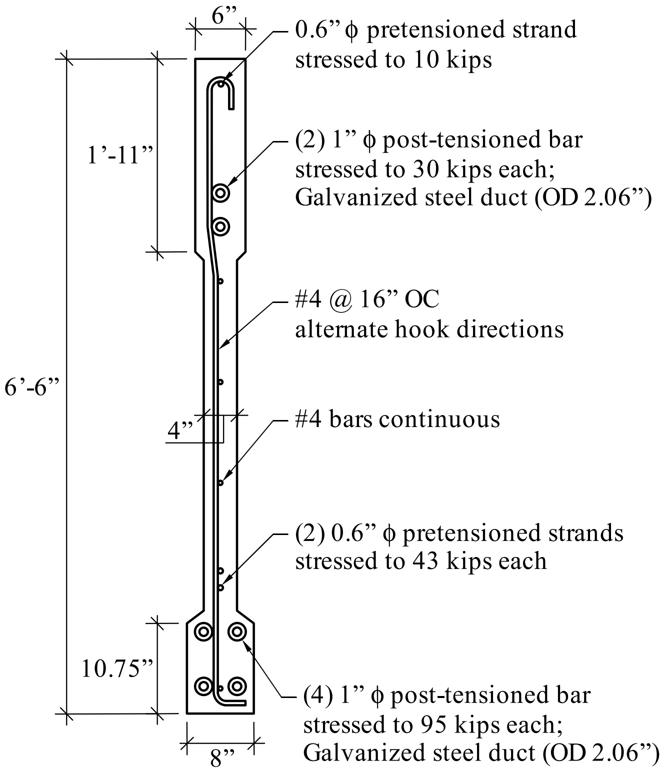

Figure 9.5. Final precast segment cross-section

Table 9.1. Section properties of precast segments

Section property name	Section property value
Area A	405.0 (in.^{2})
Height of centroid y	38.39 (in.)
Moment of inertia I_x	246,400 (in.^{4})
Moment of inertia I_z	1,136 (in.^{4})
Torsional constant J	3,765 (in.^{4})

9.3 Design of closure strip cross-section

The primary function of the closure strips was to provide adequate cover for post-tensioned bar couplers and bar coupler housings that were placed between each precast segment. Typically in segmental construction using post-tensioned bars (as opposed to strands), the maximum length of bar available is less than the span length, and it therefore becomes necessary to couple post-tensioned bars together to form longer continuous bars. This approach was required in the case of the project test girder, because the total girder length was 100 ft and the DYWIDAG post-tensioned bar was only available in mill lengths up to 60 ft. Acrylic bar coupler housings (3.2 in. outer diameter) were fabricated and cast in the closure strips to form a conduit sufficiently large to accommodate DYWIDAG post-tensioned bar couplers (2 in. diameter). The width of the closure strip (9.5 in.) was controlled by minimum concrete cover requirements for the bar coupler housings, per ACI 318-11 §7.7.3 (Figure 9.6). Closure strip cross-sectional properties are presented in Table 9.2. As noted earlier, concentrated vertical loads were applied to the top of the test girder using gravity load simulators, at locations corresponding approximately to the span length third points. In an effort to minimize localized cracking caused by the application of concentrated point loads, closure strips were located at these loading locations, which permitted the loads to be applied to a wider cross-section. Embedded steel plates also served to prevent localized cracking at the top of the closure strips. Grout tubes were provided for each post-tensioning duct at the closure strips.

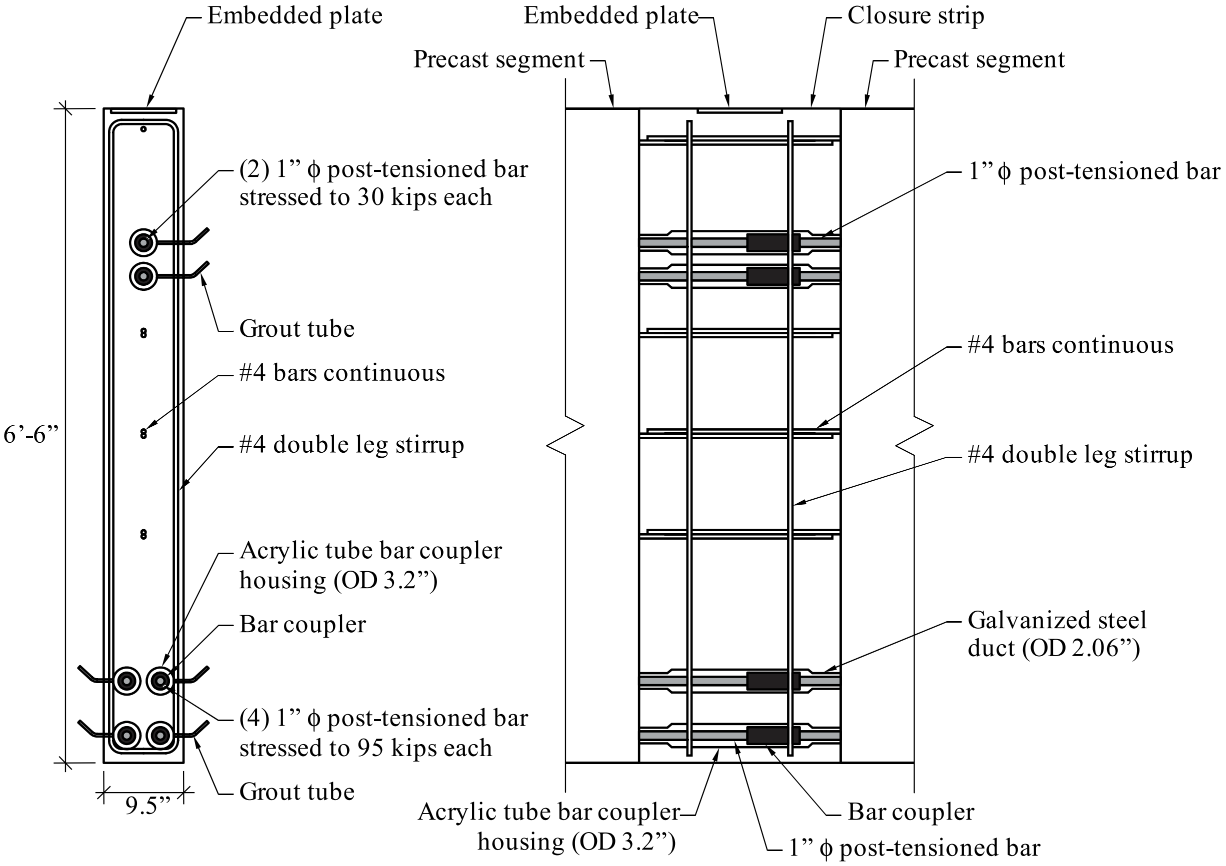

Figure 9.6. Final closure strip cross-section

Table 9.2. Section properties of closure strips

Section property name	Section property value
Area A	741.0 (in.^{2})
Height of centroid y	39.0 (in.)
Moment of inertia I_x	375,700 (in.^{4})
Moment of inertia I_z	5,573 (in.^{4})
Torsional constant J	20,640 (in.^{4})

9.4 Design of end block cross-section

As noted previously, the end blocks were designed to allow sufficient bearing surface areas for the bearing pads located at the ends of the test girder, and to provide anchorage points for the post-tensioning. For each bearing pad skew angle tested, the bearing pads had to be completely contained within the footprint of the girder end blocks (i.e., no part of the pad was permitted to protrude beyond the width of the girder end block). Consequently, the width of the end blocks (Figure 9.7) was selected so that the bearing pads had a large enough area to bear completely against the end block even at the maximum skew angle tested—a 45 deg. skewed configuration. The end block cross-sectional shape is presented in Figure 9.8, with cross-section properties presented in Table 9.3.

Anchorage zone reinforcement required for the post-tensioning bars was cast into the end blocks. In post-tensioned members, the anchorage zone is defined as the portion of the member through which the concentrated prestressing force is transferred to the concrete and distributed across the section (ACI 318-11 §2.2), and is the general expression for combined general and local zones (AASHTO 2004). In this project, DYWIDAG Systems International (DSI) engineers supplied specifications for local zone reinforcement (mild steel), including the bar sizes and configuration, and concrete strength required before stressing the bars. Separately, general zone reinforcement, was designed by the UF research team for the end blocks, and consisted of a cage of hoops and ties in both vertical and horizontal orientations. Leveling plates were cast into the concrete end blocks to provide a bearing surface for the anchor plates provided by DSI. Grout tubes for the post-tensioning duct protruded from the exterior of the end blocks. Lifting loops consisting of prestressing strand were cast in the end blocks and were designed to support and lift the test girder into place for testing after post-tensioning was complete.

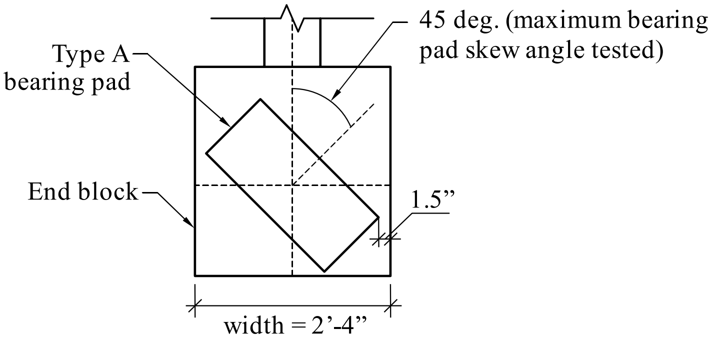

Figure 9.7. End block width, controlled by bearing pad size and skew angle

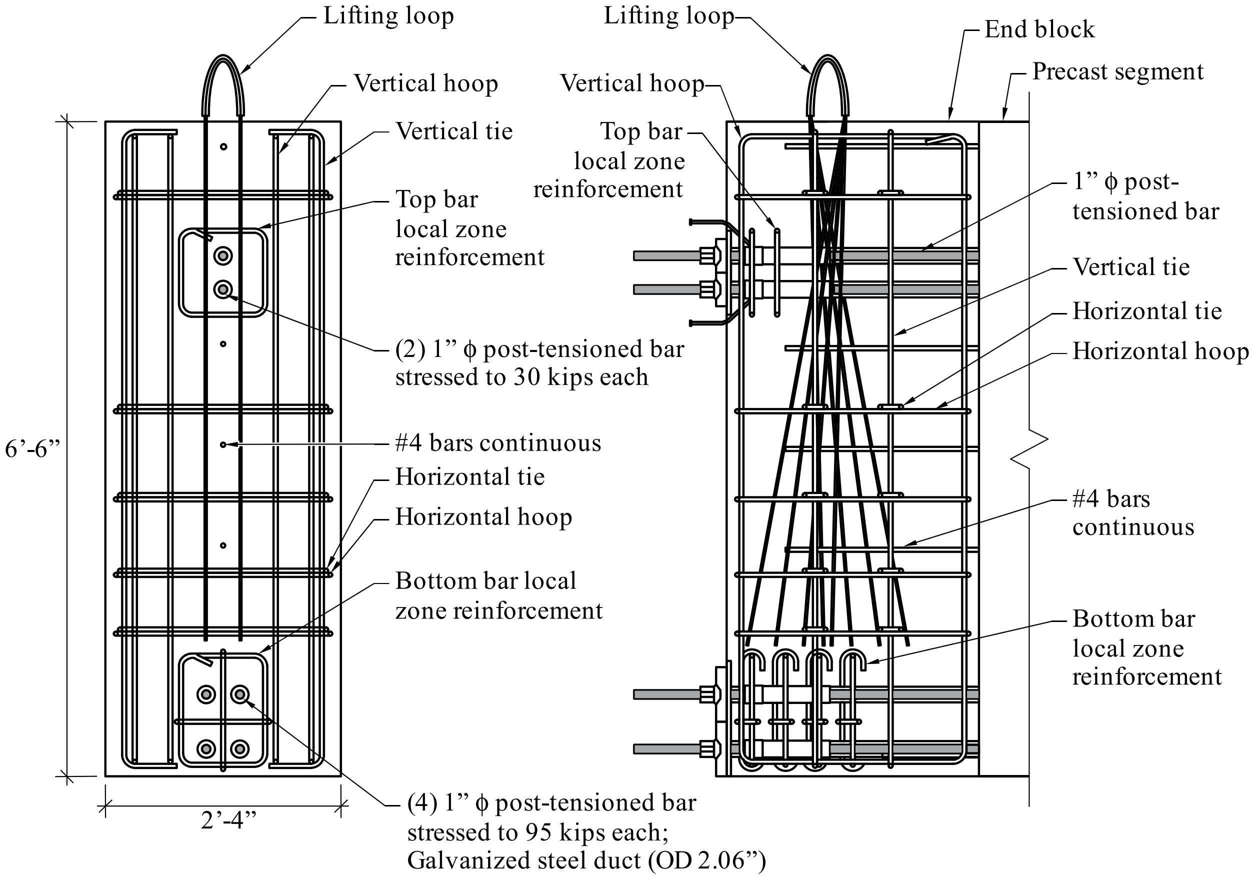

Figure 9.8. Final end block cross-section

Table 9.3. Section properties of end blocks

Section property name	Section property value
Area A	2,184 (in.^{2})
Height of centroid y	39.00 (in.)
Moment of inertia I_x	1,107,000 (in.^{4})
Moment of inertia I_z	142,700 (in.^{4})
Torsional constant J	442,200 (in.^{4})

CHAPTER 10
TEST GIRDER CONSTRUCTION

10.1 Introduction

The test girder was constructed in a segmental manner, and consisted of three (3) precast prestressed segments, two (2) closure strips, and two (2) end blocks. The precast segments were cast at Dura-Stress Inc. in Leesburg, Florida, and shipped to the FDOT M.H. Ansley Structures Research Center (referred to in this chapter as the FDOT laboratory) in Tallahassee, Florida. Oriented as shown in Figure 10.1, the closure strips and end blocks were cast in place at the FDOT laboratory, after which the test girder was post-tensioned and grouted. Cylinders cast from batches of concrete placed in the end blocks and closure strips were tested for compressive strength and modulus of elasticity. This chapter documents the construction of the test girder—including the casting of each section and post-tensioning—and summarizes the material tests performed on the cylinders cast from each batch of concrete.

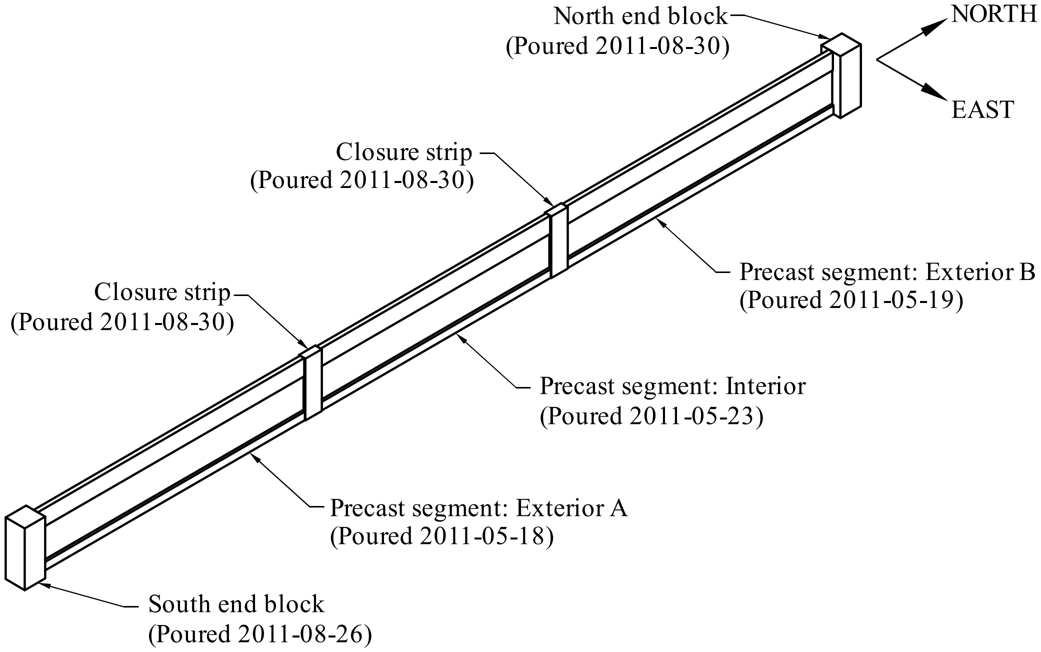

Figure 10.1. Casting dates for girder components and final orientation of girder in FDOT laboratory

10.2 Precast segments

All three precast segments were cast on a single bed, with pretensioned strands spanning continuously throughout all three precast segments (Figure 10.2). Each segment was cast (Figure 10.3) on a separate day, within five days of each other (casting dates are indicated in Figure 10.1). Although different concrete batches were used for each segment, the mix design was the same for all segments, with a specified 28-day concrete compressive strength of 6,500 psi. For each precast segment concrete batch, eleven 4 in. x 8 in. (diameter x height) cylinders were cast for later use in strength and modulus testing to determine the material properties of the test girder at the time of buckling tests. Unstressed reinforcing bars were temporarily placed in the post-tensioning ducts to increase the stiffness of the ducts while placing the concrete and to help maintain straight duct alignment (Figure 10.4). After concrete placement, tarps were draped over each segment during the curing stage (Figure 10.5). Once the concrete reached the specified strength (verified by testing cylinders from corresponding batches) required for prestress transfer, the prestressed strands were cut and the segments were left to cure without a tarp (Figure 10.6). Approximately two weeks after casting the last of the three segments, Dura-Stress transported the segments on a flatbed trailer (Figure 10.7) to the FDOT laboratory.

Figure 10.2. Precast segments formwork aligned on single pretensioning bed at Dura-Stress

Figure 10.3. Placing concrete in the precast segment formwork

Figure 10.4. Unstressed reinforcing bars placed in ducts to keep ducts straight during placing of concrete

Figure 10.5. Tarp covers applied to each segment during curing

Figure 10.6. Precast segments after formwork removed at Dura-Stress

a) b)

Figure 10.7. Precast segment arrival at the FDOT laboratory:
a) Segments on flatbed trailer; b) End view of segments

10.3 Closure strips

Closure strips located at approximately the third points of the span of the test girder were cast in place at the FDOT laboratory (casting dates are indicated in Figure 10.1). DYWIDAG bar couplers and bar coupler housings (larger diameter duct, to provide space for the bar coupler) were positioned within the closure strips (Figure 10.8). Bar coupler housings were fabricated from acrylic tube—cut in half lengthwise and clamped around duct-transition pieces—to provide visual confirmation of the location of the couplers within the closure strips. Prior to placing the concrete, the bar coupler housings were taped to ensure that no concrete seeped into the void around the couplers (Figure 10.9). Mild reinforcing steel extending from the ends of the precast segments overlapped inside the closure strips, providing additional continuity to the test girder (Figure 10.9).

Formwork for the closure strips was fabricated at the FDOT laboratory (Figure 10.10), and the closure strips were cast in place (Figure 10.11) between the precast segments. The bottom of the formwork was built up to the same elevation as the bottom surface of the precast segments, to ensure a flat, continuous bottom surface of the test girder. To protect the concrete at the top of the closure strips against localized cracking (during subsequent girder testing during which time concentrated loads would be applied at the closure strip locations), a steel plate was cast at the top of each closure strip, embedded flush with the top surface of the concrete (Figure 10.12).

Grout tubes were connected to the coupler housings (Figure 10.9) and passed through holes in the formwork, allowing the tubes to be accessible after the concrete had cured and the formwork had been removed (Figure 10.13). Both closure strips were poured on the same day (2011-08-30), from the same batch of concrete. The concrete poured in the closure strips (and end blocks) had a specified 28-day concrete compressive strength of 8,000 psi and utilized Propex Fibermesh® 150 reinforcing fibers (Figure 10.14) to aid in preventing localized section cracking, particularly at the bottom of the girder. Ten 4 in. x 8 in. cylinders were cast from the closure strip batch of concrete for later use in strength and modulus testing.

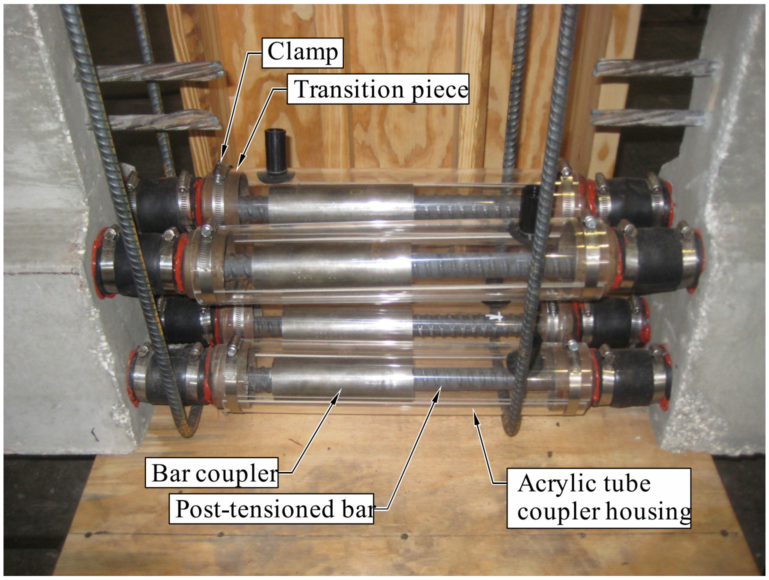

Figure 10.8. Duct couplers located within closure strips (bottom flange of girder)

Figure 10.9. Duct couplers in closure strips, sealed with tape prior to concrete placement

Figure 10.10. Closure strip formwork

Figure 10.11. Placing concrete into the closure strip formwork

Figure 10.12. Embedded steel plate at top surface of closure strip

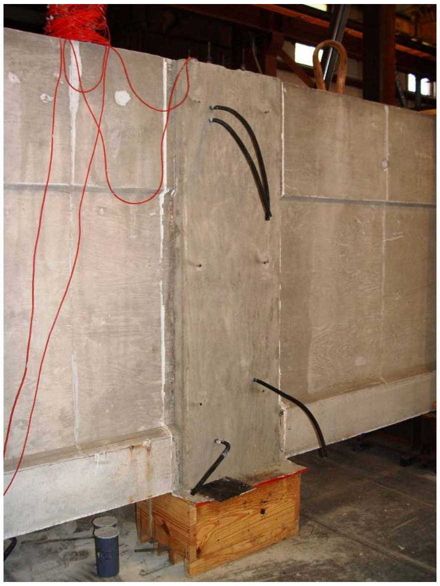

Figure 10.13. Finished closure strip with formwork removed

Figure 10.14. Concrete used in closure strip and end block concrete mix, showing presence of Propex Fibermesh® 150 reinforcing fibers

10.4 End blocks

One function of the girder end blocks was to provide a cross-section capable of accommodating post-tensioning anchorage zone reinforcement, anchor and leveling plates, and lifting loops. Like the closure strips, the end blocks were cast in place at the FDOT laboratory. Figure 10.15 shows the south end block formwork with one side wall removed to expose the interior details. Lifting loops (composed of prestressing strand) were cast into the end blocks and were designed to support and lift the completed test girder after it had been post-tensioned. Anchorage zone reinforcement (Figure 10.16), consisting of mild reinforcing steel, served to distribute the concentrated post-tensioning forces more uniformly over the concrete section. Embedded vertical leveling plates (Figure 10.16) were also cast into the end blocks to provide bearing surfaces for the post-tensioning anchor plates. Figure 10.17 shows the final configuration of the formwork for the end blocks, and Figure 10.18 shows concrete being placed in the north end block.

After formwork removal (Figure 10.19), grout tubes protruded from the faces of the end blocks so that they were accessible during the post-tensioning operation. Leveling plates cast flush with the surface of the end blocks are clearly visible in Figure 10.20a (prior to installation of the post-tensioning anchor plates and anchor nuts). Each of the two end blocks was poured from a different batch of concrete, on different days (casting dates are indicated in Figure 10.1), however the mix design for both batches was the same: specified 28-day concrete compressive strength of 8,000 psi and Propex Fibermesh® 150 reinforcing fibers to aid in preventing localized cracking. For each end block concrete batch, a minimum of ten 4 in. x 8 in. cylinders were cast for later use in strength and modulus testing.

a) b)

Figure 10.15. Open end block formwork revealing mild reinforcement and lifting loops:
a) Side view; b) Isometric view

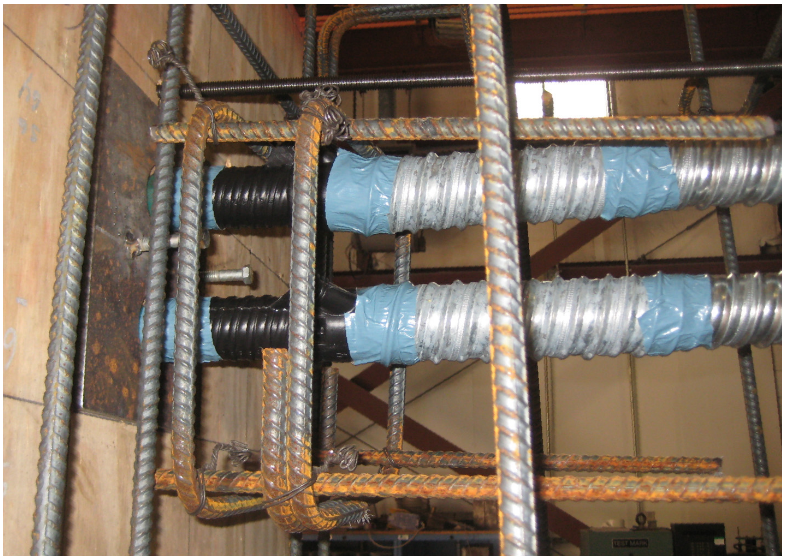

a)

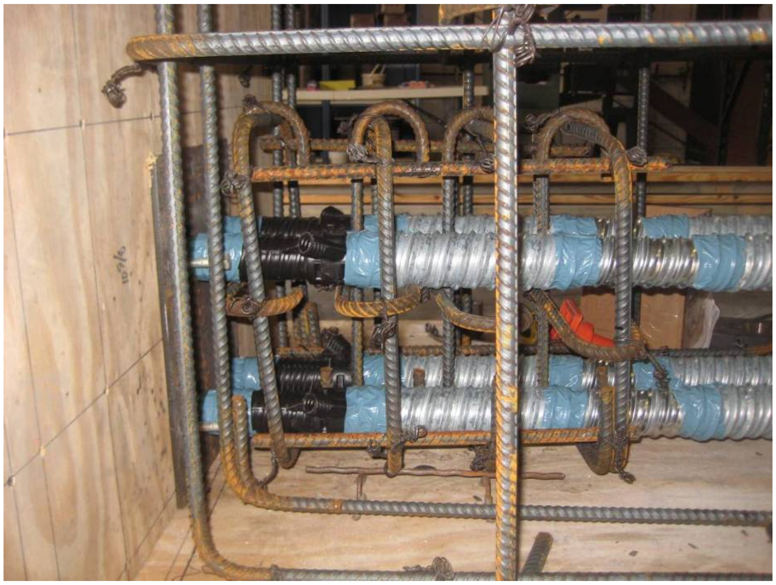

b)

Figure 10.16. Anchorage zone mild steel reinforcement in end blocks:
a) Elevation view at top of cross-section; b) Elevation view at bottom of cross-section

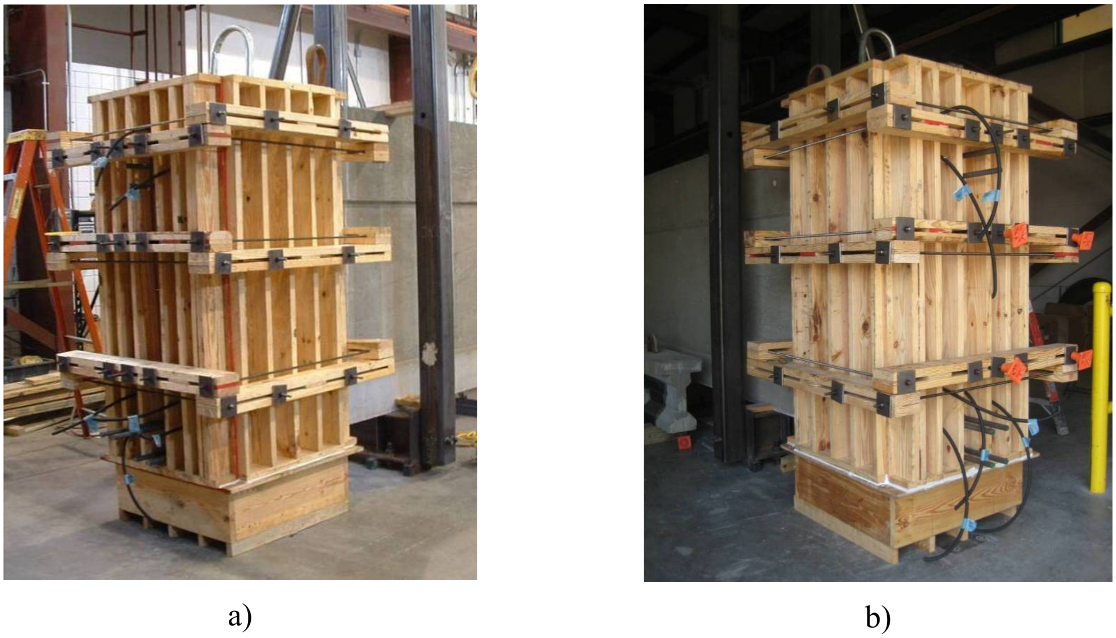

a) b)

Figure 10.17. Completed end block formwork:
a) South end block; b) North end block

Figure 10.18. Placement of concrete in north end block formwork

Figure 10.19. End block after removal of formwork

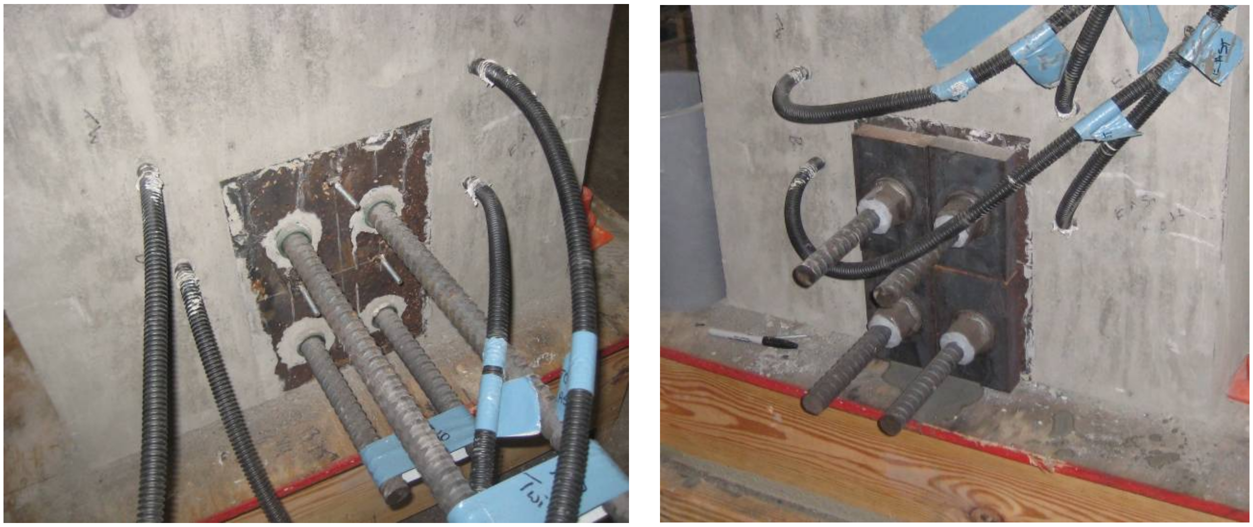

a)

b)

Figure 10.20. Leveling plates and anchor plates at bottom of end block:
a) Embedded leveling plates flush with surface of end block; b) Post tensioning anchor plates and anchor nuts installed

10.5 Material tests and properties

Each time a concrete component of the test girder was cast, 4 in. x 8 in. cylinders were also cast for the purpose of later quantifying material properties. Tests were performed to determine compressive strength (f ’c) and modulus of elasticity (E) of the cylinders at the time of the buckling tests. Approximately half of the cylinders were field-cured and the other half were moist-cured. Field-cured cylinders were cured in the casting yard with the test girder sections for precast segments and in the FDOT structures laboratory in the case of the closure strips and end blocks. Prior to removal of formwork from each cast girder component, the corresponding cylinders remained in plastic molds. After formwork removal, cylinders were demolded and cured in the open air (field-cured) or fully submerged in a tank of lime water (moist-cured, Figure 10.21). Several moist-cured cylinders were tested for compressive strength at intermediate stages of the project (e.g., prior to post-tensioning, to ensure adequate strength before stressing), the results of which are documented in Appendix C. Compressive strength and elastic modulus tests were performed within one week of the girder buckling tests (cylinders tested between 2011-12-08 and 2011-12-12; buckling tests performed between 2011-12-12 and 2011-12-15) to provide data needed for subsequent finite element model validation. Table 10.1 provides a summary of the quantity of cylinders (field and moist-cured) that were tested for compressive strength and elastic modulus within one week of buckling testing. Specific dates on which each cylinder material test was performed are documented in Appendix C.

Table 10.1. Summary of cylinder material tests performed within one week of buckling testing for each girder component

Date poured	Girder component concrete batch from which cylinders were cast	Moist-cured cylinders		Field-cured cylinders		Total cylinders
		Compressive Strength	Modulus of Elasticity	Compressive Strength	Modulus of Elasticity	
2011-05-18	Precast segment: exterior A	2	3	3	3	11
2011-05-19	Precast segment: exterior B	2	3	3	3	11
2011-05-23	Precast segment: interior	2	3	3	3	11
2011-08-26	South end block	3	3	2	3	11
2011-08-30	Closure strips	3	3	1	3	10
2011-08-30	North end block	3	3	1	3	10

Compressive strength tests were conducted in accordance with the *Standard Test Method for Compressive Strength of Cylindrical Concrete Specimens* (ASTM C39, ASTM 2001). Modulus of elasticity tests were conducted in accordance with the *Standard Test Method for Static Modulus of Elasticity and Poisson’s Ratio of Concrete in Compression* (ASTM C469, ASTM 1994). Compressive strength tests were conducted at the University of Florida (on 2011-12-08), and elastic modulus tests were conducted at the FDOT State Materials Office (SMO) laboratory in Gainesville, Florida (on 2011-12-09 and 2011-12-12). Average compressive strengths and elastic moduli measured for each component of the test girder are shown in Table 10.2. Specific results obtained for individual cylinder tests are documented in Appendix C. Qualitatively, the majority of cylinders tested for compressive strength (both moist-cured and field-cured) broke in either a Type 1 (cone) or Type 4 (shear) fracture mode (Figure 10.22).

Table 10.2. Compressive strength and modulus of elasticity of cylinders tested within one week of buckling testing

Date poured	Girder component concrete batch from which cylinders were cast	Moist-cured cylinders		Field-cured cylinders	
		Compressive Strength (psi)	Modulus of Elasticity (ksi)	Compressive Strength (psi)	Modulus of Elasticity (ksi)
2011-05-18	Precast segment: exterior A	8200	5150	6340	4620
2011-05-19	Precast segment: exterior B	8520	5200	5830	4770
2011-05-23	Precast segment: interior	7910	5070	7140	4930
2011-08-26	South end block	9120	5380	7510	4850
2011-08-30	North end block	9440	5020	7080	4230
2011-08-30	Closure strips	7580	4750	5260	3630

Figure 10.21. Moist-cured cylinders submerged in a tank of lime water


a) b)

Figure 10.22. Typical cylinder failure types observed during compressive strength testing: a) Type 1 (cone failure); b) Type 4 (shear failure)

10.6 Girder post-tensioning and grouting

The final stage of the segmental construction process involved post-tensioning the various components of the girder (end blocks, precast segments, and closure strips) together to form a continuous girder and subsequently grouting the post-tensioning ducts. On 2011-09-20, the test girder was post-tensioned using a sequence of incremental post-tensioning force applications (21 in total) that were designed to ensure that the test girder would not crack during stressing. Each bar was assigned an identification code (Figure 10.23) and stressed incrementally in the sequence documented in Table 10.3. It should be noted that, because the precast segment cross-section was so slender, there was concern that even with the use of the stressing sequence indicated in Table 10.3, incremental eccentric stressing forces might cause the girder to deflect laterally and crack prior to achieving a final symmetric post-tensioned condition. Consequently, throughout the post-tensioning and grouting operation, the test girder was braced against lateral movement at several locations along its length by inserting timber blocking between the girder and surrounding steel catch frames (Figure 10.24).

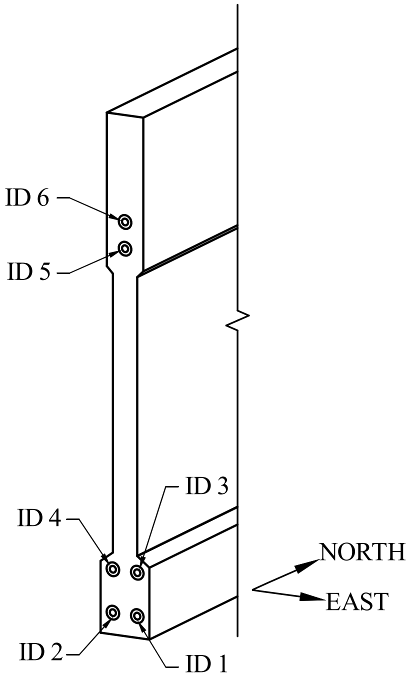

Figure 10.23. Bar identification numbers used during post-tensioning (south end of girder shown)

Table 10.3. Sequence of incremental post-tensioning forces applied to girder during stressing

Increment	Bar forces (kip)					
	ID 1	ID 2	ID 3	ID 4	ID 5	ID 6
1	19	—	—	—	—	—
2	19	—	—	19	—	—
3	19	—	19	19	—	—
4	19	19	19	19	—	—
5	31	19	19	19	—	—
6	31	19	19	31	—	—
7	31	19	31	31	—	—
8	31	31	31	31	—	—
9	31	31	31	31	6	—
10	31	31	31	31	6	6
11	31	31	31	31	6	30
12	31	31	31	31	30	30
13	64	31	31	31	30	30
14	64	31	31	64	30	30
15	64	31	64	64	30	30
16	64	64	64	64	30	30
17	95	64	64	64	30	30
18	95	64	64	95	30	30
19	95	64	86	95	30	30
20	95	95	86	95	30	30
21	95	95	95	95	30	30

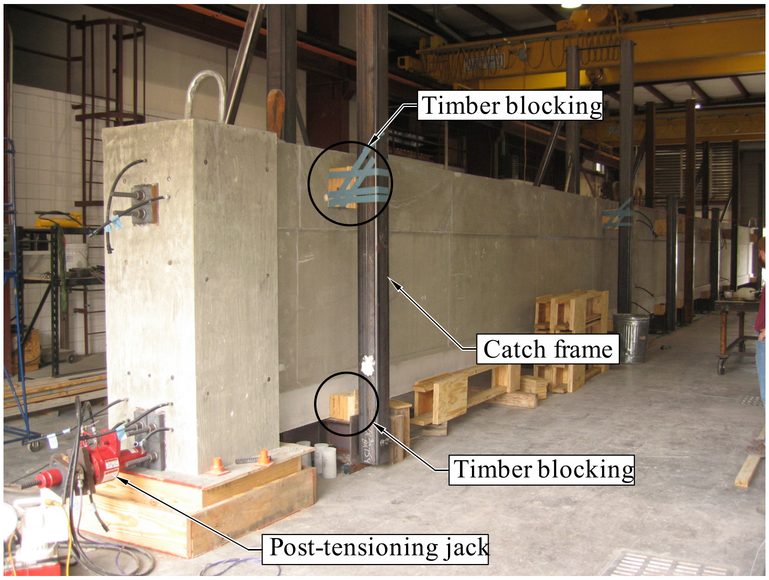

Figure 10.24. Test girder during post-tensioning, braced against steel catch frames using timber blocking

Each bar was stressed from the north end of the test girder using a DYWIDAG compact lightweight hydraulic jack (operated by a DSI technician). The jack fit over a pull rod that was threaded to the post-tensioning bar protruding from the anchor nut. The jack nose contained a ratchet device which allowed the anchor nut to be tightened (inside the jack) by turning a nut located on the exterior of the jack with a wrench (Figure 10.25). A pressure gage connected to the jack (Figure 10.26) was used to determine the force level in each bar, per the jack calibration form provided by DYWIDAG (Appendix D). Additionally, a Geokon load cell was aligned with the jack on the post-tensioned bar (Figure 10.25) with the intent of providing independent confirmation of the load level. However, the load cell readings were deemed inaccurate because the load was slightly eccentric on the load cell. Therefore, the hydraulic pressure gage (and associated calibration form) was the sole method of determining load level in each bar during the stressing sequence. Once the pressure gage indicated that the target prestress level had been attained, the anchor nut was tightened and the jack was moved onto the next bar in the sequence. Once all bars were fully stressed, the jack was moved to the south end of the beam and a series of bar liftoff tests were performed to confirm that the south end prestress levels were consistent with the north end prestress levels. These checks served two purposes: 1) to ensure that the bars and bar couplers had not snagged at any point along the length of the girder during stressing, and 2) to ensure that no bars lost any prestress force during the final increments in the stressing sequence. After all of bars were post-tensioned, the camber measured at midspan (Figure 10.27) was 11/16 in. which was in excellent agreement with the predicted camber of 3/4 in.

Upon completion of post-tensioning, the ducts surrounding the post-tensioning bars were pumped full of grout to mechanically bond the post-tensioning bars to the test girder. Grout was mixed with a CG550 single tub grout plant mixer provided by DYWIDAG (Figure 10.28) and pumped through the ducts. Grout cube samples were cast and subsequently tested in accordance with the *Standard Test Method for Compressive Strength of Hydraulic Cement Mortars* (ASTM C109, ASTM 2011) at the FDOT State Materials Office (SMO) laboratory in Gainesville, Florida (on 2011-10-26). Grout strength measurements obtained from these tests are presented in

Table 10.4. After post-tensioning and grouting, the test girder was lifted into testing position (Figure 10.29) using the lifting loops cast into each end block.

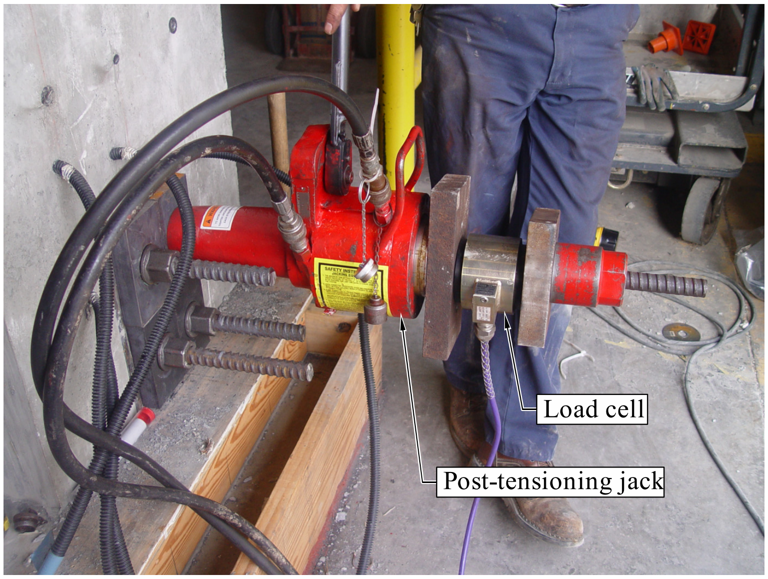

Figure 10.25. Post-tensioning jack setup

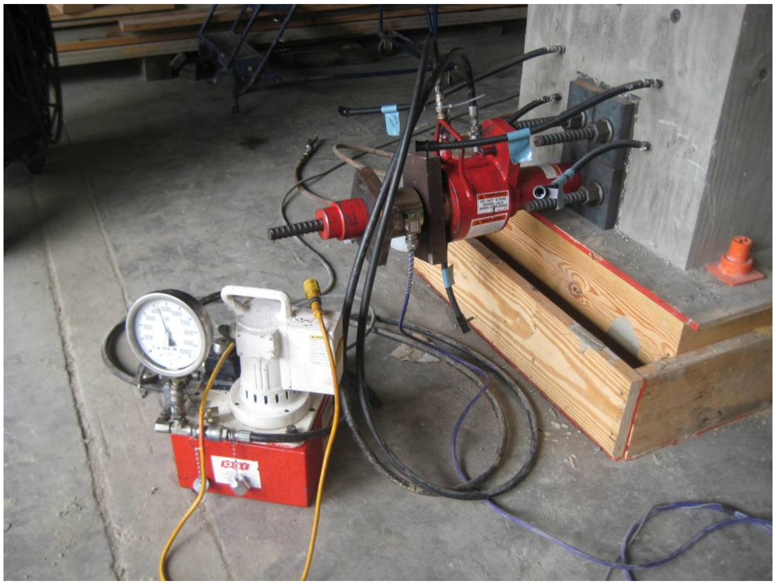

Figure 10.26. Post-tensioning jack and pressure gage

Figure 10.27. Camber measurement at midspan of test girder immediately after completion of post-tensioning

Figure 10.28. Grout mixer and high capacity air compressor

Table 10.4. Grout cube strength test results

Specimen	Strength (psi)
Cube 1	12,770
Cube 2	13,510
Cube 3	13,150
Average	13,140

Figure 10.29. Lifting the test girder into testing position, prior to end block fabrication

CHAPTER 11
GRAVITY LOAD SIMULATOR ANALYSIS, DESIGN, AND FABRICATION

11.1 Introduction

As previously discussed, concentrated vertical point loads were applied to the top of the test girder—through the use of gravity load simulators—to induce buckling (lateral deflection) of the girder in the experimental tests in a manner that did not introduce lateral stiffness into the system. Typically in experimental testing, a test specimen will deflect principally in the direction that the load is being applied. For example, when a simply-supported beam is tested in flexure, a vertical point load can be applied at midspan, and the beam will deflect vertically at the point of loading. In such a case, load application can be achieved through the use of a jack that is anchored to a stationary (effectively rigid) test frame which reacts against the test specimen. In contrast, in a buckling test of the type conducted in this study, the girder not only deflects in the direction of the applied load (vertically), but it also deflects laterally (perpendicular to the load direction). If a typical load application method—where the jack is anchored to a stationary position—were used in a buckling experiment, the load frame would resist lateral motion of the test specimen and a horizontal component of restraining force would develop (Figure 11.1). This condition is unacceptable, because the lateral force component would artificially increase the measured buckling capacity of the girder. To maintain vertical load and zero lateral restraining force as buckling occurs, a special type of load application frame (called a gravity load simulator) can be used that translates freely with the test girder as it buckles laterally. This chapter discusses the mechanics and design of the gravity load simulators designed and employed in this project, including a novel modification to previous designs (by other researchers) that improves the accuracy and performance of the system.

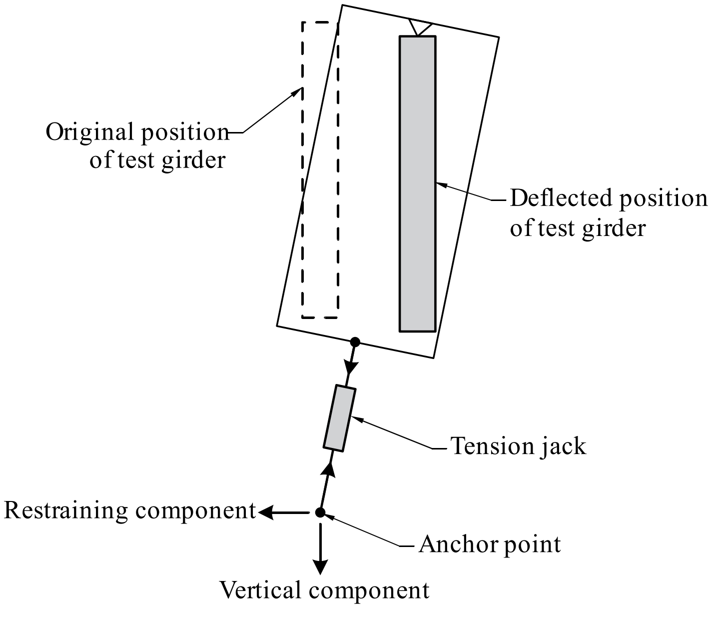

Figure 11.1. Undesirable horizontal restraining component that develops in an anchored loading system (After Yarimci et al., 1967)

11.2 Gravity load simulator

The first gravity load simulator was developed by Yarimci et al. (1967) to test structures permitted to sway. As designed, the simulator acts as a horizontally unstable truss structure (i.e., zero lateral stiffness) which provides vertical load application without horizontal restraint to the test specimen. As shown schematically in Figure 11.2, the simulator consists of two inclined arms that are connected to the ground (lab floor) and to a rigid triangle at the center of the simulator via pins. The source of load—a hydraulic jack—is attached at the base of the rigid triangle, also through a pinned connection. As is noted by Yarimci et al. (1967), "For the type of mechanism shown, equilibrium requires that the line of action of the load passes through the instantaneous center, that is, the point of intersection of the two arms. The position of the instantaneous center changes as the mechanism is deflected." With carefully chosen geometry (top width, arm length, load height, and base width; Figure 11.2), the load line of action will remain vertical and through the instantaneous center, regardless of the deflected position (Figure 11.3). Additional guidance for determining optimal geometry for the simulator can be found in Yarimci et al. (1967).

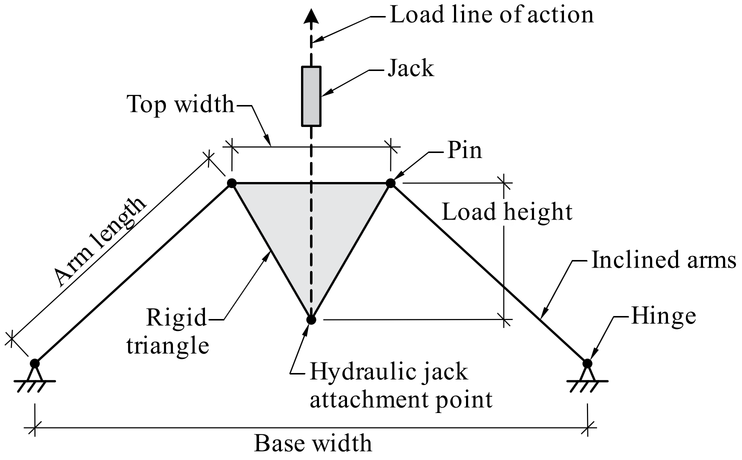

Figure 11.2. Dimensions, defined (After Yarimci et al., 1967)

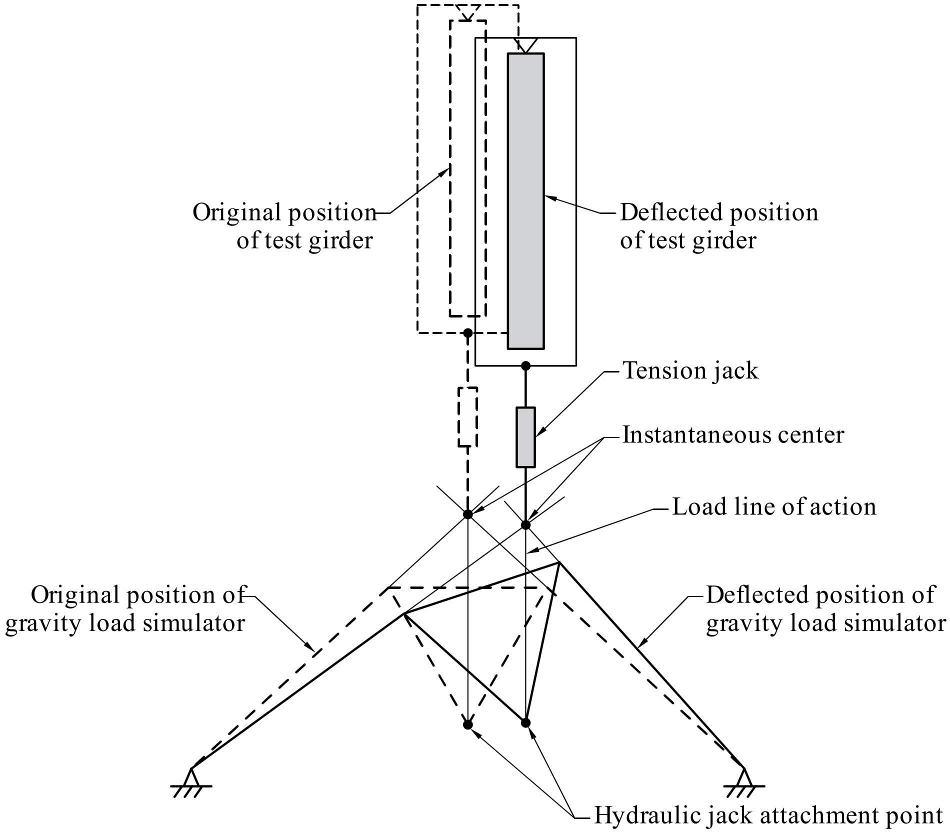

Figure 11.3. Instantaneous center (After Yarimci et al., 1967)

The original simulators, located at Lehigh University, had 80 kip load capacity and could translate laterally 16 in., for performing buckling tests on full-scale building frames (Yarimci et al., 1967). Since then, several other researchers have constructed gravity load simulators for various test programs. Lateral torsional buckling tests of steel I-shapes were conducted at University of Texas at Austin (Yura and Phillips, 1992). At the University of Texas at Houston, two simulators (6 in. displacement capacity, 150 kip load capacity) were constructed to investigate torsional bracing by simulating buckling of a two-beam system with midspan bracing (Deaver, 2003). A gravity load simulator at the Georgia Institute of Technology (7.5 in. displacement capacity, 60 kip load capacity) was used to experimentally investigate lateral-torsional buckling behavior of fiber reinforced polymer I-shaped cross-sections (Stoddard, 1997) and also to examine the lateral stability of slender rectangular reinforced concrete beams (Kalkan, 2009). Also at the Georgia Institute of Technology, a relatively large gravity load simulator (12.875 in. displacement capacity, 300 kip load capacity) was used to study the stability of prestressed concrete beams (Hurff, 2010). It should be noted that Hurff observed that the load line of action was not perfectly vertical when the simulator swayed from its original centered position. Postulating that self-weight of the simulator caused this issue, a control mechanism was installed that forced the simulator to act as a stable mechanism, in which the position of the simulator was manually adjusted until the applied load was vertical. Further investigations into the simulator self-weight issue were not conducted by Hurff.

11.3 UF/FDOT gravity load simulators

A pair of gravity load simulators (one of which is shown in Figure 11.4) were designed and fabricated for this project, with a maximum lateral deflection capacity of 16 in. and vertical load capacity of 50 kip each. The UF/FDOT simulators had the same relative geometry as the original simulator developed by Yarimci et al. (1967). In the UF/FDOT simulators, high-quality spherical roller bearings (Figure 11.5) were used to prevent binding (due to shaft bending or simulator geometry fabrication imperfections) and minimize friction at the pinned connections, thereby minimizing restraint of the simulator to lateral motion. The bearings used in the simulators were self-aligning—accommodating misalignment between the shaft and housing without increasing friction—which allowed out of plane bearing rotation of ±1.5 deg. The bearings were housed in thick plates that were bolted and welded to the simulators (Figure 11.4a). PVC end caps served as bearing seals that prevented dust from entering the bearings and creating friction (Figure 11.4b). A hydraulic jack was connected to the center pin of each simulator (Figure 11.6), allowing the hydraulic jack to rotate freely about the pin and maintain vertical load application as the simulator displaced (Figure 11.7). Two safety mechanisms were included in the design of the simulators: one temporary restraint and one permanent restraint (Figure 11.4). The temporary restraints were engaged when the simulators were not in use—removed during buckling tests—to keep each simulator from displacing laterally under its own weight. For safety during a buckling test, permanent restraint chains—which were slack during normal operation (Figure 11.4a)—connected the bottom of the rigid triangles to the base beams. The restraint chains allowed the full range of motion expected during a buckling test (expected deflection of 10 in. out of the maximum allowable displacement of 16 in.), but prevent the simulators from displacing further than desired (Figure 11.7).

The completed simulators were positioned below the test girder closure strips. Load frames were designed to transfer the vertical load from the gravity load simulator (below the test girder) to the load application point (at the top of the test girder). A threaded rod, in line with the hydraulic jack, connected the load frame to the simulator (Figure 11.7). A heat treated steel knife edge (Figure 11.8) was used to apply loads to the top of the test girder, while allowing the girder to rotate freely about the y-axis within the load frame as it buckled (Figure 11.7). When loaded, the simulators could be pushed laterally by hand from the equilibrium position, and upon release, would float back to the equilibrium position, clearly confirming that no adverse lateral restraint had been introduced into the test setup. Figure 11.9 shows a photograph of one of the gravity load simulators and load frame in testing position. Full fabrication plans for the simulators can be found in Appendix E.

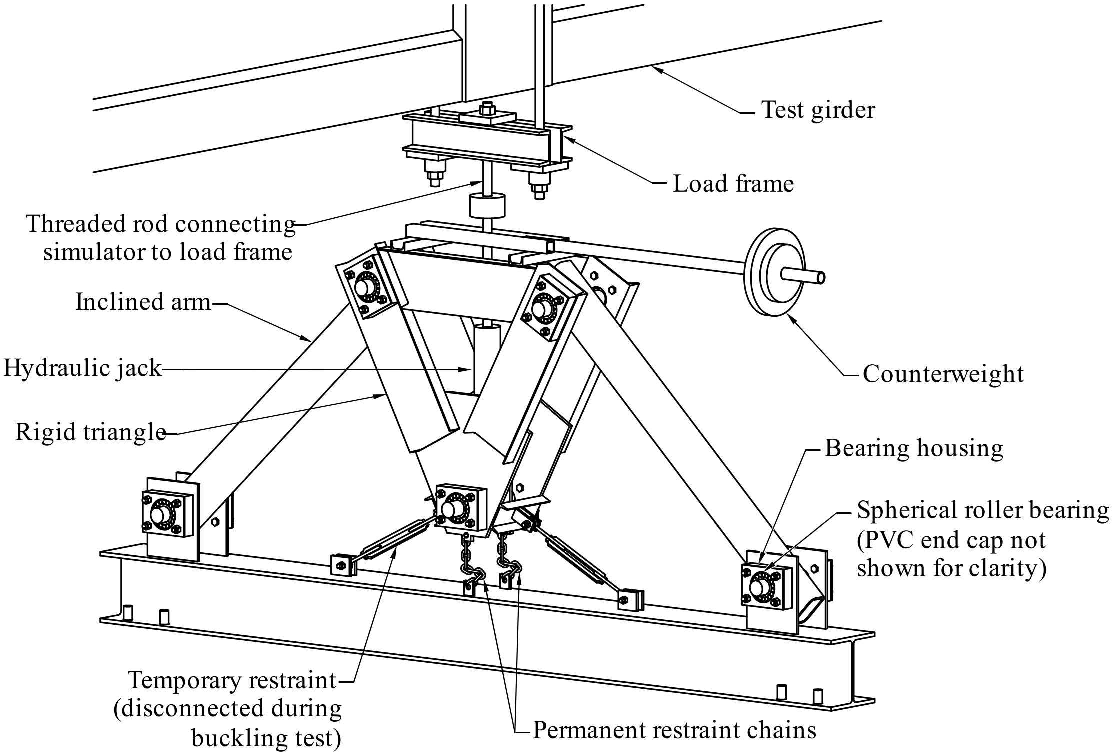

a)

b)

Figure 11.4. UF/FDOT gravity load simulator:
a)Schematic view; b) Photograph

Figure 11.5. Spherical roller bearing (photo courtesy of SKF)

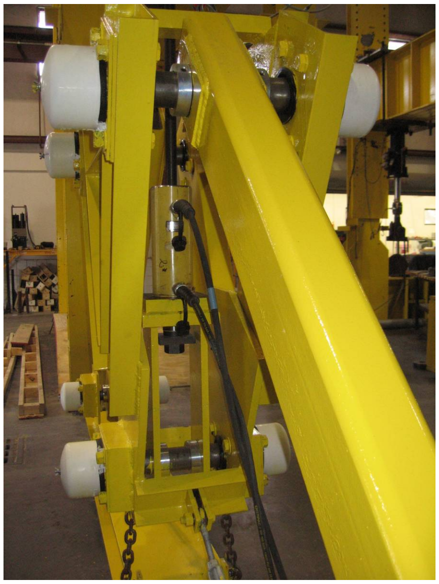

Figure 11.6. Hydraulic jack connection to simulator center pin

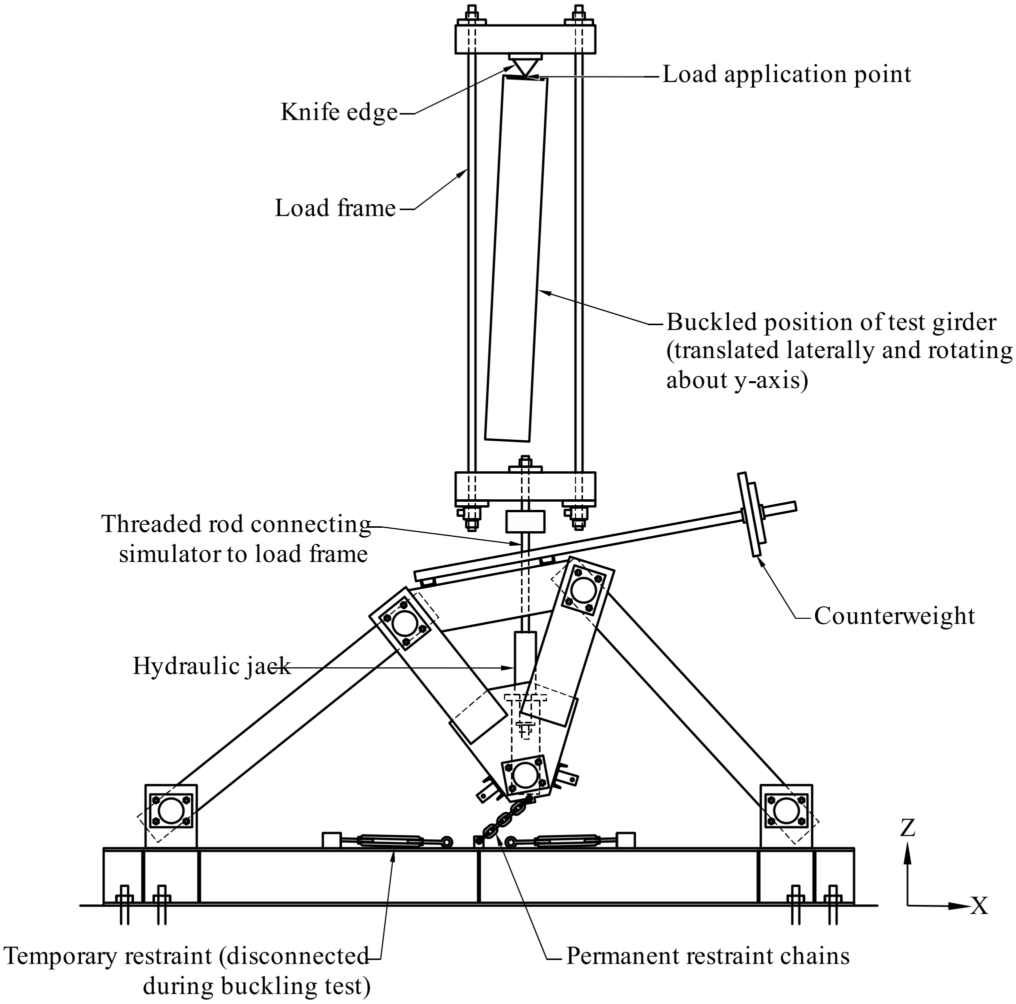

Figure 11.7. Gravity load simulator displaced shape

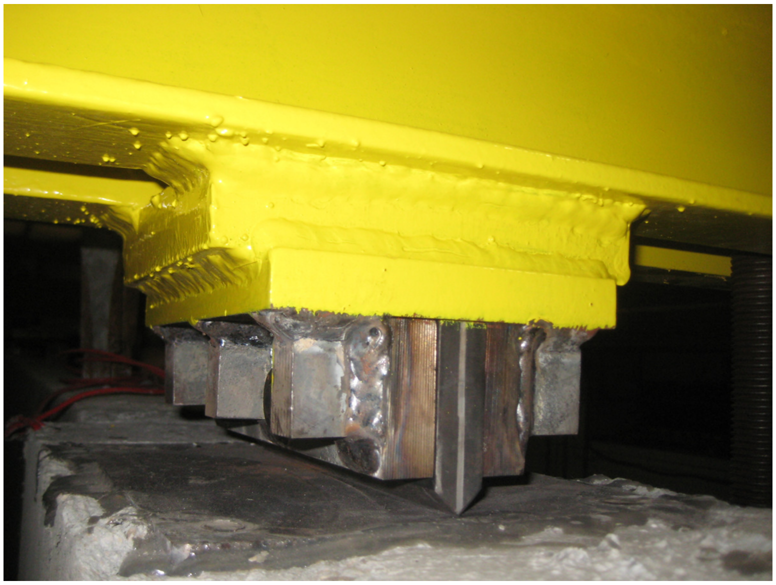

Figure 11.8. Knife edge at load application point (top of test girder)

Figure 11.9. UF/FDOT gravity load simulator and load frame in testing position

11.4 Effect of gravity load simulator self-weight

Prior to performing buckling experiments, the performance of each simulator was tested to ensure that the load line of action remained vertical. Restraining the test girder centered above the simulators, the loaded simulators maintained equilibrium as expected, and the direction of load was confirmed to be vertical using a carpenter's level. Subsequently, a trial buckling test was performed in which load was applied to the test girder and the girder was allowed to freely deflect laterally. Both simulators reached equilibrium in a position such that the applied load was not perfectly vertical. Specifically, the middle pin of each simulator was displaced further than the load application point (at the top of the test girder). This condition caused a lateral component of load to be applied to the test girder in the direction of buckling motion (Figure 11.10). With the simulators floating in this manner of equilibrium, they were pushed (by hand) until vertical alignment was reached. Upon release, each simulator floated back to the equilibrium position with a non-vertical load line of action. In the displaced configuration observed during this trial buckling test, the load line of action was not vertical as expected, indicating that additional forces (such as the weight of the simulator) affected the system during the test. As mentioned in the previous section, Hurff (2010) observed that the Georgia Tech simulator did not reach equilibrium with a vertical load orientation unless the simulator was in the undeformed (centered) position. Hurff fixed this problem by using a lateral control mechanism that caused the simulator to become a stable structure. While this solution proved effective for maintaining proper vertical load orientation, the lateral restraint provided by the control mechanism is undesirable for buckling experiments. Ideally, the girder should be permitted to deflect laterally (buckle) without restraint, which is consistent with an unbraced field condition. Thus, an alternative solution was developed in the present study which allowed unrestrained lateral motion and maintained vertical load orientation throughout the full range of motion.

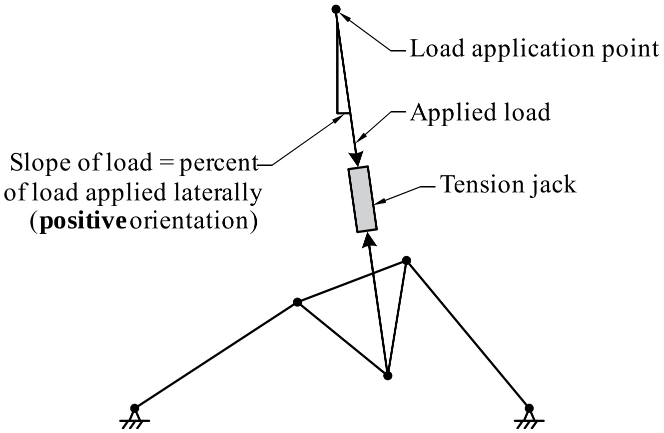

Figure 11.10. Definition of percent of simulator load applied laterally (After Yarimci et al., 1967)

To investigate how the self-weight of the gravity load simulator influences its equilibrium position, numerical models of the simulator were developed (Figure 11.11). In the initial simulator model, rigid beam elements represented the components of the simulator, the self-weights of which (due to gravity) were neglected. The inclined arm beam elements were attached to hinges at the base of the system, with end moment (M_y) releases at the connection to the rigid triangle. Moment transfer between the elements of the rigid triangle ensured that the rigid triangle acted as a single unit. The connection of the gravity load simulator at the middle pin and the load application point to the test girder (the knife edge) was represented in the model using a beam element. Releasing the end moment (M_y) of this element at the connection to the rigid triangle allowed the element to rotate freely about the middle pin of the simulator. An initial tensile strain was applied to this element, simulating the tension applied through the use of the jack during a buckling test. A prescribed displacement was then applied at the load application point, representing the lateral deflection of the test girder. The load application point was modeled as a roller support (free to rotate about the y-axis and translate along the x-axis), representing the knife edge at the top of the test girder.

Yarimci et al. (1967) describe that the theoretical load applied by a gravity load simulator is generally not truly vertical, and that a slight lateral load is applied to the test specimen as a result of this non-vertical orientation. Neglecting gravity, the results of the simulator analysis (Figure 11.12) were consistent with Yarimci et al. (1967). The analysis indicated that—within the range of lateral deflections expected in the buckling experiments—the lateral load component was, at most, approximately -0.02% of the applied vertical load. Note that the sign convention of Yarimci et al. (Figure 11.10) states that a negative percentage corresponds to a lateral load that restrains the beam, and a positive percentage corresponds to a lateral load that drives the beam in the direction of buckling. For example, the simulator analysis results (Figure 11.12) show that, when the test girder has displaced 5 in., under zero-gravity conditions, the lateral force component is approximately -0.02%. Thus, if a 10 kip load is applied vertically, 0.002 kip would develop laterally at the top of the beam, restraining the beam slightly.

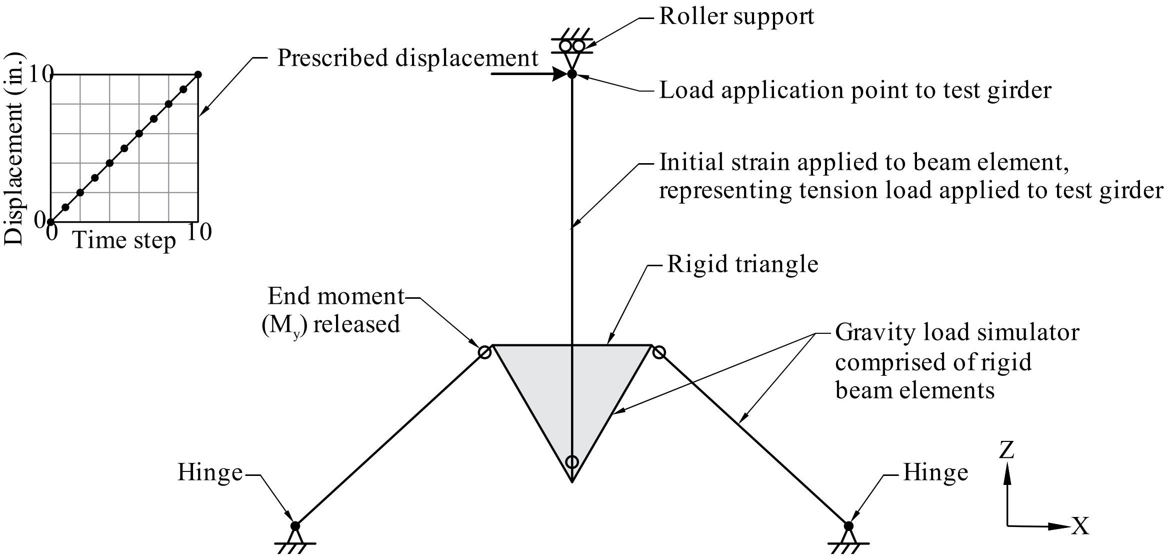

Figure 11.11. Gravity load simulator model

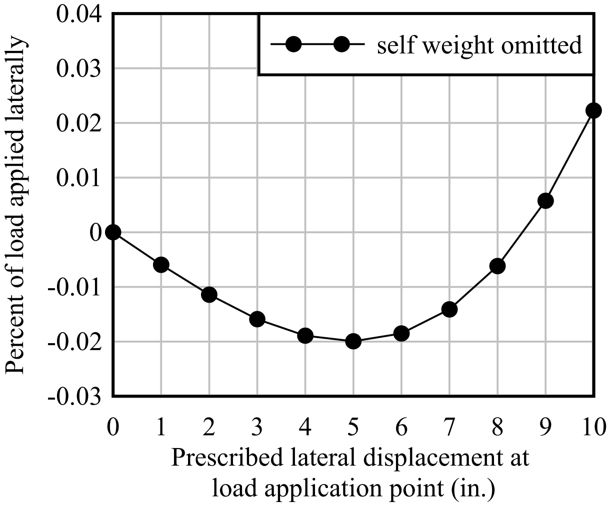

Figure 11.12. Results of simulator analysis: theoretical percent of load applied laterally to the beam at the load application point (self-weight excluded in model)

To determine the effect of self-weight on simulator equilibrium, gravity was introduced into the simulator model via mass-proportional body forces (and therefore taking the self-weight of the simulator into account), and the analysis described above was repeated. It was found that the self-weight causes much larger lateral loads to develop in the direction of buckling, and those loads increase with increasing displacement (Figure 11.13). This behavior occurs because the self-weight of the simulator is eccentric relative to the idealized instantaneous center—the point of intersection of the two inclined arms when neglecting gravity—as shown conceptually in Figure 11.14a.

Recall that Hurff (2010) corrected this problem by providing lateral restraint to the gravity load simulator. In contrast, in the present study, an alternative solution was employed that avoided restraining lateral motion. The system consisted of weights placed eccentrically from the instantaneous center which counterbalanced the eccentric self-weight of the simulator (Figure 11.14b). With appropriate counterweight magnitude and eccentricity, the effect of the simulator self-weight was corrected, and the load line of action remained vertical. The counterweights were an excellent option because there was no addition stiffness added to the system (permitting unrestrained lateral motions), and the counterweights could be adjusted to maintain vertical load regardless of the displaced shape of the test girder. The physical counterweight system was fabricated using barbell weights of various sizes, slid onto a steel pipe that was mounted to the rigid triangle of the simulator (Figure 11.15). For each simulator, two (2) 25 lbf. weights and one (1) 45 lbf. weight were available for the counterweight system. Small clamps ensured that the weights did not slide unless physically pushed along the pipe. Details of the counterweight system are included in the gravity load simulator fabrication plans, found in Appendix E.

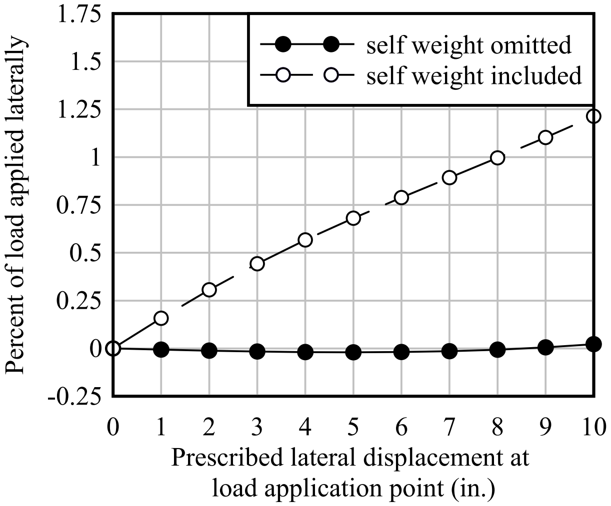

Figure 11.13. Results of simulator analysis: theoretical percent of load applied laterally to the beam at the load application point (self-weight included in model)

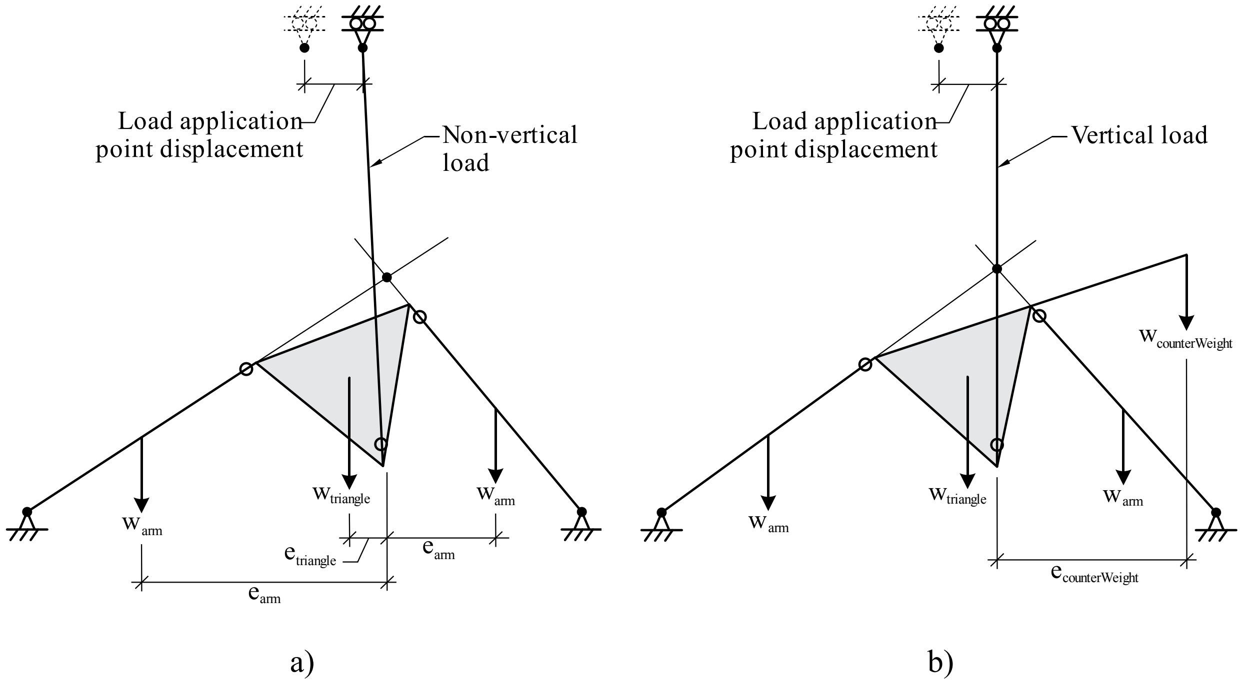

Figure 11.14. Effect of simulator self-weight and counterweights on verticalness of load line of action:
a) Counterweights omitted, load is skewed;
b) Counterweights included, load is vertical

Figure 11.15. Counterweight system

CHAPTER 12
GIRDER BUCKLING TEST PROGRAM

12.1 Buckling test setup

An overview of the test setup is shown in Figure 12.1. To accommodate the gravity load simulators, the test girder was elevated approximately 8 ft. above the lab floor and set on bearing pads that rested on rigid end supports. Because the test girder was elevated overhead, safety catch frames were designed and fabricated to support the test girder should it become fully unstable during testing. Five catch frames were fabricated: two positioned at the ends, one positioned at midspan, and two positioned near the third points (Figure 12.1). The catch frames allowed the test girder to displace up to 9 in. laterally at midspan before preventing further movement. Full fabrication plans for the catch frames can be found in Appendix F. Each end support was fabricated with the test girder suspended in the testing position. Constructed from eight solid concrete blocks, the end supports were built up one level at a time and welded together to create a rigid support (Figure 12.1). A pad of Hydro-Stone® was poured at the base and at the top of each end support, to ensure that the bearing surface for the end blocks on the ground was level and to provide a level surface for the bearing pad contact area, respectively.

12.2 Test matrix

The bearing pads used to support the ends of the test girder were the same pads previously tested to quantify roll stiffness in the first phase of this project. As shown in Chapter 6, among all bearing pad types tested, the Type A bearing pads had the least amount of variation in individual roll stiffness results under all combinations of skew and slope angles (the results are reproduced here in Figure 12.2). Therefore, pad Type A was chosen to support the ends of the girder during the buckling tests. To best illustrate the influence of roll stiffness on buckling capacity, the girder was to be tested with bearing pads oriented at the extreme values of skew and slope that were previously investigated (A-0-0, A-45-0, A-0-04, and A-45-04). Recall that, in the abbreviated naming convention, the first letter denotes pad type, the following number denotes skew angle (in degrees), and the last number denotes slope angle (in 10^{-2} radians). However, during buckling testing in test configuration A-45-04, the test girder buckled under its own self-weight (i.e., with no additional applied vertical load). Consequently, a configuration with an intermediate combination of skew and slope was required instead. Reducing skew from 45 deg. to 15 deg. increased the buckling capacity enough to allow a test to be performed with applied load and with the pad in a skewed and sloped configuration. The test matrix for the buckling tests—with number of tests performed per configuration—is presented in Table 12.1.

12.3 Test procedure

There were two main phases to the setup portion of the buckling tests: 1) imposing skew and slope angles on the bearing pad, and 2) placing the test girder on the bearing pads. After the setup portion of each buckling test (setting the bearing pads and placing the girder on the pads) was completed, the buckling test was performed. This section documents the procedure for setting up and performing the buckling tests.

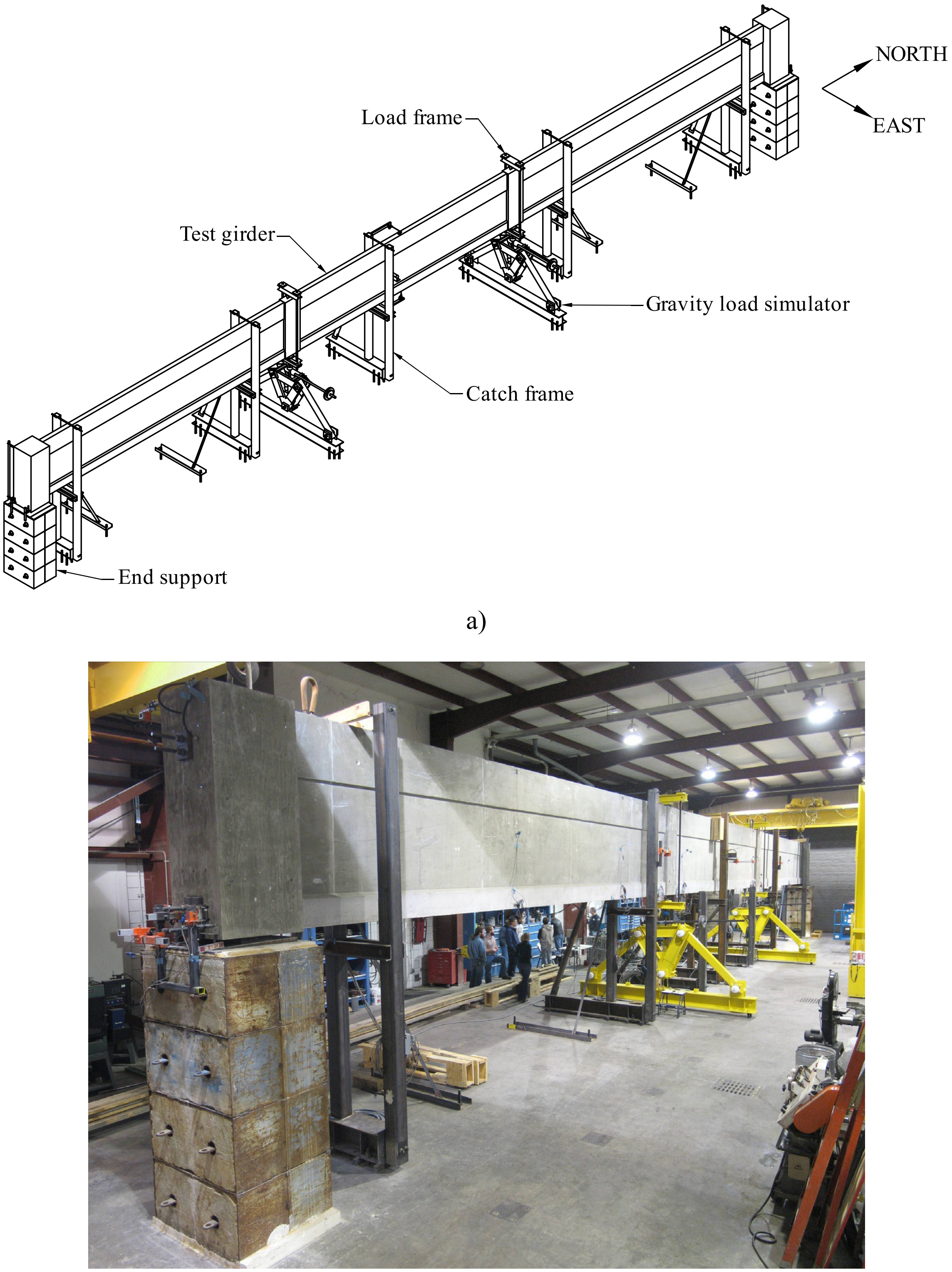

a)

b)

Figure 12.1. Overall test setup: a) Schematic; b) Photograph

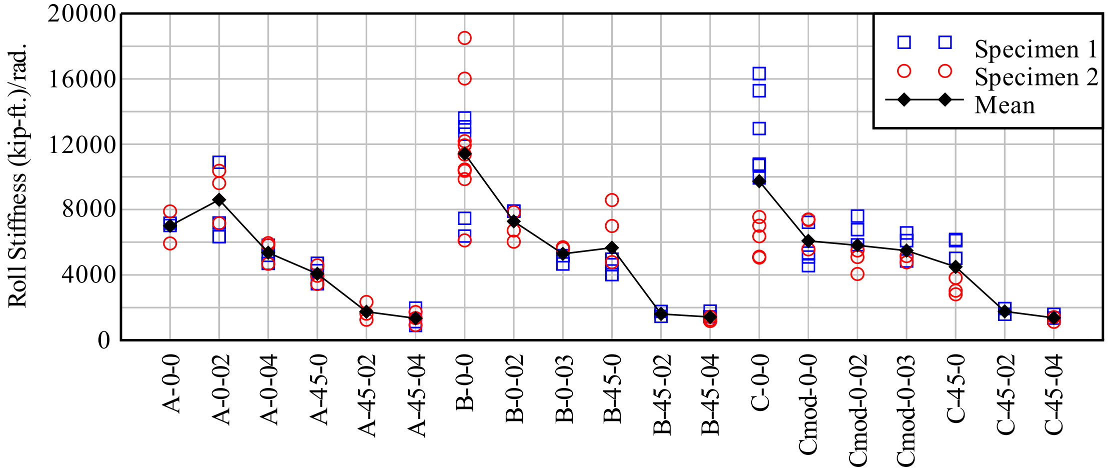

Figure 12.2. Roll stiffness results, reproduced from Chapter 6

Table 12.1. Test matrix

Test configuration	Skew angle (deg.)	Slope angle (rad.)	Number of tests performed
A-0-0	0	0	3
A-45-0	45	0	2
A-0-04	0	0.04	3
A-15-04	15	0.04	1

12.3.1 Setting skew and slope angles

Prior to performing each buckling test, bearing pads—located between the girder end blocks and rigid end supports—were oriented at the desired skew and slope angle. Skew angle was set by rotating the bearing pad about the z-axis relative to the test girder (Figure 12.3). Slope angle was set by placing a beveled plate (Figure 12.4) between the bearing pad and rigid end support (Figure 12.5). Bearing pads were oriented in the buckling tests such that the pressure distributions during buckling testing matched that of the pressure distributions during roll stiffness testing (Chapter 6). Conceptually, Figure 12.6 shows the initial pressure distribution of each test configuration, and Figure 12.7 shows the final pressure distribution for each test configuration. In the sloped tests, the thick ends of both beveled plates faced north, creating a pressure concentration on the north portion of the bearing pads. This scenario represents the pressure distribution on a pair of bearing pads that would be produced by girder grade (as opposed to girder camber).

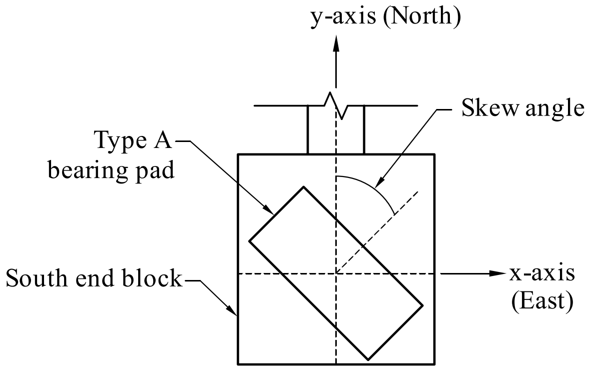

Figure 12.3. Bearing pad skew angle orientation in buckling tests

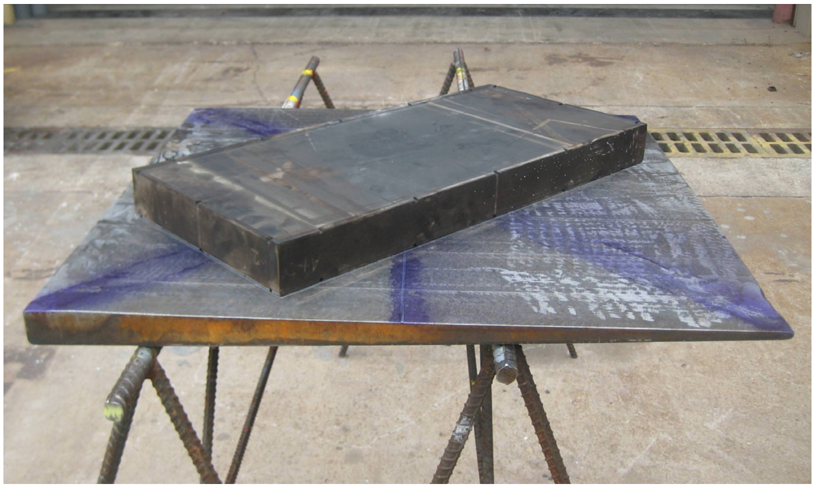

Figure 12.4. Beveled plate used to impose slope angle on bearing pads

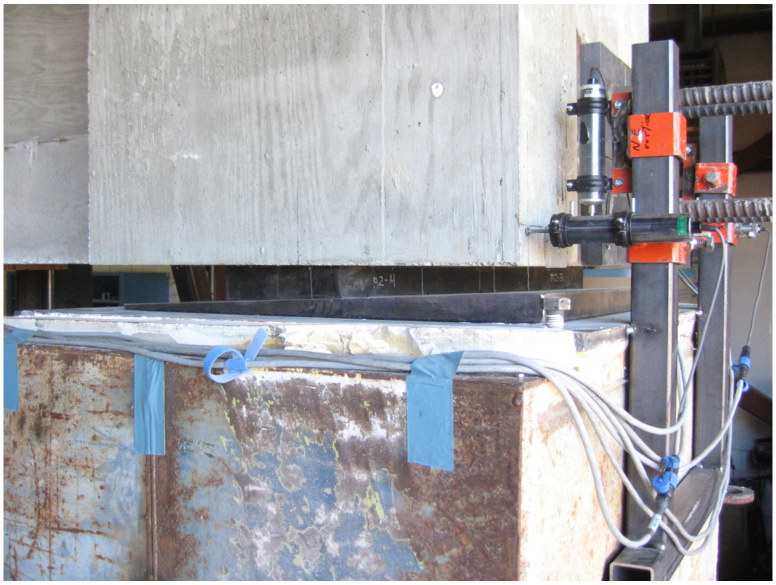

Figure 12.5. Beveled plate and bearing pad positioned between end block and end support

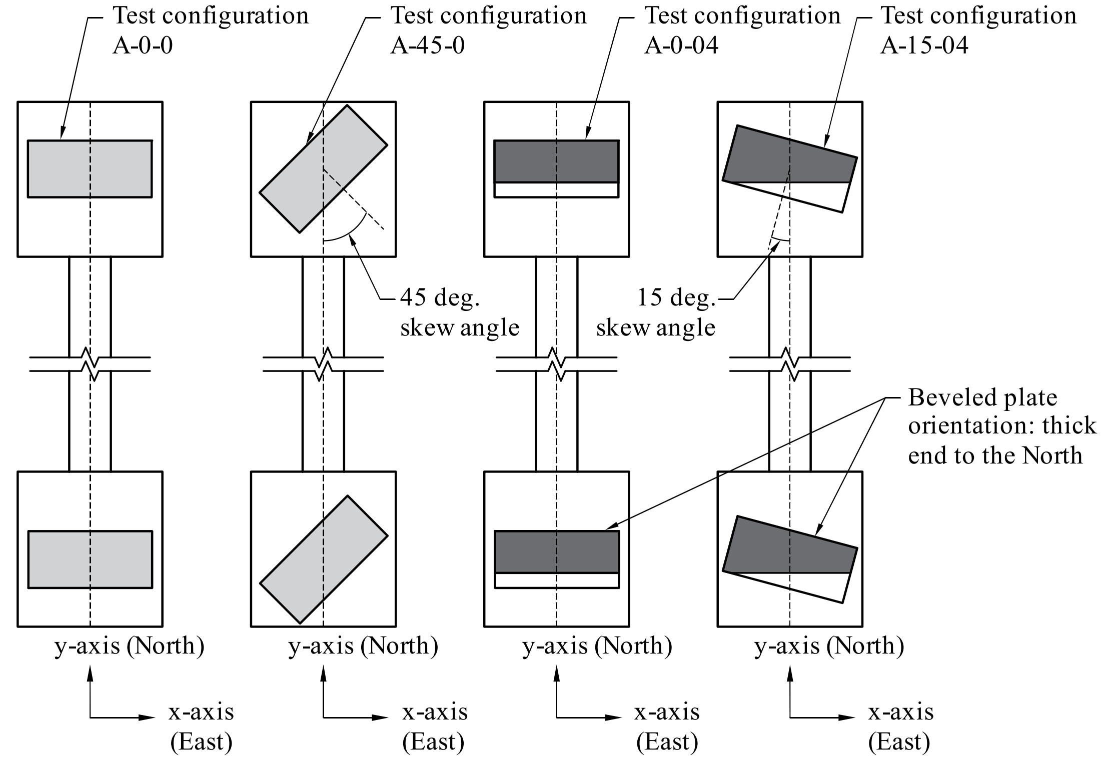

Figure 12.6. Bearing pad orientation and initial pressure distributions during buckling tests

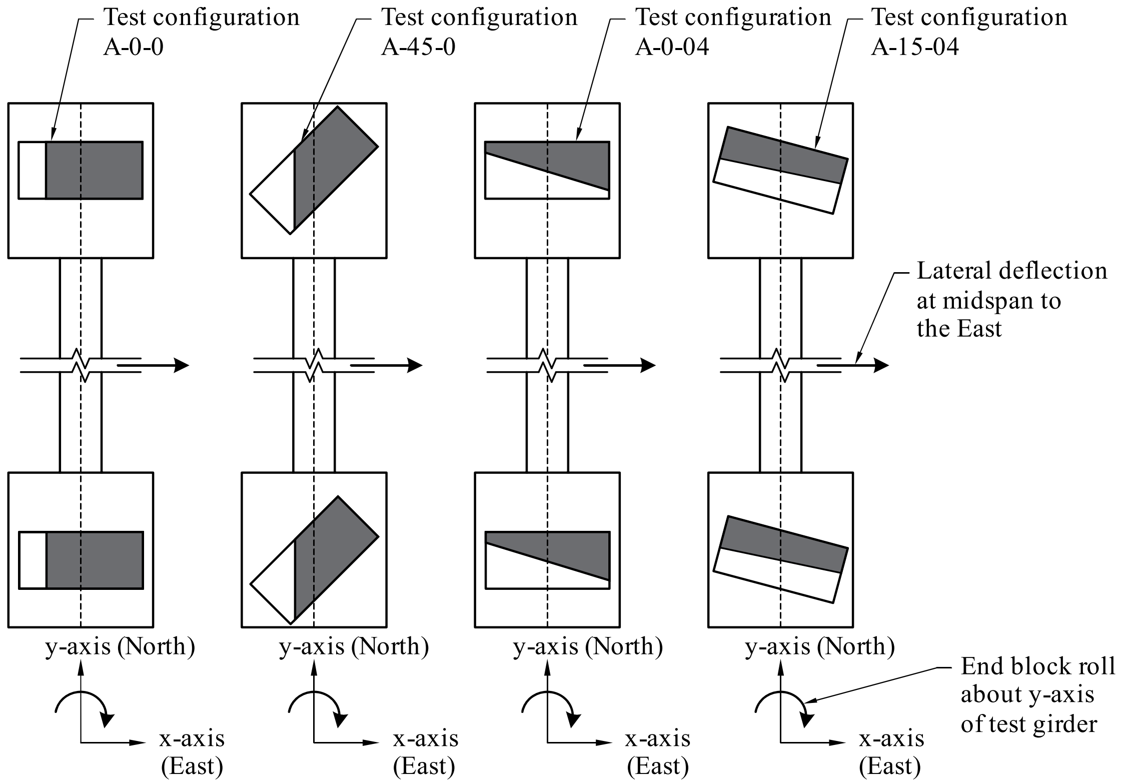

Figure 12.7. Final bearing pad pressure distributions during buckling tests

12.3.2 Placing the test girder

While the skew and slope angles of the bearing pads were being adjusted, the test girder was lifted—via lifting loops cast into the end blocks—to allow adjustments. Once the bearing pads were set at the desired angles, the test girder was lowered onto the pads for a buckling test. As shown in Figure 12.8a, the beam swept naturally (due to casting and post-tensioning tolerances) from West to East. Table 12.2 presents the initial girder sweep (measured at the height of the section centroid) that was present prior to load application in each test configuration. For most tests, a hydraulic jack was used to push the test girder toward the west at the midspan centroid, effectively removing sweep from the system (i.e., pushing the girder straight) (Figure 12.8b). The jack used to straighten the test girder was mounted to the midspan catch frame, as shown in Figure 12.9. For comparison, two different methods for placing the test girder on the bearing pads were used:

- Method A: The test girder was straightened using the jack, lowered onto the bearing pads, and then allowed to sweep freely by slowly retracting the jack, and;
- Method B: The girder was set down on the pads in the swept position.

In both methods, girder end blocking (recall Figure 10.29) was used during lifting and lowering operations. Additionally, in Method A, end blocking was also used during girder straightening. Method A was advantageous because the sweeping motion of the test girder could be directly recorded during a buckling test (as the jack was slowly retracted). However, when Method A was used, it was observed that as the test girder deflected into the swept position, torsion was introduced into the bearing pads about the z-axis. This outcome was undesirable because: 1) pad torsion is generally not present in field conditions, and 2) such torsion was not present in the isolated bearing pad roll stiffness tests conducted in the first phase of this study. To quantify the effect that torsion in the pads had on the buckling capacity of the test girder, test configuration A-0-0 was tested under both conditions (using Method A and Method B). Examining the load-displacement curves presented in Chapter 13 for test configuration A-0-0, the effect of torsion on the bearing pads was found to be insignificant. Table 12.2 summarizes the placement method of each individual test performed per configuration (e.g., A-0-0-1 was the first test performed in configuration A-0-0, A-0-0-2 was the second test performed in configuration A-0-0, etc.).

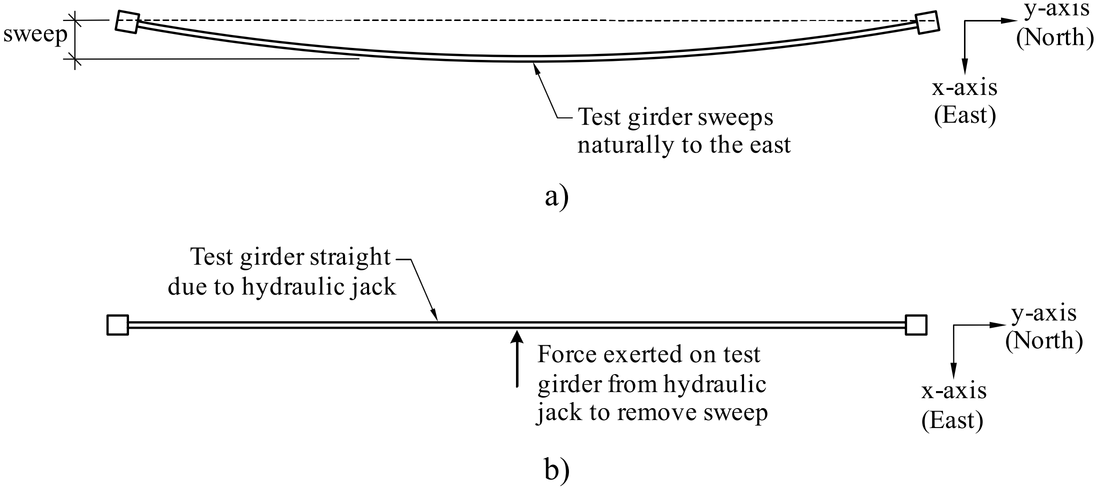

Figure 12.8. Sweep of test girder:
a) Unrestrained position; b) After hydraulic jack applied

Figure 12.9. Jack used to straighten test girder

Table 12.2. Initial girder sweep and girder placement method for each test

Test ID	Initial girder sweep (in.)	Placement method
A-0-0-1	2.61	A
A-0-0-2	2.82	A
A-0-0-3	2.87	B
A-45-0-1	2.84	B
A-45-0-2	3.09	B
A-0-04-1	2.96	A
A-0-04-2	3.49	A
A-0-04-3	3.16	A
A-15-04-1	5.69	A

12.3.3 Buckling test procedure

During each girder buckling test, load was applied iteratively to the test girder, first gradually increasing the applied load at the north gravity load simulator (GLS), until a specific target was reached, and then increasing the load at the south GLS until the loads were equal at both locations (Figure 12.10). Once the loads were approximately equal at both GLSs, the counterweight system at each GLS was adjusted. These adjustments produced lateral movements of both the girder and the GLS and were made to ensure vertical load application. The GLS load application directions were confirmed to be vertical using a carpenter's level. After the counterweights were adjusted, a test data point was established (Figure 12.10), at which time the applied GLS loads and girder deflection were measured.

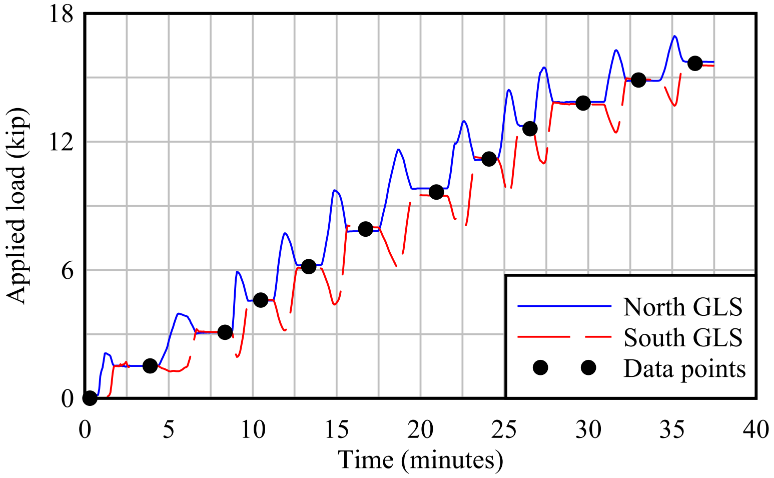

Figure 12.10. Typical load time history (test A-0-0-2 shown)

12.4 Instrumentation

Several types of instrumentation—displacement transducers (displacement sensors, lasers, and string potentiometers), load cells, and strain gages (both external and vibrating wire strain gages cast into the concrete)—were used in the buckling tests. A naming convention for the instrumentation was developed to reflect the instrument type and its specific location on the test girder. As summarized in Figure 12.11, each instrument name had the same format of T-LD-F-H, where “T” indicates the type of instrument, and “-LD-F-H” indicates the location of the measurement. For example, the instrument shown in Figure 12.11 was an external strain gage mounted to the east face of the test girder top flange. Therefore, the instrument shown in Figure 12.11 was named SG-N24-E-76, which means that the device is a strain gage (SG), located 24 ft north of midspan, mounted to the east face, at a height of 76 in. from the bottom of the girder. The full instrumentation plan (included in Appendix G) further describes the naming convention, and also provides an overview of all of the instrumentation by name.

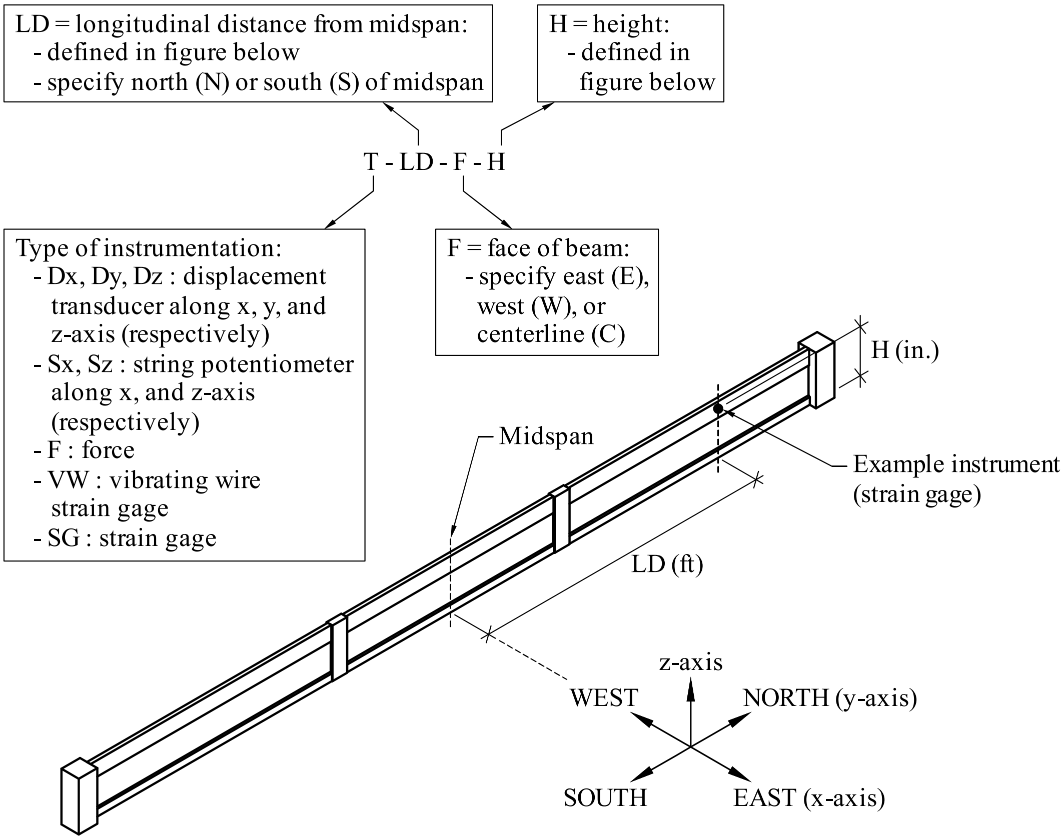

Figure 12.11. Naming convention for buckling test instrumentation

12.4.1 Displacement transducers

Displacement sensors, string potentiometers and laser gages were used to measure girder deflection at various points. All three types of displacement transducer were used at midspan, but only displacement sensors were used at the end blocks. Laser gages (Balluff model BOD 66M) measured lateral displacement at the centroid height near the gravity load simulator locations.

Because midspan lateral deflection was a key parameter measured in each buckling test, the midspan of the test girder was heavily instrumented with displacement transducers (Figure 12.12). Displacement transducers were mounted to the central catch frame and used to record midspan deflections along both the x-axis and z-axis. A laser gage (Balluff model BOD 66M) and a displacement sensor (TML model SDP-200D) were mounted next to one another at the centroid height to measure lateral displacement (along the x-axis). The laser gage (Dx-N0-W-38) was used as the primary lateral displacement measuring device during each buckling test, while the displacement sensor (Dx-S0-W-38) provided redundancy to the laser gage. String potentiometers (SpaceAge Control model 62-60-82E1) measured both lateral and vertical displacement of the test girder, providing additional redundancy to the lateral displacement measurement provided by the laser gage.

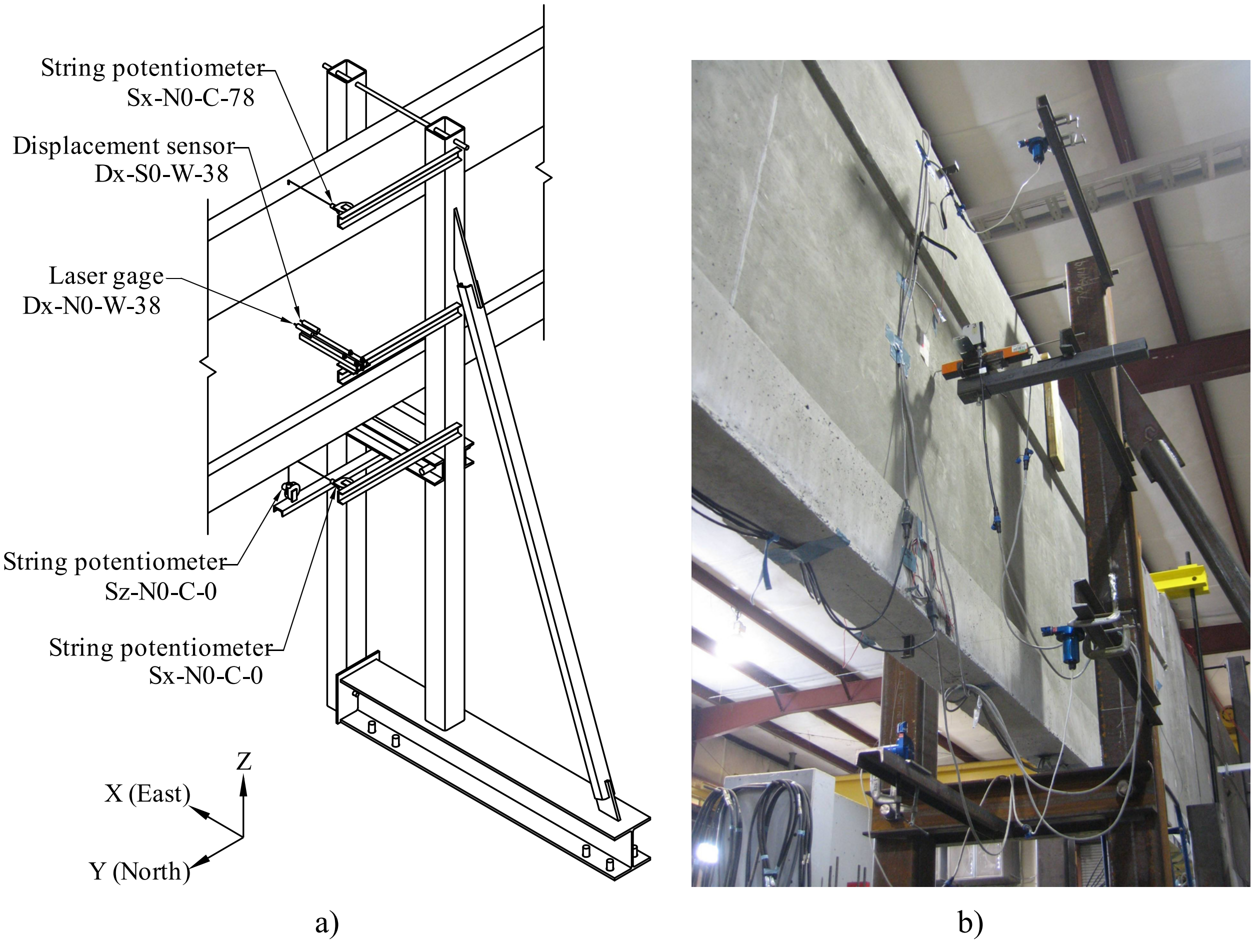

Figure 12.12. Midspan displacement transducers:
a) Schematic; b) Photograph

The end blocks were also heavily instrumented with displacement sensors, as shown in Figure 12.13. All displacement transducers monitoring the end blocks were TML model SDP-50, mounted to the rigid end supports. Vertical displacement transducers (along the z-axis, Dz) and horizontal displacement transducers (along the x-axis, Dx) were used to calculate the roll angle imposed on the bearing pad. Knowing the horizontal distance between the vertical (Dz) displacement transducers and the vertical distance between the horizontal (Dx) displacement transducers, the roll angle imposed on the bearing pad at the end block could be calculated from the relative displacement measurements, and used to confirm each other. Horizontal displacement transducers along the y-axis (Dy) were used to calculate torsional rotation in the bearing pad.

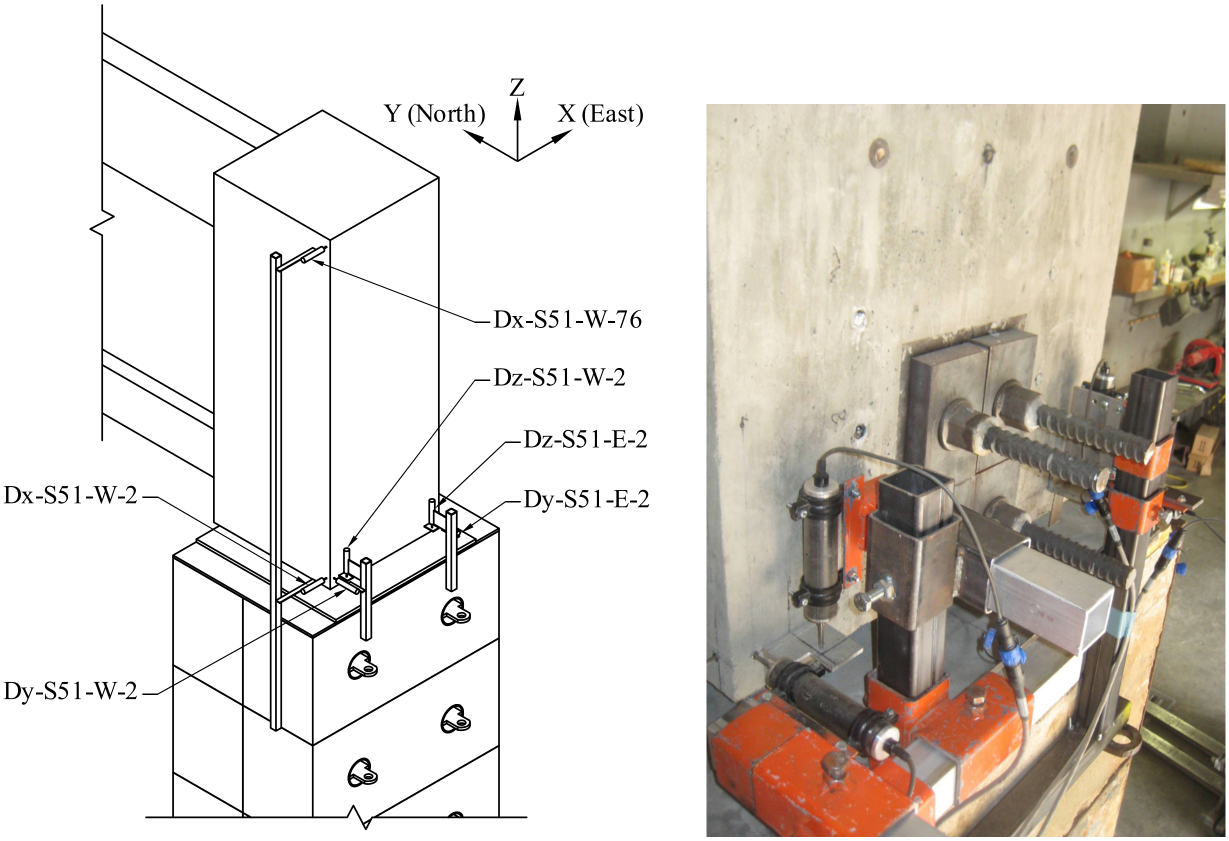

a) b)

Figure 12.13. South end block displacement transducers:
a) Schematic; b) Photograph

12.4.2 Load cells

Load cells measured the vertical load applied to the test girder at the gravity load simulator (GLS) locations. At each GLS, an Interface load cell (model 1220, 50 kip capacity) was installed in line with a threaded rod connecting the gravity load simulator to the load frame. Each such cell directly measured the load applied to the test girder (Figure 12.14). Additionally, at each GLS, a pair of Geokon load cells (model 3000, 50 kip capacity) were mounted in line with the load frame rods that flanked each side of the test girder (Figure 12.14). These load cells provided load measurements that were redundant with the Interface load cells. The average of the Interface load cell readings on each gravity load simulator (named F-N15-C and F-S15-C, located at the north and south GLSs, respectively) were used to monitor the load applied to the test girder and to determine the buckling capacity of the test girder. These load cells (F-N15-C and F-S15-C) were also used to generate the load-time history presented previously in Figure 12.10.

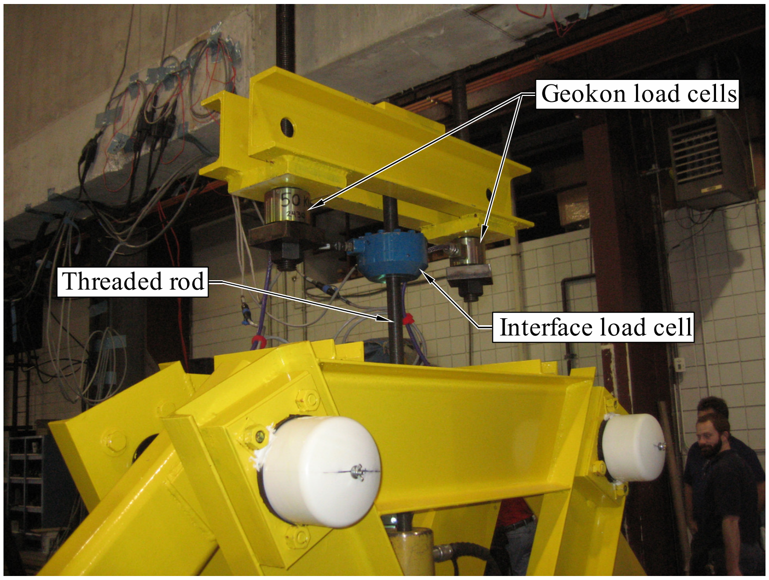

Figure 12.14. Load cells, located at gravity load simulator locations

12.4.3 Strain gages

Strain gages (both external and cast into the concrete) were used to detect cracking, if it were to occur. Several external strain gages (Kyowa 60 mm and 120 ohm) were mounted to the test girder at locations most likely to crack: on the bottom of the precast segments close to the interface with each closure strip (see Appendix G for specific locations). The remaining external strain gages were placed at increments along the length of the girder on the east and west faces of both the top and bottom flanges, to capture the strain profile if necessary. A pair of vibrating wire strain gages (Geokon model 4200) were cast into each closure strip, located vertically between the post-tensioning coupler housings (Figure 12.15). These gages were used to detect cracking should it occur in the closure strips. The vibrating wire strain gages were also used to measure total strain in the test girder over time, including strain introduced during the post-tensioning stage. In contrast, the external strain gages measured incremental (not total) strains caused by applied vertical load during each buckling test.

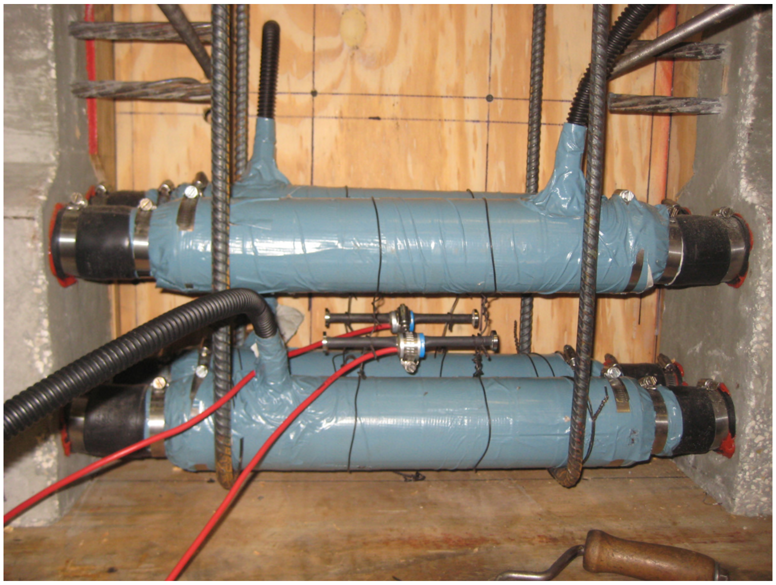

Figure 12.15. Vibrating wire strain gages, cast into closure strips

CHAPTER 13
GIRDER BUCKLING TEST RESULTS

13.1 Introduction

As introduced in Chapter 7, there were two primary goals of the second phase of this project. The first objective was to experimentally quantify the buckling capacity of the test girder supported on bearing pads with various configurations of skew and slope angles. The second objective was to use the experimental results to validate and calibrate corresponding finite element buckling models. The results of the experimental girder buckling tests are presented in this chapter, including measured data, a data curve fitting scheme, a method for calculating buckling capacities, and the computed buckling capacities. Additionally, the results of the experimental tests are compared to finite element analysis results and aspects of the validated finite element model—bearing pad roll stiffness, concrete elastic modulus specified, and load-displacement results—are presented.

13.2 Experimental buckling test results

It is important to note that, of the nine (9) individual buckling experiments performed and presented in this chapter, only one test (A-45-0-1) was carried out until complete buckling of the test girder occurred (Figure 13.1). The remaining tests were terminated close to, but before the test girder became fully unstable, thus ensuring that cracking did not occur (and therefore maintaining repeatability). Therefore, the last measured data point presented for each individual test does not indicate that buckling occurred, but rather indicates the load and displacement level at which the test was concluded.

Figure 13.1. Test girder in buckled configuration, test A-45-0-1:
a) Photograph taken above girder; b) Photograph taken below girder (note the laterally displaced positions of girder and gravity load simulator)

13.2.1 Measured load-displacement curves

For each test, vertical load was applied at the top of the test girder at the gravity load simulator locations (Figure 13.2), and midspan lateral (x-axis) displacement was measured roughly at the centroid of the test girder. Data points were established when the Interface load cell readings (F-N15-C and F-S15-C, located at the north and south GLSs, respectively) measured approximately the same applied load. In this chapter, the average of these load cell readings is defined as the load (P) applied at each GLS (Figure 13.2). Midspan lateral displacements presented in this chapter were measured using displacement sensor Dx-N0-W-38. Measured load-displacement curves for each test are shown in Figure 13.3. For each curve, the displacement of the first data point indicates the sweep of the test girder under only its own self-weight. Note that sweep was recorded using displacement sensor Dx-N0-W-38 for the tests conducted following method A (recall Section 12.3.2), whereas the sweep was measured using a tape rule for the tests conducted following method B. By shifting the displacement data along the x-axis to the origin (Figure 13.4)—corresponding to incremental midspan displacement caused by applied load—excellent repeatability is observed between tests with the same configuration.

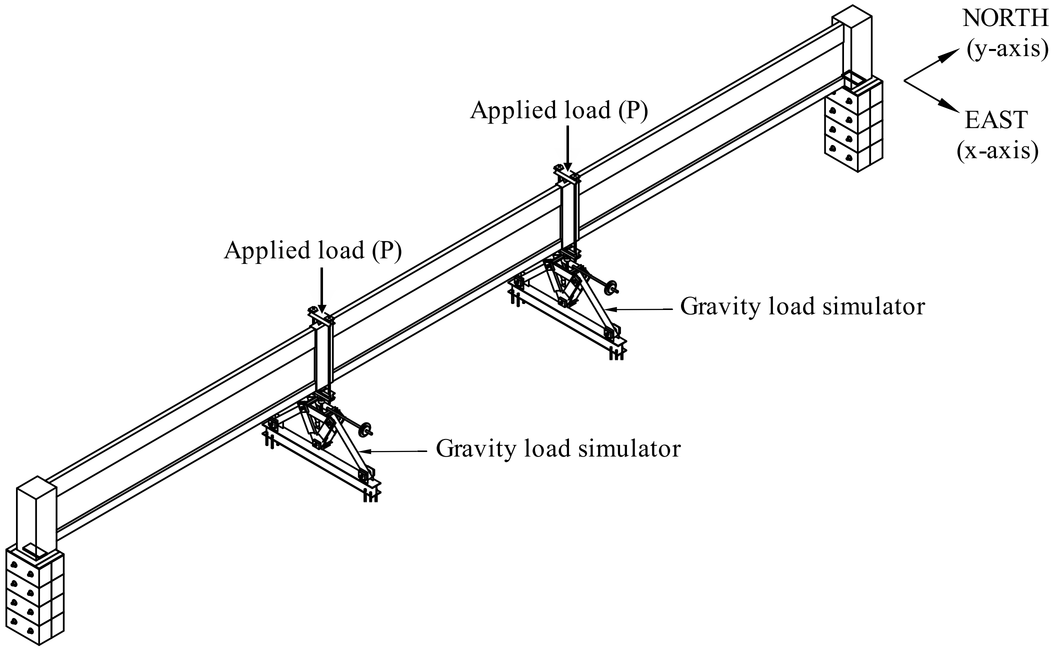

Figure 13.2. Definition of applied load (P)

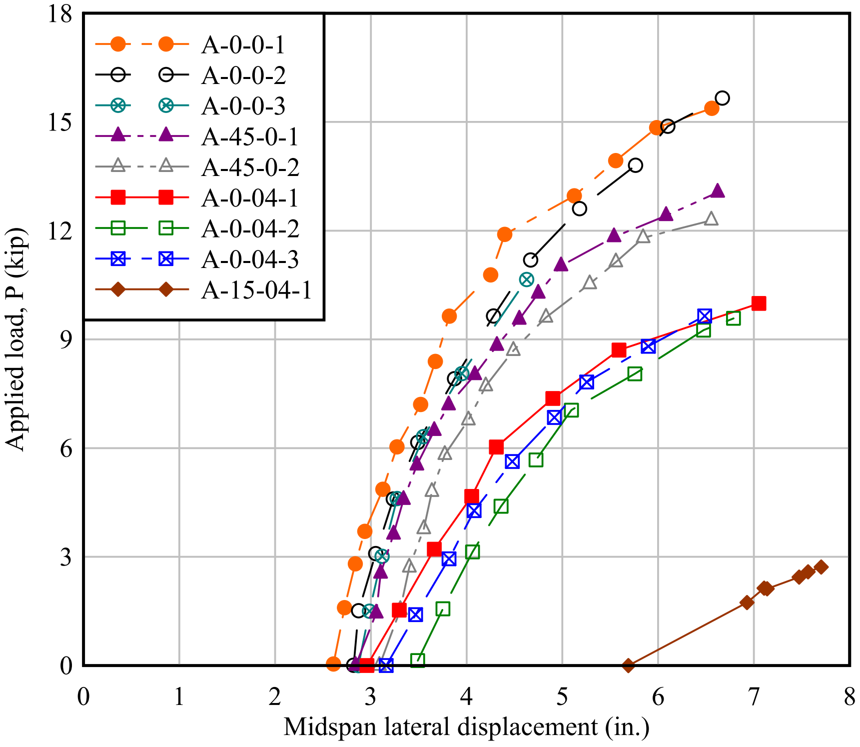

Figure 13.3. Measured absolute load-displacement data

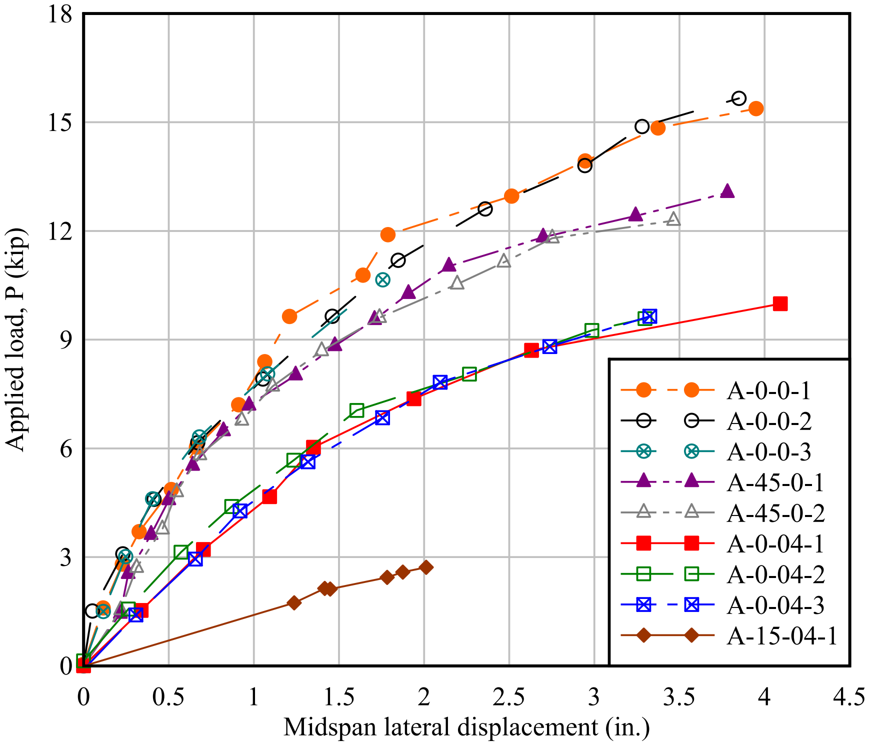

Figure 13.4. Measured incremental load-displacement data

13.2.2 Data curve fitting

A method developed by Southwell (1932) is commonly used to characterize the load-displacement behavior of buckling experiments and to determine buckling capacity without needing to perform the experimental test until complete buckling occurs. Using the Southwell method, a rectangular hyperbola passing through the origin is fitted to load-displacement data obtained from a buckling experiment using the equation:

$$x \cdot y - \beta \cdot x + \alpha \cdot y = 0 \qquad (13.1)$$

where α and β are the asymptotes of the hyperbola (Figure 13.5). Rearranging the equation provides an alternate form:

$$y = \frac{\alpha \cdot \beta \cdot x^2}{\alpha \cdot x^2 + \alpha^2 \cdot x} \qquad (13.2)$$

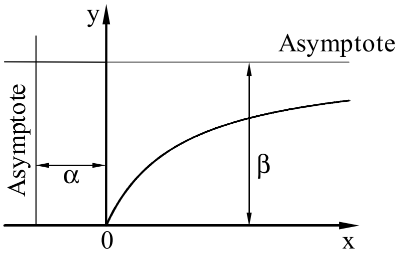

Figure 13.5. Southwell hyperbola fit

To fit a curve through multiple sets of experimental data, individual data sets (corresponding to individual tests) are commonly averaged together to form a single data set and a curve is fit through the averaged data. This approach works best when each data set includes approximately the same number of points, and data are recorded at the same interval. However, the data from the buckling tests were not recorded in this manner. As shown in Figure 13.4, data for individual tests within each configuration were measured at unequal lateral displacement intervals, and the displacement range of each test was not equal. Thus, simply averaging the data for each configuration would bias the average toward tests in which data were captured at smaller intervals. To prevent such biasing, the following procedure was used to process the data for each individual test and develop a characteristic fitted curve for each configuration:

- A hyperbola (Equation 13.2) was fit—by using least-squares error minimization—to each individual test data set (Figure 13.6a)
- The fitted hyperbolas for each test configuration were resampled at equal displacement intervals: specifically at intervals of 1/20th of the maximum displacement achieved for the configuration (Figure 13.6b)
- A single hyperbola was then fit to the cloud of resampled data points for each test configuration (Figure 13.6c)

This procedure was applied to each test configuration, producing the final hyperbola results shown in Figure 13.7.

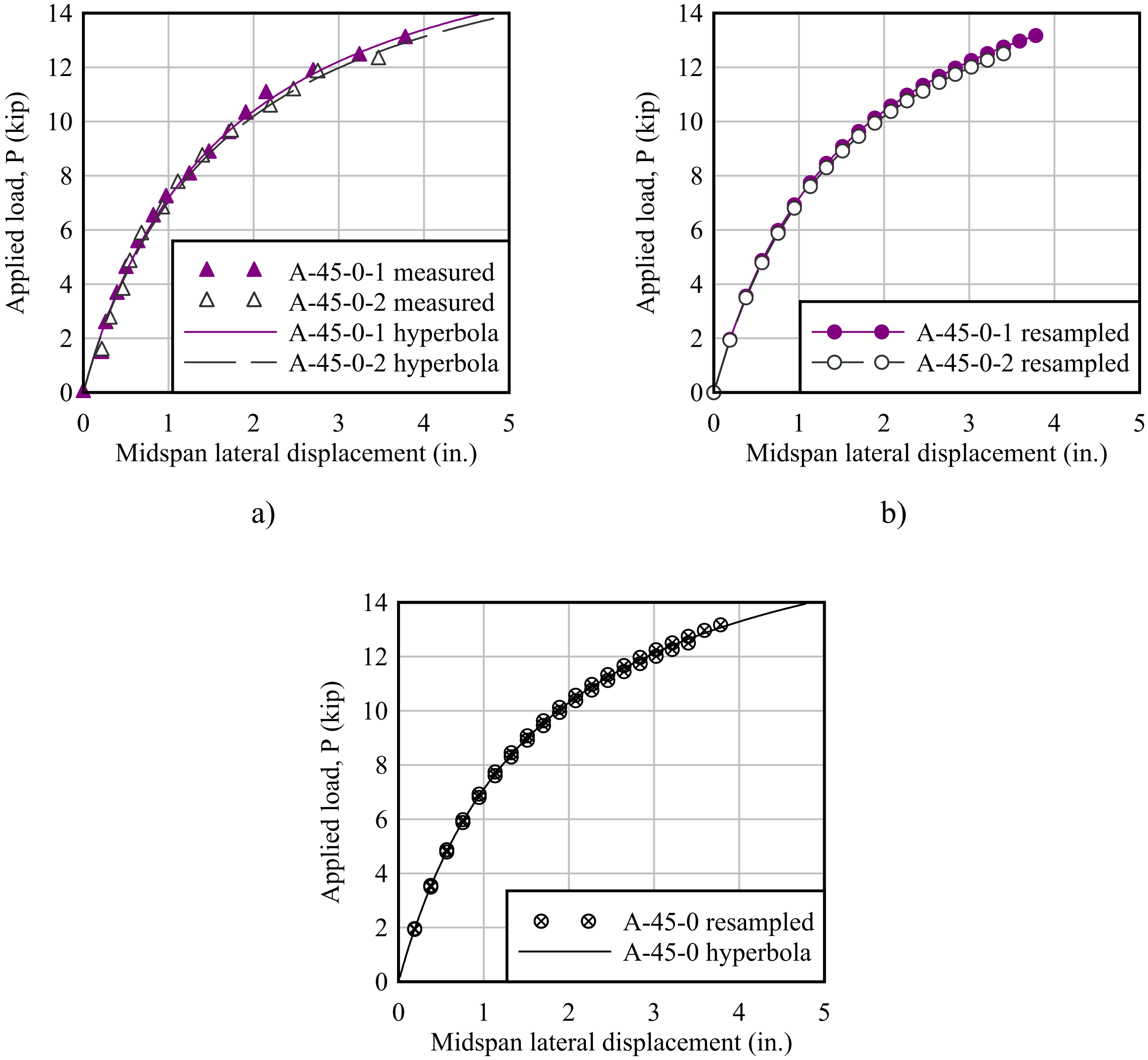

a)

b)

c)

Figure 13.6. Data curve fitting procedure:
a) Best fit hyperbolas for each individual test through measured data; b) Resampled data on hyperbola at regular interval; c) Test configuration hyperbola fit through resampled cloud of data

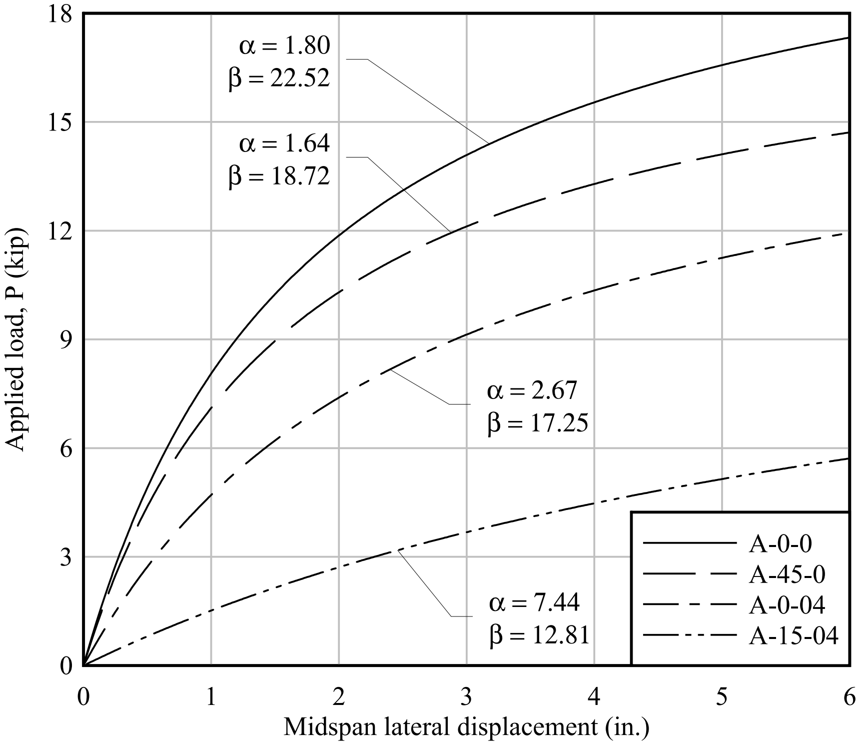

Figure 13.7. Best fit hyperbolas for each test configuration

13.2.3 Calculation of buckling capacity

Using the Southwell method (1932), buckling capacity is approximately equal to the horizontal asymptote (β, Figure 13.5) of the best fit hyperbola. Recall that among the buckling experiments conducted, one test (A-45-0-1) was conducted until complete buckling occurred. Thus, this case can be used to test the accuracy of approximating the buckling load using the fitted value β. For this test, the buckling load was experimentally measured as 13.1 kip. However, as shown in Figure 13.8, the Southwell method estimates the buckling load (β) as 18.7 kip, overestimating by 43%. As stated by Southwell (1932), the "analysis may be expected to apply best to cases in which the initial deflection [sweep] was small." In other words, the Southwell method works best when the primary instability is lateral torsional buckling. However, for the experiments conducted in this study, the test girder initial sweep was large enough that the failure mode was a mixture of lateral torsional buckling and roll-over instability as opposed to pure lateral torsional buckling instability. Due to the slenderness and post-tensioning levels necessary to elastically buckle the test girder at a 100 ft span length, the test girder had a sweep that was more than twice the level that is acceptable in practice.

As per the 2010 FDOT *Standard Specifications for Road and Bridge Construction* (FDOT 2010b), maximum allowable girder sweep was limited to 1/8 in. of sweep per 10 ft of girder length, but not to exceed 1.5 in. for Florida Bulb-Tee beams and Florida-I Beams. The minimum sweep of the test girder—in test configuration A-0-0—was 2.8 in. Because of the large initial sweep displacements, the asymptote of the hyperbola (β) is not an ideal definition of buckling load for the experiments performed in this study. Instead, an alternative definition for buckling capacity was employed, but still partially incorporating the Southwell hyperbola. Using the fitted hyperbola (Eqn. 13.2), the buckling load was defined, in this study, as the point at which the slope of the hyperbola drops below 1/10th of the initial slope (Figure 13.9). Buckling capacity determined using this rule agreed well with measured data from the one girder test case that was carried out to the point of complete buckling (A-45-0-1, as noted in the following section).

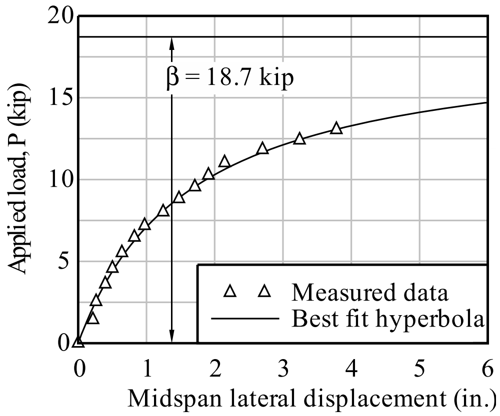

Figure 13.8. Hyperbolic curve fit and Southwell buckling load for test A-45-0-1

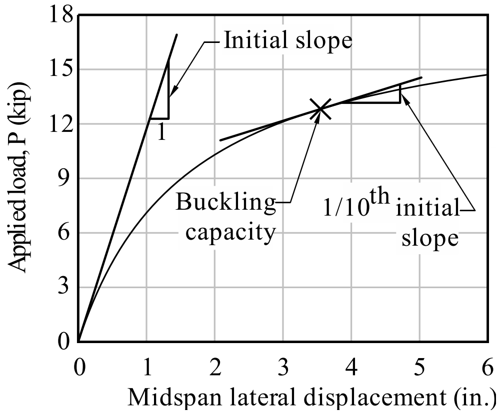

Figure 13.9. Definition of buckling capacity (A-45-0 configuration shown)

13.2.4 Buckling capacity results

Using the 10%-slope buckling definition, the ideal case, A-0-0 (non-skewed, non-sloped), had the largest buckling capacity, and the skewed, sloped case (A-15-04) had the lowest buckling capacity. The intermediate cases (A-45-0 and A-0-04) both had buckling capacities between the two extremes. Table 13.1 provides a summary of the buckling capacity for each test configuration, as well as the percent reduction in buckling capacity relative to the ideal (A-0-0) case. There was good agreement between the buckling capacity configuration A-45-0, as determined using the 10%-slope rule, and the measured buckling capacity of experimental test A-45-0-1, which completely buckled in the lab at a measured load of 13.1 kip. Using the 10%

buckling rule, the buckling capacity for configuration A-45-0 was calculated to be 12.8 kip (2.3% error relative to experimental test A-45-0-1).

Table 13.1. Buckling capacity results

Test configuration	Skew angle (deg.)	Slope angle (rad.)	Buckling capacity (kip)	Buckling capacity percent reduction from A-0-0 (%)
A-0-0	0	0	15.4	0.0%
A-45-0	45	0	12.8	16.9%
A-0-04	0	0.04	11.8	23.4%

In the case of test configuration A-15-04, determining the buckling capacity through the use of the 10% rule was not possible, because the test girder had such a large initial sweep (5.69 in., recall Table 12.2) compared to what is acceptable in practice. In the A-15-04 test, the large initial lateral displacement (sweep) caused the test girder to purely overturn, as opposed to buckle. While a hyperbola can be fit through the data, the buckling load cannot be quantified and will not be discussed in the remainder of this report.

13.3 Buckling finite element model

The results of the experimental buckling tests were used to validate the finite element modeling techniques and buckling analysis procedures. This section discusses the several components of the finite element model, including development of the moment-rotation curves that were used to represent the bearing pad, the modulus of elasticity of test girder concrete, and the results obtained from a buckling analysis of each configuration tested in the lab.

13.3.1 Moment-rotation curves from bearing pad roll stiffness tests

As originally planned, the nonlinear roll stiffnesses of the bearing pads were to be modeled using the moment-rotation curves obtained from the isolated roll bearing pad tests (Chapter 6). However, the axial (vertical) load levels on the pads were different between the isolated pad tests and the girder buckling tests. Recall from Section 5.4 that the axial load level used in the majority of the isolated bearing pad tests was chosen to be representative of the self-weight reaction caused by a long-span Florida Bulb-Tee (FBT) 78 girder. That is, the axial load levels used in the isolated bearing pad tests were chosen to be representative of typical field conditions. In contrast, due the shorter span length (limited to 100 ft) and the slender cross-section of the laboratory test girder, the axial pad loads generated by the self-weight reactions from the test girder were considerably smaller than those which would be associated with a long-span FBT or FIB girder.

This difference in axial pad load altered the moment-rotation behavior of the bearing pad during girder buckling tests, as compared to the isolated bearing pad tests. Therefore, to generate appropriate data needed for finite element model validation, additional roll stiffness tests were performed on the bearing pads under buckling testing conditions, with the bearing pads located beneath the laboratory test girder in test configuration A-0-0. Under these conditions, the bearing pads were tested “in situ.” In the remainder of this section, the in situ test procedure and results are presented, and the results are compared to the roll stiffness results obtained using the bearing pad test device (denoted as "isolated" results in this section).

For the in situ tests, a lateral load was applied to the top flange of the test girder near each end block, and the girder was allowed to roll about the y-axis of the bearing pad (Figure 13.10a). The intent in conducting the in situ tests was to determine the bearing pad roll stiffness relative to the initial girder equilibrium position (which is influenced by the presence of girder sweep).The load was applied by a hydraulic jack mounted to the catch frame at each end of the test girder, and measured with an inline load cell (Figure 13.10b). Displacement sensors, mounted at the end blocks and oriented along the x-axis (Dx), measured the relative horizontal displacement between the top and bottom of the end blocks. Knowing the vertical separation distance between each pair of sensors (Dx-N51-W-2 and Dx-N51-W-76; Dx-S51-W-2 and Dx-S51-W-76), the end block roll (rotation) angles could then be calculated. Three in situ roll tests were performed (on 2011-12-19 and 2011-12-20). The measured data are shown in Figure 13.11.

Because the goal was to determine the bearing pad roll stiffness relative to the initial equilibrium position of the girder, the moment data included in Figure 13.11 were computed only from lateral jack loads, not the combination of jack loads and eccentric gravity loads. Moreover, the data reported in Figure 13.11 include tests in which the jack loads were applied from East-to-West (in the direction opposite to the girder sweep) and from West-to-East (in the same direction as the girder sweep). The lack of an evident correlation between the test results and the loading direction indicates that this test procedure adequately captured the bearing pad roll stiffness relative to the girder equilibrium position.

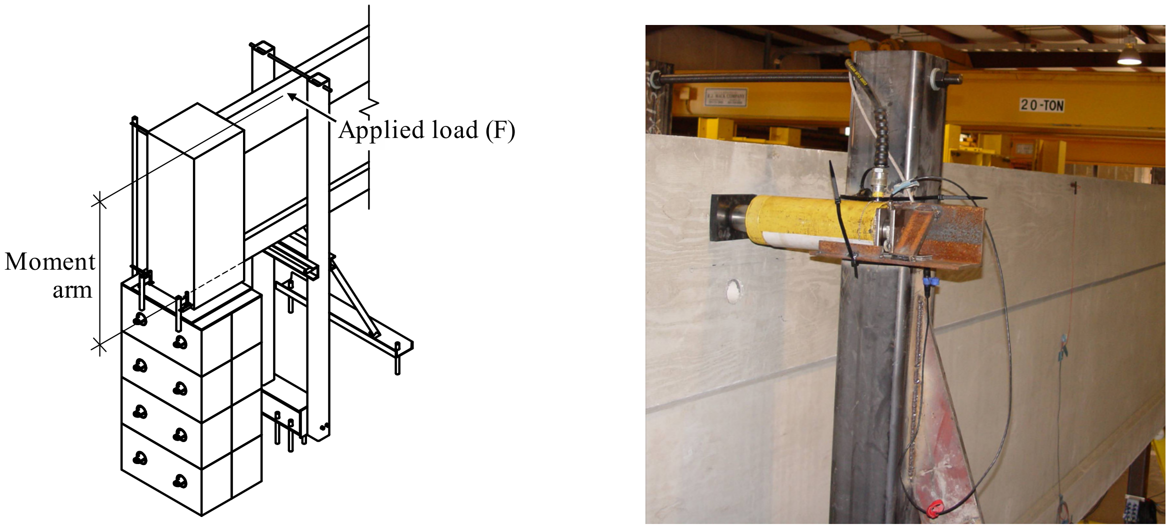

a) b)

Figure 13.10. Description of "in situ" roll test:
a) Schematic of test; b) Loading setup, mounted to catch frame

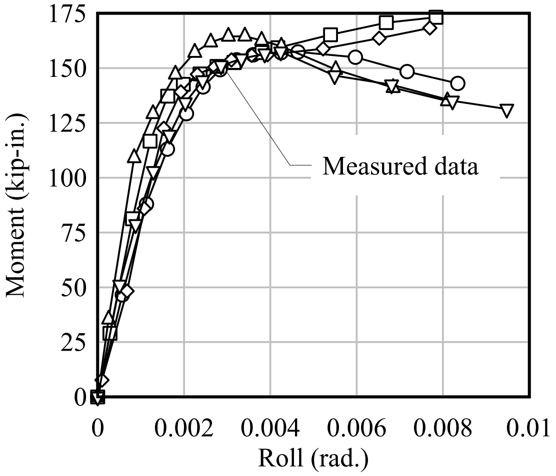

Figure 13.11. Moment-rotation data from in situ tests (A-0-0)

In the finite element model, bearing pad rotational resistance is modeled using nonlinear rotational springs which are defined by a moment-rotation curve. Therefore, the measured moment-rotation data from the laboratory in situ roll stiffness tests were averaged and subsequently fitted to a representative function for input into the finite element model. To maintain equal weight when averaging the curves, the measured load-displacement curves from individual tests (Figure 13.12a) were resampled at an equal interval of 0.0003 rad (Figure 13.12b), and the resampled curves were averaged (Figure 13.12c). The averaged data exhibit an initial, linear roll stiffness (slope of moment-rotation curve) that is followed by an apparent softening (reduction in stiffness), until the slope of the moment-rotation curve effectively equals zero and the moment-rotation curve plateaus. A sigmoid function, which has a shape that matches the average data closely, was chosen to represent the moment-rotation curves for the bearing pads. A basic sigmoid function takes the following functional form:

$$f(x) = \frac{1}{1+e^{-x}} \tag{13.3}$$

However, to fit the moment-roll curves, the basic functional form must undergo a variety of transformations. Thus, the data were fit (by using least-squares error minimization) with the following modified functional form:

$$f(x) = \gamma_0 + \frac{\gamma_1}{1+e^{-\gamma_2 \cdot x}} \tag{13.4}$$

where γ_0, γ_1, and γ_2 are parameters that determine the shape of the curve.

This same process of resampling, averaging, and fitting the data was then applied to the moment-rotation curves obtained from the isolated roll stiffness tests using the bearing pad test device. Similar to the in situ roll stiffness tests, the measured isolated bearing pad data had an initial linear stiffness that gradually decreased, closely matching the modified sigmoid curve shape. The best fit sigmoid curves for the moment-rotation curves of the isolated and in situ roll stiffness tests are shown in Figure 13.13. The functional parameters of the best fit sigmoid curve for each test configuration—both isolated and in situ roll stiffness tests—are presented in Table 13.2.

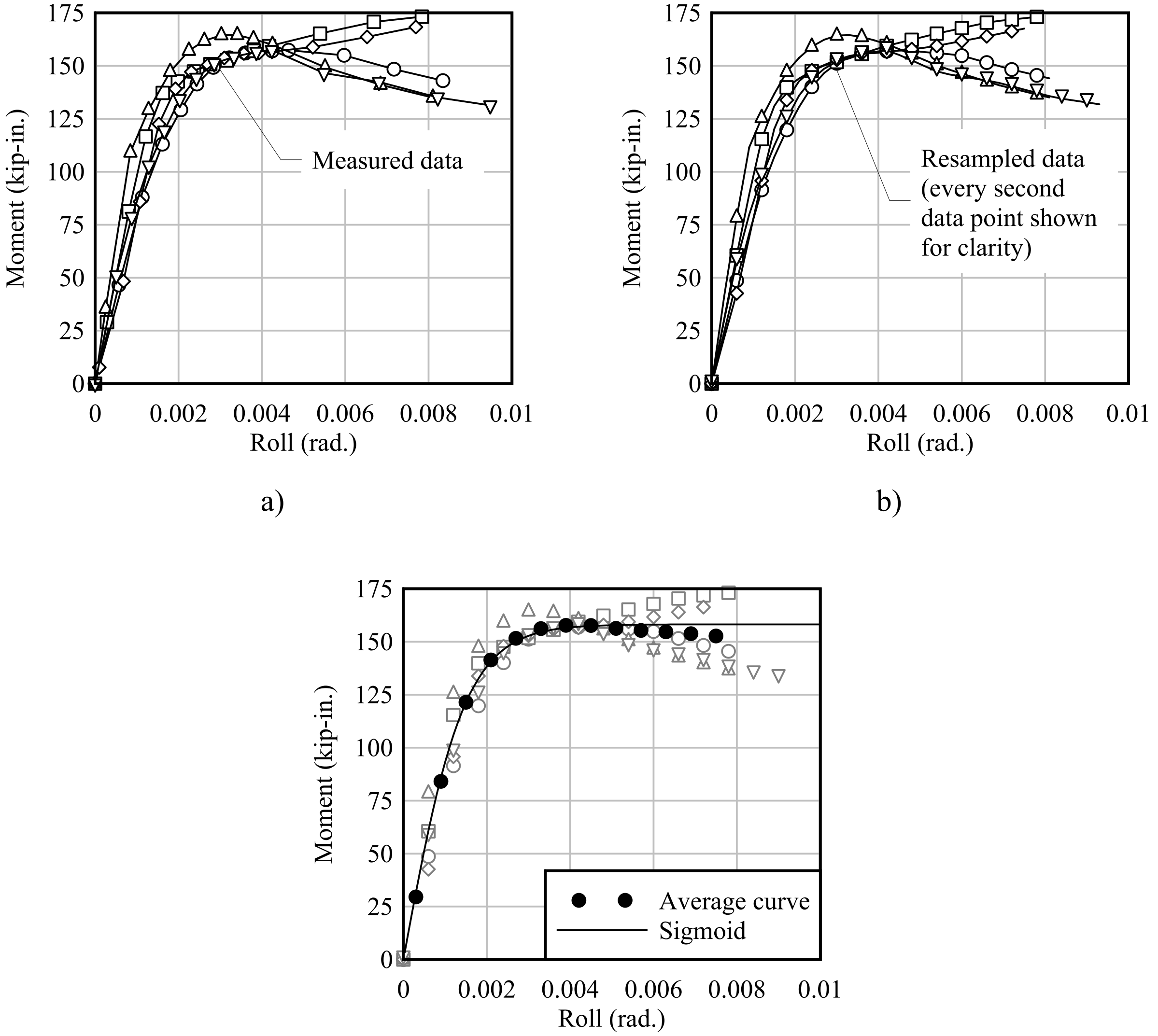

a)

b)

c)

Figure 13.12. Data curve fitting procedure, in situ case shown:
a) Measured data; b) Resampled data; c) Average curve and best fit sigmoid curve

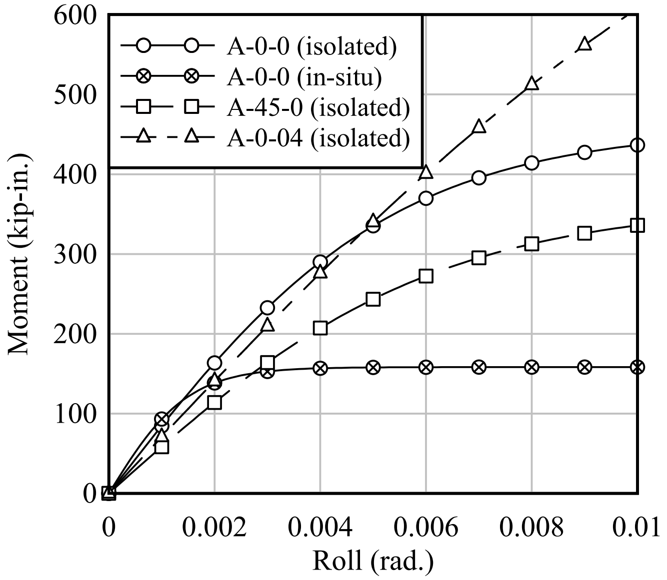

Figure 13.13. Moment-rotation curves, from isolated and in situ roll stiffness tests

Table 13.2. Sigmoid curve functional parameters for each test configuration (applicable unit set: moment = kip-in., roll angle = rad.)

Test configuration	γ_0	γ_1	γ_2
A-0-0 (isolated)	443.6	887.6	424.8
A-0-0 (in situ)	158.2	316.4	1350.7
A-45-0 (isolated)	375.2	750.5	294.8
A-0-04 (isolated)	1005.2	2010.4	140.8

13.3.2 Scaling of moment-rotation curves from isolated bearing pad tests

The axial load applied to the type A bearing pads during the isolated roll stiffness tests was approximately 92 kip, which, as noted above, was chosen to be representative of the self-weight end reactions of a realistic long-span girder (FBT or FIB sections). However, during girder buckling testing, the test girder was constrained to a 100 ft span length, which required a more slender and therefore lighter girder cross-section to be used, resulting in a reduced axial load applied to the pad. During buckling testing, the total axial load—caused by combination of girder self-weight *and* applied vertical loads—was approximately 40 kip. Thus, the ratio of axial load during buckling testing to axial load during isolated roll stiffness testing was approximately 40 kip / 92 kip = 0.43. Under this reduced axial load, the in situ moment-rotation behavior of the bearing pads was different than measured during the isolated tests, as shown in Figure 13.14. Although both the in situ and isolated moment-rotation data have similar initial roll stiffnesses, the plateau value differs significantly. As shown in Figure 13.14, the plateau of the in situ moment-rotation curve occurs at a much lower moment level than that from the isolated pad tests.

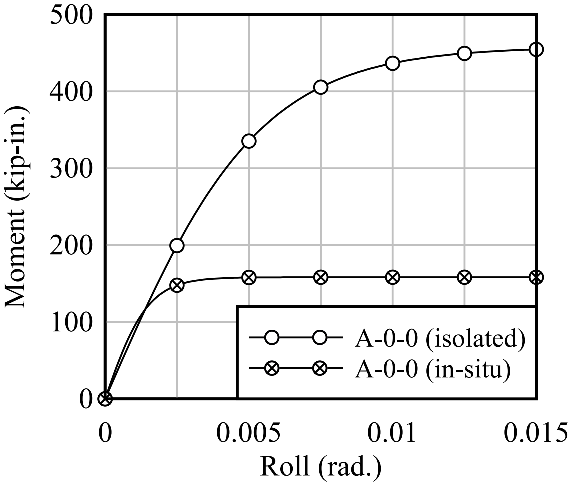

Figure 13.14. Moment-rotation curves, test configuration A-0-0, from isolated bearing pad tests and in situ tests

This difference in moment-rotation behavior can be attributed to the difference in axial pad pre-compression, which affects the contact area between the pad and the girder end block (or bearing pad test device) as roll rotation occurs. Initially, under non-sloped conditions, each bearing pad was fully in contact with the bottom of the end block (or bearing pad test device), and thus the initial roll stiffness of the bearing pad was not affected by the magnitude of axial load. However, during the in situ roll stiffness tests (and during the girder buckling tests)—in which pre-compression was reduced relative to the isolated pad tests—a smaller rotation angle was required for the end blocks to lose contact with the pads (Figure 13.15). Consequently, the in situ plateau moment was reduced relative to the plateau moment observed in the isolated pad tests. These test results suggest that the plateau moment for each situation was proportional to the level of axial pre-compression acting on the pad. Thus, the ratio of roll-off moment capacities (i.e., the plateau moments) for the in situ and isolated test cases should differ by the ratio of axial loads present during each type of testing (40 kip / 92 kip = 0.43 in this case).

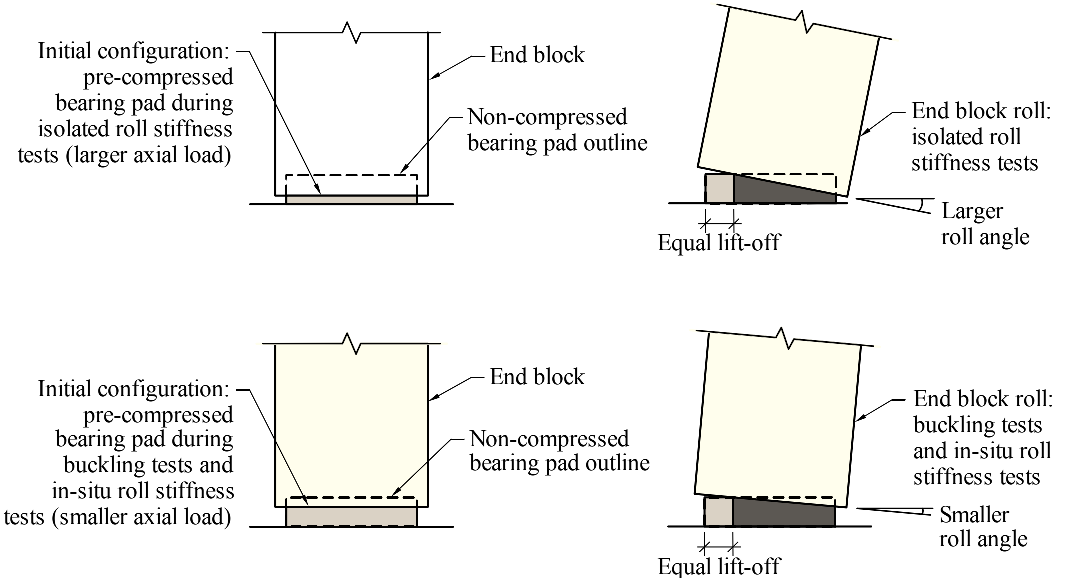

Figure 13.15. Contact areas during both isolated roll stiffness tests and buckling tests

A similar phenomenon also occurred in the sloped cases. However, the *initial* contact area of the end block (or test device) with the bearing pad was approximately proportional to axial pre-compression (Figure 13.16). Thus, the initial roll stiffness is also proportional to the pre-compression. Similar to the non-sloped cases, the roll capacity was proportional to axial pre-compression. Therefore, for sloped cases, *both* the initial stiffness and the plateau moment of the moment-rotation curve were decreased by the ratio of applied axial load (0.43 in this case).

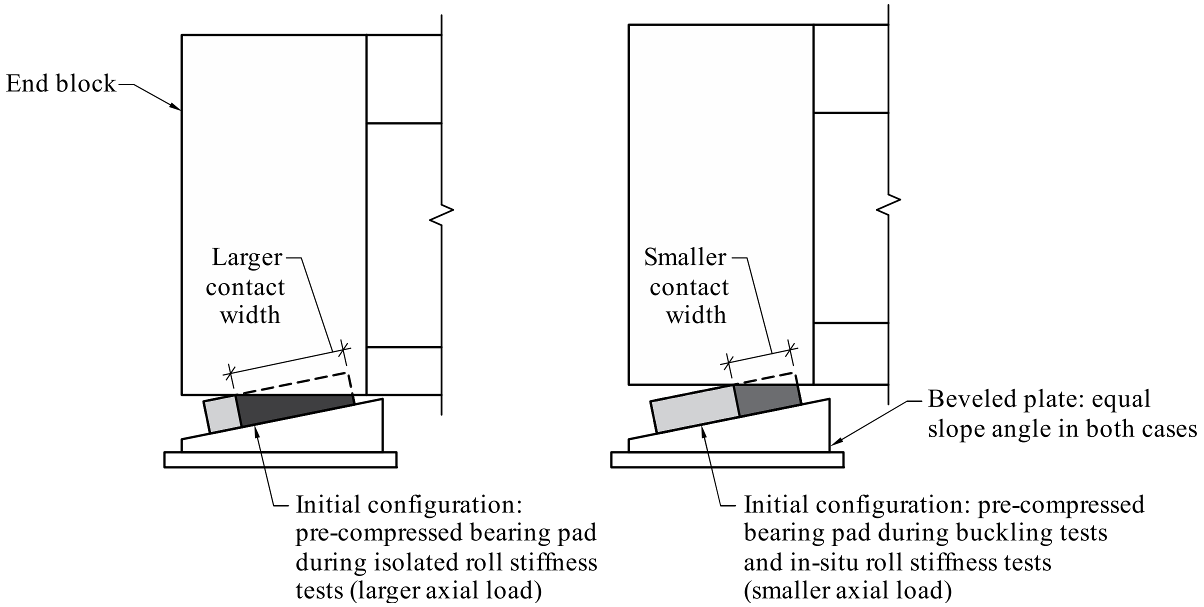

Figure 13.16. Contact areas during both isolated roll stiffness tests and buckling tests

Therefore, for use in the girder buckling finite element model, moment-rotation curves obtained from the isolated roll stiffness tests were scaled by a factor of 0.43 (equal to the ratio of axial loads). In non-sloped test configurations (A-0-0 and A-45-0), the scale factor was applied only to the plateau of the moment-rotation curve, while maintaining the initial slope (Figure 13.17a and Figure 13.17b). However, for the sloped configuration (A-0-04), the scale factor was applied to both the initial slope and the moment plateau (Figure 13.17c). Examining the moment-rotation curves from test configuration A-0-0 (Figure 13.17a), the scaled curve closely matches the in situ curve for both the initial stiffness and moment plateau. The final scaled curves for each test configuration—used in all subsequent finite element buckling analyses—are compared in Figure 13.18.

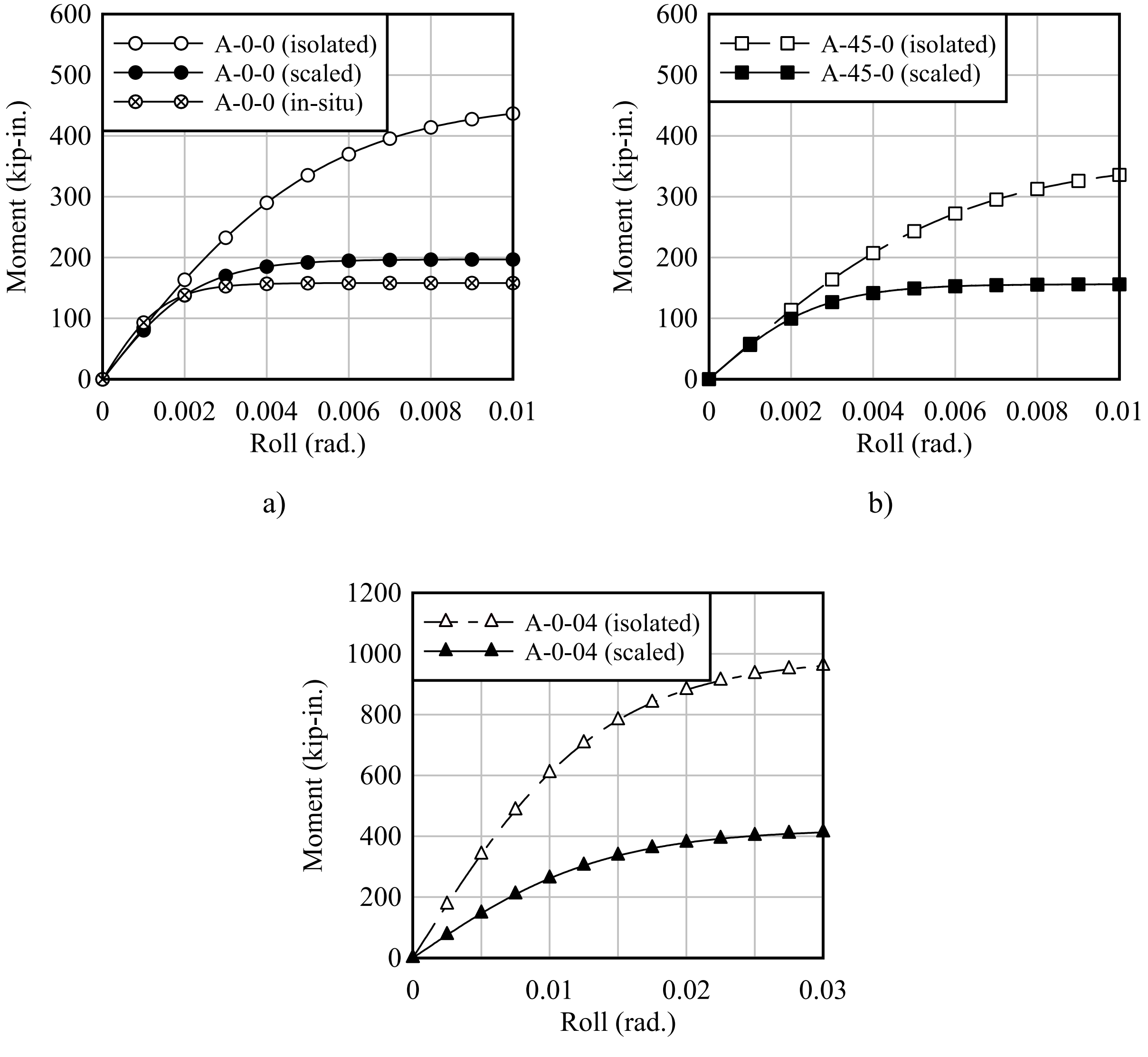

a)

b)

c)

Figure 13.17. Moment-rotation curves, from isolated roll stiffness tests (scaled and original) and in situ roll stiffness tests: a) A-0-0; b) A-45-0; c) A-0-04

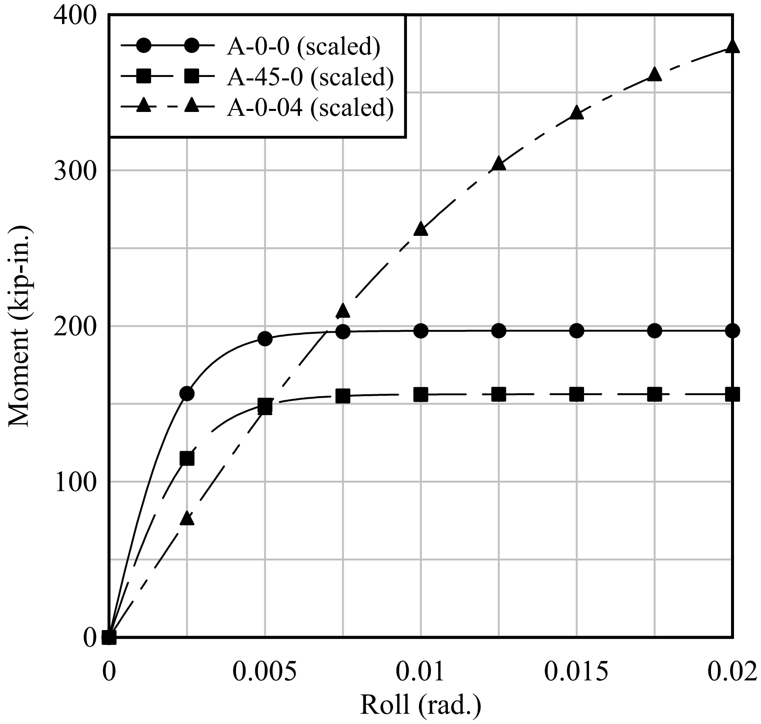

Figure 13.18. Moment-rotation curves for girder buckling model (scaled down from isolated bearing pad test results)

13.4 Elastic modulus used in finite element buckling model

Concrete components of the test girder were modeled using a linear elastic material model. As discussed in Chapter 10, the elastic modulus was determined for the precast segments using field-cured and moist-cured cylinders. The average elastic modulus for the field-cured cylinders was 4,770 ksi, and the average of the moist-cured cylinders was 5,140 ksi. Two separate finite element buckling analyses were performed for test configuration A-0-0 (using the scaled bearing pad roll stiffness curves), each with an elastic modulus corresponding to the field-cured or moist-cured results. The buckling curves predicted by both models are presented in Figure 13.19, along with the best fit hyperbola generated from the experimental data. Generally, the finite element model that employed the field-cured elastic modulus was more accurate in approximating the experimental results. This observation can be attributed to the fact that the web thickness of the precast segments matched the diameter of the concrete cylinders (4 in.). Therefore, the environmental conditions imposed on the field-cured cylinders (cured alongside the test girder) were more representative of the precast segments than were the moist-cured cylinders (which were submerged in a tank of lime water). Thus, the field-cured elastic modulus (4,770 ksi) was used in all subsequent finite element models.

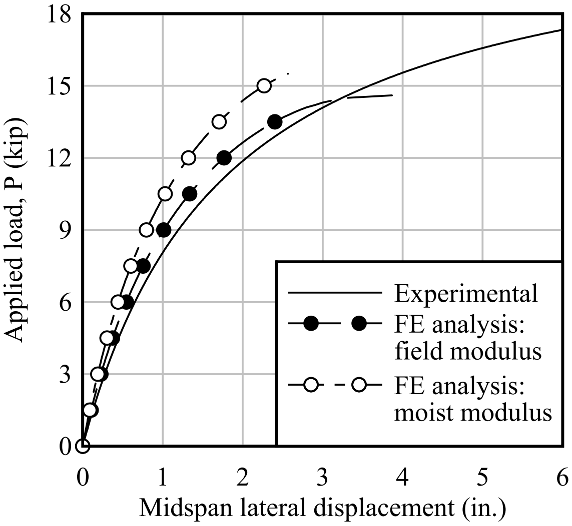

Figure 13.19. Comparison of experimental and FE buckling curves (configuration A-0-0)

13.5 Finite element buckling model results

A finite element buckling analysis was performed for each of the three test configurations, using the scaled bearing pad roll stiffness curves and field-cured elastic modulus as described in the previous sections. Using the same 10%-slope buckling definition that was applied to the experimental results, the buckling capacity of each finite element analysis was defined as the point at which the slope of the load-displacement curve dropped to below 1/10th of the initial slope. The buckling curves and capacities for each of the finite element analyses are shown in Figure 13.20, along with the buckling curves and capacities generated using hyperbolas fitted to the experimental data. The buckling capacities calculated from the experimental tests and from finite element analyses are also summarized numerically in Table 13.3.

Generally, there was good agreement between the shape of the experimental and analytical (finite element) curves—particularly in the non-sloped cases—and also between the predicted buckling capacities. In the non-sloped cases (A-0-0 and A-45-0), the finite element buckling capacity was lower than the experimental buckling capacity. However, in the sloped case (A-0-04), the initial slope and buckling capacity of the model were slightly larger than the experimental results. This disagreement can most likely be attributed to a difference in the theoretical initial contact area on the bearing pad, caused by the initial sweep that was present at the start of the experimental buckling test. If, as a simplification, linear elastic bearing pad response was assumed, then the ratio of initial contact areas between girder buckling tests and isolated roll tests would be equal to the ratio of applied axial load. Thus, scaling the isolated roll stiffness curves by the ratio of the applied axial loads should accurately reflect this difference. However, because relatively large sweep was present in the test girder, the end blocks initially rolled about the bearing pad as the test girder was being set in place. Therefore, the contact area in the buckling tests may actually have been less than the theoretical contact area accounted for by using the scale factor. Thus, the initial slope and buckling load obtained from the experimental results would be smaller than the finite element prediction (as seen in the A-0-04 case).

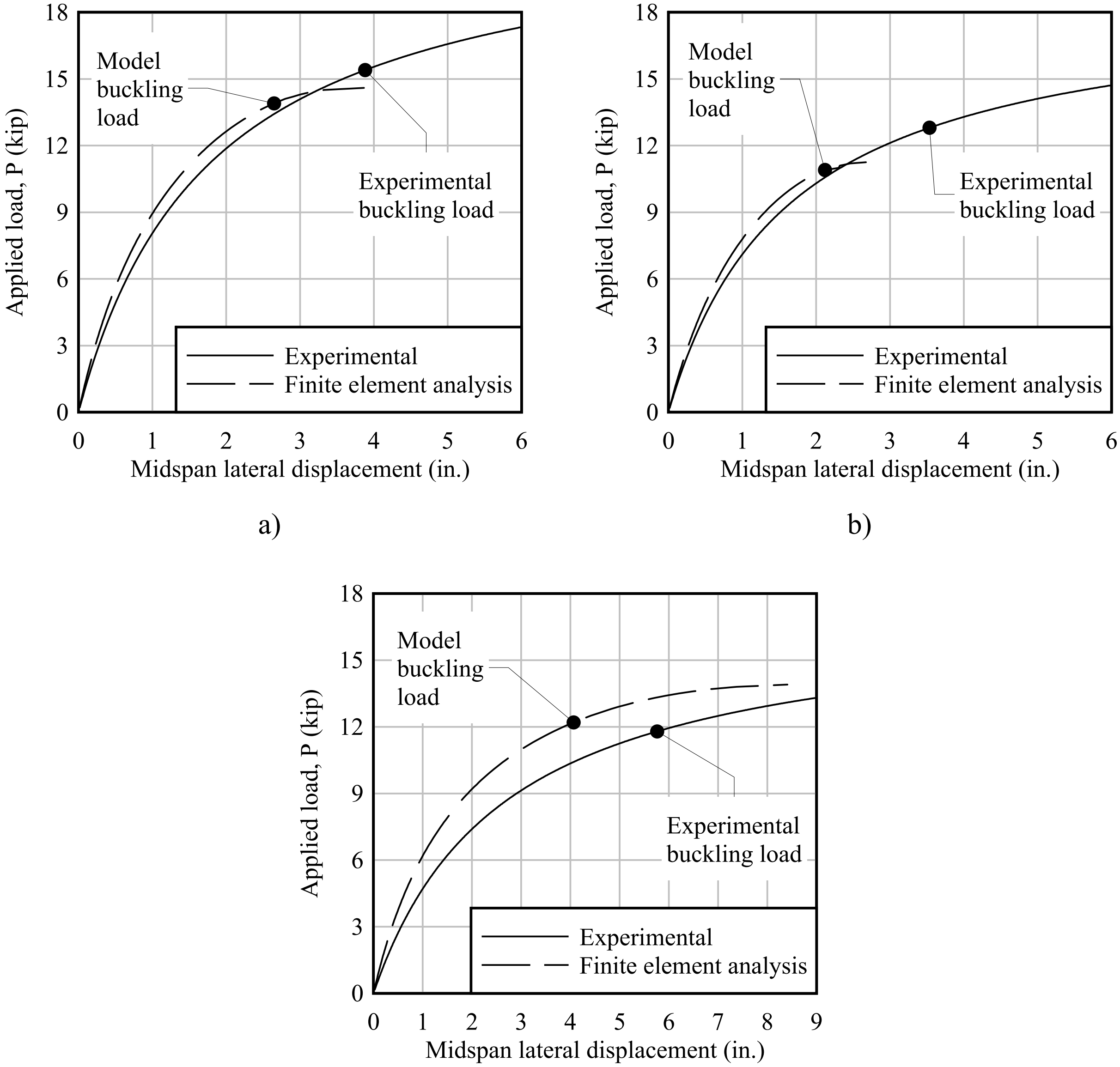

a)

b)

c)

Figure 13.20. Buckling curves from experimental tests and finite element models: a) A-0-0; b) A-45-0; c) A-0-04

Table 13.3. Experimental and finite element buckling capacities for each test configuration

Test configuration	Experimental buckling load (kip)	Finite element model buckling load (kip)	Percent difference
A-0-0	15.4	13.9	-9.7%
A-45-0	12.8	10.9	-14.9%
A-0-04	11.8	12.2	3.4%

Based on the acceptable levels of agreement observed between the shape of the experimental buckling curves and the finite element analysis buckling curves, and based on a maximum difference of 15% between experimentally and analytically determined buckling capacities, the finite element modeling and analysis methods employed in this study, and in related FDOT-sponsored research studies (specifically, BD545-36: Consolazio et al. 2007, BDK75 977-33, and BDK75 977-70), are considered to be experimentally validated to a level of accuracy that is suitable for use in the development of girder bracing recommendations.

CHAPTER 14
SUMMARY, CONCLUSIONS, AND RECOMMENDATIONS

14.1 Summary

Roll stiffnesses for various types of standard FDOT bearing pads were quantified under the effects of skew angle, slope angle, and a combination of skew and slope. A bearing pad test device was designed and fabricated to impose axial load, skew, and slope on bearing pads, and to enable measurement of roll rotation as a function of moment applied. Additionally, girder buckling capacities of a full-scale test girder were quantified under the effects of skew angle, slope angle, and a combination of skew and slope. The pads used to support each end of the test girder were the same pads previously tested to determine roll stiffness. Gravity load simulators were designed and fabricated to apply vertical loads to the test girder without imposing artificial lateral restraint. In both types of testing (bearing pad and girder buckling), multiple test repetitions were performed under identical conditions, to ensure that reasonable repeatability of the data was achieved.

14.2 Conclusions and recommendations

Based on the isolated bearing pad roll stiffness test results, for all three FDOT pad types tested, substantial reductions in roll stiffness arose from the combined effects of skew and slope. Although not as severe as the combination of skew and slope, it was also found that skew angle alone significantly reduced the roll stiffness of a bearing pad. Regarding the buckling tests, reductions in buckling capacities resulted from the imposition of skew or slope angle alone. A severe reduction in buckling capacity was observed when skew and slope were combined, with the most extreme case (A-45-04) causing the test girder to buckle under its own self-weight without any superimposed loads.

It is therefore recommended that consideration be given to requiring that bearing pads be oriented to match girder alignment to eliminate the effects of skew angle. Similarly, the effects of slope should be minimized or eliminated by continuing to require the use of either beveled bearing plates or sloped beam seats. These measures would eliminate the adverse effects of skew and slope, both of which have been analytically and experimentally demonstrated to reduce bearing pad roll stiffness and girder buckling capacity.

It is also recommended that further analytical studies be conducted to examine the effects of bearing pad roll stiffness on Florida I-Beam (FIB) girders, at typical design span lengths. Such studies can be executed using the finite element buckling modeling techniques documented in this report. The buckling capacity determination rule—in which the buckling load is defined as the point at which the slope of the load-deflection curve drops below 10% of the initial value—should continue to be used in future studies to determine girder buckling capacity.

REFERENCES

AASHTO (2004). *Load and Resistance Factor Design (LRFD) Bridge Design Specifications*. American Association of State Highway and Transportation Officials, Washington D.C.

AASHTO (1997). *M251-97: Standard Specifications for Plain and Laminated Elastomeric Bridge Bearings*. American Association of State Highway and Transportation Officials, Washington D.C.

ADINA (2011). *Theory and Modeling Guide, Volume I: ADINA Solids & Structures*. ADINA R&D, Inc., Watertown, MA.

Allen, D. T., Cook, R. A., and Ansley, M. H. (2010). "Shear Stiffness of Neoprene Bearing Pads Under Long-Term Loads", *Transportation Research Record: Journal of the Transportation Research Board,* No. 2172, Washington, D.C., pp. 38–46.

ASTM C469 (1994). "Standard Test Method for Static Modulus of Elasticity and Poisson's Ratio of Concrete in Compression." American Society of Testing and Materials, ASTM International, West Conshohocken, PA.

ASTM C39 (2001). "Standard Test Method for Compressive Strength of Concrete Cylinders Cast in Place in Cylindrical Molds." American Society of Testing and Materials, ASTM International, West Conshohocken, PA.

ASTM D4014-03 (2003). "Standard Specification for Plain and Steel-Laminated Elastomeric Bearings for Bridges." American Society for Testing and Materials, ASTM International, West Conshohocken, PA.

ASTM C109 (2011). "Test Method for Compressive Strength of Hydraulic Cement Mortars (Using 2-in. or [50-mm] Cube Specimens)." American Society for Testing and Materials, ASTM International, West Conshohocken, PA.

Consolazio, G. R., Hamilton III, H. R., Bui L., and Chung J. (2007). *Lateral Bracing of Long-Span Florida Bulb-Tee Girders.* Structures Research Report No. 2007/52290, Department of Civil and Coastal Engineering, University of Florida, Gainesville, FL.

Deaver, J. E. (2003). *Laboratory Tests on Torsional Braces for Steel Bridge Girders with Normal Supports*. Masters thesis, Department of Civil and Environmental Engineering, University of Houston, Houston, TX.

Doody, M. E., and Noonan, J. E. (1999). "Long-Term Performance of Elastomeric Bridge Bearings." *Transportation Research Record: Journal of the Transportation Research Board*. No. 1688, Washington, D.C., pp. 139-146.

FDOT (2010a). *FDOT Design Standards Specification*. Structures Design Office, Florida Department of Transportation, Tallahassee, FL.

FDOT (2010b). *FDOT Standard Specifications for Road and Bridge Construction*. Florida Department of Transportation, Tallahassee, FL.

FDOT (2012). *FDOT Structures Design Guidelines*. Structures Design Office, Florida Department of Transportation, Tallahassee, FL.

Gent, A. N. (2001). *Engineering with Rubber: How to Design Rubber Components*. 2nd Edition, Hanser Gardner Publications Inc., Cincinnati, OH.

Green, T., Yazdani, N., Spainhour, L., and Cai, S. C. (2001). “Effect of Bearing Stiffness and Skew Angle on Performance of Precast Concrete Bridges.” *Transportation Research Record: Journal of the Transportation Research Board*. No. 1770, Washington, D.C., pp. 27-33.

Hurff, J. B. (2010). *Stability of Precast Prestressed Concrete Bridge Girders Considering Imperfections and Thermal Effects*. Doctoral dissertation, School of Civil and Environmental Engineering, Georgia Institute of Technology, Atlanta, GA.

Kalkan, I. (2009). *Lateral Torsional Buckling of Rectangular Reinforced Concrete Beams*. Doctoral dissertation, School of Civil and Environmental Engineering, Georgia Institute of Technology, Atlanta, GA.

Lehman, D. E., Roeder, C. W., and Larsen, R. A. (2005). “Design of Cotton Duck Bridge Bearing Pads.” *Journal of Bridge Engineering*, American Society of Civil Engineers, Vol. 10, Issue 5, pp. 555-563.

Mast, R. F. (1989). “Lateral Stability of Long Prestressed Concrete Beams, Part 1.” *PCI Journal*, Vol. 34, No. 1, pp. 34-53.

Mast, R. F. (1993). “Lateral Stability of Long Prestressed Concrete Beams, Part 2.” *PCI Journal*, Vol. 38, No. 1, pp. 70-88.

Muscarella J. V., and Yura, J. A. (1995). *An Experimental Study of Elastomeric Bridge Bearings with Design Recommendations*. *FHWA/TX-98/1304-3*.

PCI (2003). *PCI Bridge Design Manual.* Precast/Prestressed Concrete Institute, Chicago, Illinois.

Stoddard, W. P. (1997). *Lateral-Torsional Buckling Behavior of Polymer Composite I-Shaped Members*. Doctoral dissertation, School of Civil and Environmental Engineering, Georgia Institute of Technology, Atlanta, GA.

Vidot-Vega, A. L., Possiel B., Robinson B., Kowalsky M. J., and Gabr M. A. (2009). “Evaluation of Rotational Stiffness of Elastomeric Bearing Pad-Anchor Bolt Connections on Deep Foundation Bents.” *Journal of Bridge Engineering*, American Society of Civil Engineers, Vol. 14, Issue 6, pp. 487-495.

Yarimci, E., Yura, J. A., and Lu, L. W. (1967). “Techniques for Testing Structures Permitted to Sway.” *Experimental Mechanics*, Vol. 7, No. 8, pp. 321-331.

Yazdani, N., Eddy, S., and Cai, C. (2000). “Effect of Bearing Pads on Precast Prestressed Concrete Bridges.” *Journal of Bridge Engineering*, American Society of Civil Engineers, Vol. 5, Issue 3, pp. 224-232.

Yura, J.A., Kumar, A., Yakut, A., Topkaya, C., Becker, E., and Collingwood, J. (2001). *NCHRP Report No. 449: Elastomeric Bridge Bearings: Recommended Test Methods*, Washington D.C.

Yura, J.A., and Phillips, B.A. (1992). *Bracing Requirements for Elastic Steel Beams.* Research Report 1239-1, Center for Transportation Research, The University of Texas, Austin, TX.

APPENDIX A
BEARING PAD TEST DEVICE FABRICATION PLANS

This appendix includes drawings for the fabrication of the bearing pad test device, used in the isolated roll stiffness tests.

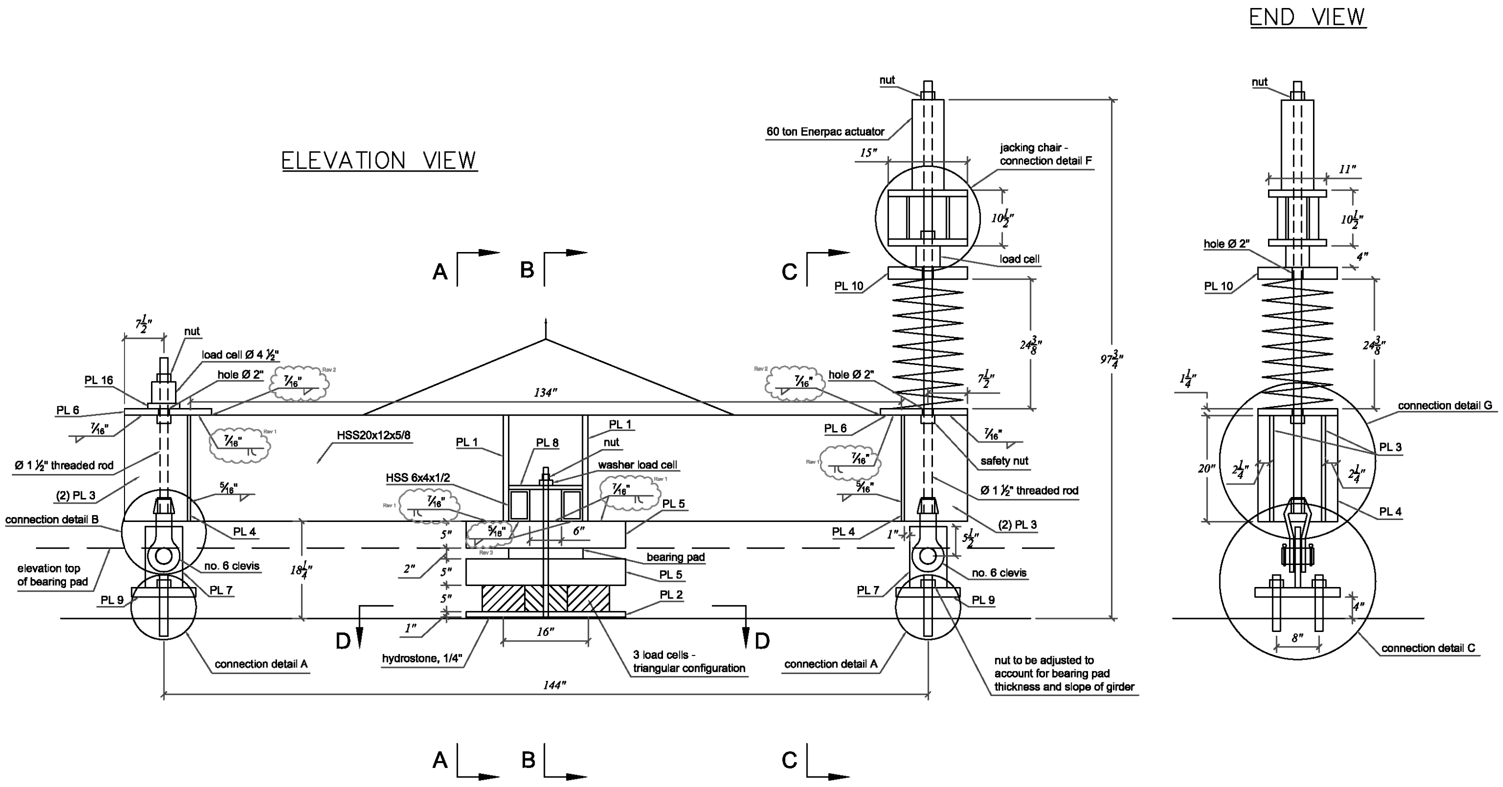

REVISIONS			Experimental Validation of Bracing Recommendations for Long-Span Concrete Girders		
Revision 1: 2009-07-29	*Revision 3: 2009-08-06*		*University of Florida*	*Bearing Pad Test Device*	*Sheet 1 of 5*
Revision 2: 2009-08-03					

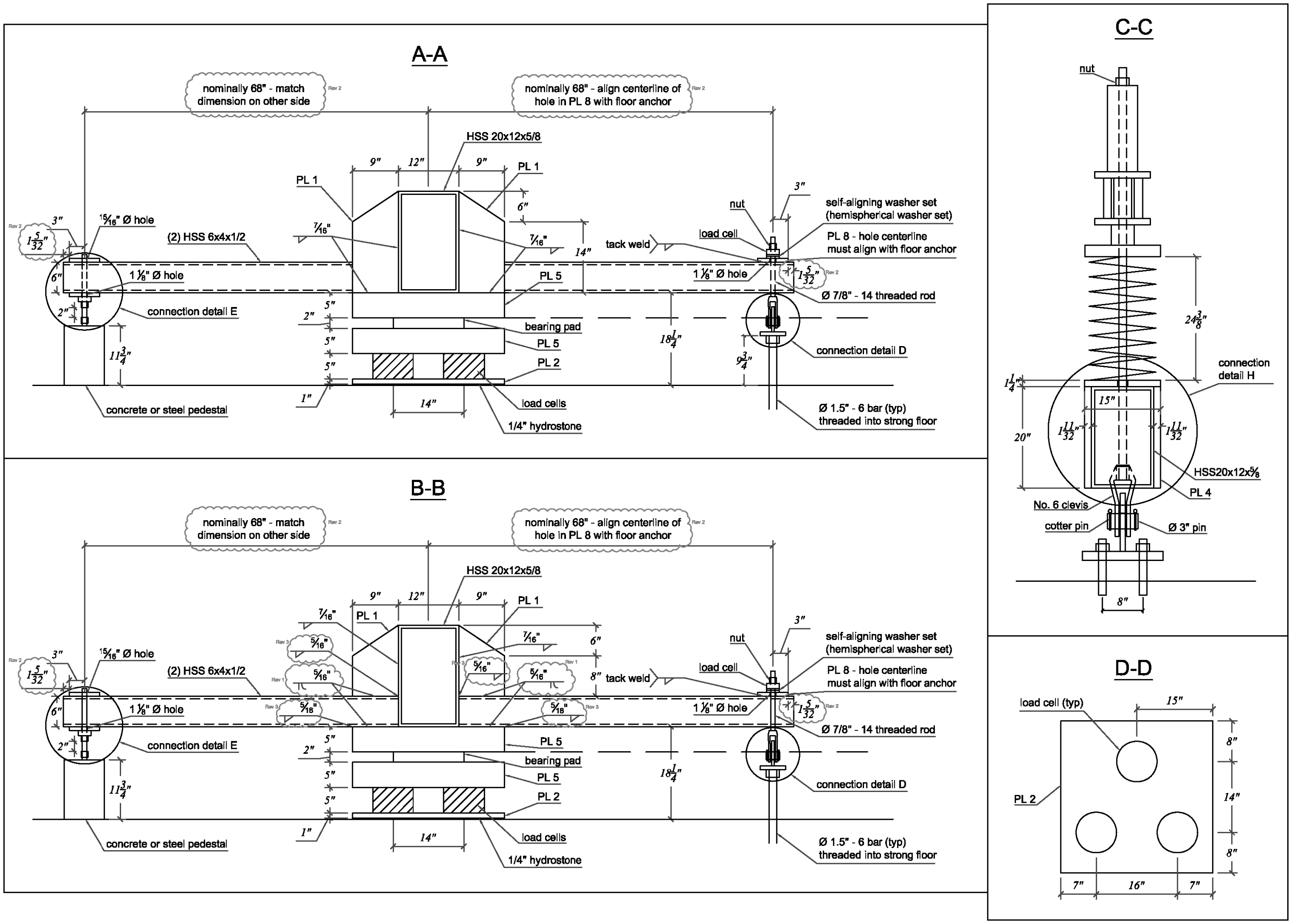

REVISIONS

Revision 1: 2009-07-29
Revision 2: 2009-08-03
Revision 3: 2009-08-06

Experimental Validation of Bracing Recommendations for Long-Span Concrete Girders

University of Florida

Bearing Pad Test Device

Sheet 2 of 5

Connection Detail A

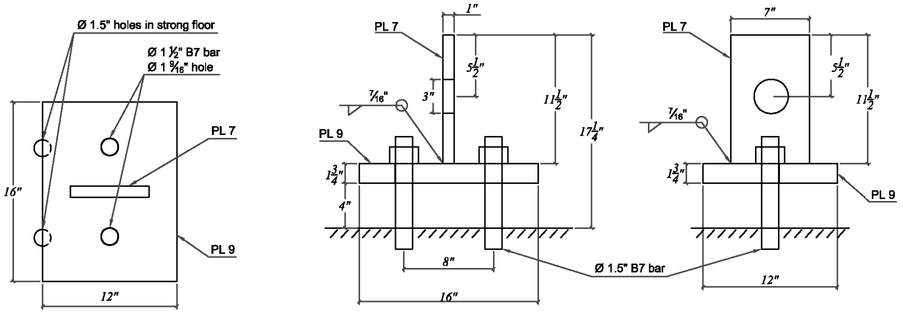

Connection Detail C

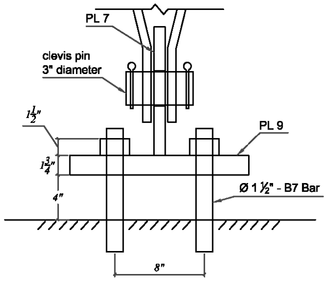

Connection Detail B

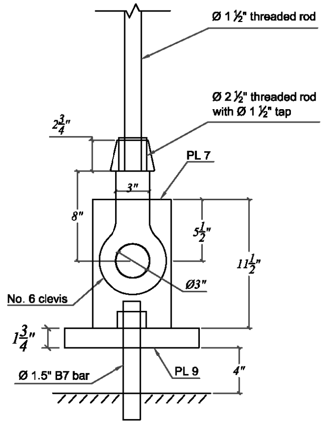

Connection Detail D

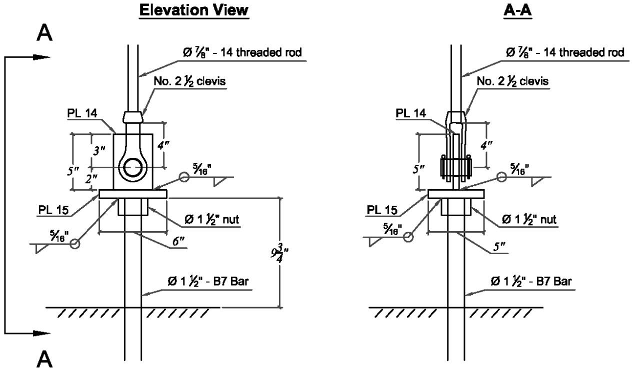

Connection Detail E

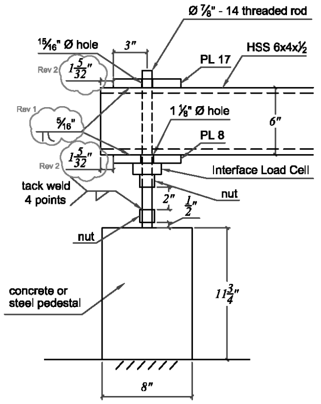

REVISIONS		
Revision 1: 2009-07-29	Revision 3: 2009-08-06	
Revision 2: 2009-08-03		

Experimental Validation of Bracing Recommendations for Long-Span Concrete Girders

University of Florida	*Bearing Pad Test Device*	*Sheet 3 of 5*

Connection Detail F - JACKING CHAIR

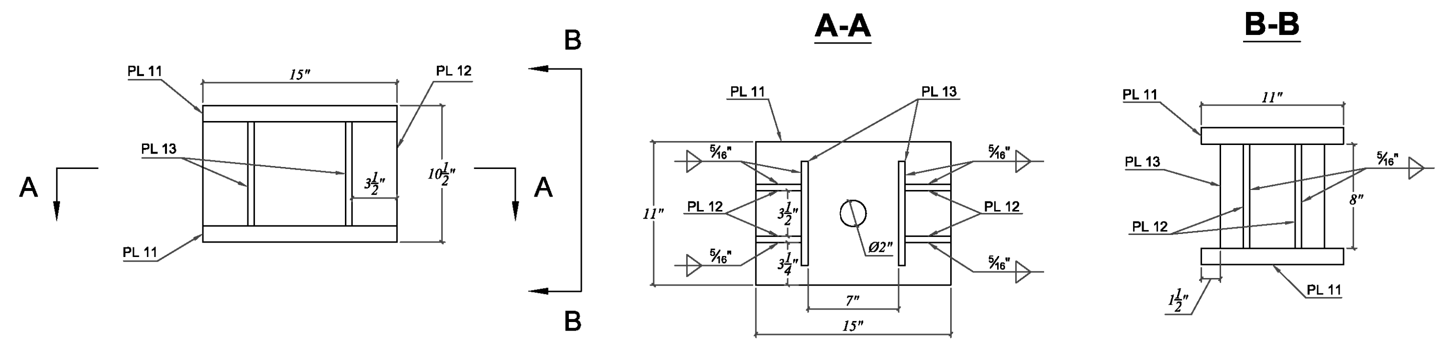

Connection Detail G

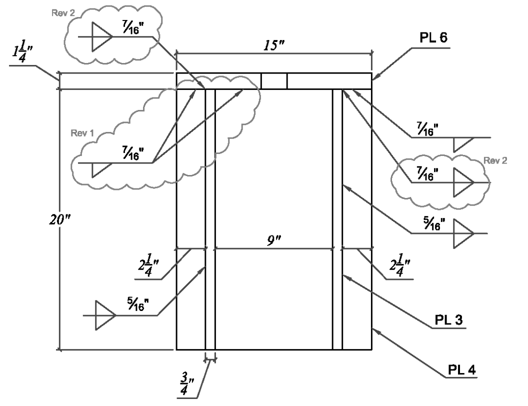

Connection Detail H

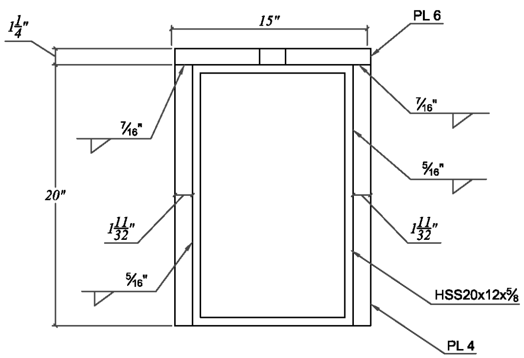

REVISIONS		
Revision 1: 2009-07-29	*Revision 3: 2009-08-06*	
Revision 2: 2009-08-03		

Experimental Validation of Bracing Recommendations for Long-Span Concrete Girders

University of Florida	*Bearing Pad Test Device*	*Sheet 4 of 5*

PLATE LIST

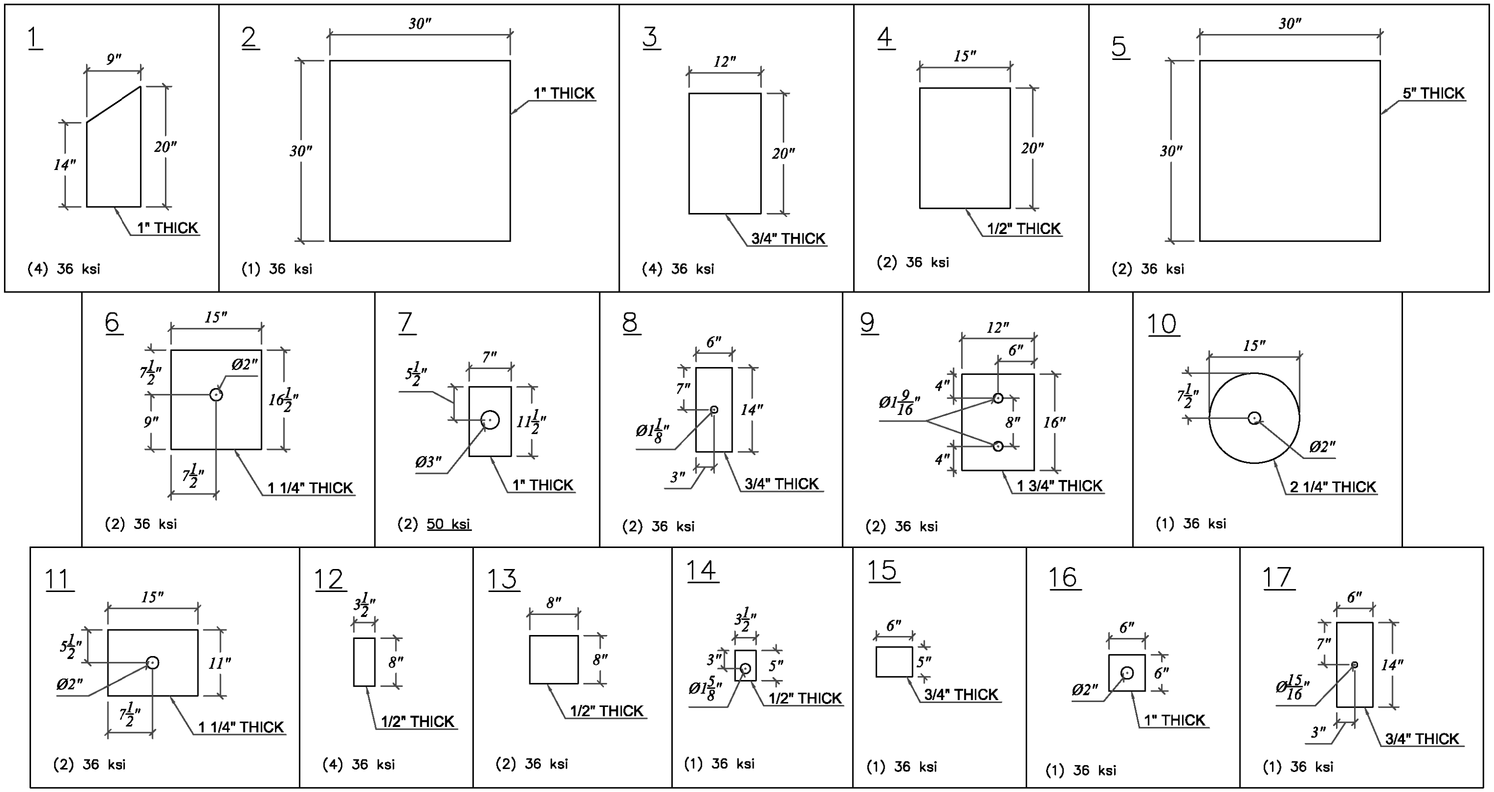

REVISIONS		
Revision 1: 2009-07-29	*Revision 3: 2009-08-06*	
Revision 2: 2009-08-03		

Experimental Validation of Bracing Recommendations for Long-Span Concrete Girders

University of Florida	*Bearing Pad Test Device*	*Sheet 5 of 5*

APPENDIX B
FULL-SCALE TEST GIRDER FABRICATION PLANS

This appendix includes drawings for the fabrication of the test girder, used in the full-scale buckling tests.

General Notes:

Materials

Concrete shall be FDOT class V, mix design number 05-1364
f'c (28 day) = 6,500 psi
fci (release) = 4,000 ksi

REV 2

The same concrete batch(s) shall be used for all three (3) specimens.

Mild reinforcement shall be ASTM A615 grade 60 (fy 60 ksi).

Prestressing strand shall be ASTM A416 270 ksi Lo-Lax.

Fabricator shall provide data sheets from concrete, strand, and rebar suppliers.

Fabricator shall provide report of strand stressing.

Fabricator shall provide material samples to UF/FDOT as follows:

(8) 6" dia x 12" cylinders from each concrete batch: (4) cylinders cure with girder, (4) lab cure

(8) 36" pieces of prestressing strands free from sand, dust, etc.
Samples taken directly off of reel

Schedule

REV 2

Fabrication schedule to be determined.

Contact Megan Salvetti at UF at least one (1) week prior to stress, casting, detensioning, and shipping: 561-866-2531 or meg8253@ufl.edu.

Other

Fabricator shall be responsible for fabrication of "precast segments". Fabricator will transport these three (3) segments from the fabrication facility to:
FDOT Structures Research Center
2007 East Paul Dirac Drive
Tallahassee, FL 32310

Delivery time to be coordinated with FDOT.

Upon completion and delivery of "precast segments" by Fabricator, FDOT shall fabricate "closure pours (CP)" and "solid end blocks (EB)".

Unless otherwise noted, fabrication of girders shall follow typical procedures and practices for FDOT bridge girders.

Cover beams with heavy tarp during curing.

Inspections will be provided by on-site FDOT personnel and by UF.

No patch-work or finishing is required.

Production:
Contact Megan Salvetti
(561) 866-2531
at least one (1) week prior to
stressing, casting, detensioning,
and shipping

Contact: Megan Salvetti meg8253@ufl.edu 561-866-2531				*Revisions:*	*REV 1 : 2011-01-03*	
					REV 2 : 2011-02-23	
General notes	*2011-06-24*	*University of Florida*	*Sheet 01 of 10*		*REV 3 : 2011-06-24*	

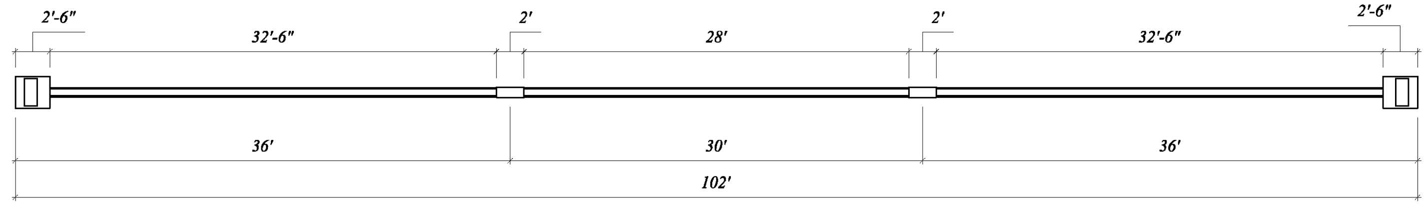

PLAN VIEW

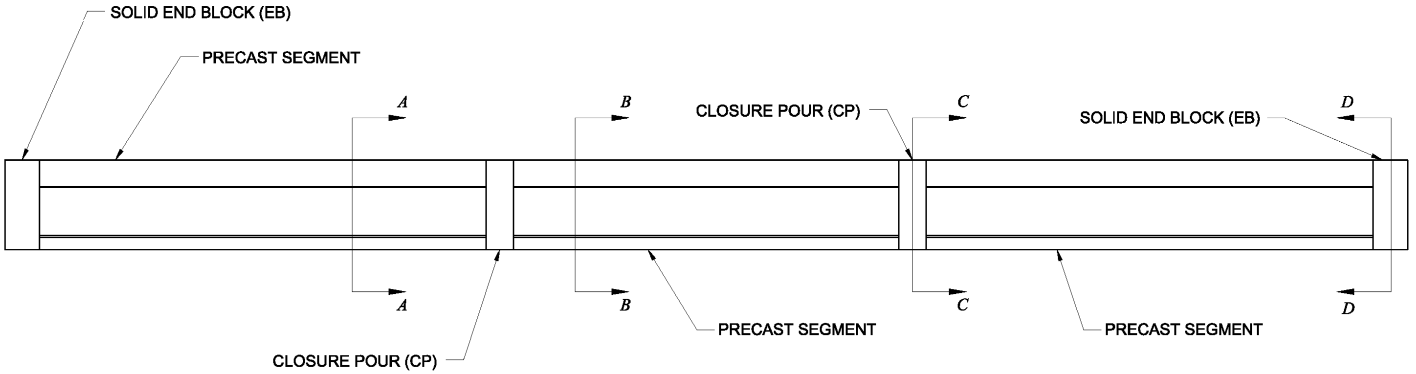

ELEVATION VIEW

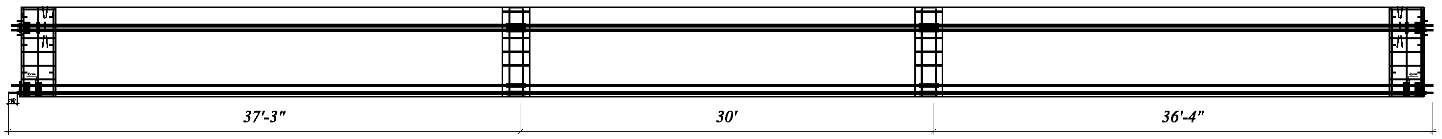

ELEVATION VIEW - POST-TENSION LENGTHS
MILD REINFORCEMENT OMMITED IN PRECAST SEGMENTS FOR CLARITY

SCALE: $^3/_{32}$" = 1'-0"

REV 2

Contact: Megan Salvetti meg8253@ufl.edu 561-866-2531				*Revisions:*	*REV 1 : 2011-01-03*
					REV 2 : 2011-02-23
Test girder	*2011-06-24*	*University of Florida*	*Sheet 02 of 10*		*REV 3 : 2011-06-24*

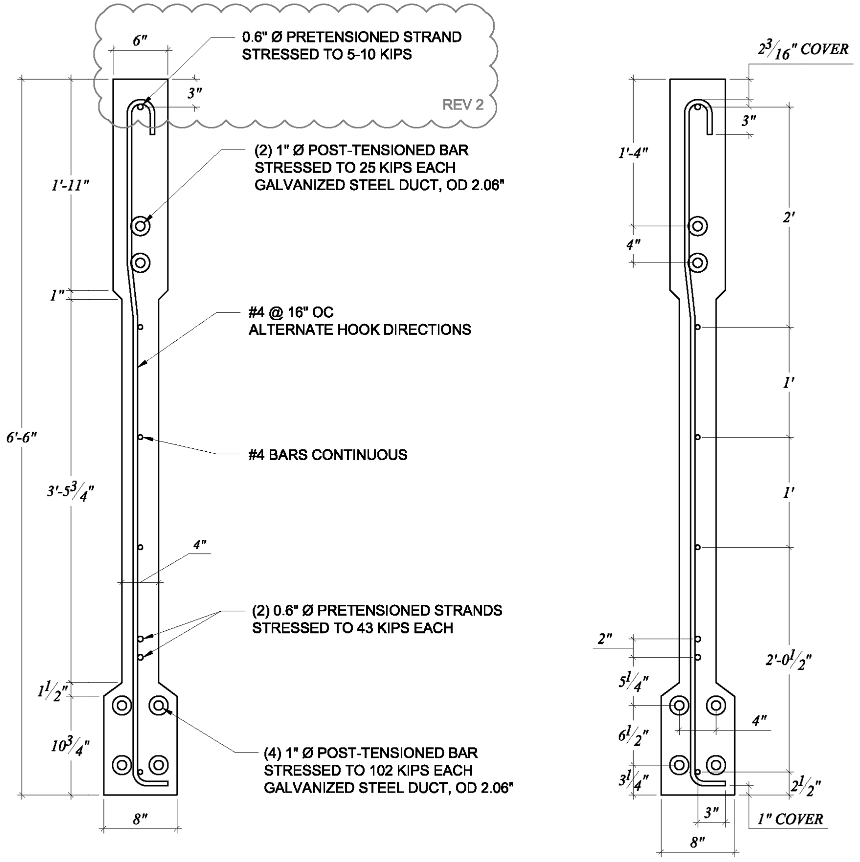

SECTION A-A DETAILS
EXTERIOR PRECAST SEGMENT

SCALE: ¾"=1'-0"

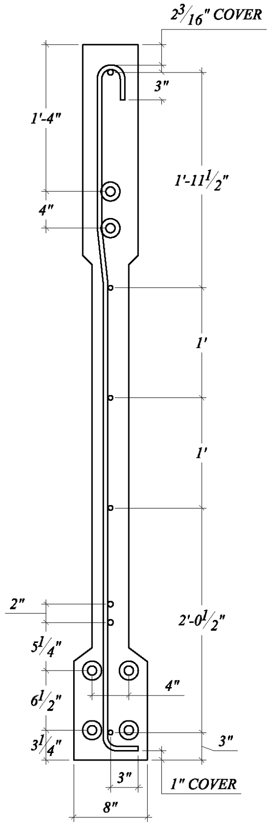

SECTION B-B DETAILS
INTERIOR PRECAST SEGMENT

SCALE: ¾"=1'-0"

REV 2

Contact: Megan Salvetti meg8253@ufl.edu 561-866-2531				Revisions:	REV 1 : 2011-01-03 REV 2 : 2011-02-23 REV 3 : 2011-06-24
Precast segment details	2011-06-24	University of Florida	Sheet 03 of 10		

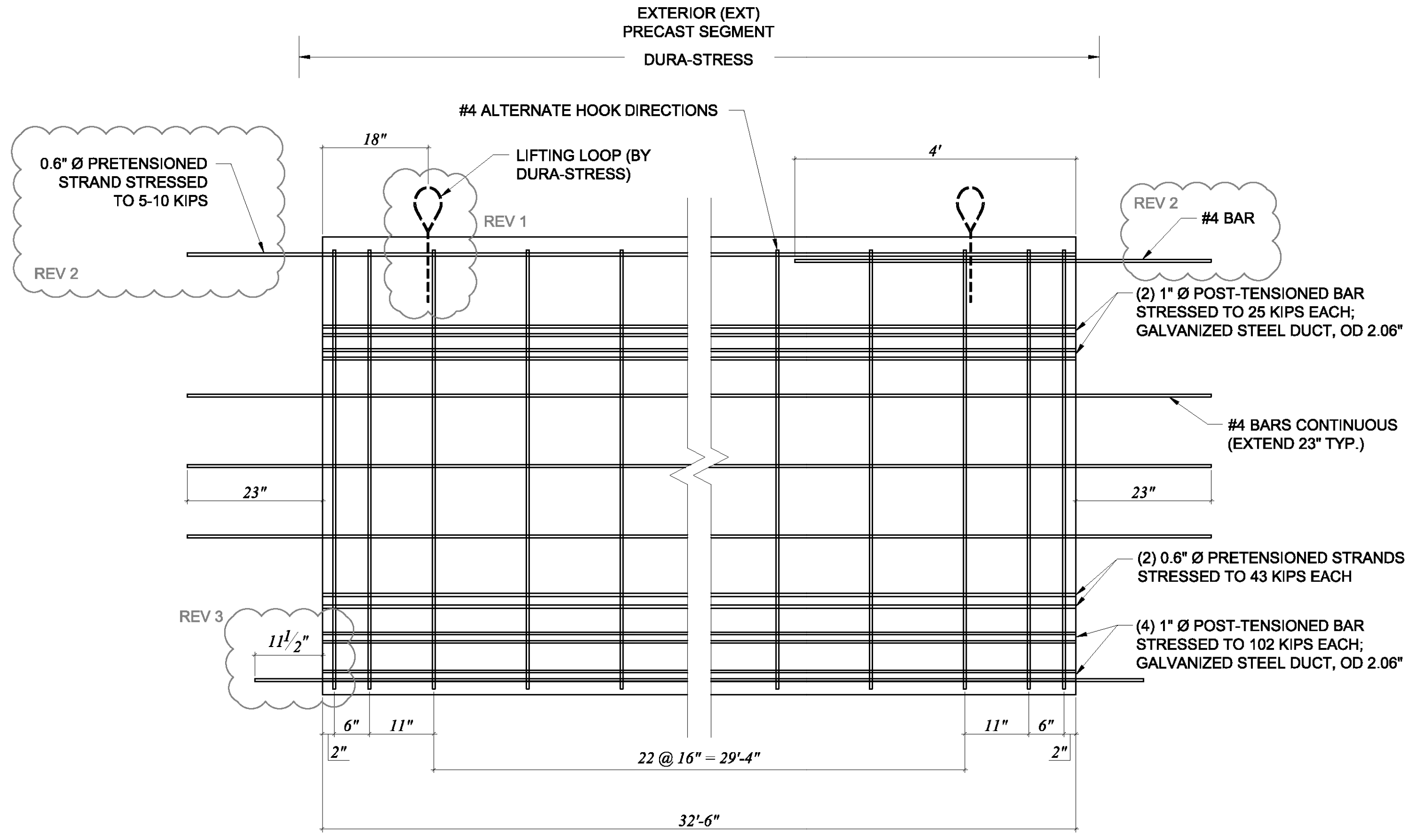

EXTERIOR PRECAST SEGMENT - ELEVATION
REINFORCEMENT DETAILS

SCALE: $\frac{1}{2}$"=1'-0"

Contact: Megan Salvetti meg8253@ufl.edu 561-866-2531				*Revisions:*	*REV 1 : 2011-01-03*
					REV 2 : 2011-02-23
Exterior precast segment details	*2011-06-24*	*University of Florida*	*Sheet 04 of 10*		*REV 3 : 2011-06-24*

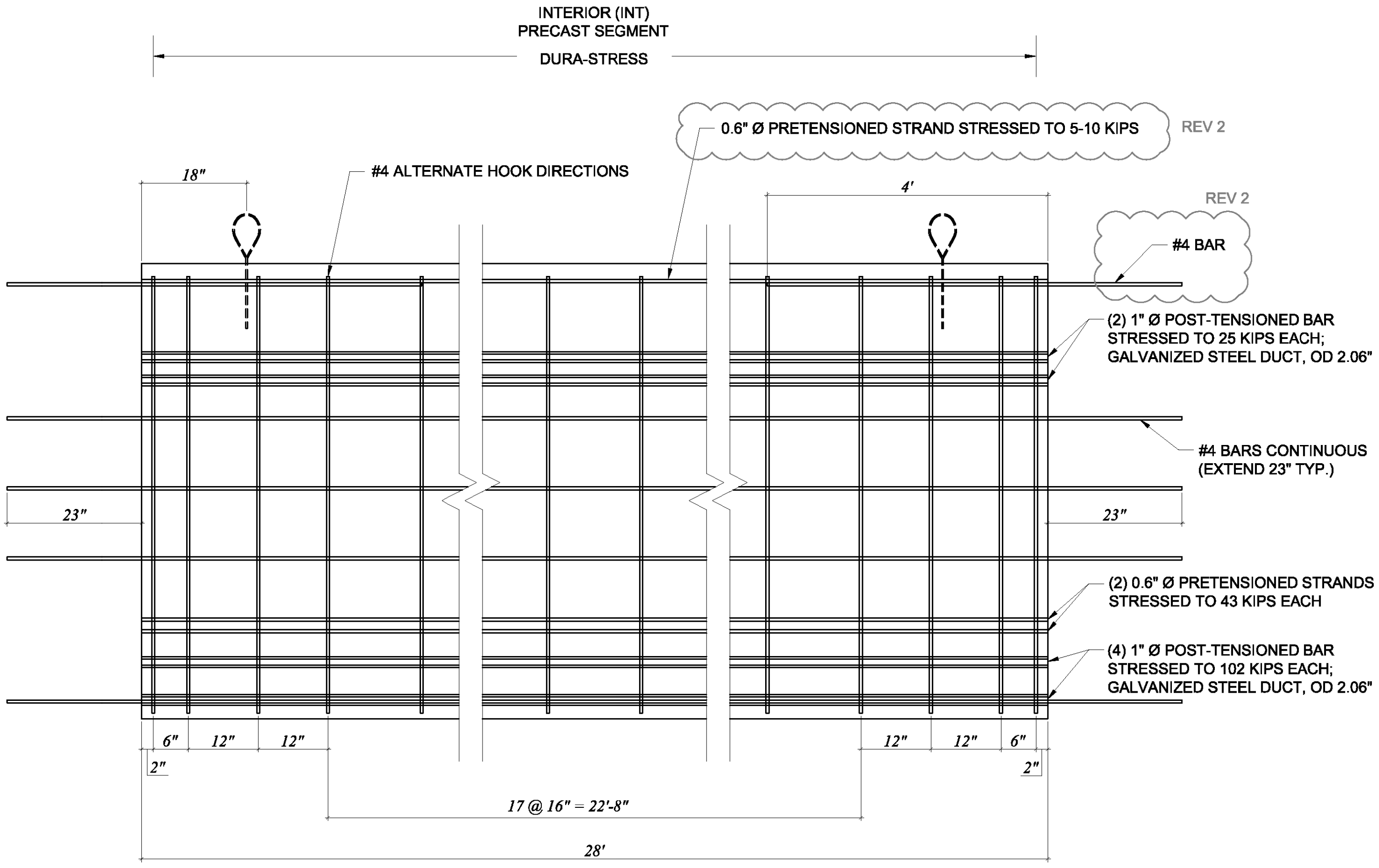

INTERIOR PRECAST SEGMENT - ELEVATION
REINFORCEMENT DETAILS

SCALE: ½"=1'-0"

Contact: Megan Salvetti meg8253@ufl.edu 561-866-2531				*Revisions:*	*REV 1 : 2011-01-03*	
					REV 2 : 2011-02-23	
Interior precast segment details	*2011-06-24*	*University of Florida*	*Sheet 05 of 10*		*REV 3 : 2011-06-24*	

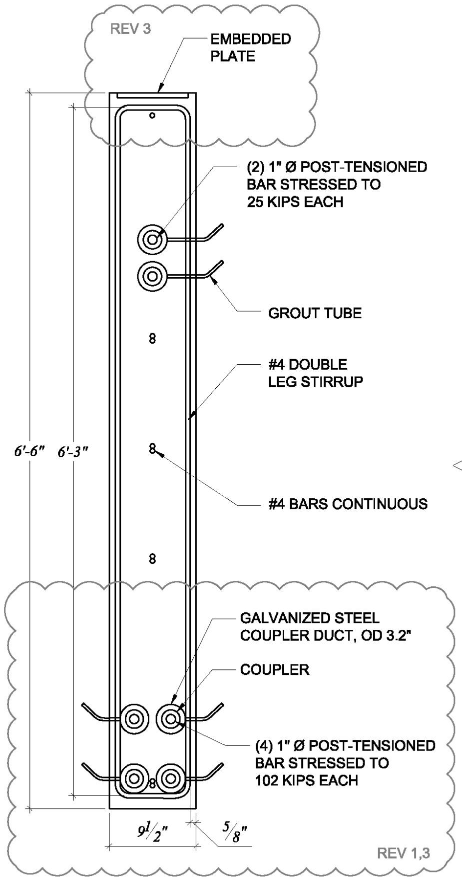

SECTION C-C DETAILS
(CLOSURE POUR - CP)

SCALE: ¾"=1'-0"

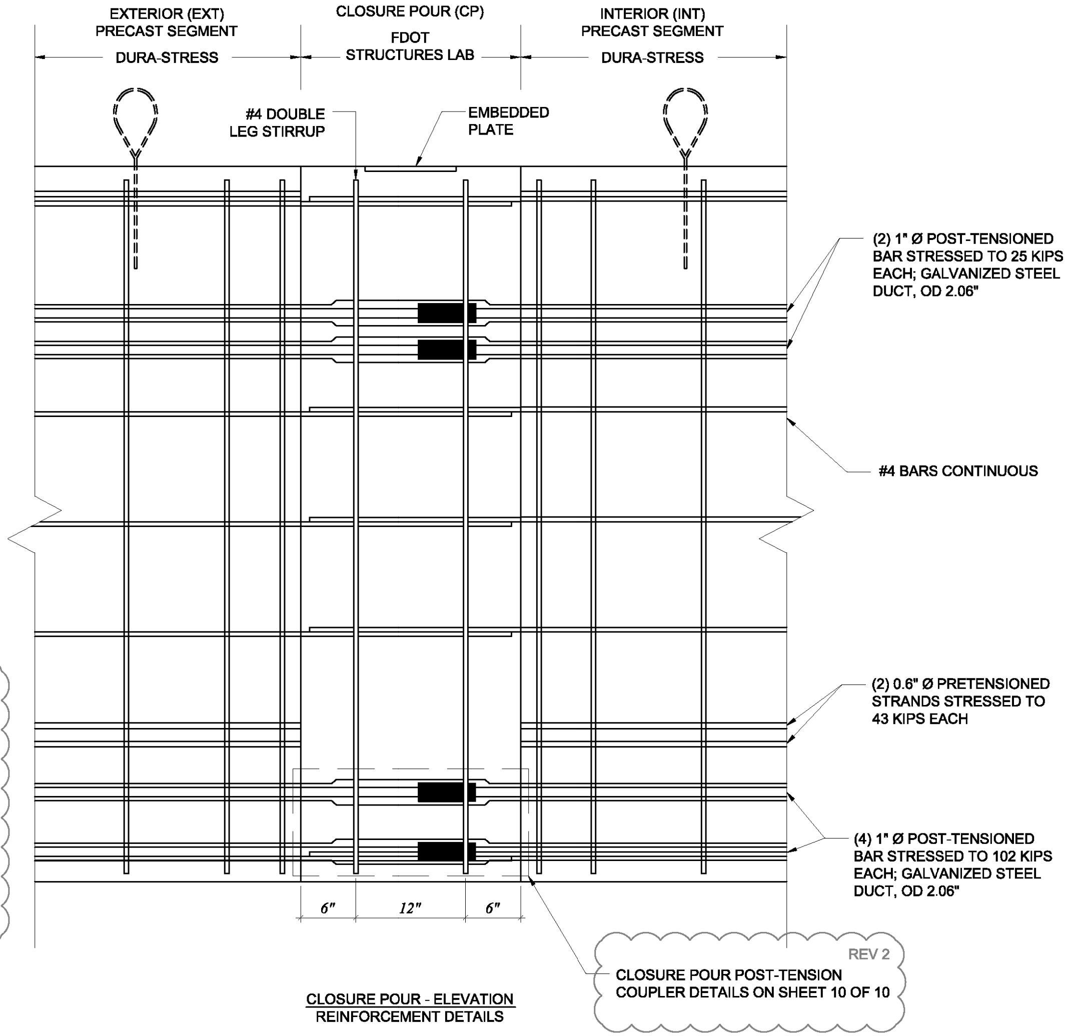

CLOSURE POUR - ELEVATION
REINFORCEMENT DETAILS

SCALE: ¾"=1'-0"

Contact: Megan Salvetti meg8253@ufl.edu 561-866-2531				*Revisions:*	*REV 1 : 2011-01-03*	
Closure pour details	*2011-06-24*	*University of Florida*	*Sheet 06 of 10*		*REV 2 : 2011-02-23*	
					REV 3 : 2011-06-24	

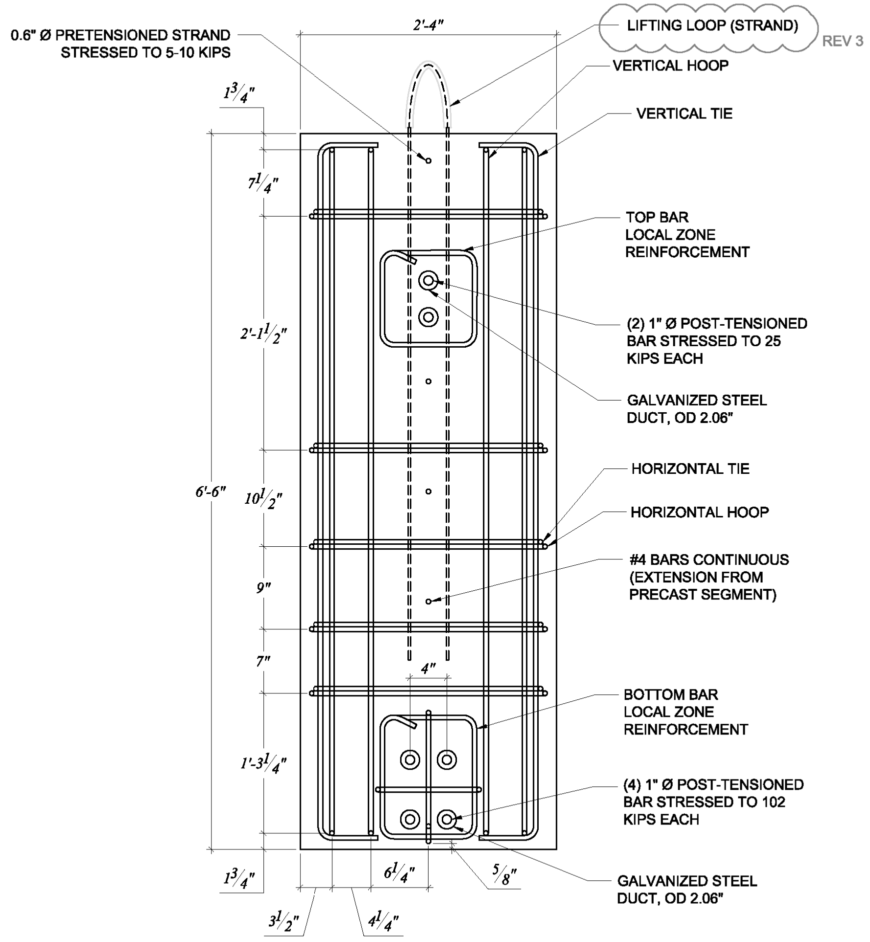

SECTION D-D
(SOLID END BLOCK - EB)

SCALE: 3/4"=1'-0"

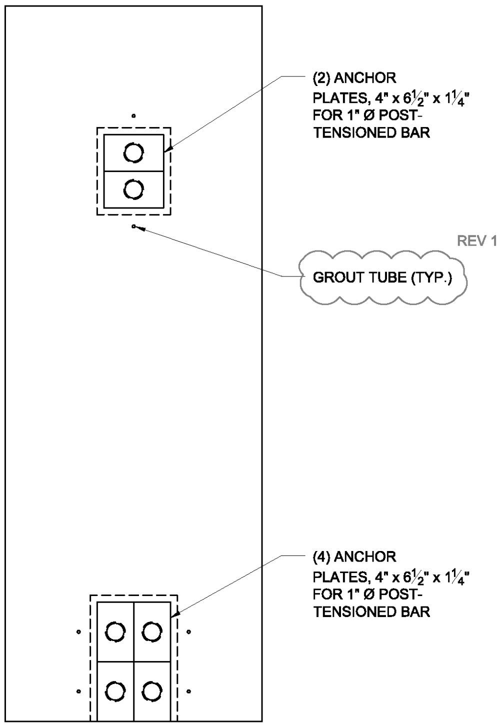

END ELEVATION
(SOLID END BLOCK - EB)

SCALE: 3/4"=1'-0"

NOTES:
1. ALL END BLOCK MILD REINFORCEMENT IS DETAILED ON SHEET 9 OF 10.
2. ALL MILD REINFORCEMENT IS BAR SIZE #4.
3. ALL CONCRETE COVER IS 1" OR GREATER UNLESS OTHERWISE NOTED.

Contact: Megan Salvetti meg8253@ufl.edu 561-866-2531				*Revisions:*	*REV 1 : 2011-01-03*
					REV 2 : 2011-02-23
REV 3 *End block details*	*2011-06-24*	*University of Florida*	*Sheet 07 of 10*		*REV 3 : 2011-06-24*

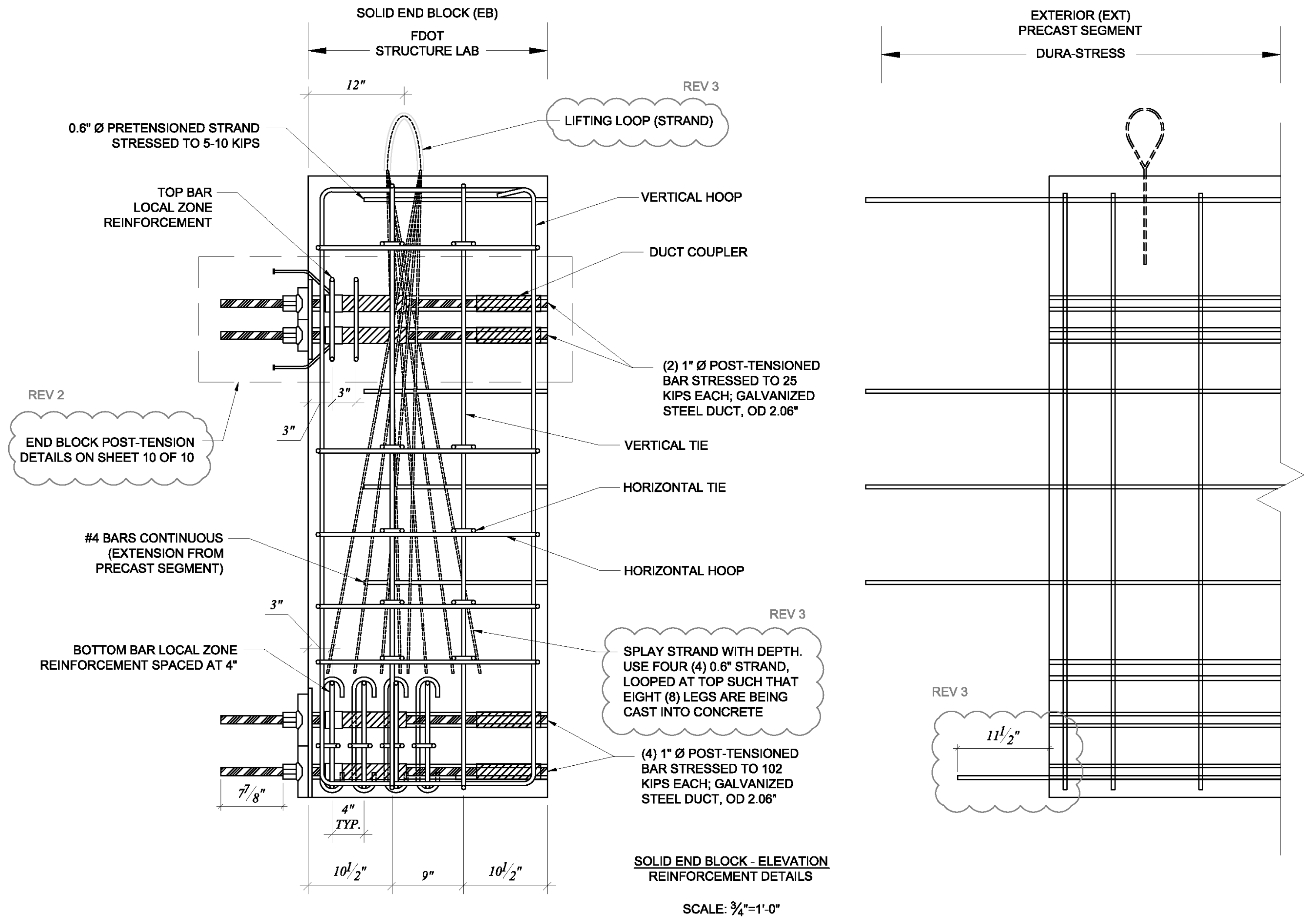

SOLID END BLOCK - ELEVATION
REINFORCEMENT DETAILS

SCALE: $\frac{3}{4}$"=1'-0"

Contact: Megan Salvetti meg8253@ufl.edu 561-866-2531

REV 3 *End block details*	*2011-06-24*	*University of Florida*	*Sheet 08 of 10*	*Revisions:*	*REV 1 : 2011-01-03* *REV 2 : 2011-02-23* *REV 3 : 2011-06-24*

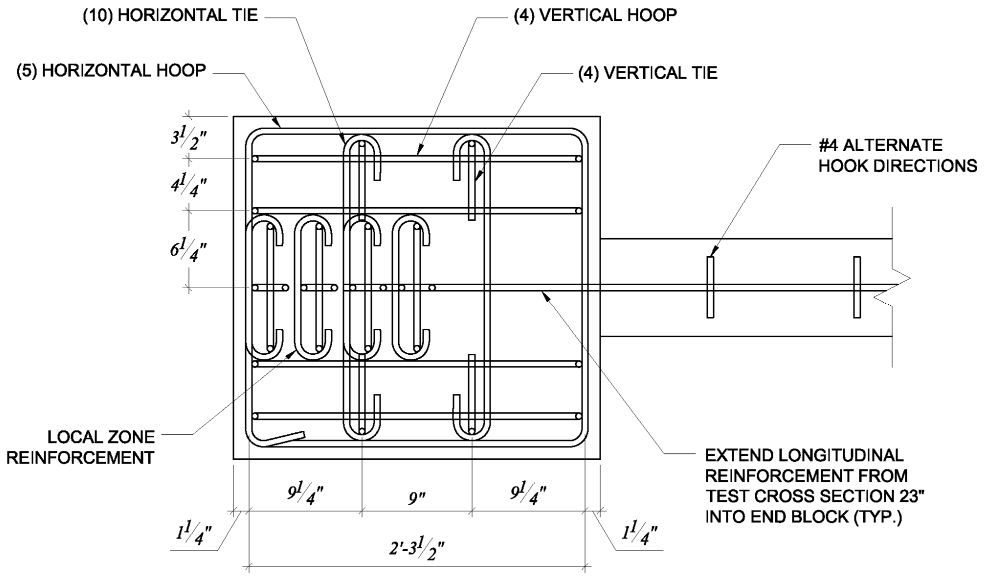

END BLOCK TO PRECAST SEGMENT CONNECTION - PLAN VIEW
ALL BARS ARE SIZE #4. PRETENSIONED STRANDS AND POST-TENSIONED BARS NOT SHOWN FOR CLARITY.

SCALE: 1"=1'-0"

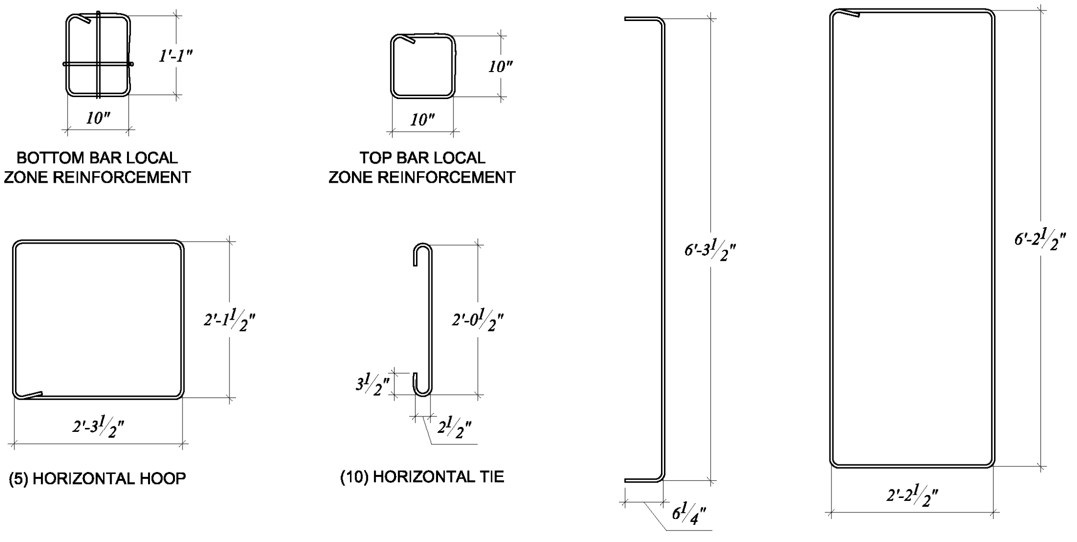

BOTTOM BAR LOCAL ZONE REINFORCEMENT

TOP BAR LOCAL ZONE REINFORCEMENT

(5) HORIZONTAL HOOP

(10) HORIZONTAL TIE

(4) VERTICAL TIE

(4) VERTICAL HOOP

END BLOCK REINFORCEMENT DETAILS
ALL BARS ARE SIZE #4
SCALE: ½"=1'-0"

Contact: Megan Salvetti meg8253@ufl.edu 561-866-2531

REV 3 *End block reinforcement details*	*2011-06-22*	*University of Florida*	*Sheet 9 of 10*
Revisions:	*REV 1 : 2011-01-03*	*REV 2 : 2011-02-23*	*REV 3 : 2011-06-24*

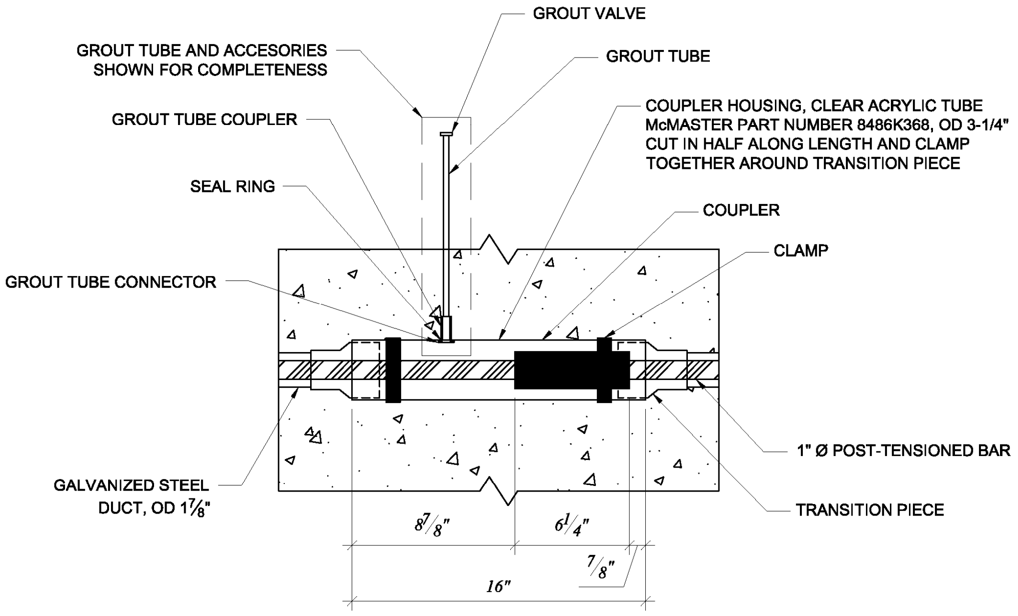

CLOSURE POUR - POST-TENSION DETAILS
MILD REINFORCEMENT NOT SHOWN FOR CLARITY
SCALE: 1½"=1'-0"

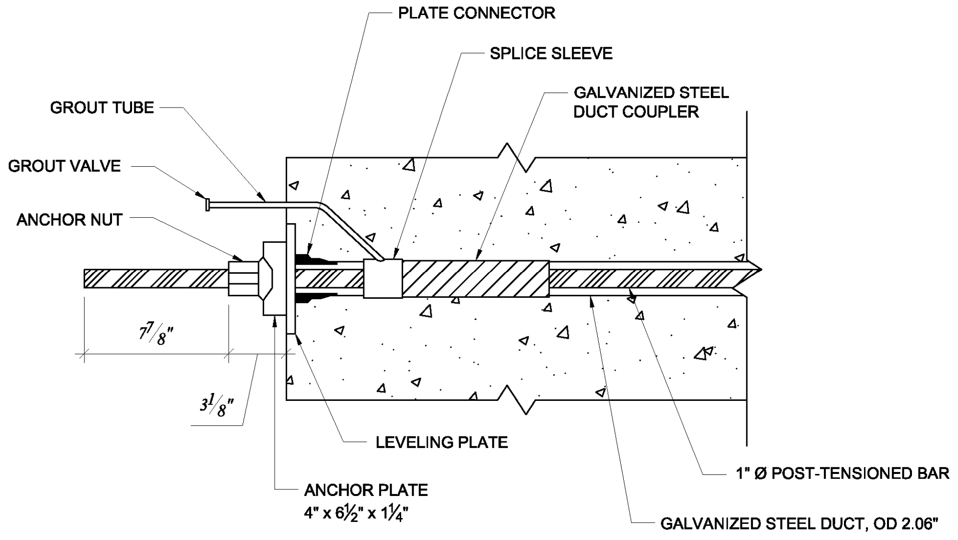

SOLID END BLOCK - POST-TENSION DETAILS
MILD REINFORCEMENT NOT SHOWN FOR CLARITY
SCALE: 1½"=1'-0"

Contact: Megan Salvetti meg8253@ufl.edu 561-866-2531

Post-tension connection details	*2011-06-22*	*University of Florida*	*Sheet 10 of 10*

Revisions:	*REV 1 : 2011-01-03*	*REV 2 : 2011-02-23*	*REV 3 : 2011-06-24*	

APPENDIX C
COMPRESSIVE STRENGTH AND ELASTIC MODULUS TEST RESULTS

This appendix includes the compressive strength and elastic modulus test results, from cylinders cast from the test girder, used in the full-scale buckling tests.

Table C.1. Compressive strength test results performed for each girder component

Date poured	Batch	Curing	Date tested	Age (days)	Fracture type	Compressive strength (psi)
5/18/2011	Precast segment: Exterior A	moist	28 day	28	-	7540
		moist	9/19/2011	124	1	8828
		moist	12/8/2011	204	4	7564
		moist	12/8/2011	204	1	-
		field	*12/8/2011*	*204*	*4*	*6368*
		field	*12/8/2011*	*204*	*4*	*6131*
		field	*12/8/2011*	*204*	*4*	*6514*
5/19/2011	Precast segment: Exterior B	moist	28 day	28	-	7720
		moist	9/19/2011	123	1,2	9154
		moist	12/8/2011	203	4	8160
		moist	12/8/2011	203	1	8238
		field	*12/8/2011*	*203*	*4*	*5956*
		field	*12/8/2011*	*203*	*4*	*5680*
		field	*12/8/2011*	*203*	*1*	*5858*
5/23/2011	Precast segment: Interior	moist	28 day	28	-	8070
		moist	9/19/2011	119	1,2	9004
		moist	12/8/2011	199	irregular	6646
		moist	12/8/2011	199	4	8088
		field	*12/8/2011*	*199*	*4*	*6348*
		field	*12/8/2011*	*199*	*4*	*7855*
		field	*12/8/2011*	*199*	*4*	*7223*

8/26/2011	South end block	moist	9/13/2011	18	4	8812
		moist	9/13/2011	18	4	8806
		moist	12/8/2011	104	1	9060
		moist	12/8/2011	104	1	9514
		moist	12/8/2011	104	4	8783
		field	*12/8/2011*	*104*	*4*	*7693*
		field	*12/8/2011*	*104*	*1*	*7335*
8/30/2011	North end block	moist	9/13/2011	14	4	8346
		moist	9/13/2011	14	4	8154
		moist	12/8/2011	100	1	9490
		moist	12/8/2011	100	1	8808
		moist	12/8/2011	100	1	10016
		field	*12/8/2011*	*100*	*1*	*7082*
8/30/2011	Closure pours	moist	9/13/2011	14	4	6124
		moist	9/13/2011	14	4	6322
		moist	12/8/2011	100	1	8292
		moist	12/8/2011	100	4	7366
		moist	12/8/2011	100	irregular	7090
		field	*12/8/2011*	*100*	*4*	*5264*

Table C.2. Elastic modulus test results performed for each girder component

Date poured	Batch	Curing	Date tested	Age (days)	Poisson's ratio	Modulus of Elasticity (ksi)
5/18/2011	Precast	moist	12/9/2011	205	0.34	5450

	segment: Exterior A	moist	12/9/2011	205	0.31	5000
		moist	12/9/2011	205	0.23	5000
		field	12/9/2011	*205*	0.27	4550
		field	12/9/2011	*205*	0.28	4750
		field	12/9/2011	*205*	0.27	4550
5/19/2011	Precast segment: Exterior B	moist	12/9/2011	205	0.32	5600
		moist	12/9/2011	205	0.2	5000
		moist	12/9/2011	205	0.3	5000
		field	12/9/2011	*205*	*0.31*	*4650*
		field	12/9/2011	*205*	*0.31*	*4950*
		field	12/9/2011	*205*	*0.29*	*4700*
5/23/2011	Precast segment: Interior	moist	12/12/2011	208	0.27	5000
		moist	12/12/2011	208	0.27	5050
		moist	12/12/2011	208	0.27	5150
		field	12/9/2011	*205*	*0.32*	*5050*
		field	12/9/2011	*205*	*0.28*	*5000*
		field	12/9/2011	*205*	*0.27*	*4750*
8/26/2011	South end block	moist	12/12/2011	208	0.27	5500
		moist	12/12/2011	208	0.27	5250
		moist	12/12/2011	208	0.28	5400
		field	12/9/2011	*205*	*0.25*	*4600*
		field	12/9/2011	*205*	*0.25*	*4950*
		field	12/9/2011	*205*	*0.27*	*5000*
8/30/2011	North end	moist	12/12/2011	208	0.27	5000

	block	moist	12/12/2011	208	0.31	5050
		moist	12/12/2011	208	0.26	5000
		field	12/9/2011	*205*	*0.27*	*4300*
		field	12/9/2011	*205*	*0.26*	*4250*
		field	12/9/2011	*205*	*0.26*	*4150*
8/30/2011	Closure pours	moist	12/12/2011	208	0.25	4600
		moist	12/12/2011	208	0.28	5050
		moist	12/12/2011	208	0.31	4600
		field	12/9/2011	*205*	*0.27*	*3700*
		field	12/9/2011	*205*	*0.26*	*3700*
		field	12/9/2011	*205*	*0.25*	*3500*

APPENDIX D
DYWIDAG JACK CALIBRATION FORM

This appendix includes the DYWIDAG jack calibration form, used to determine the prestress levels in the post-tensioned bars, in the full-scale buckling tests.

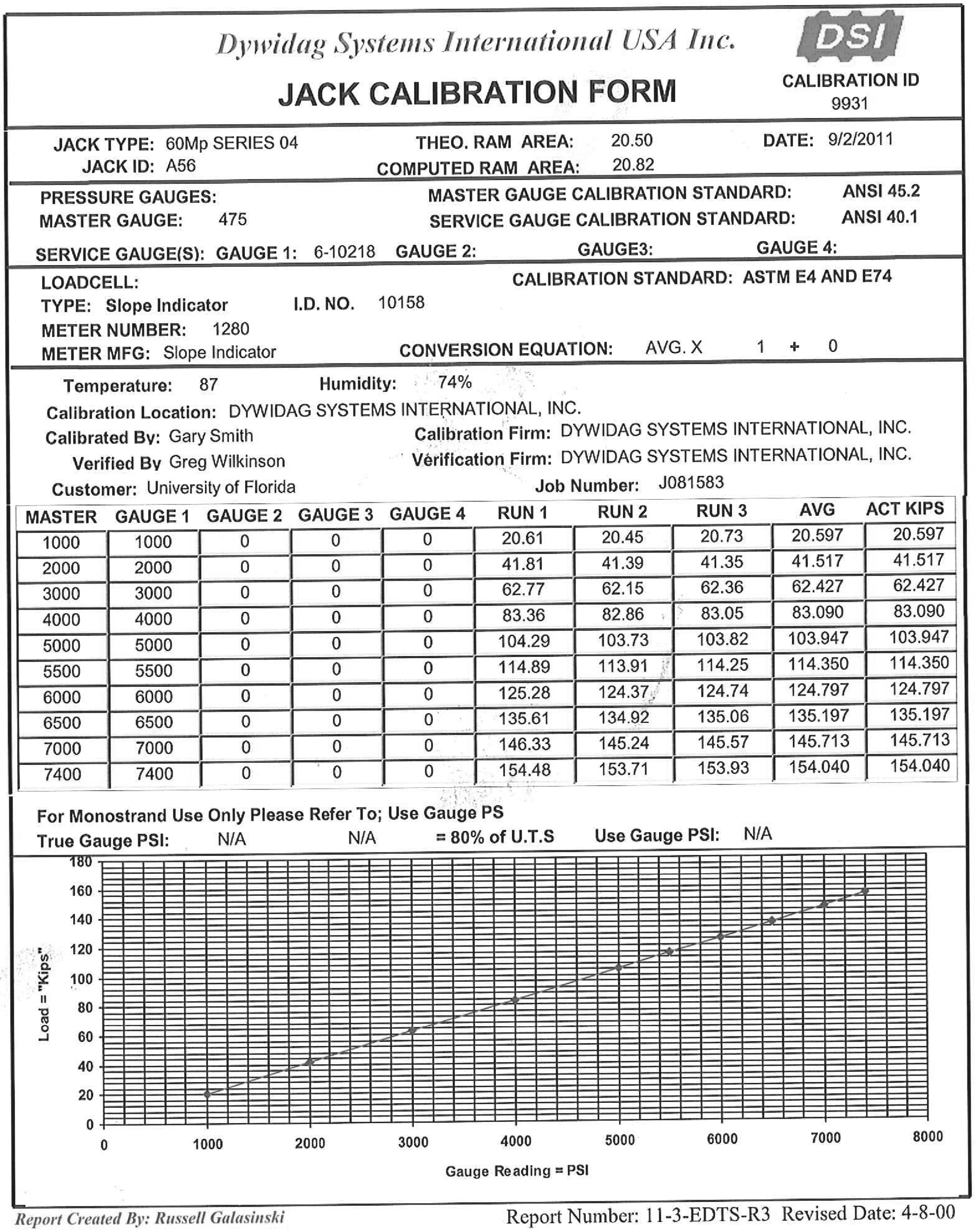

Dywidag Systems International USA Inc.

DSI

JACK CALIBRATION FORM

CALIBRATION ID
9931

JACK TYPE: 60Mp SERIES 04
JACK ID: A56
THEO. RAM AREA: 20.50
COMPUTED RAM AREA: 20.82
DATE: 9/2/2011

PRESSURE GAUGES:
MASTER GAUGE: 475
MASTER GAUGE CALIBRATION STANDARD: ANSI 45.2
SERVICE GAUGE CALIBRATION STANDARD: ANSI 40.1

SERVICE GAUGE(S): GAUGE 1: 6-10218 **GAUGE 2:** **GAUGE3:** **GAUGE 4:**

LOADCELL:
CALIBRATION STANDARD: ASTM E4 AND E74
TYPE: Slope Indicator **I.D. NO.** 10158
METER NUMBER: 1280
METER MFG: Slope Indicator
CONVERSION EQUATION: AVG. X 1 + 0

Temperature: 87 **Humidity:** 74%
Calibration Location: DYWIDAG SYSTEMS INTERNATIONAL, INC.
Calibrated By: Gary Smith **Calibration Firm:** DYWIDAG SYSTEMS INTERNATIONAL, INC.
Verified By Greg Wilkinson **Verification Firm:** DYWIDAG SYSTEMS INTERNATIONAL, INC.
Customer: University of Florida **Job Number:** J081583

MASTER	GAUGE 1	GAUGE 2	GAUGE 3	GAUGE 4	RUN 1	RUN 2	RUN 3	AVG	ACT KIPS
1000	1000	0	0	0	20.61	20.45	20.73	20.597	20.597
2000	2000	0	0	0	41.81	41.39	41.35	41.517	41.517
3000	3000	0	0	0	62.77	62.15	62.36	62.427	62.427
4000	4000	0	0	0	83.36	82.86	83.05	83.090	83.090
5000	5000	0	0	0	104.29	103.73	103.82	103.947	103.947
5500	5500	0	0	0	114.89	113.91	114.25	114.350	114.350
6000	6000	0	0	0	125.28	124.37	124.74	124.797	124.797
6500	6500	0	0	0	135.61	134.92	135.06	135.197	135.197
7000	7000	0	0	0	146.33	145.24	145.57	145.713	145.713
7400	7400	0	0	0	154.48	153.71	153.93	154.040	154.040

For Monostrand Use Only Please Refer To; Use Gauge PS
True Gauge PSI: N/A N/A **= 80% of U.T.S** **Use Gauge PSI:** N/A

Report Created By: Russell Galasinski

Report Number: 11-3-EDTS-R3 Revised Date: 4-8-00

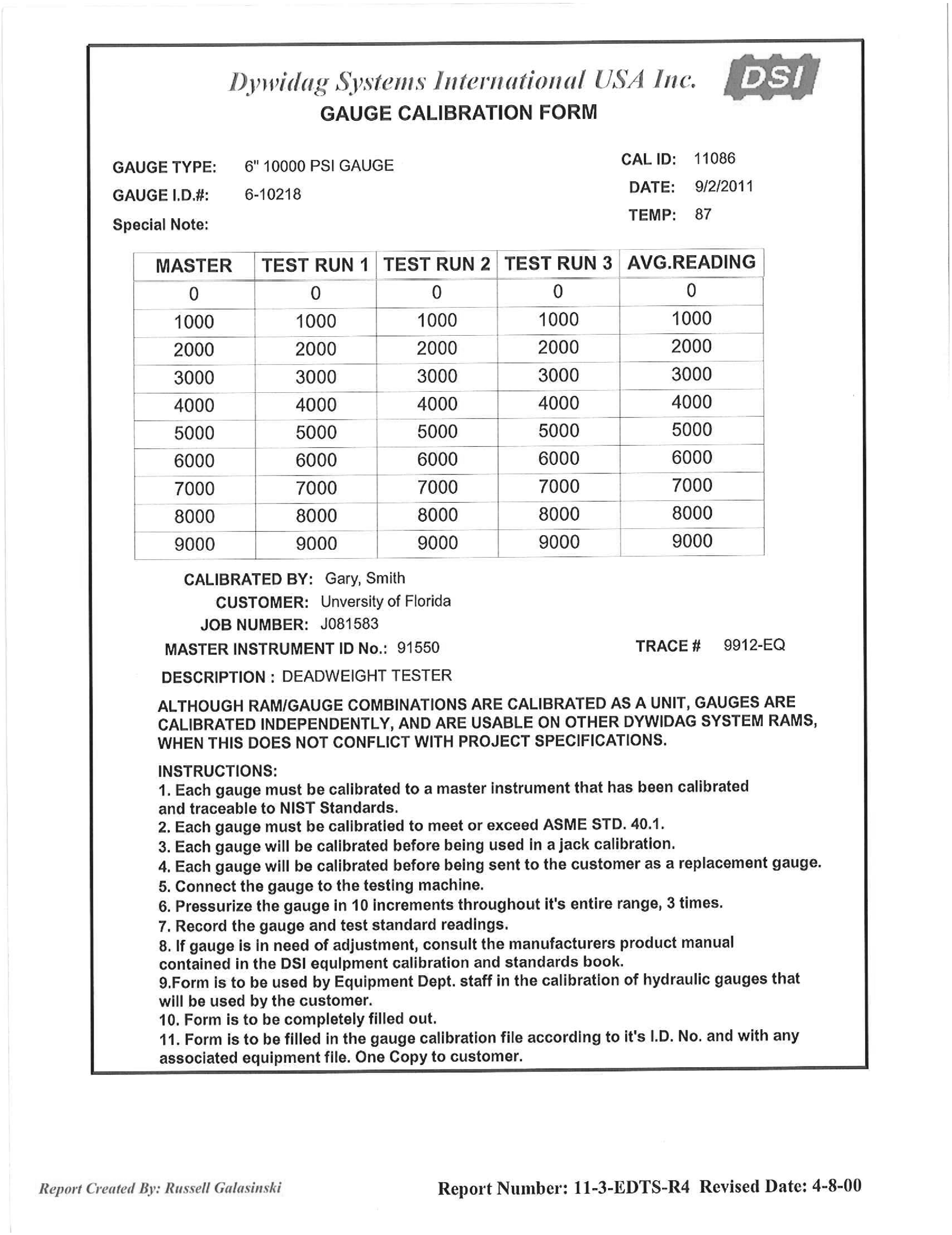

Dywidag Systems International USA Inc. DSI

GAUGE CALIBRATION FORM

GAUGE TYPE: 6" 10000 PSI GAUGE

GAUGE I.D.#: 6-10218

Special Note:

CAL ID: 11086

DATE: 9/2/2011

TEMP: 87

MASTER	TEST RUN 1	TEST RUN 2	TEST RUN 3	AVG.READING
0	0	0	0	0
1000	1000	1000	1000	1000
2000	2000	2000	2000	2000
3000	3000	3000	3000	3000
4000	4000	4000	4000	4000
5000	5000	5000	5000	5000
6000	6000	6000	6000	6000
7000	7000	7000	7000	7000
8000	8000	8000	8000	8000
9000	9000	9000	9000	9000

CALIBRATED BY: Gary, Smith

CUSTOMER: Unversity of Florida

JOB NUMBER: J081583

MASTER INSTRUMENT ID No.: 91550

TRACE # 9912-EQ

DESCRIPTION : DEADWEIGHT TESTER

ALTHOUGH RAM/GAUGE COMBINATIONS ARE CALIBRATED AS A UNIT, GAUGES ARE CALIBRATED INDEPENDENTLY, AND ARE USABLE ON OTHER DYWIDAG SYSTEM RAMS, WHEN THIS DOES NOT CONFLICT WITH PROJECT SPECIFICATIONS.

INSTRUCTIONS:

1. **Each gauge must be calibrated to a master instrument that has been calibrated and traceable to NIST Standards.**
2. **Each gauge must be calibratied to meet or exceed ASME STD. 40.1.**
3. **Each gauge will be calibrated before being used in a jack calibration.**
4. **Each gauge will be calibrated before being sent to the customer as a replacement gauge.**
5. **Connect the gauge to the testing machine.**
6. **Pressurize the gauge in 10 increments throughout it's entire range, 3 times.**
7. **Record the gauge and test standard readings.**
8. **If gauge is in need of adjustment, consult the manufacturers product manual contained in the DSI equipment calibration and standards book.**
9. **Form is to be used by Equipment Dept. staff in the calibration of hydraulic gauges that will be used by the customer.**
10. **Form is to be completely filled out.**
11. **Form is to be filled in the gauge calibration file according to it's I.D. No. and with any associated equipment file. One Copy to customer.**

Report Created By: Russell Galasinski

Report Number: 11-3-EDTS-R4 Revised Date: 4-8-00

APPENDIX E
GRAVITY LOAD SIMULATOR FABRICATION PLANS

This appendix includes drawings for the fabrication of the gravity load simulators, used in the full-scale buckling tests.

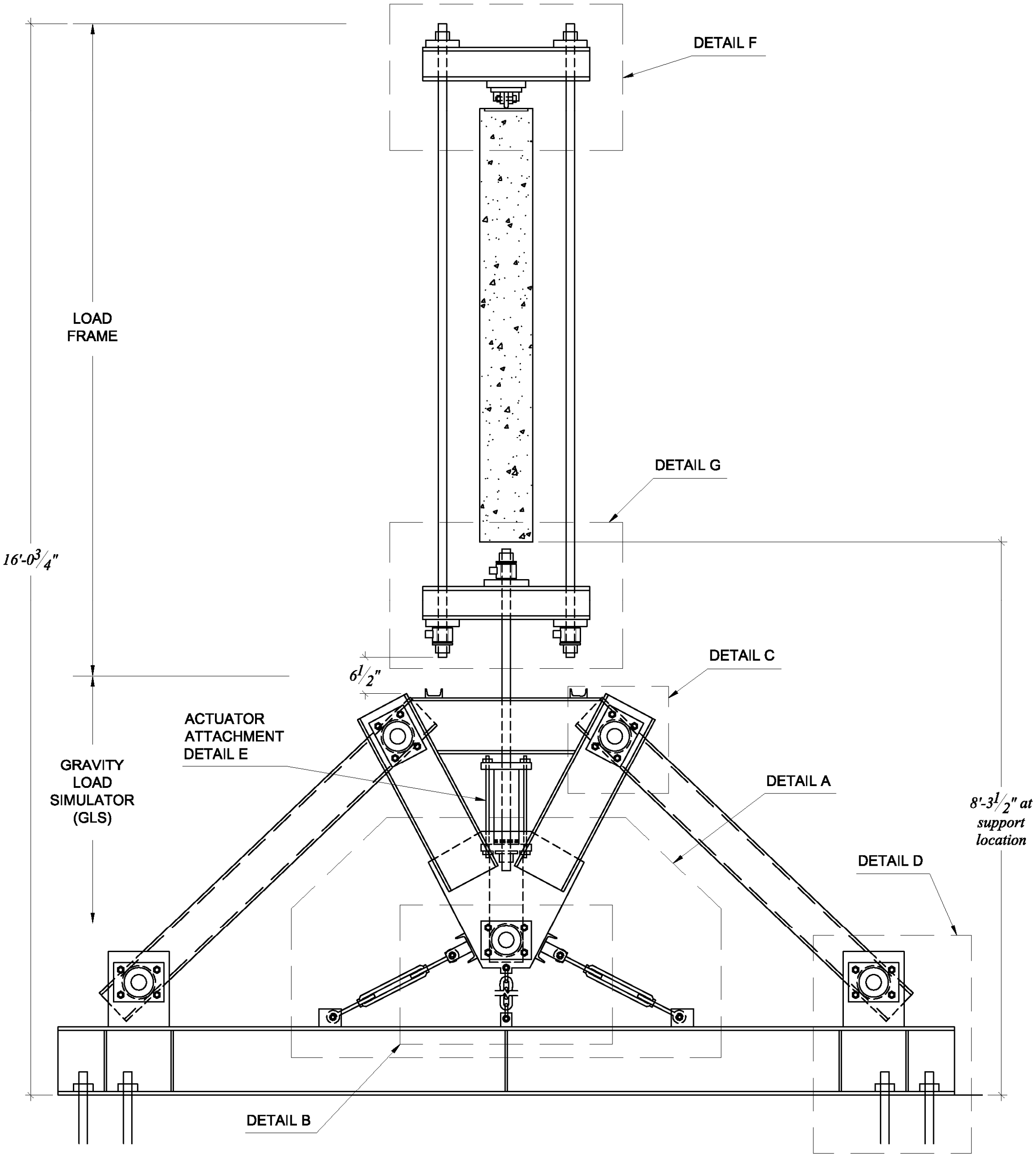

GRAVITY LOAD SIMULATOR AND LOAD FRAME
ELEVATION VIEW

SCALE: $\frac{1}{2}$"=1'-0"

Experimental Validation of Bracing Recommendations for Long-Span Concrete Girders			
Overview of GLS and load frame	*2011-06-24*	*University of Florida*	*Sheet 01 of 16*
Revisions:			

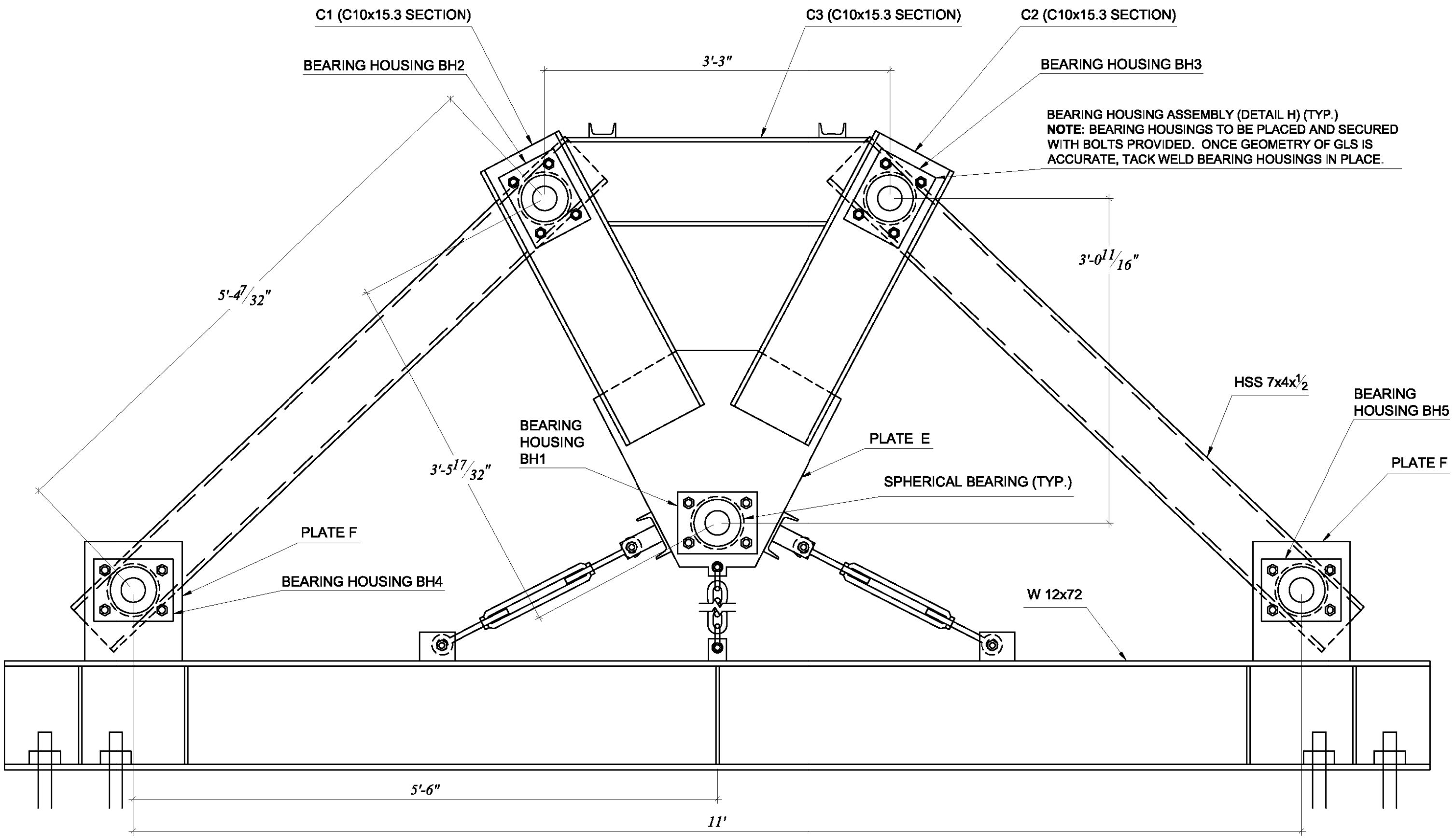

NOTE: THE GEOMETRY OF THE GRAVITY LOAD SIMULATOR IS THE MOST IMPORTANT ASPECT OF THE DESIGN. ACCURATE DIMENSIONS BETWEEN THE SPHERICAL BEARINGS OF THE GLS TO THOSE SHOWN ON THIS SHEET ARE PIVOTAL TO ENSURE VERTICAL LOAD APPLICATION.

GRAVITY LOAD SIMULATOR
ELEVATION VIEW
SCALE: $\frac{3}{4}$"=1'-0"

Experimental Validation of Bracing Recommendations for Long-Span Concrete Girders				*Revisions:*		
GLS elevation view	*2011-06-24*	*University of Florida*	*Sheet 02 of 16*			

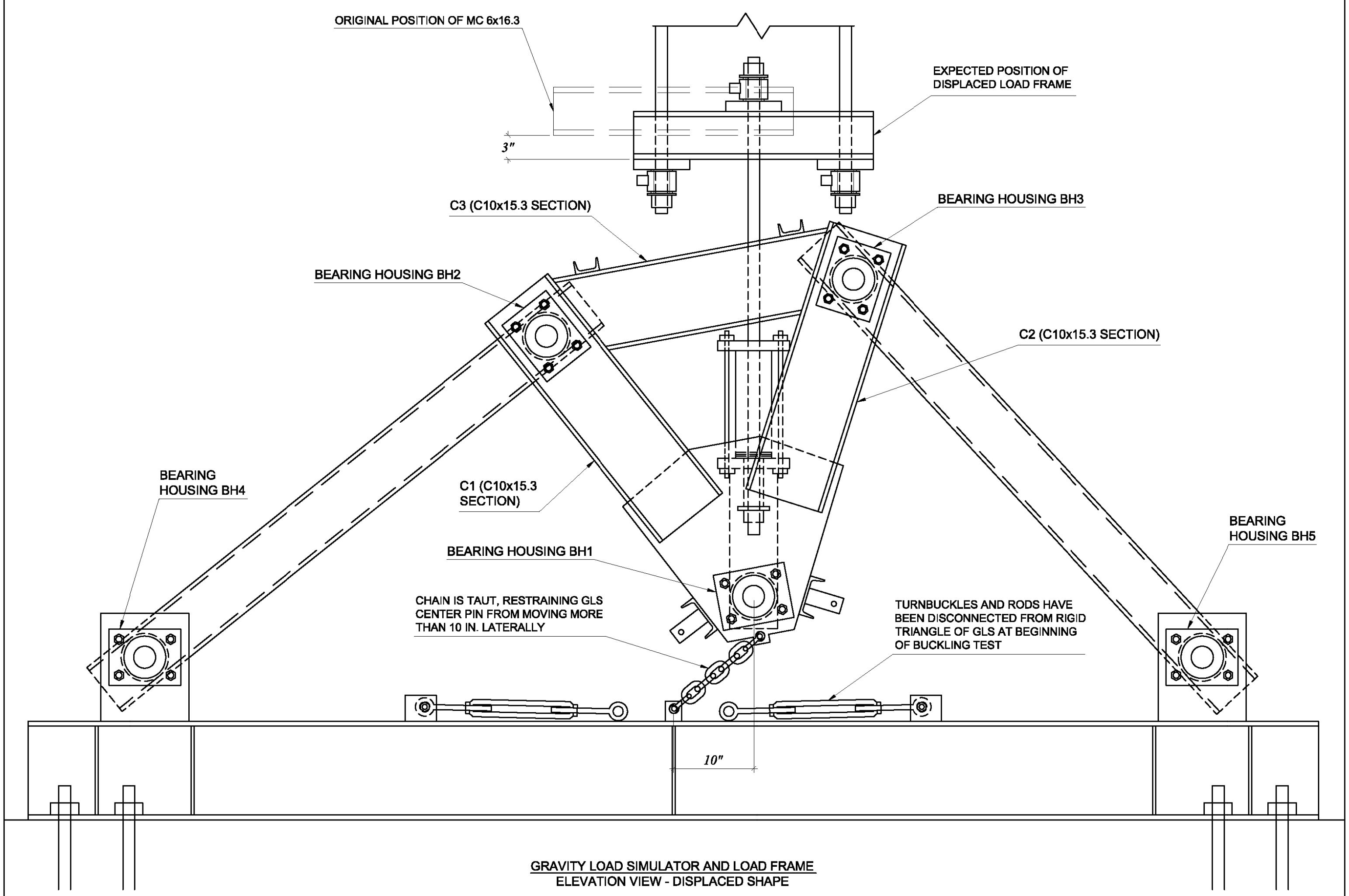

GRAVITY LOAD SIMULATOR AND LOAD FRAME
ELEVATION VIEW - DISPLACED SHAPE

SCALE: $\frac{3}{4}$"=1'-0"

Experimental Validation of Bracing Recommendations for Long-Span Concrete Girders				*Revisions:*		
GLS elevation view	*2011-06-24*	*University of Florida*	*Sheet 03 of 16*			

EYE AND EYE TURNBUCKLE ASSEMBLY:
McMASTER PART 2999T59

RESTRAINT MECHANISM:
CHAIN: McMASTER PART 3387T41
SHACKLES: McMASTER PART 8947T23

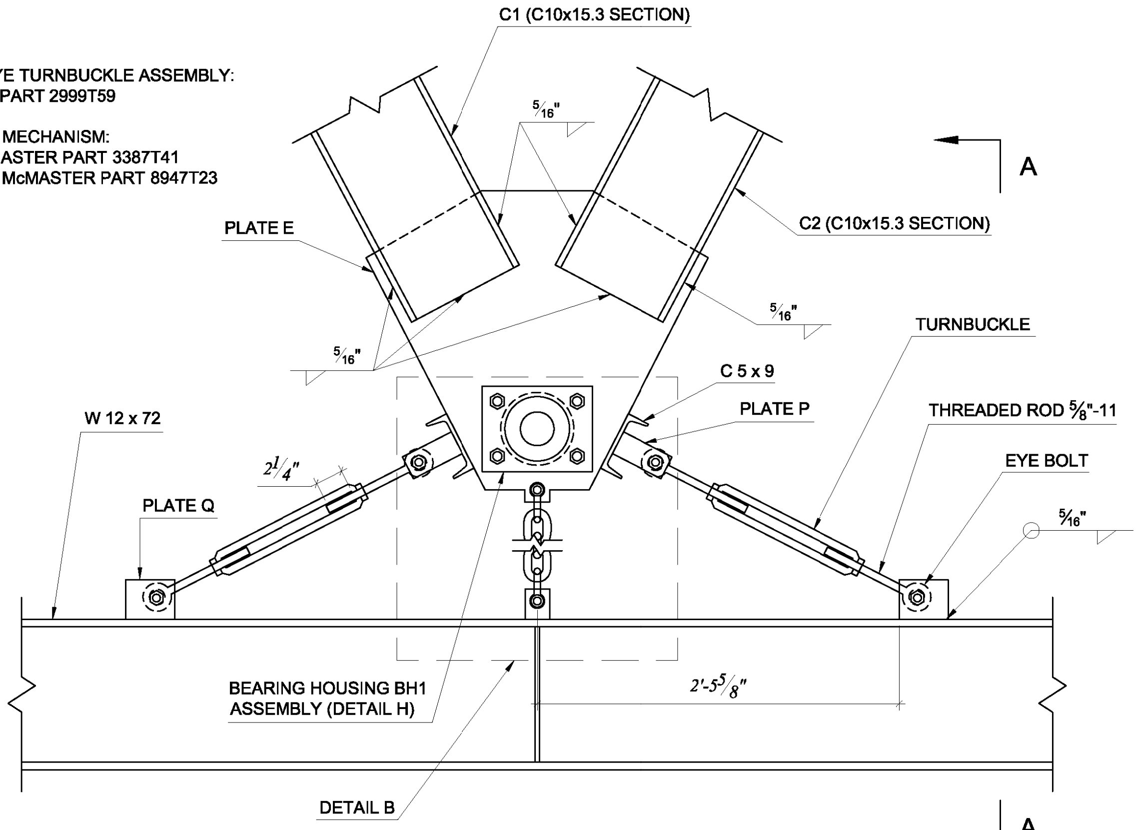

DETAIL A
(ACTUATOR AND COMPONENTS NOT SHOWN FOR CLARITY)

SCALE: 1"=1'-0"

Experimental Validation of Bracing Recommendations for Long-Span Concrete Girders				*Revisions:*		
GLS details	*2011-06-24*	*University of Florida*	*Sheet 04 of 16*			

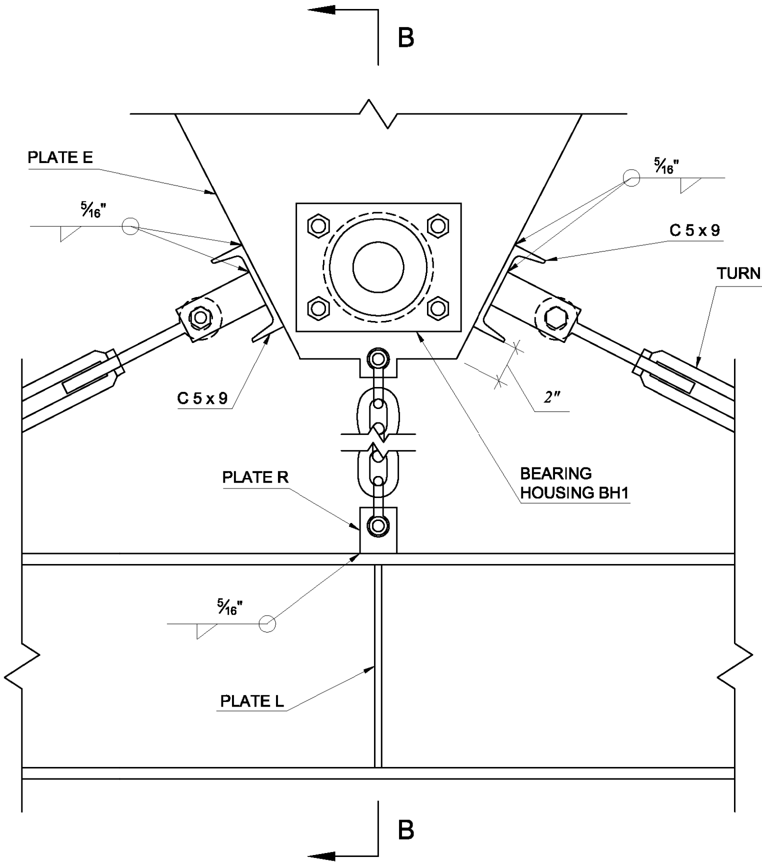

DETAIL B
BEARING HOUSING ASSEMBLIES AND
TURNBUCKLES OMMITTED FOR CLARITY

SCALE: 1½"=1'-0"

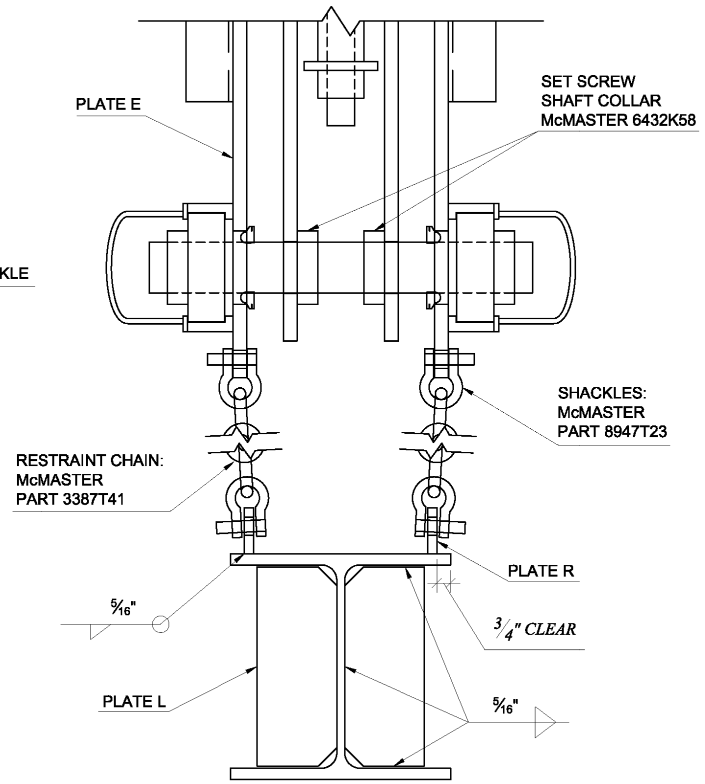

SECTION B-B
BEARING HOUSING ASSEMBLIES AND
TURNBUCKLES OMMITTED FOR CLARITY

SCALE: 1½"=1'-0"

Experimental Validation of Bracing Recommendations for Long-Span Concrete Girders

GLS details	*2011-06-24*	*University of Florida*	*Sheet 05 of 16*	*Revisions:*

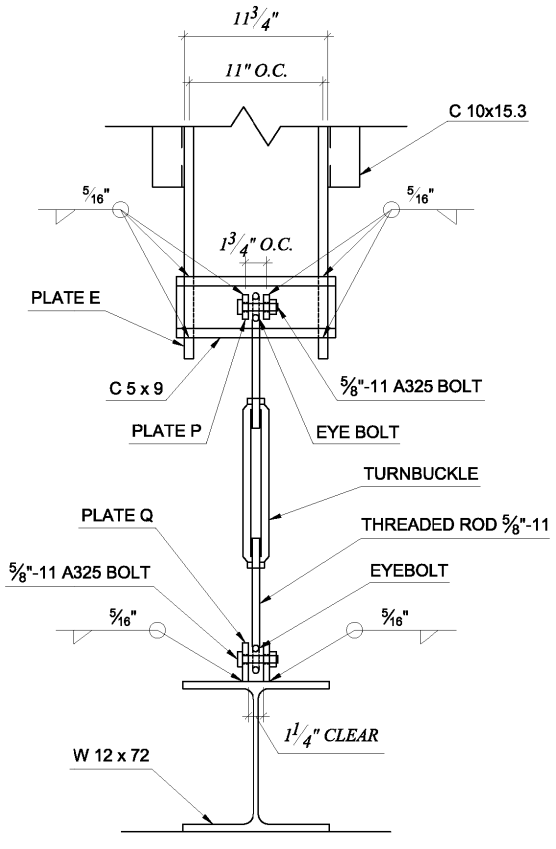

SECTION VIEW A-A
SCALE: 1"=1'-0"

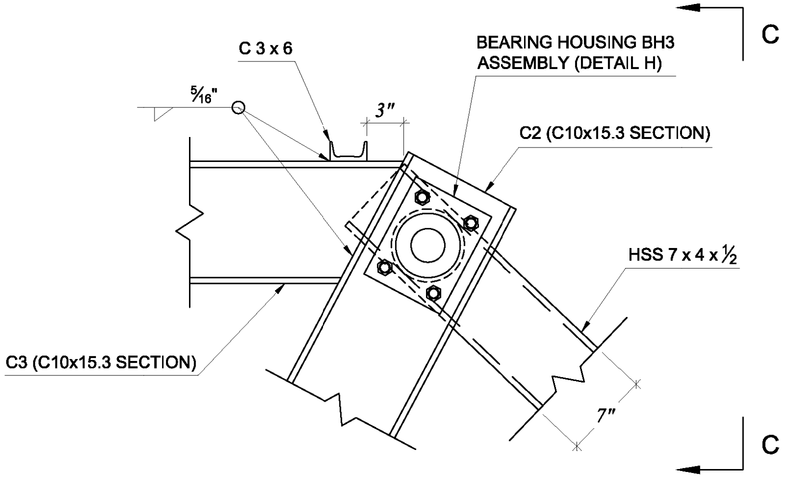

DETAIL C
SCALE: 1"=1'-0"

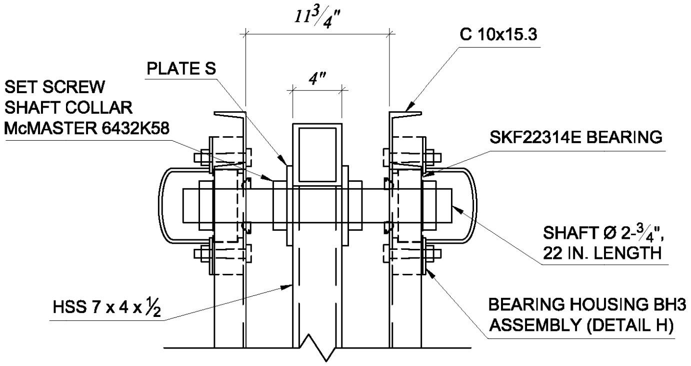

END VIEW C-C
SCALE: 1"=1'-0"

Experimental Validation of Bracing Recommendations for Long-Span Concrete Girders				*Revisions:*
GLS details	*2011-06-24*	*University of Florida*	*Sheet 06 of 16*	

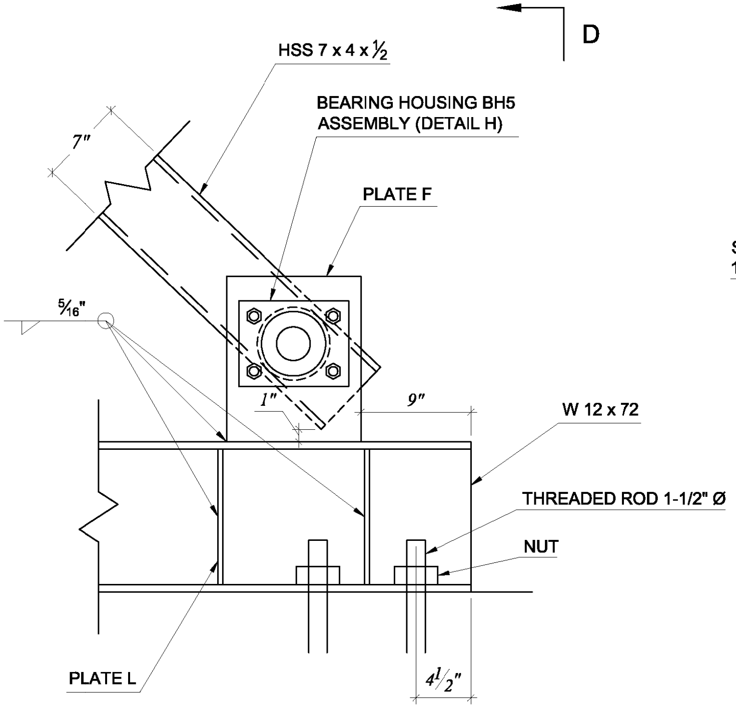

DETAIL D
SCALE: 1"=1'-0"

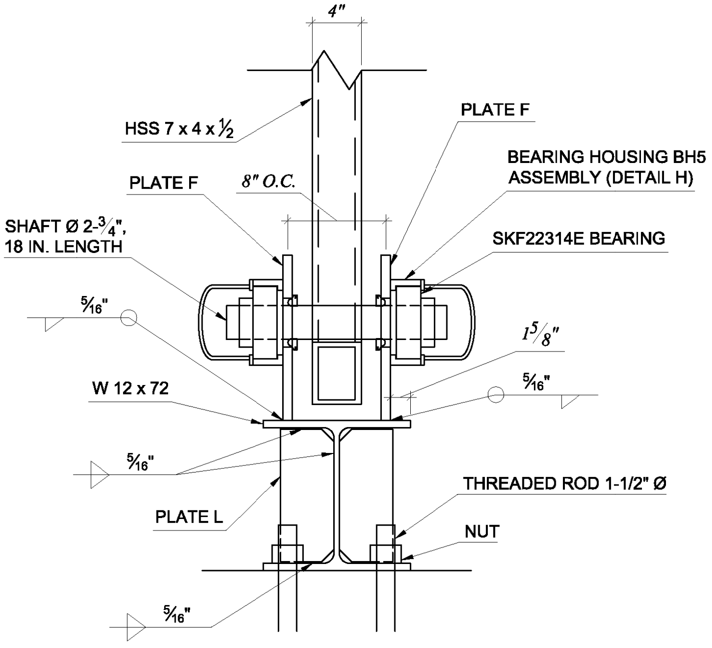

END VIEW D-D
SCALE: 1"=1'-0"

Experimental Validation of Bracing Recommendations for Long-Span Concrete Girders				*Revisions:*
GLS details	*2011-06-24*	*University of Florida*	*Sheet 07 of 16*	

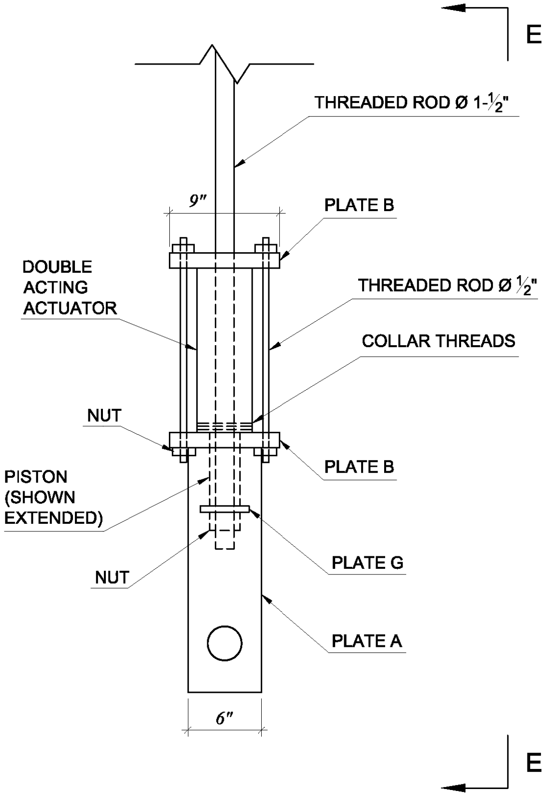

DETAIL E
SCALE: 1"=1'-0"

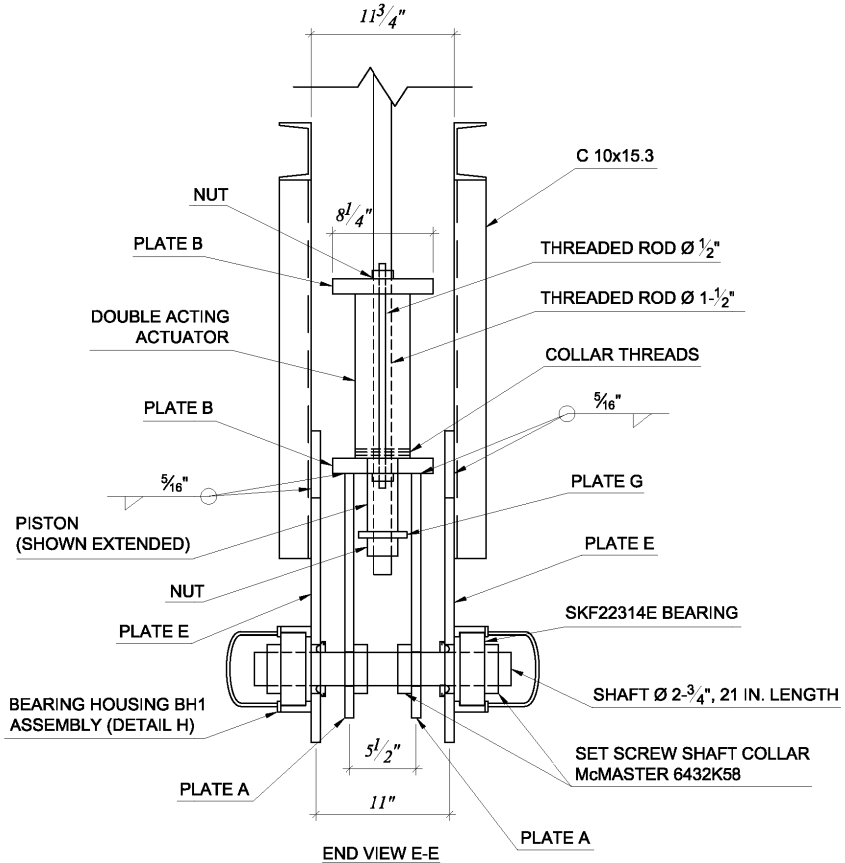

END VIEW E-E
SCALE: 1"=1'-0"

Experimental Validation of Bracing Recommendations for Long-Span Concrete Girders				*Revisions:*		
GLS details	*2011-06-24*	*University of Florida*	*Sheet 08 of 16*			

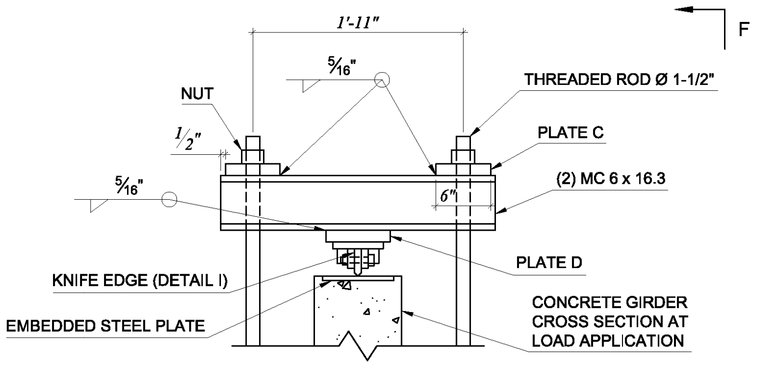

DETAIL F
SCALE: 3⁄4"=1'-0"

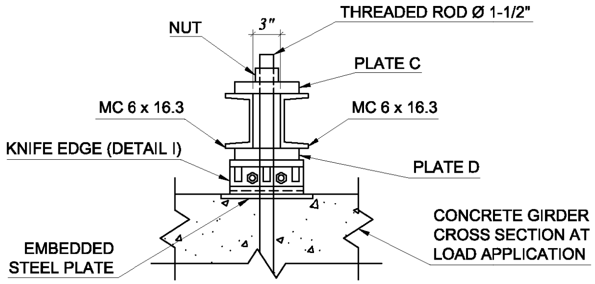

END VIEW F-F
SCALE: 3⁄4"=1'-0"

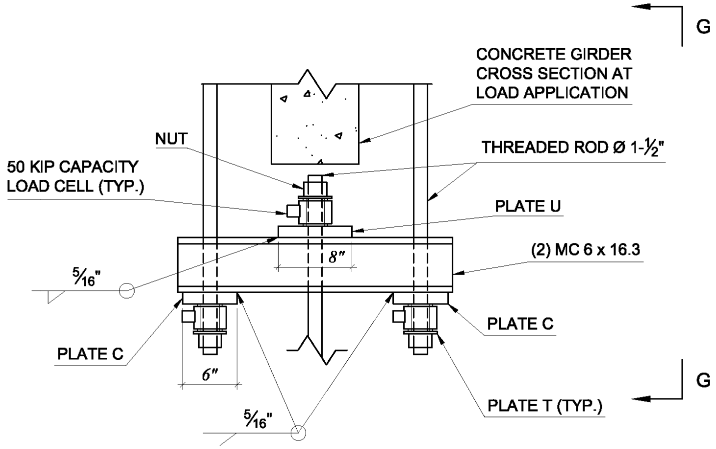

DETAIL G
SCALE: 3⁄4"=1'-0"

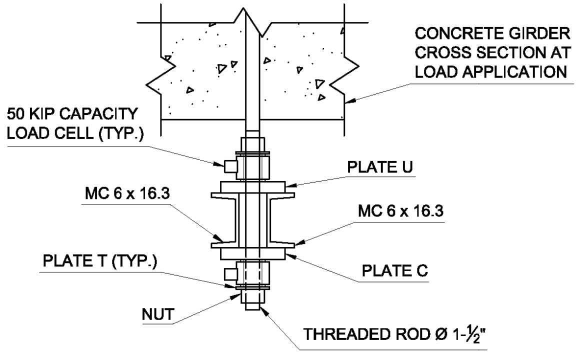

END VIEW G-G
SCALE: 3⁄4"=1'-0"

Experimental Validation of Bracing Recommendations for Long-Span Concrete Girders				*Revisions:*		
Load frame details	*2011-06-24*	*University of Florida*	*Sheet 09 of 16*			

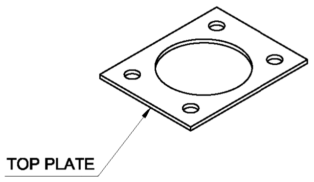

TOP PLATE
ISOMETRIC VIEW
SCALE: 1½" = 1'-0"

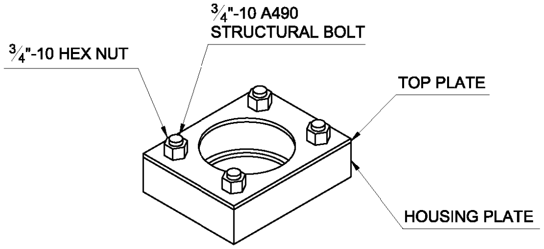

BEARING HOUSING ASSEMBLY
ISOMETRIC VIEW
SCALE: 1½" = 1'-0"

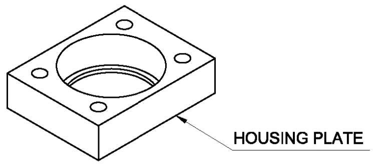

HOUSING PLATE
ISOMETRIC VIEW
SCALE: 1½" = 1'-0"

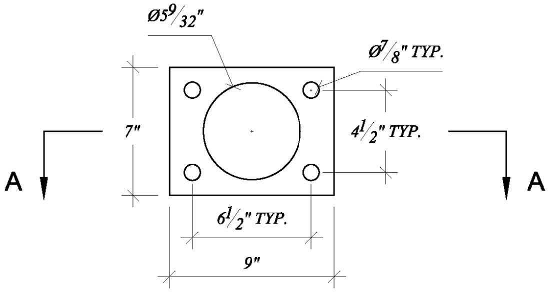

TOP PLATE
PLAN VIEW
SCALE: 1½" = 1'-0"

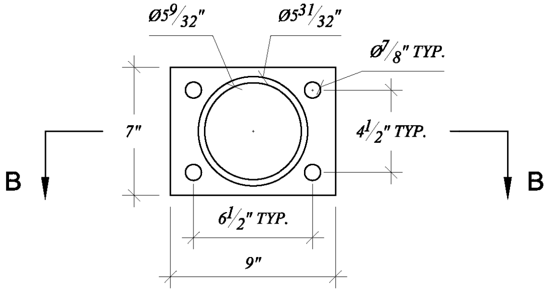

HOUSING PLATE
PLAN VIEW
SCALE: 1½" = 1'-0"

NOTES:
- REQUIRE TWENTY (20) BEARING HOUSING ASSEMBLIES.
- STEEL PLATES MUST BE A36 STEEL AS SPECIFIED BY ASTM STANDARDS.
- BEARING TO BE INSTALLED IN HOUSING: SKF22314E. SPECIFICATIONS FOR BEARING SENT PREVIOUSLY.

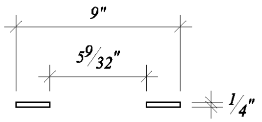

TOP PLATE
SECTION A-A VIEW
SCALE: 1½" = 1'-0"

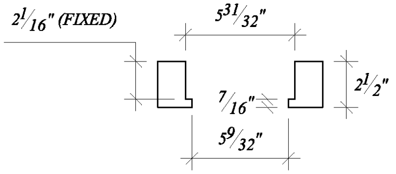

HOUSING PLATE
SECTION B-B VIEW
SCALE: 1½" = 1'-0"

DETAIL H
SCALE: 1½" = 1'-0"

Experimental Validation of Bracing Recommendations for Long-Span Concrete Girders				*Revisions:*		
Detail H: bearing housing assembly	*2011-06-24*	*University of Florida*	*Sheet 10 of 16*			

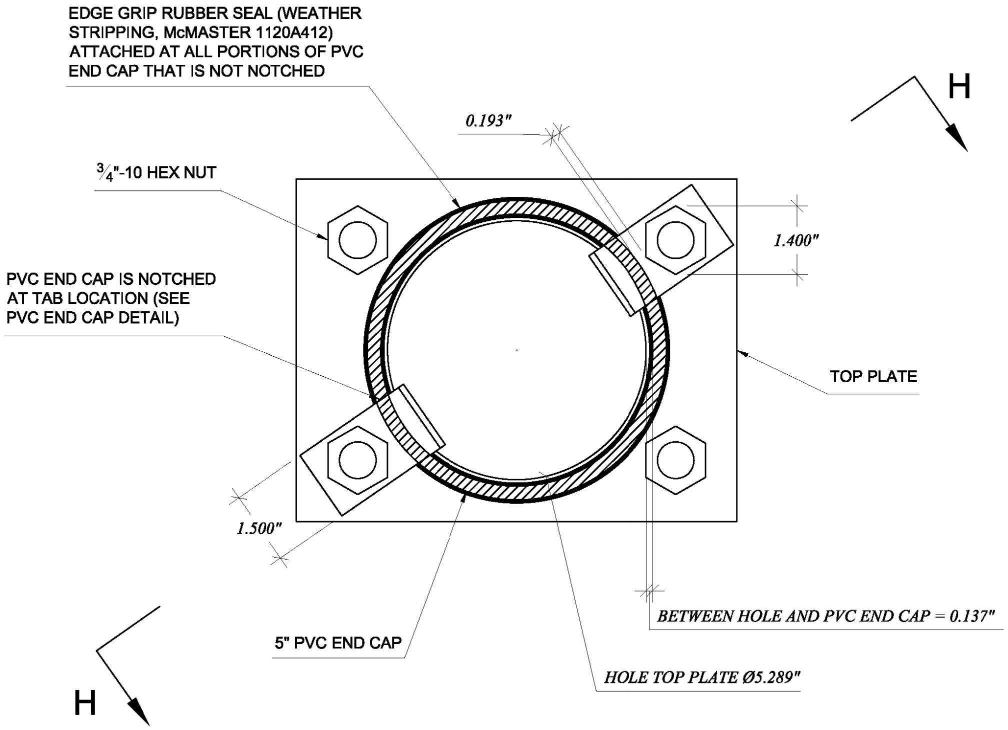

PLAN VIEW OF BEARING HOUSING
ASSEMBLY AND BEARING SEAL
SCALE: 4" = 1'-0"

Experimental Validation of Bracing Recommendations for Long-Span Concrete Girders				*Revisions:*		
Detail H: bearing seal	*2011-06-24*	*University of Florida*	*Sheet 11 of 16*			

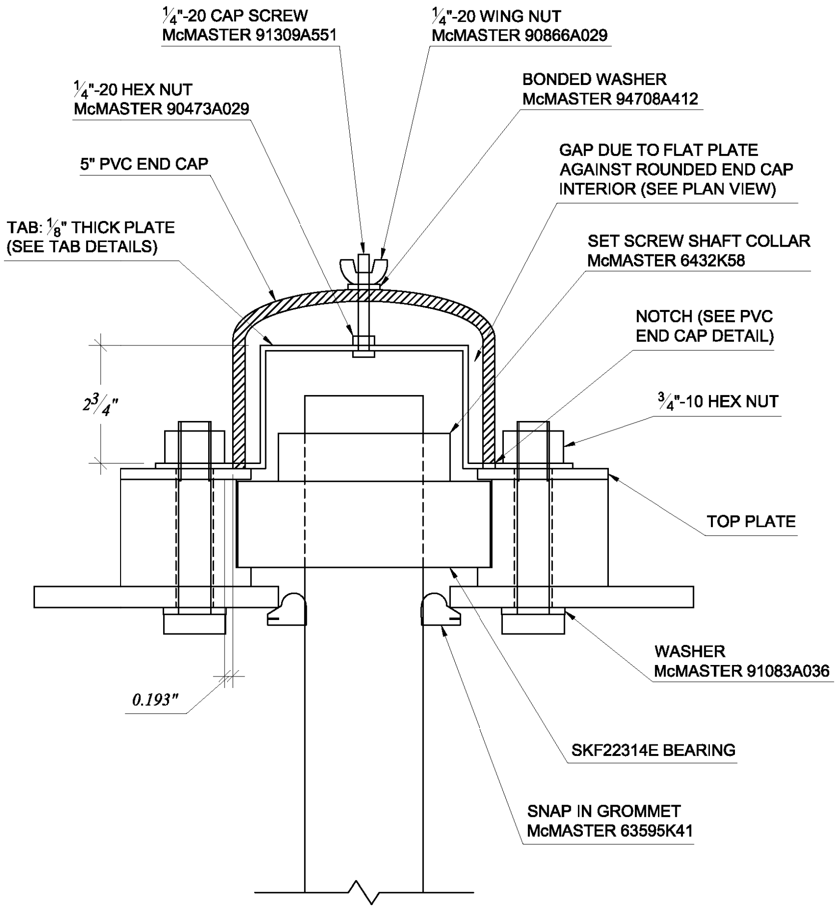

SECTION H-H
BEARING SEAL AND BEARING HOUSING ASSEMBLY
SCALE: 3½" = 1'-0"

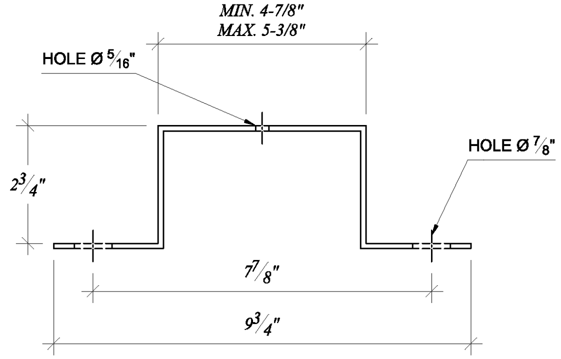

TAB DETAILS
⅛" THICK PLATE
SCALE: 3½" = 1'-0"

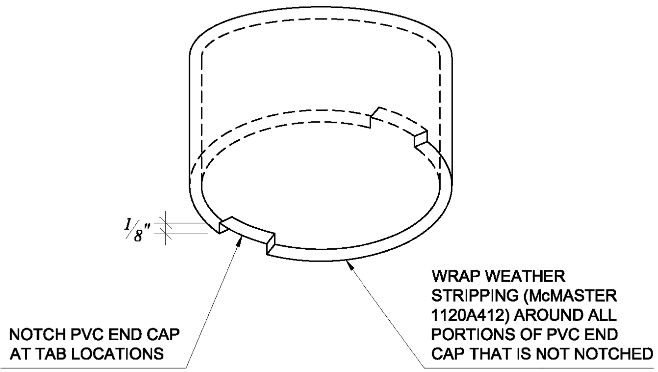

PVC END CAP DETAIL
SCALE: 3½" = 1'-0"

Experimental Validation of Bracing Recommendations for Long-Span Concrete Girders				*Revisions:*		
Detail H: bearing seal	*2011-06-24*	*University of Florida*	*Sheet 12 of 16*			

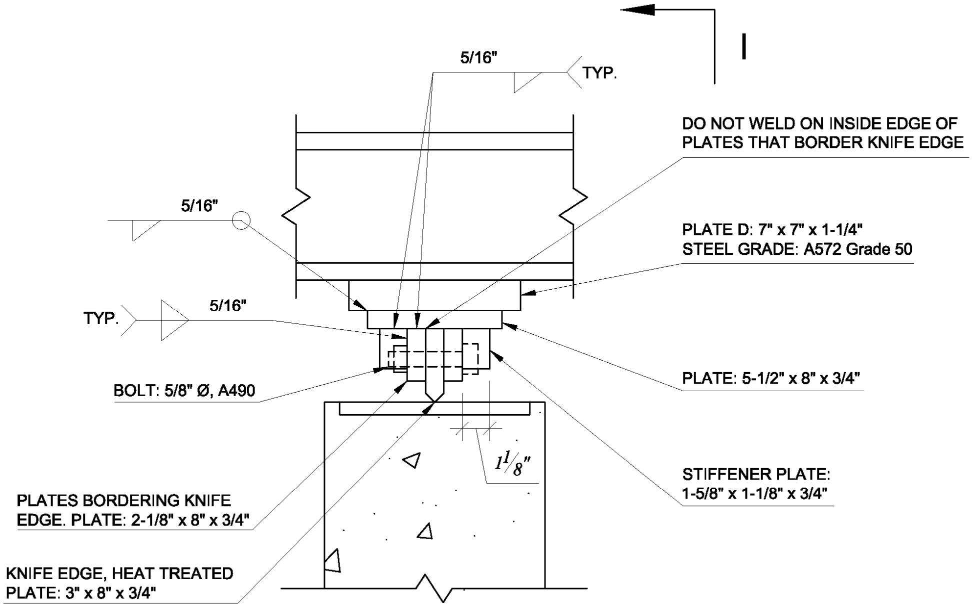

NOTE: ALL STEEL ON THIS SHEET HAS A YIELD STRENGTH OF 70 KSI UNLESS INDICATED OTHERWISE

DETAIL I
KNIFE EDGE DETAIL
SCALE: 2"=1'-0"

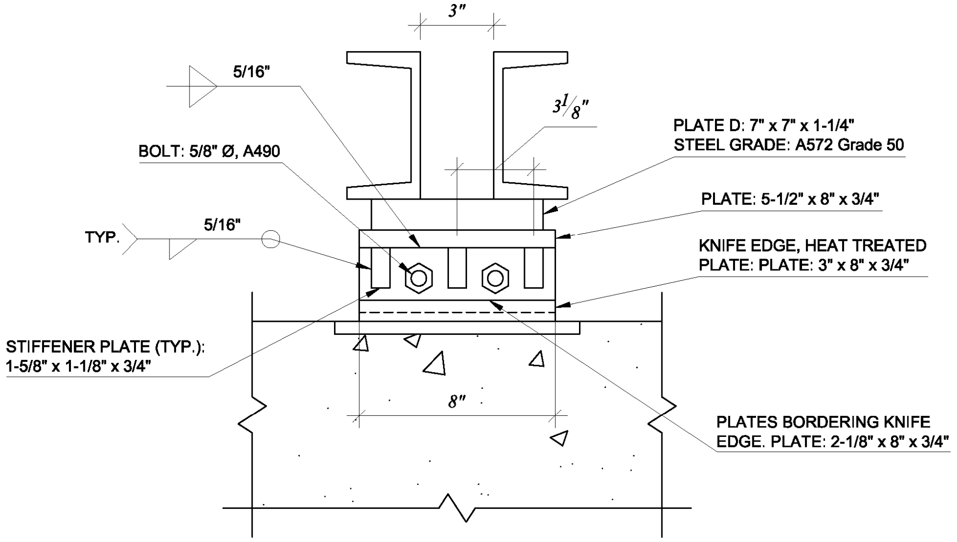

END VIEW I-I: KNIFE EDGE DETAIL
SCALE: 2"=1'-0"

Experimental Validation of Bracing Recommendations for Long-Span Concrete Girders

Detail I: knife edge details	*2011-06-24*	*University of Florida*	*Sheet 13 of 16*
Revisions:			

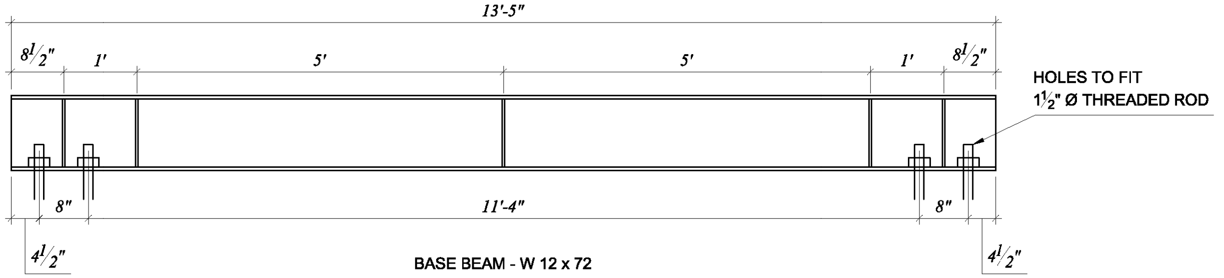

BASE BEAM - W 12 x 72

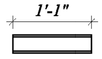

BRIDGING CHANNELS
AT TOP OF RIGID
TRIANGLE - C 3 x 6

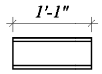

BRIDGING CHANNELS FOR
TURNBUCKLE RESTRAINT
SYSTEM - C 5 x 9

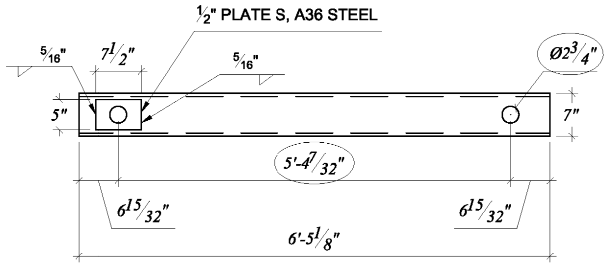

INCLINED ARMS - HSS 7 x 4 x ½

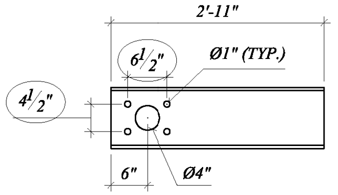

LEFT AND RIGHT ARMS (C1 AND C2) OF
RIGID TRIANGLE - C 10 x 15.3

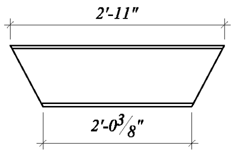

TOP ARM (C3) OF
RIGID TRIANGLE - C 10 x 15.3

NOTE: KEY DIMENSIONS ASSOCIATED WITH SPHERICAL BEARING LOCATIONS ARE CIRCLED.

GRAVITY LOAD SIMULATOR STEEL MEMBERS
DETAILS OF HOLE SIZE/LOCATION, STIFFENER LOCATION

SCALE: ½"=1'-0"

Experimental Validation of Bracing Recommendations for Long-Span Concrete Girders				*Revisions:*		
GLS steel member list	*2011-06-24*	*University of Florida*	*Sheet 14 of 16*			

DIMENSION MUST MATCH ON
EACH PAIR OF PLATES PER GLS
TO MAINTAIN VERTICAL LOAD

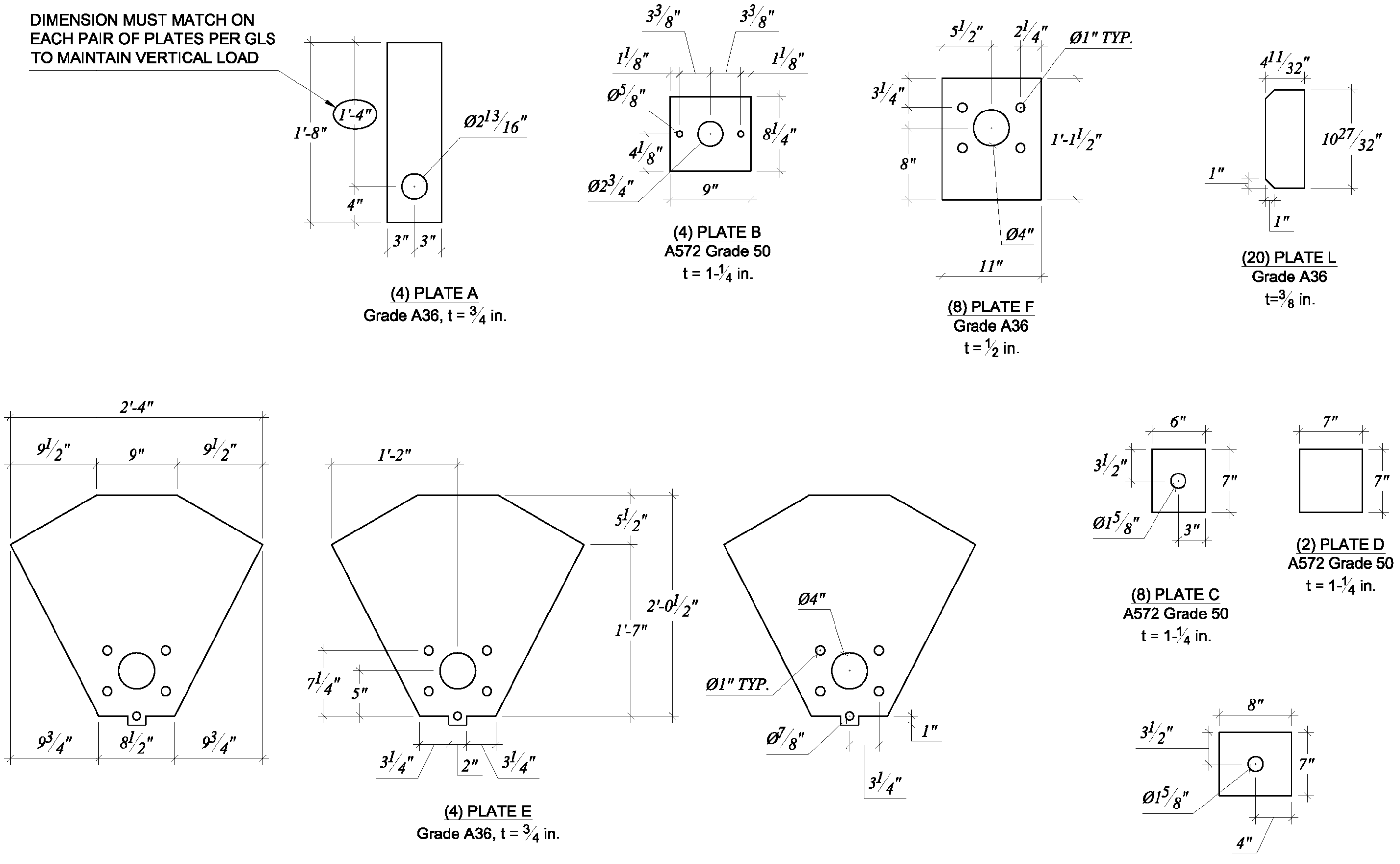

(4) PLATE A
Grade A36, $t = \frac{3}{4}$ in.

(4) PLATE B
A572 Grade 50
$t = 1\text{-}\frac{1}{4}$ in.

(8) PLATE F
Grade A36
$t = \frac{1}{2}$ in.

(20) PLATE L
Grade A36
$t=\frac{3}{8}$ in.

(4) PLATE E
Grade A36, $t = \frac{3}{4}$ in.

(8) PLATE C
A572 Grade 50
$t = 1\text{-}\frac{1}{4}$ in.

(2) PLATE D
A572 Grade 50
$t = 1\text{-}\frac{1}{4}$ in.

(2) PLATE U
A572 Grade 50
$t = 1\text{-}\frac{1}{4}$ in.

PLATE LIST - GLS
SCALE: $\frac{3}{4}$"=1'-0"

Experimental Validation of Bracing Recommendations for Long-Span Concrete Girders

GLS plate list | *2011-06-24* | *University of Florida* | *Sheet 15 of 16*

Revisions:

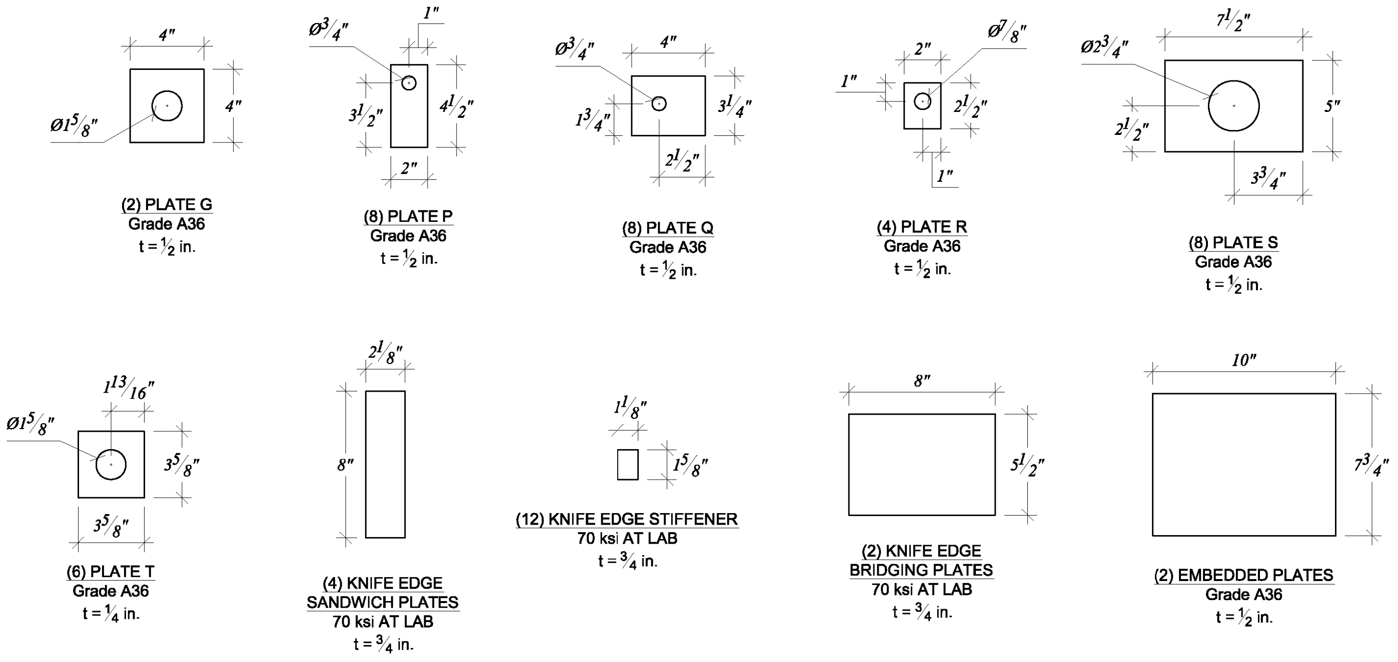

PLATE LIST - GLS

SCALE: 1-$\frac{1}{2}$"=1'-0"

Experimental Validation of Bracing Recommendations for Long-Span Concrete Girders				*Revisions:*
GLS plate list	*2011-06-24*	*University of Florida*	*Sheet 16 of 16*	

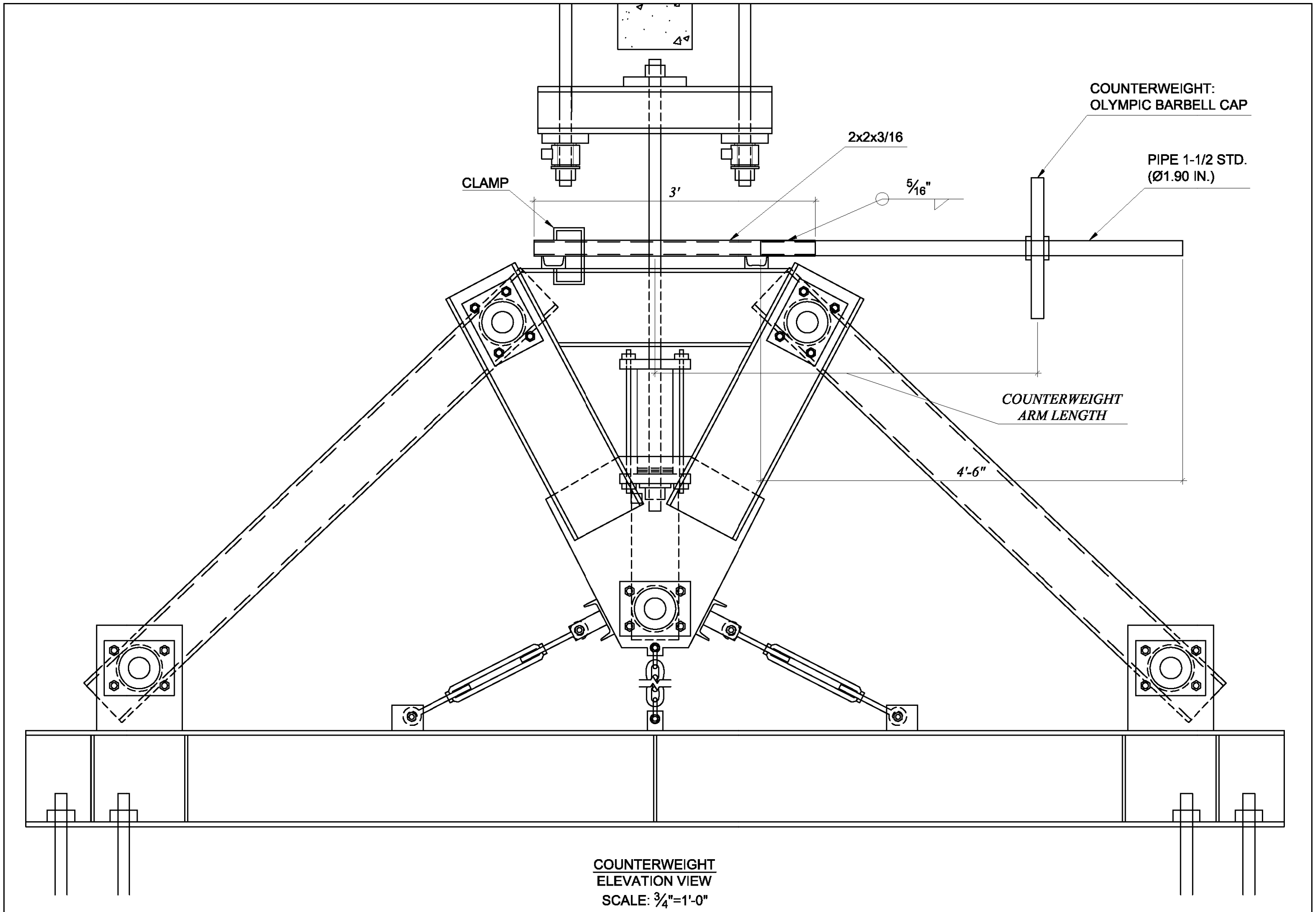

COUNTERWEIGHT
ELEVATION VIEW
SCALE: $\frac{3}{4}$"=1'-0"

Experimental Validation of Bracing Recommendations for Long-Span Concrete Girders				*Revisions:*
GLS counterweight plans	*2011-12-07*	*University of Florida*	*Sheet 01 of 02*	

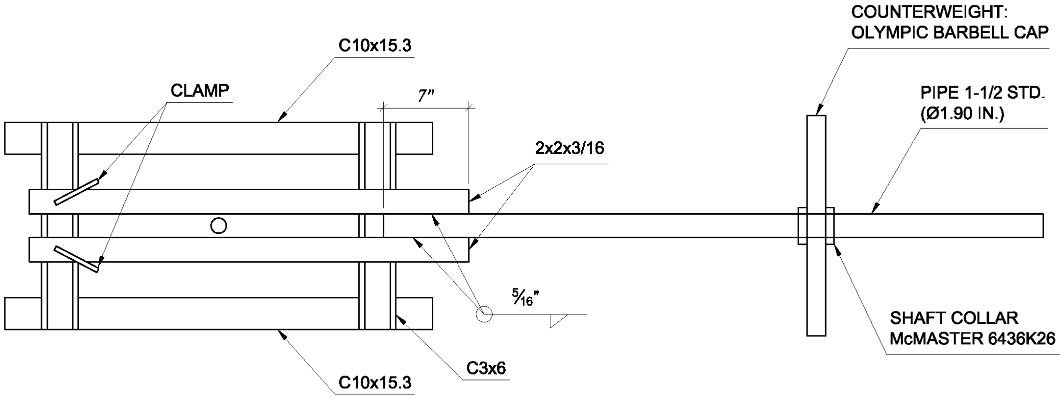

COUNTERWEIGHT
PLAN VIEW
SCALE: 1"=1'-0"

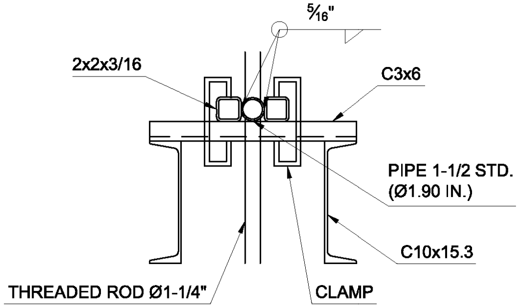

COUNTERWEIGHT
END VIEW
SCALE: 1"=1'-0"

Experimental Validation of Bracing Recommendations for Long-Span Concrete Girders				*Revisions:*		
GLS counterweight plans	*2011-12-07*	*University of Florida*	*Sheet 02 of 02*			

APPENDIX F
CATCH FRAMES FABRICATION PLANS

This appendix includes drawings for the fabrication of the gravity load simulators, used in the full-scale buckling tests.

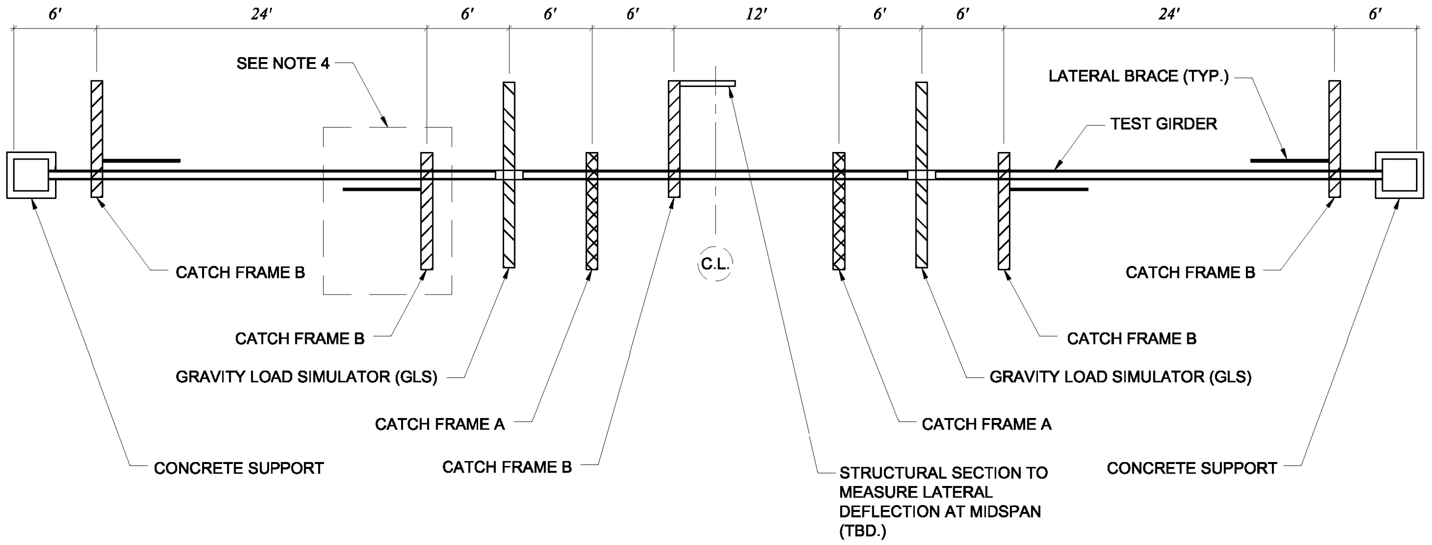

PLAN VIEW
LOCATIONS OF CATCH FRAMES (A AND B) AND GRAVITY LOAD
SIMULATORS RELATIVE TO LENGTH OF TEST GIRDER

SCALE: $^{3}/_{32}$" = 1'-0"

NOTES:

1. TO PREVENT UNACCEPTABLE NEGATIVE MOMENT AT THE ENDS OF THE BEAM, LIFT TEST GIRDER WITH CRANES AT THE ENDS OF THE BEAM ONLY.
2. CRANES SHALL BE LOCKED TOGETHER, SO THAT THERE IS ONE CONTROL FOR BOTH ENDS, WITH A SINGLE OPERATOR AT MIDSPAN.
3. USE FOAMBOARD OR PLYWOOD TO CUSHION COLUMNS OF CATCH FRAMES AS TEST GIRDER IS BEING LIFTED. THIS PREVENTS LATERAL MOVEMENT DURING LIFTING, BUT CAN BE REMOVED TO ALLOW LATERAL DISPLACEMENT DURING A TEST.
4. DETAILED VIEWS OF CATCH FRAME AND LATERAL BRACING ARE SHOWN ON SHEET 05 AND SHEET 06. ORIENTATION OF LATERAL BRACING SHOWN ABOVE.

Experimental Validation of Bracing Recommendations for Long-Span Concrete Girders				*Revisions:*	*REV 1 : 2011-03-08*	
Catch frame and GLS locations	*2011-03-08*	*University of Florida*	*Sheet 01 of 07*			

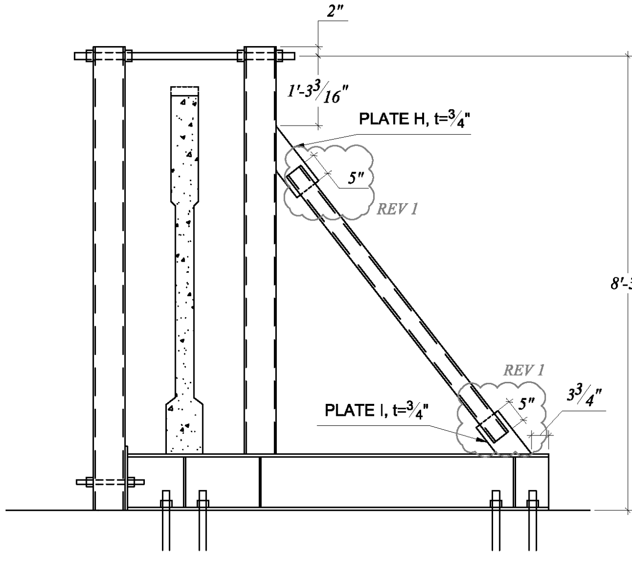

ELEVATION VIEW - CATCH FRAME A
BEAM SUPPORTED BY CATCH FRAME DURING
CLOSURE POUR AND END BLOCK CASTING
(LATERAL BRACING OMITTED FOR CLARITY)

SCALE = $^{3}/_{8}$" = 1'-0"

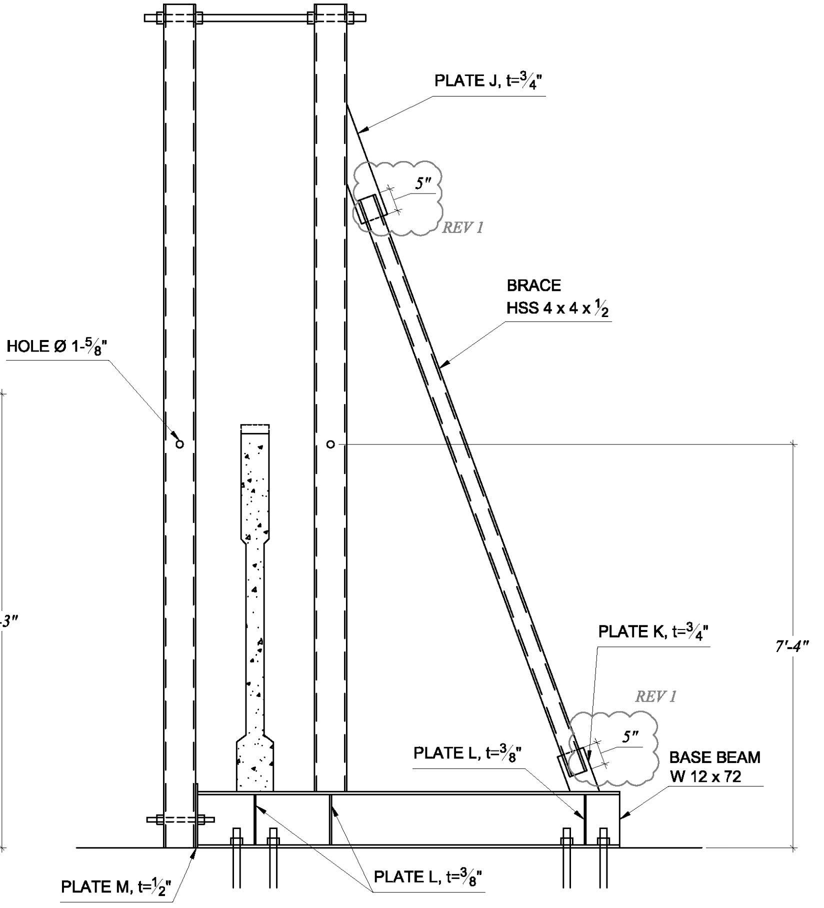

ELEVATION VIEW - CATCH FRAME B
BEAM SUPPORTED BY CATCH FRAME DURING
CLOSURE POUR AND END BLOCK CASTING
(LATERAL BRACING OMITTED FOR CLARITY)

SCALE = $^{3}/_{8}$" = 1'-0"

Experimental Validation of Bracing Recommendations for Long-Span Concrete Girders				*Revisions:*	*REV 1 : 2011-03-08*	
Catch frames A and B	*2011-03-08*	*University of Florida*	*Sheet 02 of 07*			

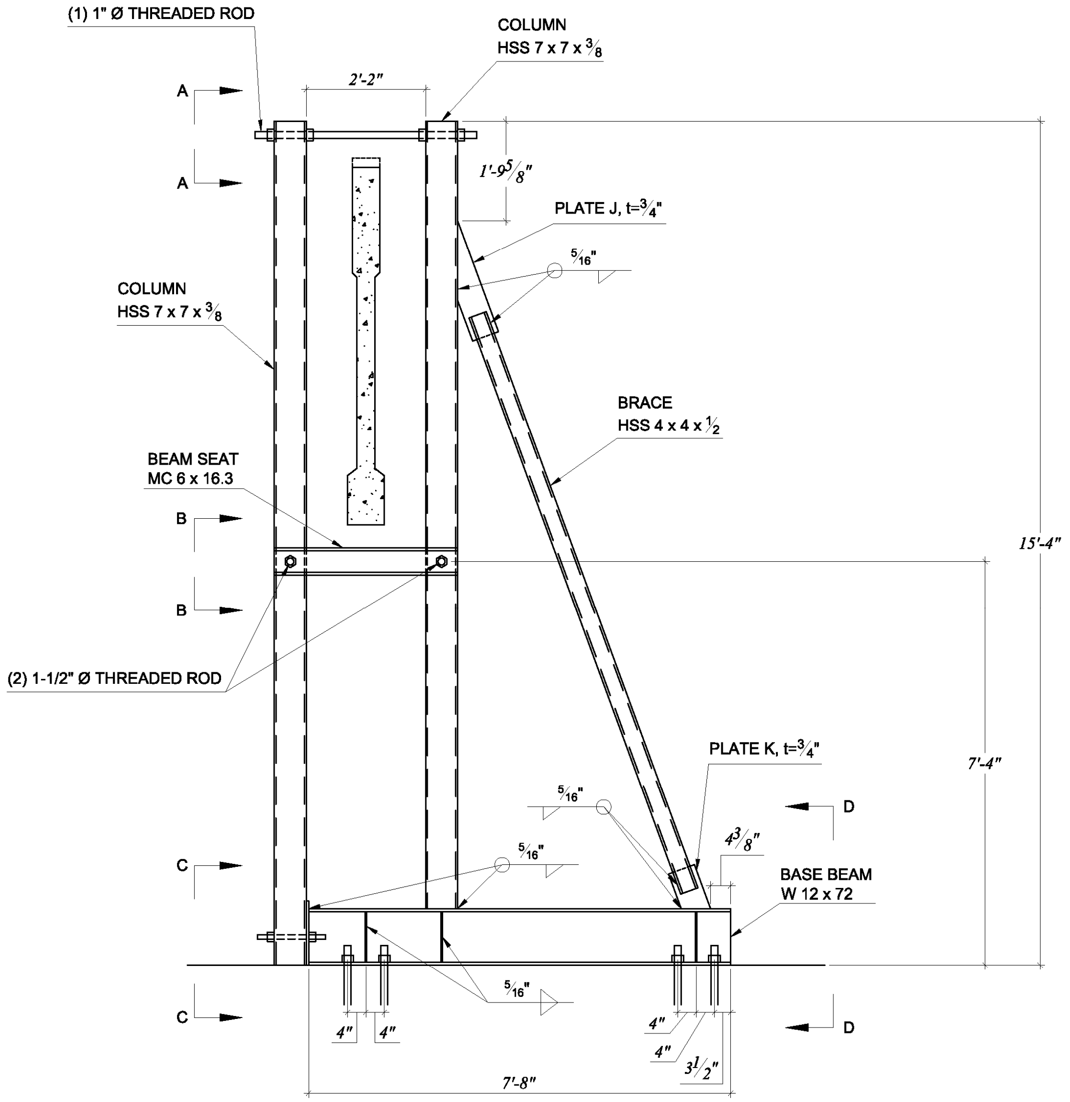

ELEVATION VIEW - CATCH FRAME B
TEST GIRDER SUSPENDED DURING BUCKLING TEST
(LATERAL BRACING OMITTED FOR CLARITY)

SCALE = 3/8" = 1'-0"

Experimental Validation of Bracing Recommendations for Long-Span Concrete Girders

Catch frame B details	*2011-03-08*	*University of Florida*	*Sheet 03 of 07*
Revisions:	*REV 1 : 2011-03-08*		

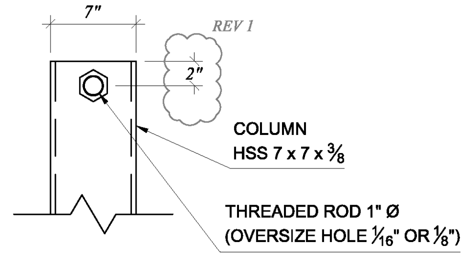

END VIEW A-A

SCALE: 1"=1'-0"

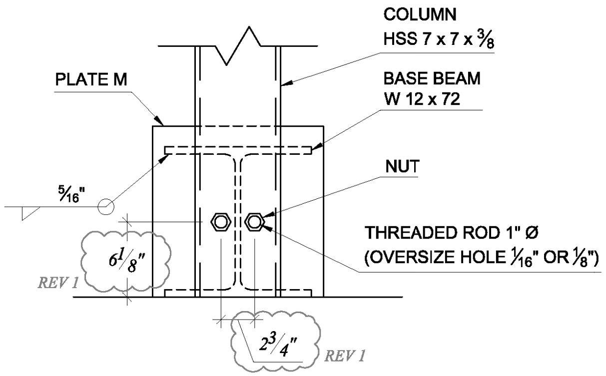

END VIEW C-C

SCALE: 1"=1'-0"

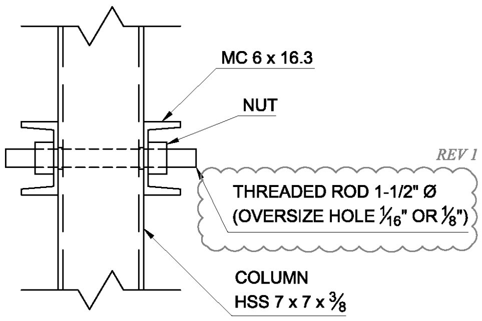

END VIEW B-B

SCALE: 1"=1'-0"

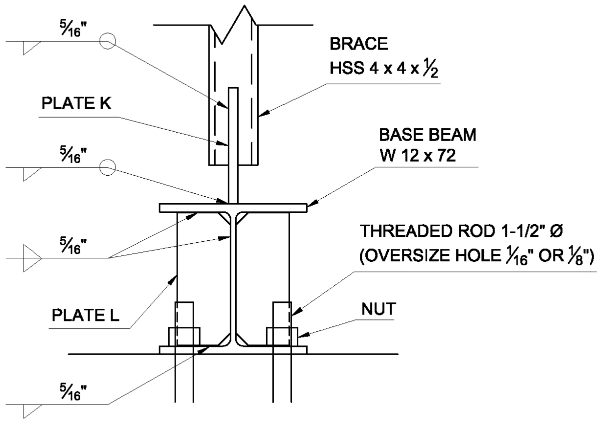

END VIEW D-D

SCALE: 1"=1'-0"

Experimental Validation of Bracing Recommendations for Long-Span Concrete Girders				*Revisions:*	*REV 1 : 2011-03-08*
Connection details	*2011-03-08*	*University of Florida*	*Sheet 04 of 07*		

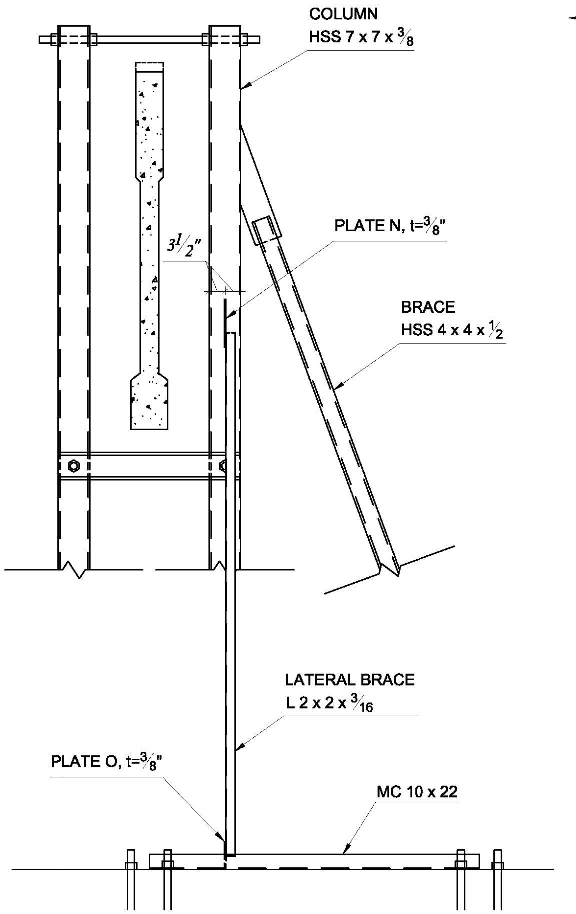

ELEVATION VIEW - CATCH FRAME B
TEST GIRDER SUSPENDED DURING BUCKLING TEST
(LATERAL BRACING INLCUDED)

SCALE = $^3/_8$" = 1'-0"

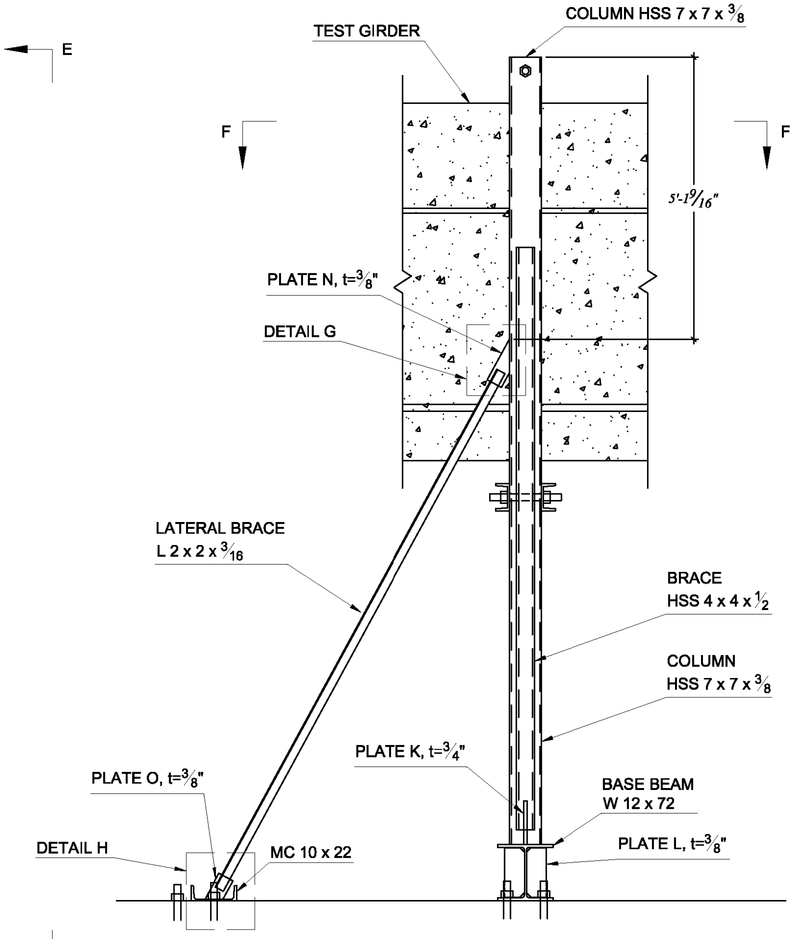

END VIEW E-E
TEST GIRDER SUSPENDED DURING BUCKLING TEST
(LATERAL BRACING INLCUDED)

SCALE = $^3/_8$" = 1'-0"

Experimental Validation of Bracing Recommendations for Long-Span Concrete Girders				*Revisions:*	*REV 1 : 2011-03-08*	
Catch frame lateral bracing details	*2011-03-08*	*University of Florida*	*Sheet 05 of 07*			

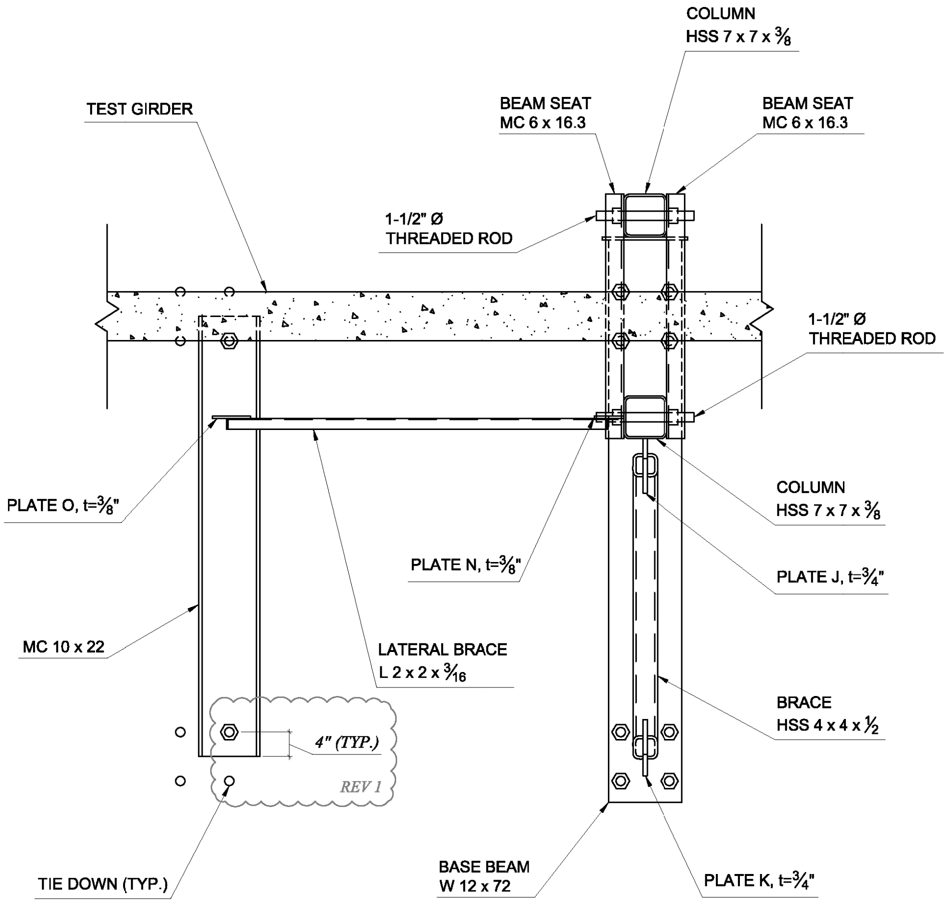

SECTION F-F
CATCH FRAME WITH LATERAL BRACE

SCALE: ½"=1'-0"

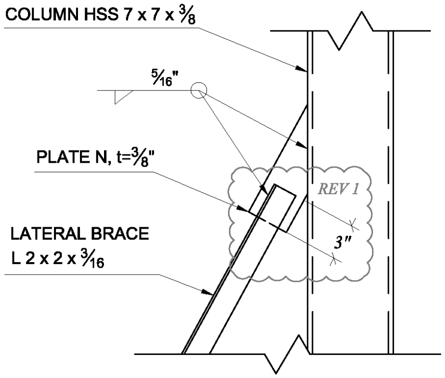

DETAIL G

SCALE: 1"=1'-0"

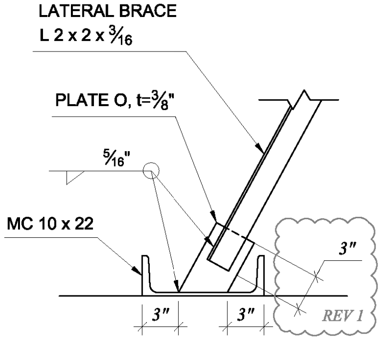

DETAIL H

SCALE: 1"=1'-0"

Experimental Validation of Bracing Recommendations for Long-Span Concrete Girders				*Revisions:*	*REV 1 : 2011-03-08*	
Catch frame lateral bracing details	*2011-03-08*	*University of Florida*	*Sheet 06 of 07*			

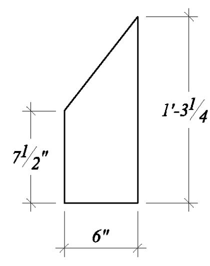

(2) PLATE H
Grade A36, t=¾ in.

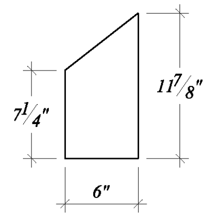

(2) PLATE I
Grade A36, t=¾ in.

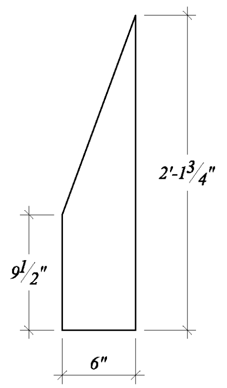

(5) PLATE J
Grade A36, t=¾ in.

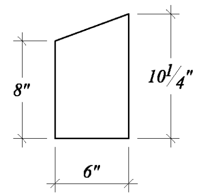

(5) PLATE K
Grade A36, t=¾ in.

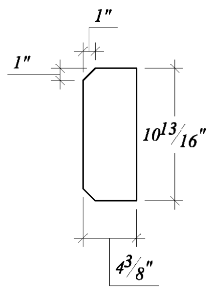

(58) PLATE L
Grade A36, t=⅜ in.

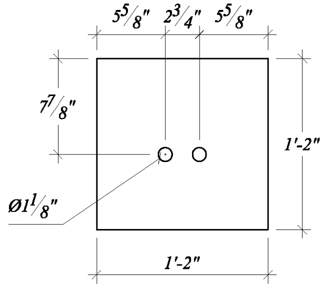

(7) PLATE M
Grade A36, t=½ in.

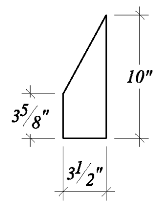

(4) PLATE N
Grade A36, t=⅜ in.

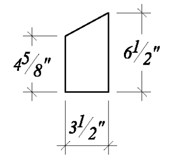

(4) PLATE O
Grade A36, t=⅜ in.

REV 1

PLATE LIST - CATCH FRAMES
ALL PLATES WERE PURCHASED FROM NAMASCO
SCALE: 1"=1'-0"

Experimental Validation of Bracing Recommendations for Long-Span Concrete Girders				*Revisions:*	*REV 1 : 2011-03-08*	
Catch frame plate list	*2011-03-08*	*University of Florida*	*Sheet 07 of 07*			

APPENDIX G
BUCKLING TESTS INSTRUMENTATION PLAN

This appendix includes drawings of the instrumentation used in the full-scale buckling tests.

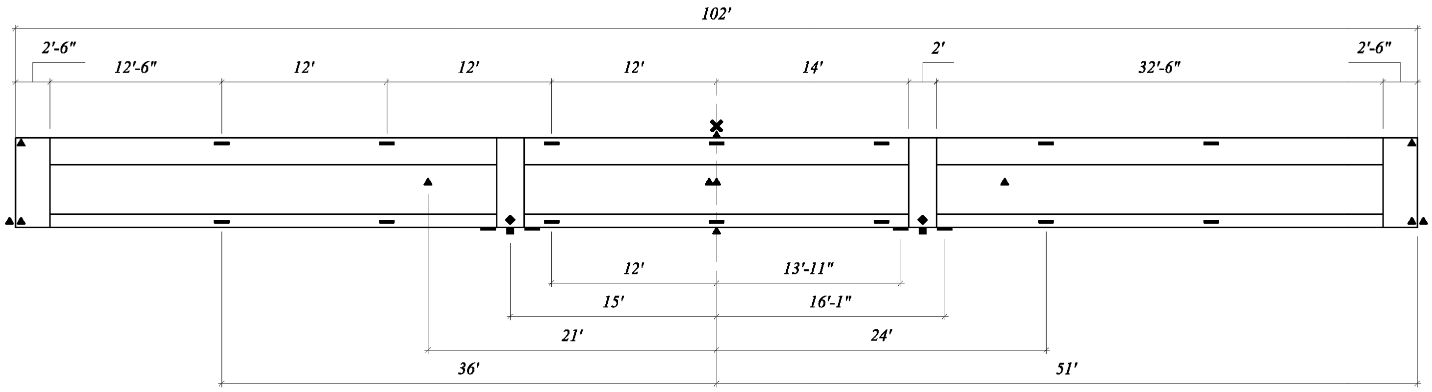

SOUTH ◄——●——► NORTH (Y-AXIS)

ELEVATION VIEW
INSTRUMENTATION LOCATIONS
SCALE: $^{3}/_{32}$" = 1'-0"

KEY

- ▲ DISPLACEMENT (LVDT OR STRING POT)
- ■ LOAD CELL
- — STRAIN GAGE
- ◆ VIBRATING WIRE STRAIN GAGE
- ✖ INCLINOMETER

NAMING SYSTEM:
T - LD - F - H, where:

T = type of instrumentation
- Dx, Dy, Dz : displacement transducer along x, y, and z-axis (respectively)
- Sx, Sz : string potentiometer along x, and z-axis (respectively)
- F : force
- VW : vibrating wire strain gage
- SG : strain gage
- Rx, Ry : rotation about x and y-axis (respectively)

LD = longitudinal distance from midspan
- N0 : at midspan
- N21 : 21' North of midspan
- S21 : 21' South of midspan, etc.

F = face of beam
- E : East
- W : West
- C: Center

H = height
- 0 : mount to bottom of beam
- 2 : mount 2" from bottom, etc.

For example, Dx-S21-W-38 : measures displacement along the x-axis, 21' South of midspan, mounted on the West face, 38" from the bottom of the beam.

INSTRUMENTATION SUMMARY:

INCLINOMETER
Rx-N0-C-78
Ry-N0-C-78

LVDT (50mm STROKE):

Dx-S51-W-2	Dx-N51-W-2
Dx-S51-W-76	Dx-N51-W-76
Dy-S51-E-2	Dy-N51-E-2
Dy-S51-W-2	Dy-N51-W-2
Dz-S51-E-2	Dz-N51-E-2
Dz-S51-W-2	Dz-N51-W-2

LVDT (100mm STROKE):
Dx-S21-W-38
Dx-N0-W-38
Dx-N21-W-38

LVDT (200mm STROKE):
Dx-S0-W-38

STRING POTENTIOMETER:
Sx-N0-C-0
Sz-N0-C-0
Sx-N0-C-78

LOAD CELL
(50 KIP CAPACITY):
F-S15-E
F-S15-C
F-S15-W
F-N15-E
F-N15-C
F-N15-W

VIBRATING WIRE
STRAIN GAGE
(CAST IN CONCRETE):
VW-S15-E-6.5
VW-S15-W-6.5
VW-N15-E-6.5
VW-N15-W-6.5

STRAIN GAGE (60 mm):
SG-N0-E-2
SG-N0-E-76
SG-N0-W-2
SG-N0-W-76

SG-S12-E-2	SG-N12-E-2
SG-S12-E-76	SG-N12-E-76
SG-S12-W-2	SG-N12-W-2
SG-S12-W-76	SG-N12-W-76
SG-S14-E-0	SG-N14-E-0
SG-S14-W-0	SG-N14-W-0
SG-S16-E-0	SG-N16-E-0
SG-S16-W-0	SG-N16-W-0
SG-S24-E-2	SG-N24-E-2
SG-S24-E-76	SG-N24-E-76
SG-S24-W-2	SG-N24-W-2
SG-S24-W-76	SG-N24-W-76
SG-S36-E-2	SG-N36-E-2
SG-S36-E-76	SG-N36-E-76
SG-S36-W-2	SG-N36-W-2
SG-S36-W-76	SG-N36-W-76

Experimental Validation of Bracing Recommendations for Long-Span Concrete Girders

Instrumentation summary | *2011-10-27* | *University of Florida* | *Sheet 01 of 11*

Revisions:

REV 1 : 2011-10-27

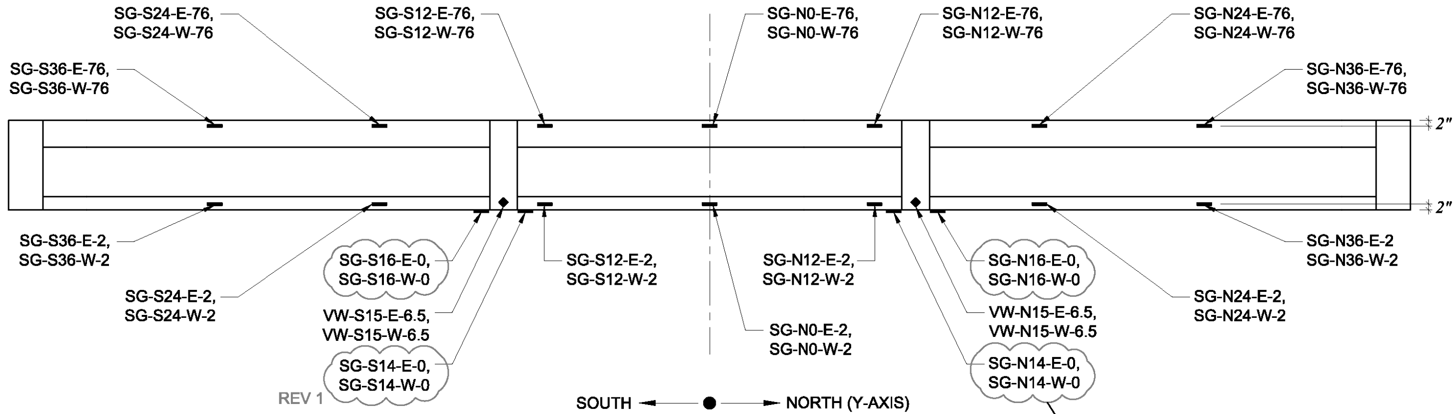

ELEVATION VIEW - STRAIN INSTRUMENTATION SUMMARY
DISPLACEMENT AND LOAD INSTRUMENTATION OMITTED FOR CLARITY
SCALE: $\frac{3}{32}$" = 1'-0"

NOTE: PLACE ALL OF THE GAGES AT THE BOTTOM (N14, N16, S14, S16) ON PRECAST SIDE, AS CLOSE TO THE INTERFACE BETWEEN THE PRECAST SEGMENT AND THE CLOSURE POUR AS POSSIBLE. PLACE EACH GAGE 1" FROM THE EDGE OF THE BEAM (~6" APART).

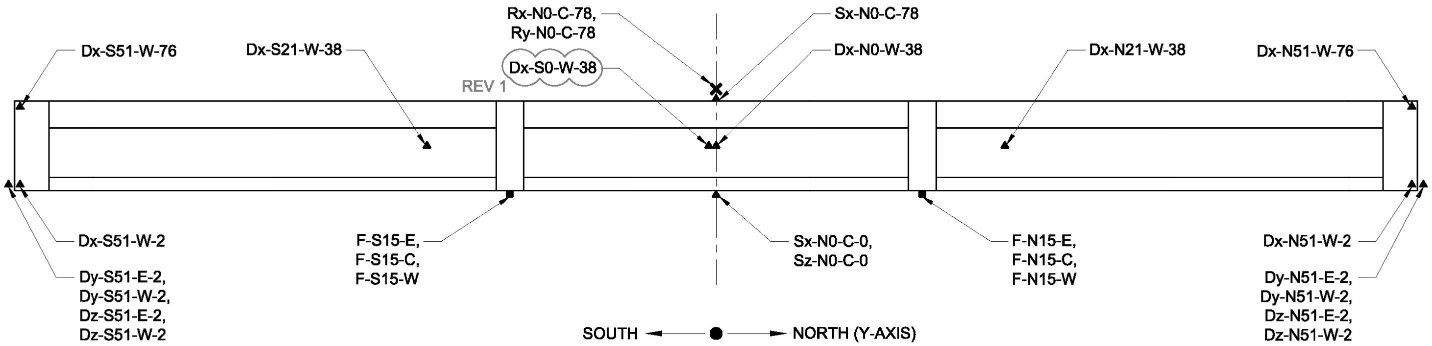

ELEVATION VIEW - DISPLACEMENT AND LOAD INSTRUMENTATION SUMMARY
STRAIN INSTRUMENTATION OMITTED FOR CLARITY
SCALE: $\frac{3}{32}$" = 1'-0"

Experimental Validation of Bracing Recommendations for Long-Span Concrete Girders

Instrumentation locations	*2011-10-27*	*University of Florida*	*Sheet 02 of 11*

Revisions:

REV 1 : 2011-10-27

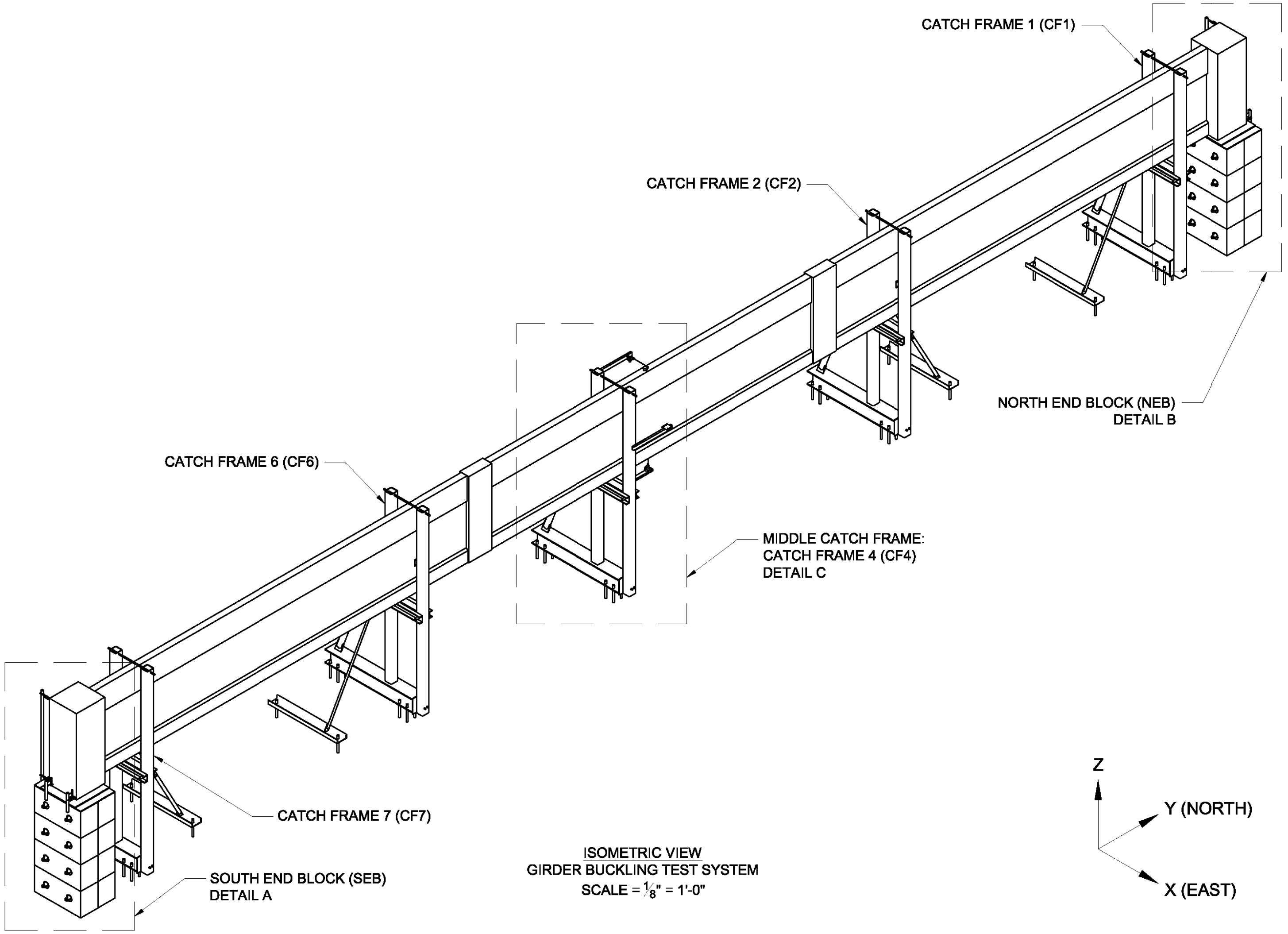

ISOMETRIC VIEW
GIRDER BUCKLING TEST SYSTEM
SCALE = $\frac{1}{8}$" = 1'-0"

Experimental Validation of Bracing Recommendations for Long-Span Concrete Girders				*Revisions:*	*REV 1 : 2011-10-27*	
Instrumentation plan overview	*2011-10-27*	*University of Florida*	*Sheet 03 of 11*			

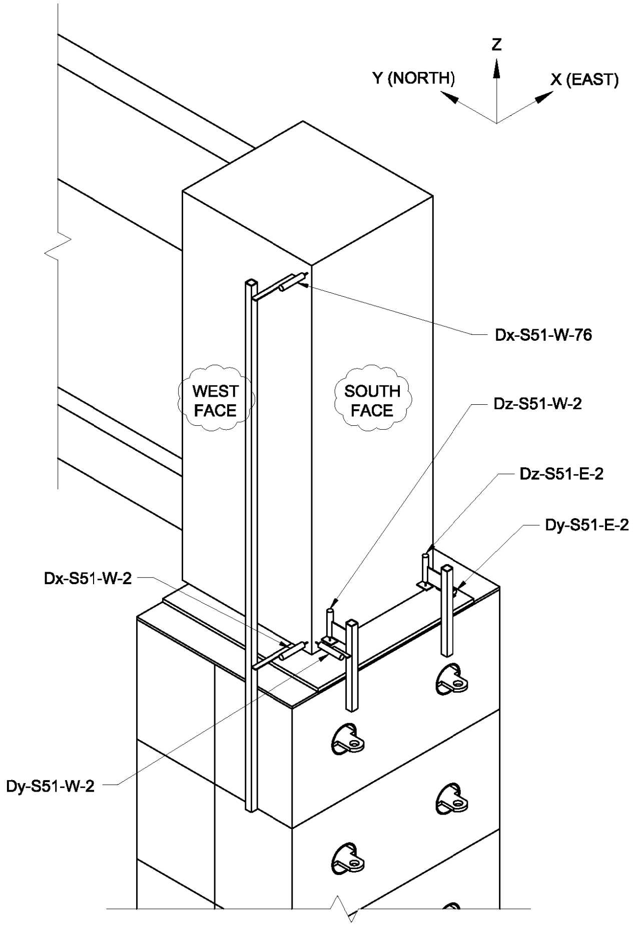

DETAIL A
SOUTH END BLOCK ISOMETRIC VIEW
SCALE: ½"=1'-0"

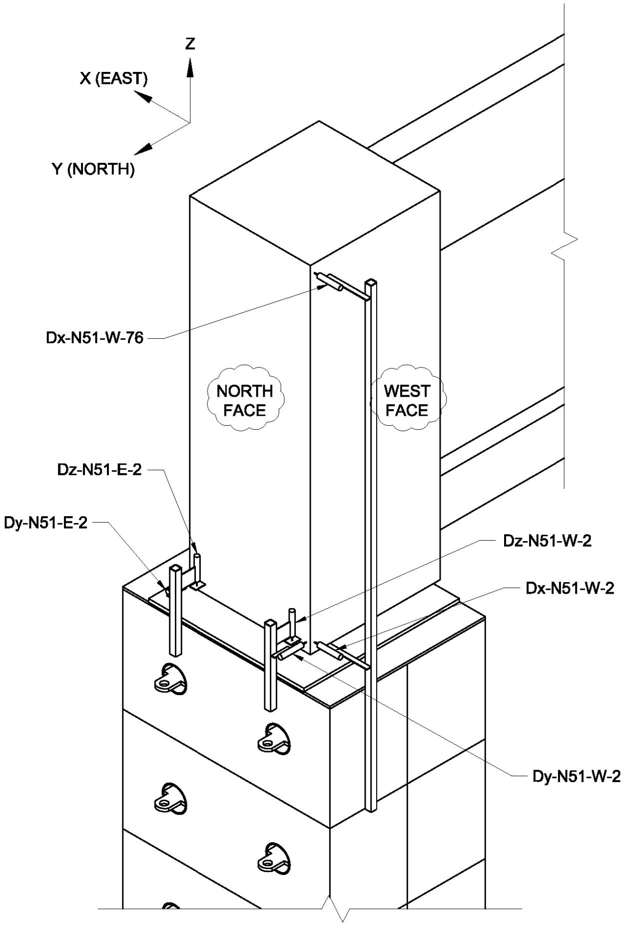

DETAIL B
NORTH END BLOCK ISOMETRIC VIEW
SCALE: ½"=1'-0"

Experimental Validation of Bracing Recommendations for Long-Span Concrete Girders				*Revisions:*	*REV 1 : 2011-10-27*	
End block LVDTs	*2011-10-27*	*University of Florida*	*Sheet 04 of 11*			

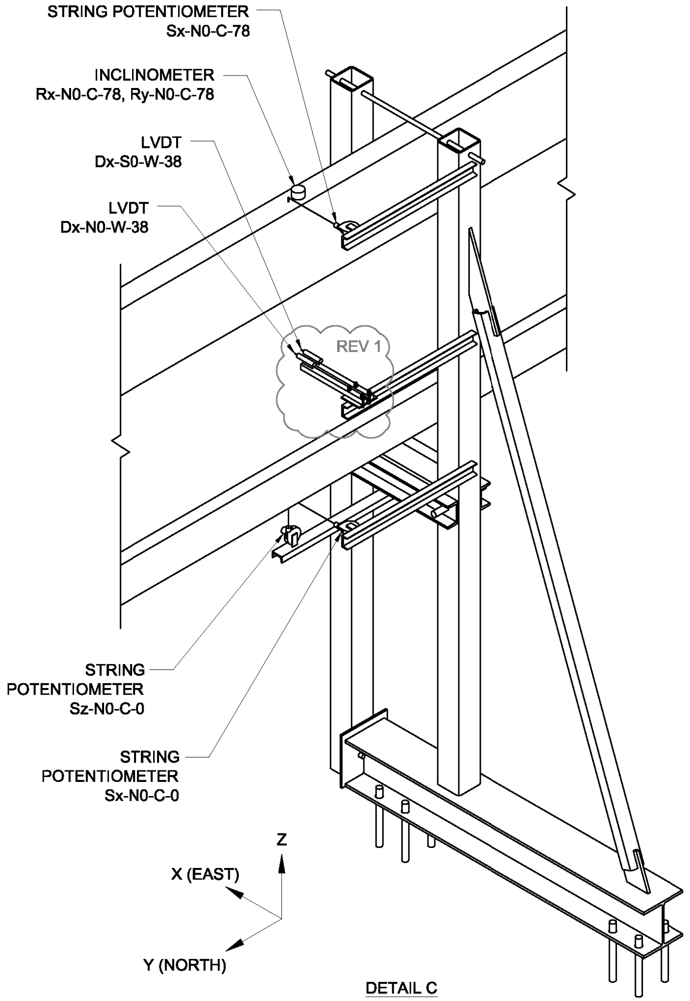

DETAIL C
MIDDLE CATCH FRAME (CF4)
SCALE = $\frac{3}{8}$" = 1'-0"

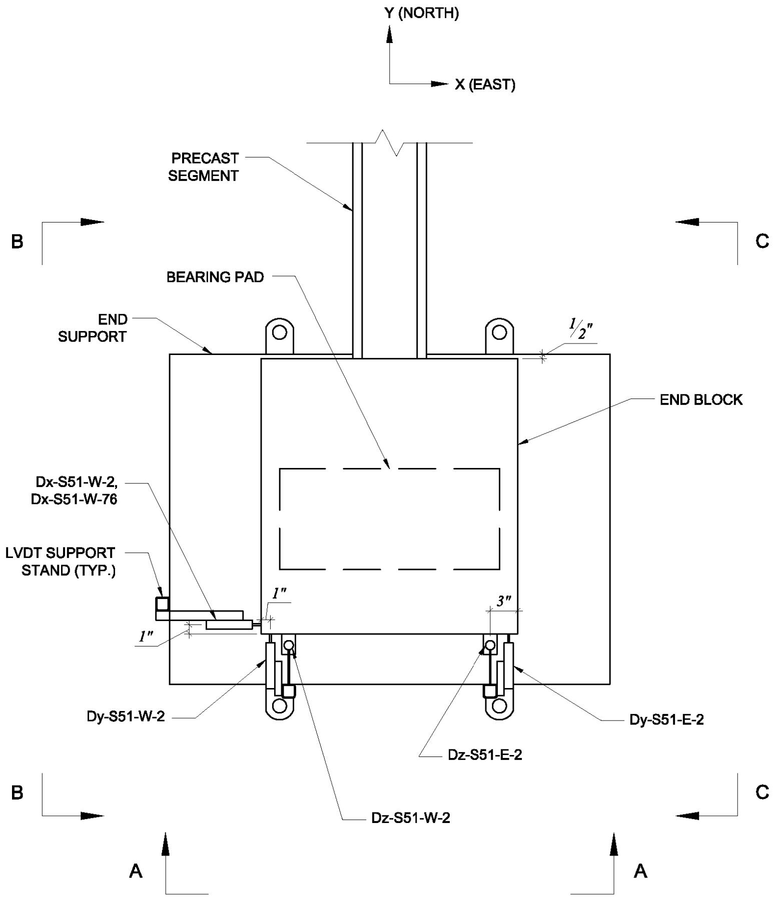

PLAN VIEW
SOUTH END SUPPORT
SCALE: $\frac{3}{4}$"=1'-0"

Experimental Validation of Bracing Recommendations for Long-Span Concrete Girders				*Revisions:*	*REV 1 : 2011-10-27*	
Instrumentation plan	*2011-10-27*	*University of Florida*	*Sheet 05 of 11*			

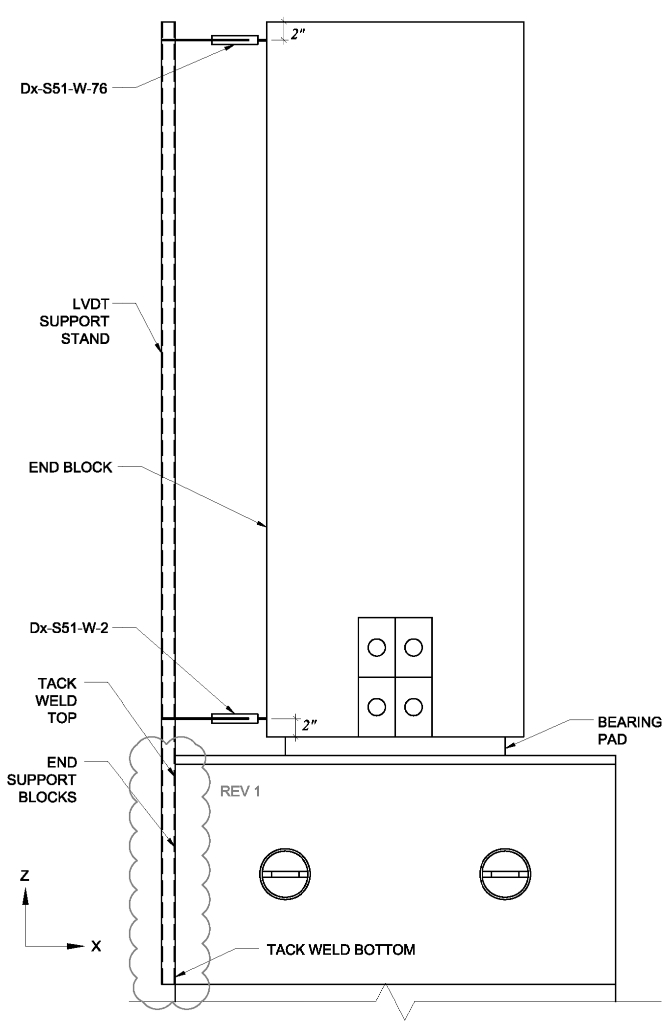

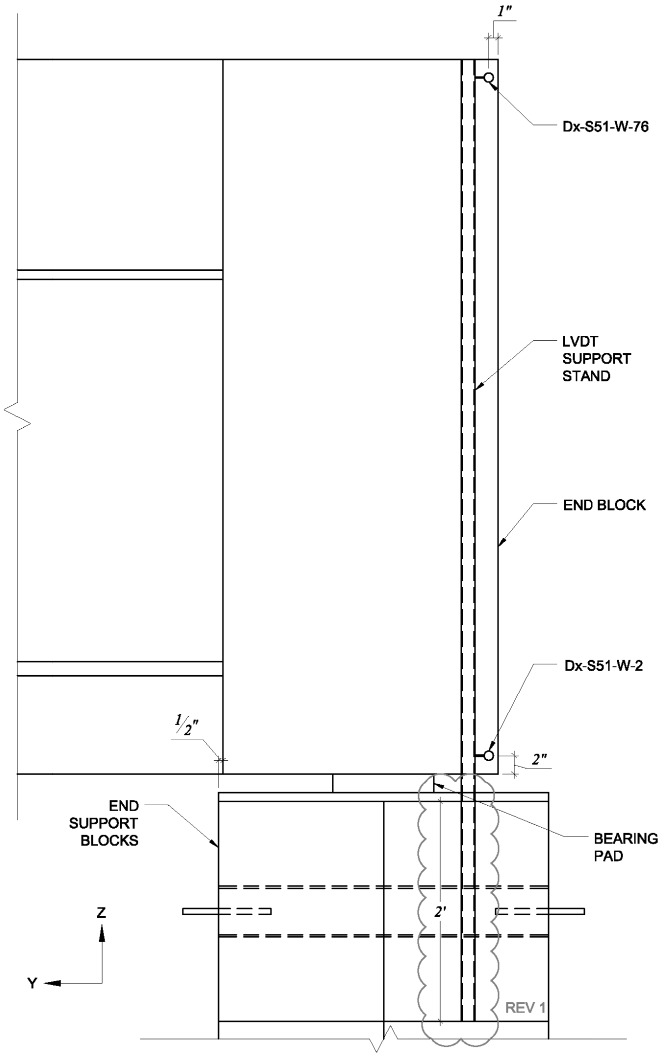

Experimental Validation of Bracing Recommendations for Long-Span Concrete Girders

End block LVDTs: Dx | *2011-10-27* | *University of Florida* | *Sheet 06 of 11*

Revisions:

REV 1 : 2011-10-27

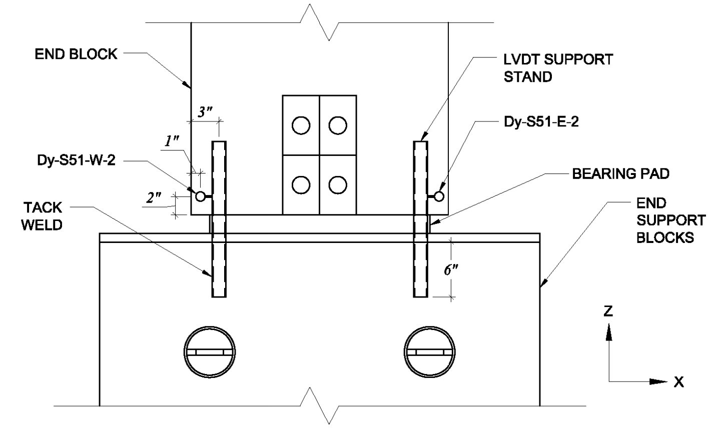

SOUTH END SUPPORT - ELEVATION VIEW A-A
(Dx AND Dz OMITTED FOR CLARITY)
SCALE: ¾"=1'-0"

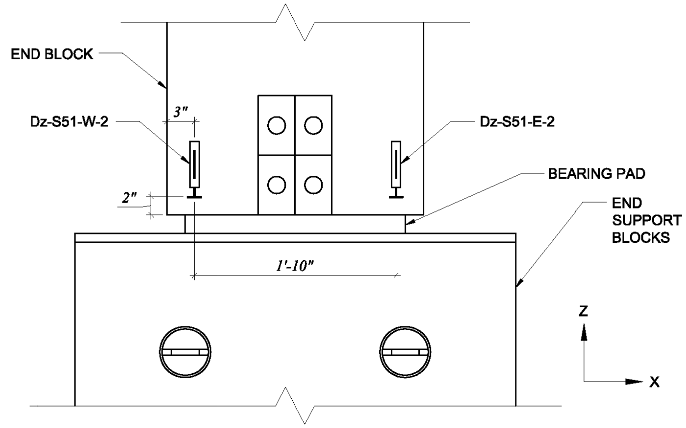

SOUTH END SUPPORT - ELEVATION VIEW A-A
(Dx AND Dy OMITTED FOR CLARITY)
SCALE: ¾"=1'-0"

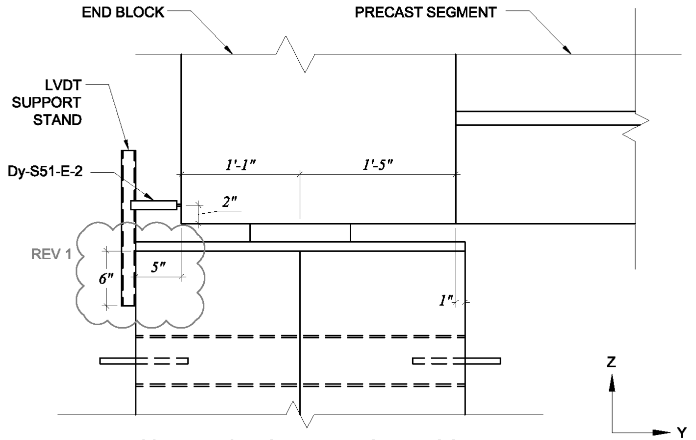

SOUTH END SUPPORT - ELEVATION VIEW C-C
(Dx AND Dz OMITTED FOR CLARITY)
SCALE: ¾"=1'-0"

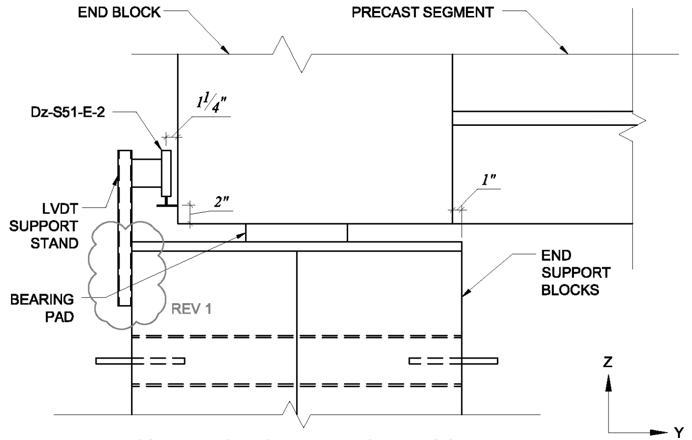

SOUTH END SUPPORT - ELEVATION VIEW C-C
(Dx AND Dy OMITTED FOR CLARITY)
SCALE: ¾"=1'-0"

Experimental Validation of Bracing Recommendations for Long-Span Concrete Girders				*Revisions:*	*REV 1 : 2011-10-27*	
End block LVDTs: Dy and Dz	*2011-10-27*	*University of Florida*	*Sheet 07 of 11*			

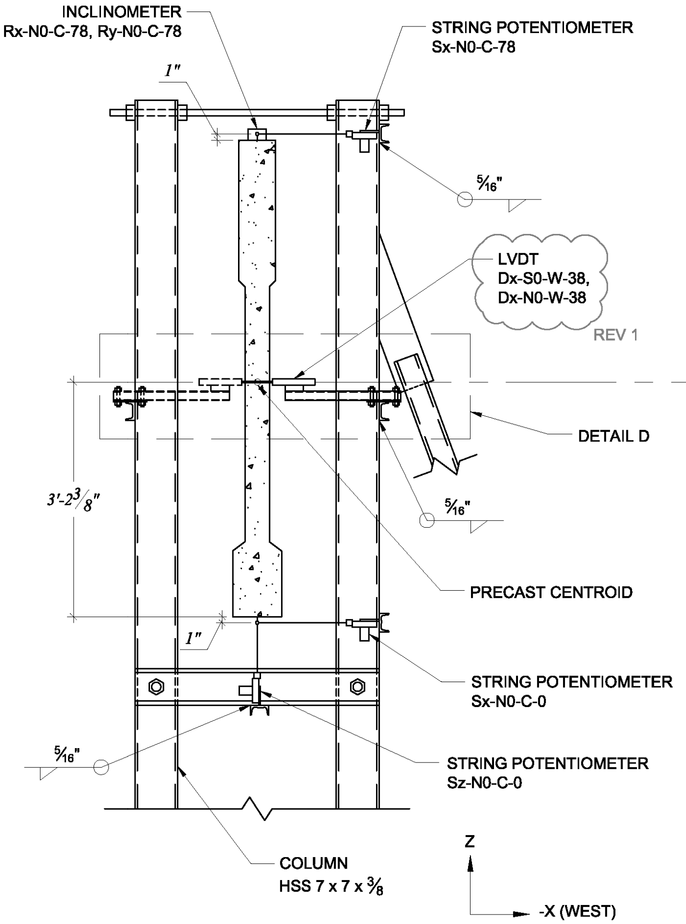

ELEVATION VIEW
MIDDLE CATCH FRAME (CF4)
SCALE = ½" = 1'-0"

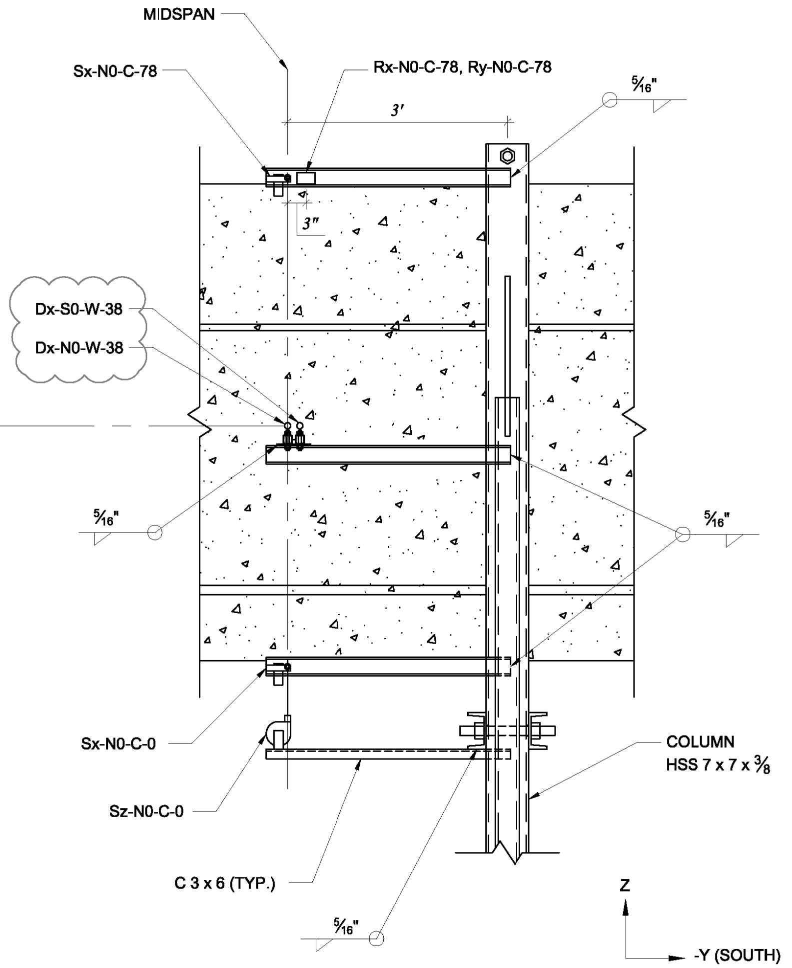

END VIEW
MIDDLE CATCH FRAME (CF4)
SCALE = ½" = 1'-0"

Experimental Validation of Bracing Recommendations for Long-Span Concrete Girders				*Revisions:*	*REV 1 : 2011-10-27*	
Catch frame 4 instrumentation	*2011-10-27*	*University of Florida*	*Sheet 08 of 11*			

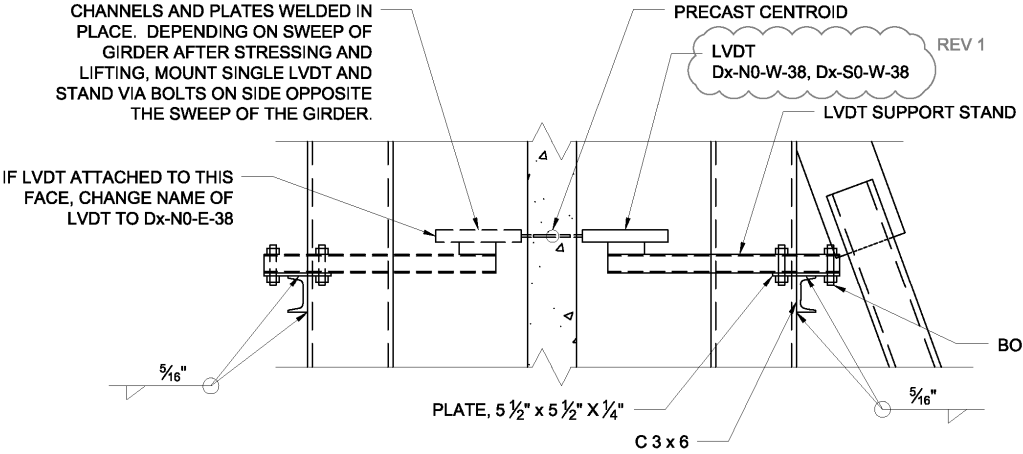

DETAIL D: ELEVATION VIEW
LVDT CONNECTION AT MIDDLE CATCH FRAME (CF4)
SCALE: 1"=1'-0"

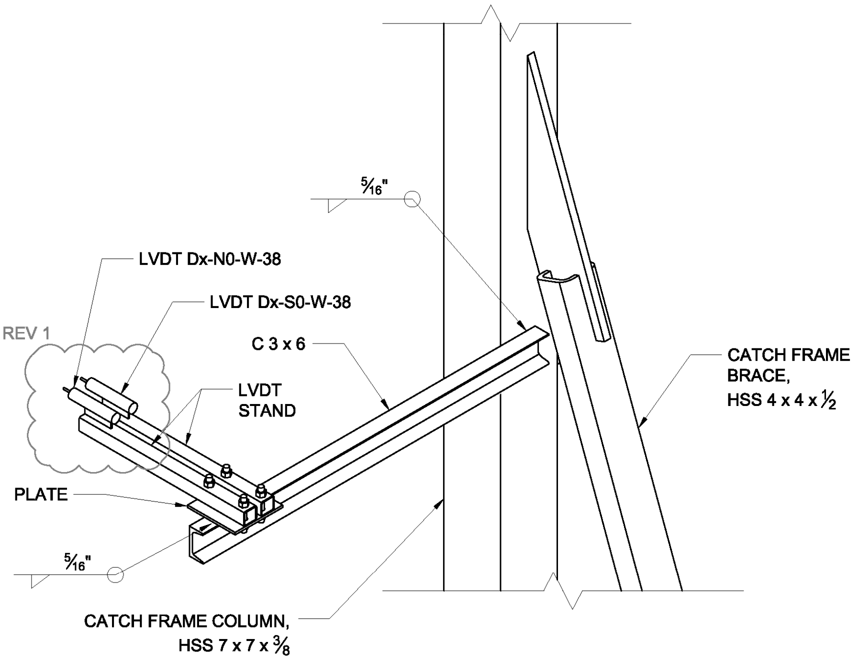

DETAIL D: ISOMETRIC VIEW
LVDT CONNECTION AT MIDDLE CATCH FRAME (CF4)
SCALE: 1"=1'-0"

Experimental Validation of Bracing Recommendations for Long-Span Concrete Girders			
Catch frame 4 instrumentation details	*2011-10-27*	*University of Florida*	*Sheet 09 of 11*
Revisions:	*REV 1 : 2011-10-27*		

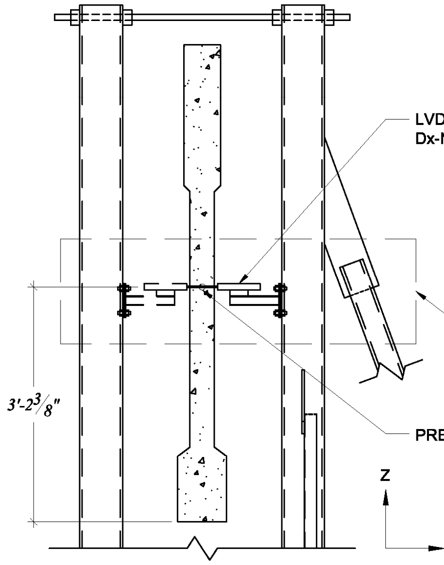

ELEVATION VIEW
CATCH FRAMES 2 AND 6
SCALE = ½" = 1'-0"

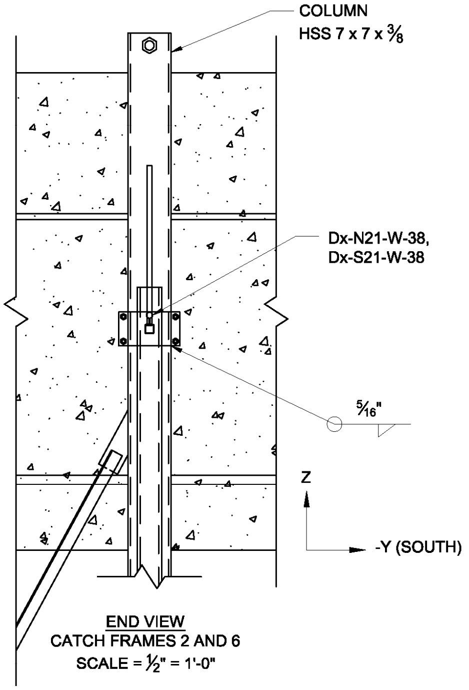

END VIEW
CATCH FRAMES 2 AND 6
SCALE = ½" = 1'-0"

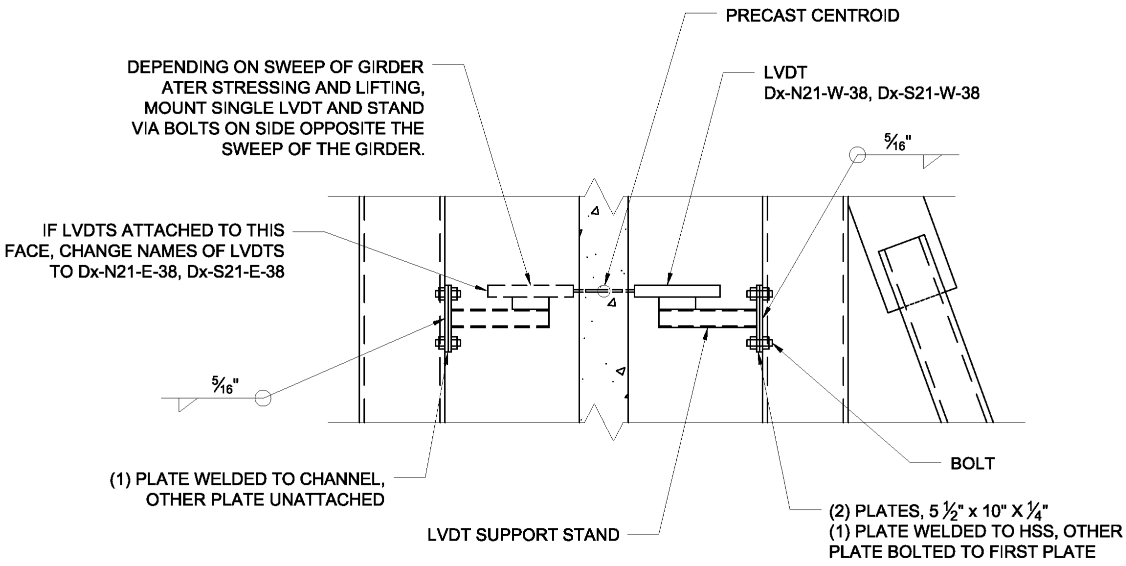

DETAIL E
LVDT CONNECTION AT CATCH FRAMES 2 AND 6
SCALE: 1"=1'-0"

Experimental Validation of Bracing Recommendations for Long-Span Concrete Girders			
CF2 and CF4 instrumentation	*2011-10-27*	*University of Florida*	*Sheet 10 of 11*
Revisions:	*REV 1 : 2011-10-27*		

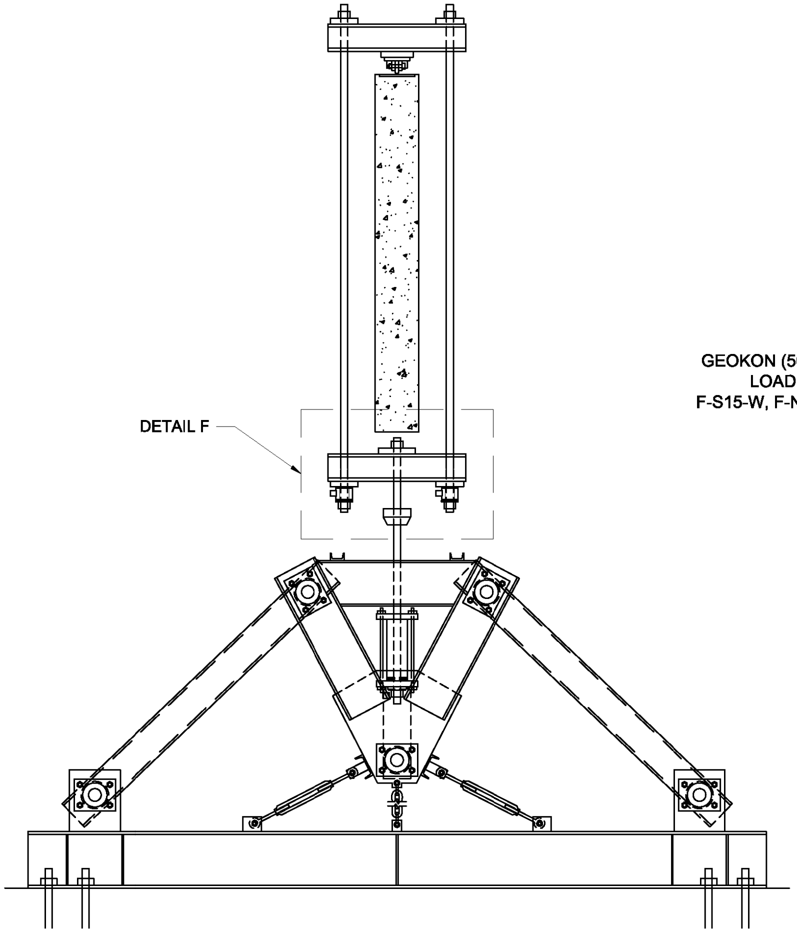

GRAVITY LOAD SIMULATOR AND LOAD FRAME
ELEVATION VIEW
SCALE: $\frac{3}{8}$"=1'-0"

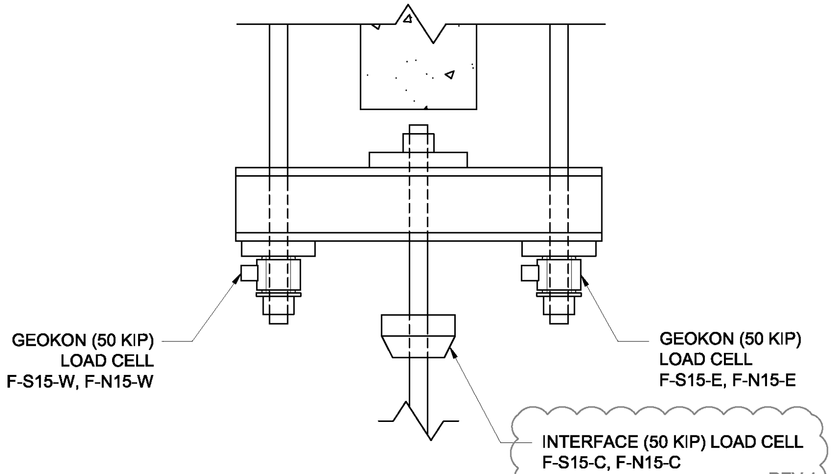

DETAIL F
SCALE: 1"=1'-0"

Experimental Validation of Bracing Recommendations for Long-Span Concrete Girders				*Revisions:*	*REV 1 : 2011-10-27*	
Load frame instrumentation	*2011-10-27*	*University of Florida*	*Sheet 11 of 11*			